In pattern forming systems, such as out-of-plane magnetized ferromagnetic samples, magnetic patterns occur in a variety of shapes and sizes. The mechanism of pattern transformation is, however, not well understood due to the lack of experiments featuring sufficient spatial as well as temporal resolution. Since thermal fluctuations can be regarded as the main driving force for domain pattern transformations, a non-stroboscopic measurement technique is necessary. For this purpose, a photoemission electron microscope was equipped to obtain magnetic contrast by the effect of threshold photoemission magnetic circular dichroism. This measurement setup offers a high spatial (<100nm) as well as temporal (<450μs) resolution and was used to investigate the magnetic domain pattern of the ferromagnetic model system of ultrathin Fe and Ni films on Cu(001). Moreover, the transformation of domain patterns triggered by changes of external stimuli could be recorded and investigated. In addition, the fingerprint of different, local domain patterns (topological defects) have been analyzed with respect to thermal fluctuations. The threshold photoemission magnetic circular dichroism is explained in detail by a one-step as well as a three-step photoemission model calculation within the framework of LSDA+DMFT band structure calculations.

Universitätsverlag Regensburg

ISBN 978-3-86845-098-9

gefördert von:

Alumni der physikalischen Fakultät der Universität Regensburg e.V.

Universität Regensburg

Matthias Kronseder

Dissertationsreihe Physik - Band 32

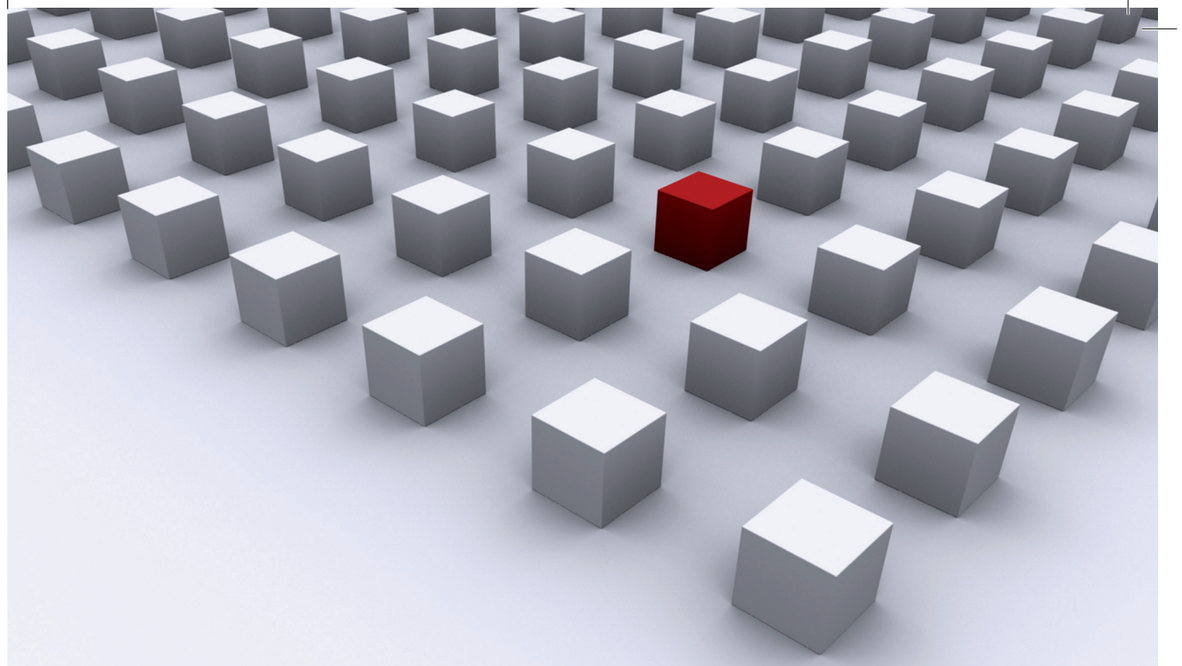

Matthias Kronseder

Pattern evolution and fluctuations in a magnetic model system

Universitätsverlag Regensburg

Matthias Kronseder

32

Dissertationsreihe Physik

Matthias Kronseder

Pattern evolution and fluctuations in a magnetic model system

Pattern evolution and fluctuations in a magnetic model system

Dissertation zur Erlangung des Doktorgrades der Naturwissenschaften (Dr. rer. nat.)
der Fakultät für Physik der Universität Regensburg
vorgelegt von

Matthias Kronseder
Pfakofen
2013

Die Arbeit wurde von Prof. Dr. Christian H. Back angeleitet.
Das Promotionsgesuch wurde am 22.11.2012 eingereicht.

Prüfungsausschuss:	Vorsitzende:	Prof. Dr. Karsten Rincke
	1. Gutachter:	Prof. Dr. Christian H. Back
	2. Gutachter:	Prof. Dr. Jascha Repp
	weiterer Prüfer:	Prof. Dr. Franz Gießibl

Dissertationsreihe der Fakultät für Physik der Universität Regensburg, Band 32

Herausgegeben vom Präsidium des Alumnivereins der Physikalischen Fakultät:
Klaus Richter, Andreas Schäfer, Werner Wegscheider, Dieter Weiss

Matthias Kronseder

Pattern evolution and fluctuations in a magnetic model system

Universitätsverlag Regensburg

Bibliografische Informationen der Deutschen Bibliothek.
Die Deutsche Bibliothek verzeichnet diese Publikation
in der Deutschen Nationalbibliografie. Detailierte bibliografische Daten
sind im Internet über http://dnb.ddb.de abrufbar.

1. Auflage 2013

Leibnizstraße 13, 93055 Regensburg

Konzeption: Thomas Geiger
Umschlagentwurf: Franz Stadler, Designcooperative Nittenau eG
Layout: Matthias Kronseder
Druck: Docupoint, Magdeburg
ISBN: 978-3-86845-098-9

Weitere Informationen zum Verlagsprogramm erhalten Sie unter:
www.univerlag-regensburg.de

Pattern evolution and fluctuations in a magnetic model system

Dissertation
zur Erlangung des Doktorgrades
der Naturwissenschaften
(Dr. rer. nat.)
der Fakultät für Physik
der Universität Regensburg

vorgelegt von

Matthias Kronseder

Diplom Physiker
aus Pfakofen

Januar 2013

Promotionsgesuch eingereicht am: 22.11.2012

Die Arbeit wurde angeleitet von: Prof. Dr. Christian H. Back

Prüfungsausschuss:	Vorsitzender:	Prof. Dr. Karsten Rincke
	1. Gutachter:	Prof. Dr. Christian H. Back
	2. Gutachter:	Prof. Dr. Jascha Repp
	weiterer Prüfer:	Prof. Dr. Franz Gießibl

Contents

Chapter 1

Introduction and Measurement Technique

1.1 Introduction

In ferromagnetic ultra thin films a strong perpendicular anisotropy can cause the magnetization vector to be aligned perpendicular to the film plane. The resulting competition between the positive, short range exchange interaction and the negative but long range dipole interaction leads to the spatial separation of spin-up and spin-down states on mesoscopic as well as macroscopic length scales. As a result the order parameter is modulated on length scales determined by the strength of the competing interactions. Magnetic pattern formation can manifest itself in a variety of shapes and sizes. The most widely studied phases are stripe and bubble domains. According to theory [1], the ground state pattern in zero applied magnetic field is the domain pattern with stripes aligned in parallel. In such systems thermal energy is expressed by excitations, such as topological defects or instabilities of the stripes, which reduce the order of the system. The proliferation and the increase in density of these excitations with increasing temperature eventually leads to the transformation of a stripe domain pattern into a less ordered domain structure with smaller domain width. Only little is known about the mechanisms of pattern transformations, its dynamics and the role of thermal fluctuations in truly 2D systems. What is more, the competing interactions constitute in a natural manner a source for frustration, since the energy arising from both interactions cannot be minimized simultaneously. It has been shown [2] that the smallest amount of disorder in combination with this uniform frustration leads to the generation of a vast amount of metastable states with nearly equal energies. This phenomenon is referred to as self-generated glassiness. This glassy behav-

ior, in turn, is responsible for the appearance of non-equilibrium states as well as large relaxation times for any pattern change or even for individual domain wall movements.

Pattern formation caused by competing interactions is omnipresent in nature [3–5] and evidenced e.g. in Turing-type [6–10] reaction-diffusion systems like the skins of animals, or completely different systems ranging from liquid crystals to high-temperature superconductors. Since all these diverse pattern forming systems show similar behavior in the vicinity of phase transitions, the phenomenon of universality classes can be applied, where each member of a universality class shows the exact same critical behavior. A thorough understanding of one of these systems may therefore also lead to a better understanding of others.

In this thesis a new approach for fast acquisition of images with magnetic contrast has been successfully implemented in a high resolution, wide-field photoemission electron microscope. This approach comprises a large magnetic contrast (up to $\sim 10\,\%$), first published in 2006 [11], as well as a table-top experimental setup capable of image acquisition with magnetic contrast at frame rates of up to several thousand frames per second and at a spatial resolution of about $\leq 100\,\mathrm{nm}$. Magnetic circular dichroism in the vicinity of the threshold of photoemission is the key element of this new technique and is theoretically described within this thesis [12]. Results of band structure calculations and the successful application of two photoemission models are presented in chapters 3 and 4.

The static properties of the model system Fe/Ni/Cu(001) are investigated in chapter 6 and 7 (in particular section 7.1). This magnetic model system combines a large magnetic contrast as well as a magnetic out-of-plane region in a small thickness range, hence exhibits a spin-reorientation transition. Emphasis is placed on the evolution of the domain width due to variation of external parameters such as temperature, magnetic field and the perpendicular anisotropy. Based on the exponential dependence of the domain width on these parameters, a comprehensive model for the evolution of the equilibrium domain width and for the dynamic properties of the non-equilibrium domain width is developed and successfully applied to experiments. Moreover, the generation of a metastable state in the domain pattern on macroscopic length scales and its subsequent decay into the ground state, which is strongly reminiscent of the abrupt condensation in supercooled liquids, is experimentally achieved and explained by this model.

Despite vast experimental and theoretical investigations of the static properties of domain patterns on the one hand, and ultra fast dynamics of the underlying spin system (in the range of ∼ns and below) on the other hand, the dynamics in the intermediate time scale (from ∼ns to minutes) has largely remained "terra incognita" for pattern forming magnetic systems. However, exactly this region is crucial for the process of pattern formation as well

as pattern transformation. The new experimental setup now provides a link between these two limiting time scales. What is more, the dynamical fingerprint of individual topological defects as well as of large domain areas is investigated on various time scales (ranging from hundreds of μs to minutes). Needless to say that stroboscopic imaging techniques are not useful for the experimental investigation of statistical processes such as fluctuations.

1.2 Measurement Technique: TP-MCD-PEEM

Although the measurement setup used in this thesis is composed mostly from standard parts such as the photoemission electron microscope (PEEM), a short introduction to this

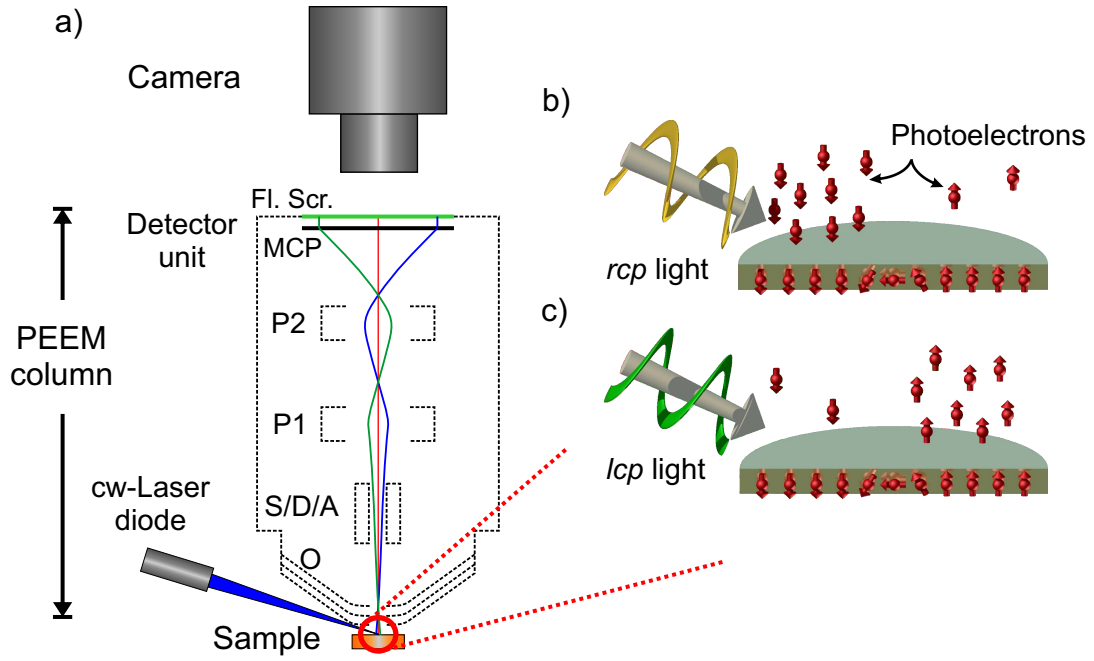

Figure 1.1: *a) The measurement setup comprises the illumination unit with a high-power* cw*-Laser diode, a standard PEEM and a camera, in our case a low-noise, high-sensitivity camera as well as a high-speed camera. The PEEM comprises the objective lens (O), Stigmator/Deflector/Apertures (S/D/A) and two projective lenses (P1, P2). In b), a ferromagnetic sample with, for instance, a single domain wall leads to different intensities of the local photoemission current when illuminated with circularly polarized light. The signal is opposite for the two circularities, i.e. right (left) circular polarization [*rcp *(*lcp*)] b) and c), respectively.*

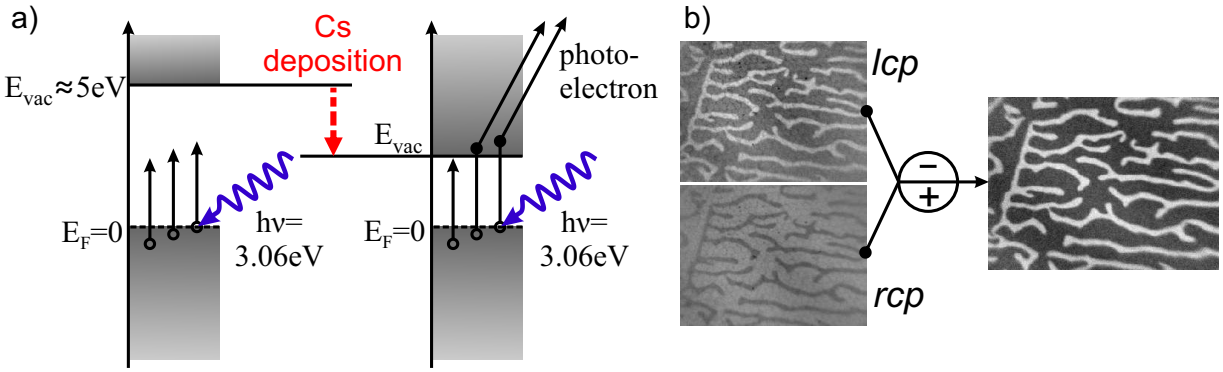

Figure 1.2: *a) Since high-power* cw *laser diodes are only available in the visible light range, the work function of the ferromagnetic sample* E_{vac} *has to be lowered, e.g. by depositing Cs on top of the sample. By illuminating the sample with* rcp *(*lcp*) light, the magnetic state is already visible. In order to reduce the non-magnetic contrast the TP-MCD asymmetry is calculated from two images taken with* rcp *and* lcp *illumination (FOV* $160 \times 120 \mu m^2$*, with an applied magnetic field of 0.7 Oe).*

ensemble of techniques will be given at the beginning of this thesis. Photoelectrons are generated by illuminating the metallic sample to be investigated with light. The electron microscope images and magnifies the distribution of these photoelectrons onto a detection unit. The detection unit is a multi-channel electron multiplier (MCP) and a fluorescence screen; finally a CCD-camera records the image. This is schematically shown in Fig. 1.1 a). Within this thesis two different cameras are used. The first one is a low noise, high-sensitivity camera (Hamamatsu, C6464-05G) and the second one is a high-speed camera (VisionResearch, Phantom V200). In order to obtain a large photocurrent necessary for fast image acquisitions, a high-power illumination unit is required. In addition, the effect of space charge has to be as low as possible, in order to avoid blurring of the image and to operate at the maximum resolution of the microscope. Hence, the operation of high-power *pulsed* lasers with low repetition rates is improper for this purpose. In contrast, high-power *cw*[1] laser diodes are available in the visible range, in addition they are cheap, robust and easy to use.

Magnetic contrast is obtained by exploiting the threshold photoemission magnetic circular dichroism (TP-MCD) effect, which roughly represents the MCD-effect in the vicinity of the Fermi-edge instead of extracting electrons from core shells as done by X-ray magnetic circular dichroism. This contrast technique will be thoroughly described in chapters 3 and 4. Fig. 1.1 b) and c) schematically show the contrast mechanism. For a ferromagnetic sample with, for instance, a single domain wall, the illumination with circularly polar-

[1] *cw* means continuous-wave.

ized light leads to different intensities of the photocurrents obtained from the individual domains. Reversing the circularity reverses the local photocurrent intensities. Obtaining two images with different circularities of light and applying the definition of the MCD-asymmetry, which will be introduced in Eq. (3.3), reveals the magnetic structure of the sample and eliminates any non-magnetic contrast, as shown in Fig. 1.2 b).

The investigated samples are single-crystalline, ultra thin, ferromagnetic Ni and Fe/Ni films grown on the substrate Cu(001). These samples have work function values around $\sim 5\,\mathrm{eV}$. Unfortunately, there are no high-power *cw* lasers available for this energy range. Instead, in this thesis a low cost, high power *cw* laser diode operating at 405 nm (3.06 eV) with an output power of up to $\sim 600\,\mathrm{mW}$ is used. In order to generate photoelectrons a reduction of the work function of the samples is required. This can be achieved, for instance, by depositing small amounts of metallic elements possessing a lower work function on top of the sample. In our case the alkali metal Cesium (Cs) is used, since the effect of reducing the work function is very stable compared to other metals like Ho or Gd and the evaporation can be done during PEEM operation. However, the deposition of Cs adatoms also affects the magnetic properties in such a way that the ratio between surface anisotropy and exchange interaction of the ferromagnetic thin films is changed. This effect is investigated in detail in section 7.1.3.

Chapter 2

Summary of Results

In the present work a new approach for the investigation of thermal fluctuations in domain patterns has been successfully implemented. The magnetic contrast technique is theoretically described in the first part of this thesis, where the main result is shown in Fig. 2.1 a)-d). The threshold photoemission magnetic circular dichroism effect (TP-MCD) of Ni/Cu(001) amounts to about $\sim 10\,\%$ magnetic asymmetry, as shown in Fig. 2.1 b). In collaboration with the theory group of H. Ebert [13], the TP-MCD effect of Ni/Cu(001) was theoretically described by band structure calculations in the framework of dynamical mean field theory within the local spin density approximation (LSDA-DMFT) in combination with photoemission calculations (one-step photoemission model). The results, as

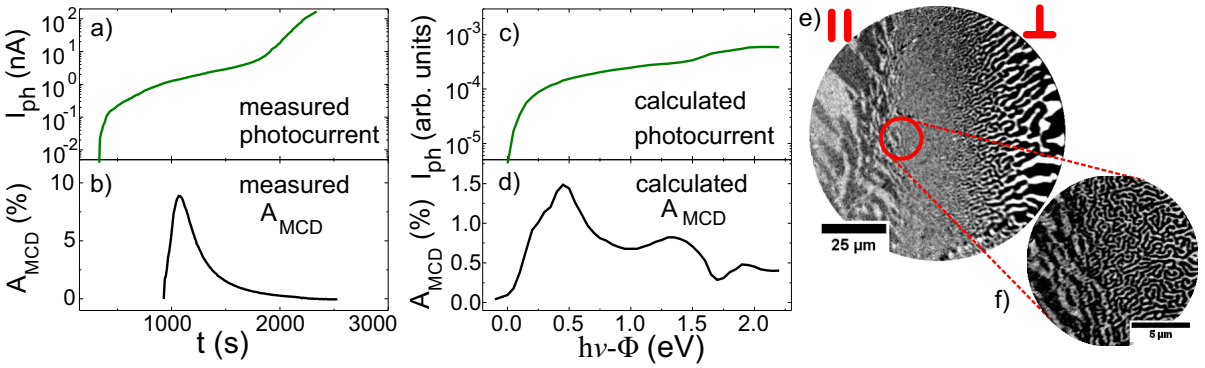

Figure 2.1: *TP-MCD effect and TP-MCD PEEM images.*

shown in Fig. 2.1 c) and d), are in qualitative agreement with experiments (Fig. 2.1 a) and b)) and explain the large magnetic contrast as well as the rapid decay beyond $\sim 0.5\,\mathrm{eV}$ electron kinetic energy due to the non-dichroic signal from surface resonances. In addition, a three-step photoemission model, where the spin-polarization of the initial photoemission states is calculated, is successfully applied and provides further insight into the origin of this magnetic dichroism.

The large dichroic effect allows to record magnetic domain patterns using only one circularity of the light. This is particularly important when domain dynamics are recorded at high frame rates. The large magnetic contrast of the system Fe/Ni/Cu(001) allows the observation of in-plane as well as out-of-plane domains, as shown in Fig. 2.1 e) and f). Consequently, the dependence of the spin-reorientation transition on temperature can be measured (Fig. 2.2 a)). In particular, the movement of the onset of the in-plane magnetization while heating the sample is measured, which has been predicted by theory but has so far not been confirmed experimentally. Furthermore, the dependence of the domain width on temperature and film thickness of ultra thin ferromagnetic Fe/Ni/Cu(001) samples is measured (Fig. 2.2 b)). Based on the evolution of the domain width and the movement

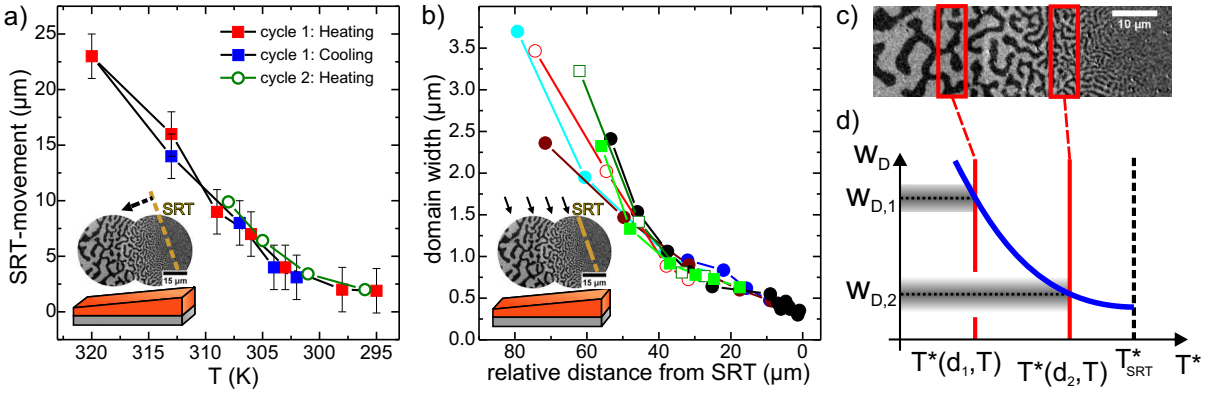

Figure 2.2: *Thickness and temperature dependence of the domain structure and model description.*

of the spin-reorientation transition with respect to variations in film thickness and temperature, a comprehensive model for the evolution of the equilibrium and non-equilibrium domain width in the vicinity of the SRT is developed, see Fig. 2.2 d). The effect of thermal energy on the local domain width leads to variations of the domain width, as can be seen in the red slices in Fig. 2.2 c). This variation is indicated by the grey shaded area in Fig. 2.2 d). In any real magnetic sample the energy landscape in configuration space is corrugated due to pinning sites. In out-of-plane magnetized samples, however, the competition between exchange and dipole interaction may lead to a uniform frustration and thereby to a large amount of metastable states (self-generated glassiness). It is still a subject of controversy which kind of pinning sites (structural defects or the glassy nature) dominates the energy landscape.

Any pattern transformation driven by thermal fluctuations has a certain finite rate of change determined by thermal energy and the local corrugation of the energy landscape. As a consequence of a parameter change faster than the inherent reaction time, a

metastable state of the whole domain pattern emerges. This can be realized by cooling the system and subsequently decreasing the surface anisotropy abruptly. At room temperature a reduction of the surface anisotropy is accompanied by a transformation of the domain pattern into a smaller domain structure. At reduced temperatures, however, the decay into the ground state of the domain pattern occurred in form of a transition front, as shown in the left part of Fig. 2.3. This transition front is strongly reminiscent to the condensation front in supercooled liquids. The time delay between each image shown in

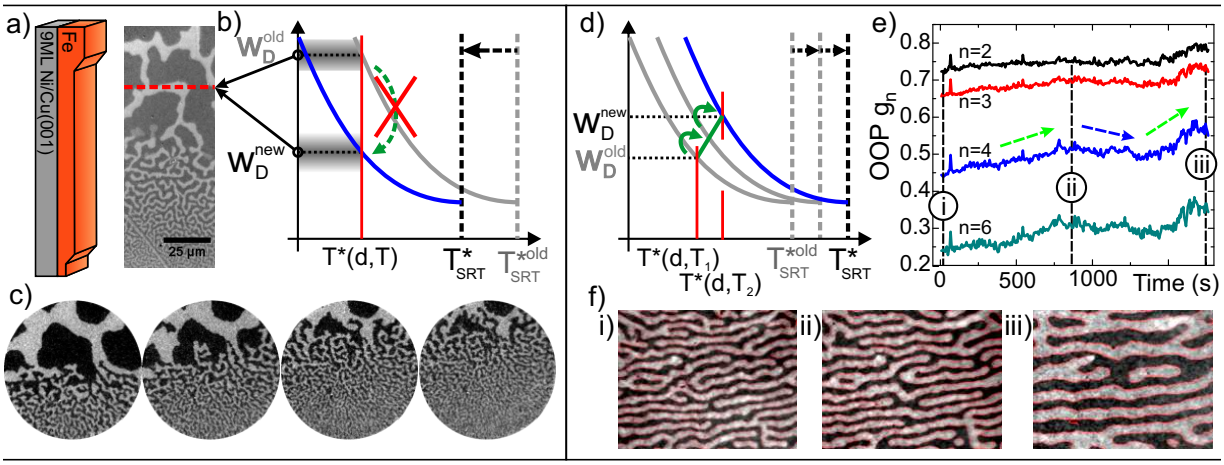

Figure 2.3: *Decay of metastable state and inverse heating.*

Fig. 2.3 c) was 2 minutes (field of view is 32.5 μm in diameter). The application of our model to this non-equilibrium domain width evolution is depicted in Fig. 2.3 b). The metastable domain pattern occurs due to an energetically unfavorable direct transition from the initially large domain width (w_D^{old}) to the final small domain width (w_D^{new}). The activation of the transition front occurs in the region of the spin-reorientation transition, where the energy barrier between final and initial domain width is small. The translation of the transition front can be attributed to the local reduction of the dipolar energy. In addition, the order of the system strongly decreases due to this melting process. The reverse process, i.e. ordering of the domain pattern by cooling the system, requires, in general, a very small cooling rate. This is due to the fact that the relaxation time of each individual domain jump increases with decreasing temperature, hence the transition speed is slowed down. In this thesis the inverse process is realized, i.e. increasing the temperature while simultaneously increasing the domain width. This process favors the affinity towards ordering of the domain pattern while increasing the domain width, since the relaxation time decreases with increasing temperature. The increasing order is captured by the orientational order parameters (OOP), which is shown in Fig. 2.3 e). The ordering process shows

a certain dynamics which is indicated by the green and blue arrows. The images i) to iii) (field of view was $28\times22\,\mu m^2$) in Fig. 2.3 f) show the domain patterns for different acquisition times as indicated in Fig. 2.3 e). Again the model supports an explanation for the increase in the domain width while increasing the temperature, as depicted in Fig. 2.3 d).

The determination of the real-space, real-time fluctuation properties of individual domain patterns as well as individual topological defects was the main goal of this thesis. The evaluation of the fluctuation properties with respect to changed domain area as well as dwell time revealed a dependence of the fluctuations on the domain width. The absolute

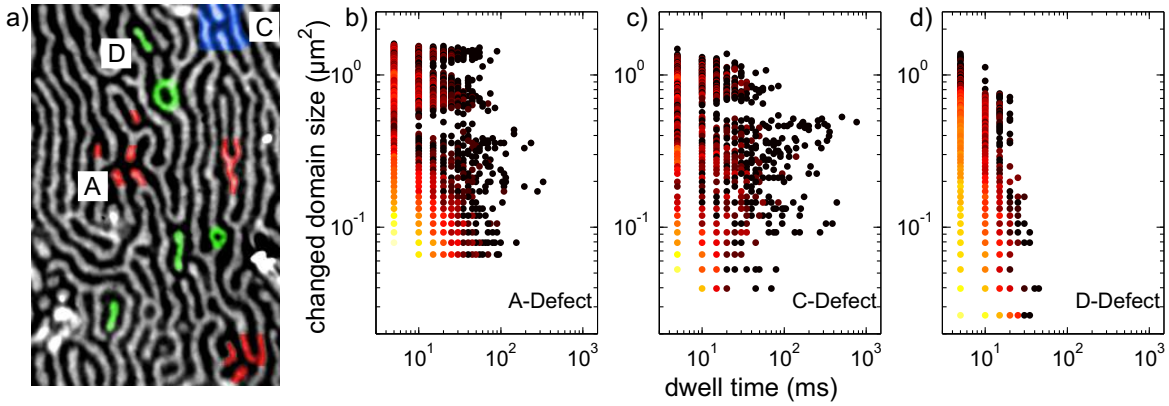

Figure 2.4: *Fluctuation properties of different topological defects.*

fluctuating domain area increases with increasing domain width, while the relative changed domain area decreases with increasing domain width, where the normalization is done with respect to the changed area. This behavior is expected, since in a narrow domain structure the geometrical constraints are much larger than in a broader domain structure, hence the absolute fluctuating domain area is smaller for a narrow domain pattern. The relative change of domain area increases with decreasing domain width indicating that the influence of thermal energy depends on the domain width and increases with decreasing domain width. In addition, the smaller domain pattern is closer to the spin-reorientation transition, which may induce further fluctuations. Remarkable is the presence of a large amount of fluctuations which was unknown so far. Furthermore, the fluctuation properties of individual topological defects (A, C and D) are investigated, since the increase of their number and the proliferation of such defects are responsible for the transformation of domain patterns. The inspection of the fluctuation properties of individual topological defects, as shown in Fig. 2.4 reveals that most likely only A-type defects are responsible for pattern transformations, since only this type of defect exhibits large scale fluctuations on long time scales.

Chapter 3

Theoretical Background of TP-MCD

The purpose of this chapter is to explain the contrast mechanism of threshold photoemission magnetic circular dichroism (TP-MCD) which is used in this thesis to investigate the magnetic domain structure of ferromagnetic ultra thin films. A number of ingredients is needed to fully explain this effect ranging from band structure calculation methods to surface states and photoemission models.

The TP-MCD effect was demonstrated for the first time in 2006 by Nakagawa and Yokoyama, who combined the TP-MCD effect with photoemission electron microscopy (PEEM) in order to investigate magnetic samples, in their case out-of-plane magnetized Ni/Cu(001) [11]. Additionally, this group also measured the dependence of the TP-MCD asymmetry on the maximum kinetic energy of the photoelectrons, i.e. the dependence on the work function for a fixed photon energy. The maximum asymmetry of about 12 % was found around the threshold of photoemission. A theoretical explanation for this large asymmetry was performed by Kronseder et al. in 2011 [12] using a combination of band structure calculations within the framework of dynamical mean field theory and the one-step photoemission model. In addition, the three-step photoemission model was used to calculate the spin-polarization of the relevant initial states.

3.1 Background of TP-MCD; Definition

Parts of this chapter have been published in [12].

The combination of exchange interaction and spin-orbit coupling (SOC) gives rise to magnetic circular dichroism (MCD) in ferromagnetic materials. In a typical experiment an incoming photon with circular polarization promotes an initial state electron into an empty final state with a transition probability given by the dipole matrix element, which is given by Fermi's golden rule

$$W_{i\to f} = \frac{2\pi}{\hbar}\left|\langle f|\mathcal{H}'|i\rangle\right|^2 \delta(\varepsilon_f - \varepsilon_i - \hbar\omega) \ , \tag{3.1}$$

where $\mathcal{H}'$ is the dipole operator, ε_f and ε_i are the energies of the final and initial states, respectively, and $\hbar\omega$ is the energy of the incident photon. Since the spin-orbit interaction for core shells is large (∼12-20 eV) spin-split transitions can easily be separated and the resulting X-ray magnetic circular dichroism (XMCD) in ferromagnetic $3d$-transition metals is typically large (∼30 %) and easy to interpret. In the valence band the spin-orbit interaction is much weaker (∼100 meV) and therefore the magneto-optical Kerr effect (MOKE) for visible light is typically very small (∼0.01 %). However, due to the large exchange splitting ($0.6 - 2.6$ eV), MCD and magnetic linear dichroism (MLD) effects can be large in valence band photoemission as well. This enhancement is due to the narrow angular distribution of the emitted photoelectrons as well as the energy selection compared to a photon-in photon-out technique such as MOKE which integrates over the entire k-space and does not allow for energy selection. Thus for particular materials and crystallographic orientations MCD and MLD effects can also be large in total yield valence band photoemission. This, however, is only valid, if the photon energy is either selected within a certain range or the work function of the material is reduced to value close to the photon energy used, which will become clear in this thesis. If the photon energy and the work function are comparable, essentially only electrons propagating normal to the sample surface (i.e. the $k_\perp$ direction) contribute to the photoemission process. Large TP-MCD has been demonstrated by Nakagawa et al. for the case of perpendicularly magnetized Ni/Cu(001) [11, 14] and also by Hild et al. for Co/Pt(111) [15].

The MCD-asymmetry is defined as [16]

$$A_{\mathrm{MCD}} = \frac{I(\uparrow\uparrow) - I(\uparrow\downarrow)}{I(\uparrow\uparrow) + I(\uparrow\downarrow)} = \frac{I(\downarrow\downarrow) - I(\downarrow\uparrow)}{I(\downarrow\downarrow) + I(\downarrow\uparrow)} \ , \tag{3.2}$$

where $I(\mathbf{M}, \mathbf{h})$ are the photocurrents obtained by parallel (antiparallel) alignment of the magnetization direction and the photon helicity [$I(\uparrow\uparrow)$ and $I(\uparrow\downarrow)$, respectively]. The latter equation leads to

$$A_{MCD} \sim \mathbf{M} \cdot \mathbf{h} \ , \tag{3.3}$$

where **h** is the helicity of the incoming photons, with eigenvalues ± 1, and **M** is the magnetization direction. Magnetization $\uparrow(\downarrow)$ refers to a magnetization direction out-of-plane (into-the-plane) and helicity $\uparrow(\downarrow)$ corresponds to right (left) circularly polarized [*rcp* (*lcp*)] light [16].

3.2 Band Structure Calculations of Fe, Co, Ni

Since all electronic properties of a system are encoded in the band structure particular attention is paid to its computation. In this thesis all band structure calculations are results of the spin-polarized relativistic Korringa-Kohn-Rostoker Green's function (SPR-KKR) code from the group of H. Ebert [13]. The SPR-KKR method offers the advantage to incorporate in a natural manner other techniques of computational physics, such as *dynamical mean field theory* for example, in order to describe a system under consideration as realistically as possible. Another advantage of this method with respect to ferromagnetic transition metals is the treatment of relativistic effects such as spin-orbit coupling and magnetic effects, e.g. exchange interaction, on an equal footing [17], leading to a realistic description of photoelectric effects such as the magneto optical Kerr effect (MOKE) or magnetic circular dichroism. Since SPR-KKR is a multiple scattering theory [13], this method naturally incorporates the scattering behavior of excited states, which again favors this method for purposes of photoemission. Since its original formulation by Pendry and co-workers [18] its applicability has been advanced by many contributions. One of these is the inclusion of realistic surface potentials, which will be discussed in more detail in section 3.3.

The theoretical background of SPR-KKR band structure calculations is the Green's function method, which treats electrons in their quantum mechanical wave interpretation moving through a system on paths with scattering and non-scattering sections. However, from a mathematical point of view the Green's function method is a way to solve an inhomogeneous differential equation, such as

$$[\zeta - H(\mathbf{r})]G(\mathbf{r}, \mathbf{r}'; \zeta) = \delta(\mathbf{r} - \mathbf{r}') \ , \tag{3.4}$$

where $H(\mathbf{r})$ is the Hamiltonian of the underlying system and $\zeta \, \epsilon \, \mathcal{C}$ is the complex energy, with $\varepsilon = \mathrm{Re}(\zeta)$. The solution of the Schrödinger equation

$$H(\mathbf{r})\Psi_\alpha(\mathbf{r}) = \varepsilon_\alpha \Psi_\alpha(\mathbf{r}) \tag{3.5}$$

follows then from the relation[1]

$$G(\mathbf{r},\mathbf{r}';\zeta) = \sum_{\alpha} \frac{\Psi_\alpha(\mathbf{r})\Psi^*_\alpha(\mathbf{r}')}{\zeta - \varepsilon_\alpha} \ . \tag{3.6}$$

In general, the Green's function G describes the evolution of a wave function in space-time. Every point $\mathbf{r}'$ where the wave function has a nonzero amplitude at $t' = 0$ serves as a source for the generation of a wave function at time t. This is in general known as *Huygens' principle*[2]. Hence the Green's function given in Eq. (3.6) contains all information about the electron distribution in the system under consideration [19]. With the knowledge of the system's Green's function (in particular the retarded Green's function[3] $G^+(\mathbf{r},\mathbf{r}';\zeta)$) all properties of interest such as the charge and magnetization densities can be calculated

$$n(\mathbf{r}) = -\frac{1}{\pi}\Im \int^{E_F} \mathrm{d}E \ G^+(\mathbf{r},\mathbf{r},\varepsilon) \tag{3.7}$$

$$m(\mathbf{r}) = -\frac{1}{\pi}\Im \int^{E_F} \mathrm{d}E \ \beta\sigma_z G^+(\mathbf{r},\mathbf{r},\varepsilon) \tag{3.8}$$

$$\langle O \rangle = -\frac{1}{\pi}\Im \int^{E_F} \mathrm{d}E \int \mathrm{d}^3r \ O \, G^+(\mathbf{r},\mathbf{r},\varepsilon) \ , \tag{3.9}$$

where the last equation is the expectation value of an arbitrary operator to be defined.

Going one step further towards real systems one needs to solve the following differential equation, i.e. the Hamiltonian, in relativistic form

$$\left[\frac{\hbar}{i}c\boldsymbol{\alpha}\cdot\boldsymbol{\nabla} + \beta mc^2 + V_{\text{eff}}(\mathbf{r}) + \beta\boldsymbol{\sigma}\cdot\mathbf{B}_{\text{eff}}(\mathbf{r})\right]\Psi_i(\mathbf{r}) = \varepsilon_i\Psi_i(\mathbf{r}) \ , \tag{3.10}$$

[1] Following [19] and introducing an abstract Dirac notation instead of the real space representation for Eq. (3.4), one ends up with $[\zeta - \hat{H}]\hat{G} = \hat{1}$, with the following notations

$$\begin{aligned} \Psi_\alpha(\mathbf{r}) &= \langle \mathbf{r}|\Psi_\alpha\rangle \\ \delta(\mathbf{r}-\mathbf{r}') &= \langle \mathbf{r}|\mathbf{r}'\rangle \\ G(\mathbf{r},\mathbf{r}';\zeta) &= \langle \mathbf{r}|\hat{G}(\zeta)|\mathbf{r}'\rangle \\ \sum_\alpha |\Psi_\alpha\rangle\langle\Psi_\alpha| &= \hat{1} \ . \end{aligned}$$

If all eigenvalues of $(\zeta - \hat{H})$ are unequal to zero, then the solution is simply $\hat{G}(\zeta) = \frac{1}{\zeta - \hat{H}}$.

[2] *Huygens' principle* states, that each point on an advancing wavefront acts as an independent source of (spherical) wavelets. The surface of tangency to these secondary wavelets determines successive positions of the wavefront at later times [20].

[3] In general, there are two solutions. One advancing in time and one retarding in time, called G^- and G^+, respectively. In order to ensure causal propagation, i.e. that $\Psi(\mathbf{r},t)$ should be determined by values of $\Psi(\mathbf{r}',t')$ at times $t' < t$ lying in the past, one must use the retarded Green function, G^+, from [20].

where $V_{\text{eff}}(\mathbf{r})$ and $\mathbf{B}_{\text{eff}}(\mathbf{r})$ are effective potential and magnetic field to be defined, respectively. α and β are the standard Dirac matrices, $\boldsymbol{\sigma}$ are the (4x4) Pauli matrices, and ε_i is the energy eigenvalue of the four-component one-electron Dirac spinor $\Psi_i(\mathbf{r})$ [21]. The main problem of equation (3.10) is that even for simple crystals the number of particles and states is huge. Therefore other techniques of computational physics have to be incorporated in order to make the problem tractable. One of the most successful and often used approaches for this purpose is the *density functional theory* (DFT).

3.2.1 Density Functional Theory (DFT)

DFT converts the many-body problem arising from a N-electron system with many degrees of freedom into an effective single-body problem with fewer degrees of freedom [22–24]. This method was introduced by Hohenberg and Kohn, and Sham [25, 26], who showed that the ground-state energy of a system can be found by minimizing a universal energy-functional of the charge and magnetization densities. Based on this, the appropriate Kohn-Sham-Dirac equation, i.e. the result of the minimization process, reads [24, 27]

$$\left[\frac{\hbar}{i}c\boldsymbol{\alpha}\cdot\boldsymbol{\nabla}+\beta mc^2+V_{\text{eff}}[n(\mathbf{r}),\mathbf{m}(\mathbf{r})]+\beta\boldsymbol{\sigma}\cdot\mathbf{B}_{\text{eff}}[n(\mathbf{r}),\mathbf{m}(\mathbf{r})]\right]\Psi_i(\mathbf{r})=\varepsilon_i\Psi_i(\mathbf{r})\ , \tag{3.11}$$

where V_{eff} is an effective potential comprising external classical as well as exchange-correlation potentials and $\mathbf{B}_{\text{eff}}$ is an effective magnetic field given by

$$\begin{aligned} V_{\text{eff}}[n(\mathbf{r}),\mathbf{m}(\mathbf{r})] &= V_{\text{ext}}+e^2\int\frac{n(\mathbf{r}')}{|\mathbf{r}-\mathbf{r}'|}\mathrm{d}\mathbf{r}'+\frac{\delta E_{xc}[n(\mathbf{r}),\mathbf{m}(\mathbf{r})]}{\delta n(\mathbf{r})} \\ \mathbf{B}_{\text{eff}}[n(\mathbf{r}),\mathbf{m}(\mathbf{r})] &= \mathbf{B}_{\text{ext}}(\mathbf{r})+\frac{\delta E_{xc}[n(\mathbf{r}),\mathbf{m}(\mathbf{r})]}{\delta\mathbf{m}(\mathbf{r})}\ . \end{aligned} \tag{3.12}$$

The charge and magnetization densities are connected to the wave function of the electronic system by [21]

$$\begin{aligned} n(\mathbf{r}) &= \sum_i^{occ}\Psi_i^\dagger(\mathbf{r})\Psi_i(\mathbf{r}) \\ m(\mathbf{r}) &= \sum_i^{occ}\Psi_i^\dagger(\mathbf{r})\beta\sigma\Psi_i(\mathbf{r})\ . \end{aligned} \tag{3.13}$$

Eqs. (3.11) and (3.13) have to be solved self-consistently[4], which is shown schematically in Fig. 3.1. This self-consistent field (SCF) cycle has to be repeated until some convergence criteria adapted to the respective needs are fulfilled.

[4]Consider, that the result of Eq. (3.11) leads to the result of Eq. (3.13) and vice versa.

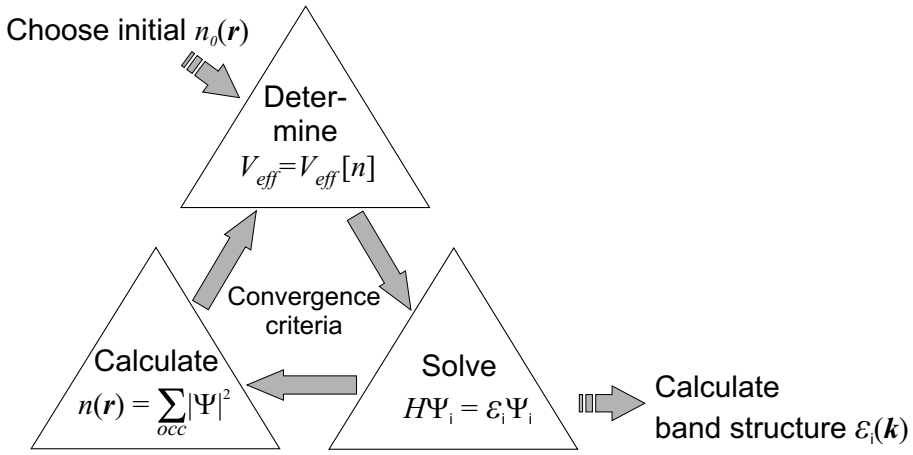

Figure 3.1: *The SCF cycle, modified taken from [28, 29]. The initial electronic density $n_0(\mathbf{r})$ is the starting point for the iteration process, which is repeated until the appropriate convergence criteria are fulfilled.*

At this point, all difficulties in solving the many-body problem have been converted into the unknown exchange and correlation energy functional $E_{xc}[n(\mathbf{r}), \mathbf{m}(\mathbf{r})]$ [29]. Unfortunately, there is no explicit prescription how the real form of the functionals can be obtained [24].

3.2.2 Local Density Approximation - LDA

For simplicity, in the following the spin-dependence of the Hamiltonian and therefore the dependence of the energy functional on the spin will be disregarded, i.e. $E_{xc}[n(\mathbf{r}), \mathbf{m}(\mathbf{r})] = E_{xc}[n(\mathbf{r})]$. As the real form of the exchange and correlation energy cannot be calculated rigorously, since this would be as extensive as solving the initial Hamiltonian Eq. (3.10), the explicit form of E_{xc} has to be approximated by derivations from simpler systems such as the uniform electron gas. Using the uniform electron gas, also called the *jellium model*, in order to approximate the exchange and correlation energy leads to the so-called *local density approximation* (LDA). Within this approximation the electron density is regarded to vary only on length scales much larger than the Wigner-Seitz radius[5] and can therefore be simplified, leading directly to a simple relation between the exchange energy and the electron density

$$E_{xc}[n] \approx \int \mathrm{d}^3 r \, \varepsilon_{xc}(n(\mathbf{r}))\, n(\mathbf{r}) \ ,$$

[5]The Wigner-Seitz radius is the pendant in real space to the Brillouin zone in k-space.

where $\varepsilon_{xc}(n(\mathbf{r}))$ is the exchange-correlation energy density, to be obtained from homogeneous electron gas results. This is only a simple function and not a functional [25,26,28][6]. Band structure calculations within LDA have been proven to be very successful in the description of the itinerant electron system, due to the model system LDA is derived from.

However, due to the high density of d-states at the Fermi energy, the valence bands in many transition metals are neither completely delocalized nor fully localized. Therefore, in order to describe such systems as realistically as possible, one has to go beyond LDA and needs to incorporate the local as well as the itinerant behavior on an equal footing. A first approach to reach this equalization has been done in the framework of LDA+U.

3.2.3 LDA+U

LDA+U is an extension of LDA, where the "on-site" electron-electron repulsion U has been taken into account as well the intra-atomic exchange interaction J. One reason for this extension is to compensate systematic errors LDA produces for molecules and solids. This is based on changes in the orbital composition of the total wave function by going from atoms to solids, which LDA predicts incorrectly, confer [30]. Another reason for the extension to LDA+U is the almost neglected local character of the valence electrons in transition metals, again a consequence of the underlying free electron gas model of LDA. The pronounced local character of d-states can be regarded as a spatial confinement causing a strong Coulombic repulsion among these electrons [24]. This in turn leads to strong interactions among valence electrons, also known as "correlation". In order to satisfy the requirement of this correlation effect an additional energy term $E^U[n]$ needs to be added to the total energy functional in LDA+U, which is usually called the Hubbard term. In addition, the intra-atomic exchange energy due to the Pauli principle is also comprised within $E^U[n]$ [31]

$$E^U[n] = \frac{U}{2} \sum_{m\sigma \neq m'\sigma'} n_m^\sigma n_{m'}^{\sigma'} - \frac{J}{2} \sum_{m \neq m', \sigma'} n_m^\sigma n_{m'}^\sigma \ , \tag{3.15}$$

where n_m^σ is the occupation number of the mth orbital and σ is the spin index. Unfortunately, the Hubbard term already contains in a natural manner some electron-electron interactions which have already been taken into account by LDA. Hence, simply adding

[6] The exact exchange and correlation energy is given by the expansion [26]

$$E_{xc}[n] = \int \mathrm{d}^3 r \, \varepsilon_{xc}(n) n + \int \mathrm{d}^3 r \, \varepsilon^{(2)}(n) \, |\nabla n|^2 + \cdots \ . \tag{3.14}$$

the Hubbard term to the LDA-energy results in energy contributions occurring artificially twice. Therefore these double-counted contributions have to be subtracted. This is expressed by the term E^{dc}. Summarizing, one ends up with the following energy functional for the LDA+U approach [30, 32, 33]

$$E^{LDA+U}[n] = E^{LDA}[n] + E^{U}[n] + E^{dc}[n] \ . \tag{3.16}$$

3.2.4 Dynamical Mean Field Theory - DMFT

A second approach to treat the itinerant as well as the local character of valence electrons in transition metals is a kind of *mean field theory* described in the following. The correlation of valence electrons due to the on-site Coulomb interaction as described above can be illustrated as an interaction of a single electron with a mean-field generated by all other electrons. However, since each electron strongly interacts with all the other electrons, in turn, the influence of a single electron on the mean-field cannot be disregarded. Therefore the mean-field is not static, but possesses a dynamic character [24] and the corresponding theory is referred to as *dynamical mean field theory* (DMFT).

In DMFT a particular lattice site is regarded as a single impurity atom surrounded by a bath of electrons. The considered lattice site then fluctuates among different atomic configurations by exchanging electronic states with the bath [24], described by a function $\Delta(\omega)$[7]. This exchange process, which occurs at time scales $\frac{1}{\omega}$, leads to the effect that the exchange field is a function of frequency ω, making it a *dynamic* mean-field. All terms of interactions can then be combined into a single function, called *self-energy* $\Sigma[\Delta(\omega)]$, which can be written in wave-vector dependent fashion $\Sigma_{\mathbf{k}}$. In general, the self-energy is the contribution to the particle's energy due to the interaction between a freely moving state, represented by the free Green's function G^0, and the system itself [8]. The Dyson equation is the mathematical expression of this fact and inversely the self-energy is defined by this equation

$$G_k(E) = G_k^0(E) + G_k^0(E)\,\Sigma_k(E)\,G_k(E) \ . \tag{3.17}$$

Unfortunately, the functional $\Sigma_k(E)$ cannot be calculated exactly, due to its k-dependence[9]. However, Metzner and Vollhardt showed [34] that for infinite dimensions ("$d = \infty$") the self-energy would be k-independent and therefore the functional becomes calculable. In addition, they could also show that the situation of $d = 3$ is quite close to that of infinite dimensions [34]. In band structure calculations the self-energy enters via the Green's

[7] $\Delta(\omega)$ is the hybridization function, and represents the probabilities for an electronic state to enter or leave an atomic site.

[8] A famous pendant in particle physics is the cloud of particles always carried along by photons.

[9] This is the same problem as to know all states just to calculate one particular state.

function of the corresponding Hamiltonian due to the substitution of the one-particle energy $\varepsilon(\mathbf{k})$ from Eq. (3.10) by $\varepsilon(\mathbf{k}) - \Sigma_{\mathbf{k}}$ [35]. A detailed discussion about local exchange-correlation effects is given in [25,26,28,30–33,36,37]. Further information about DFT and DMFT can be found in [23,24,34,38].

3.3 Surface States and Surface Potential

The surface of a crystal represents not only an abrupt termination of the lattice periodicity right at the surface layer. Its impact on the crystal potential and hence on the electronic structure, extends over several lattice constants into the crystal and into the vacuum region [39]. From a standard textbook calculation of the wave functions for half-infinite crystals, e.g. [40] page 266, it follows that there are two individual solutions for this problem, distinguished by individual $\mathbf{k}$-vector ranges. The first and more obvious solution consists of a periodic function within the crystal (real $\mathbf{k}$) and an exponential decay into the vacuum region (complex $\mathbf{k}$), as can be seen in Fig. 3.2 b). This solution is almost a Bloch function as for an infinitely extended crystal, which leads to the effect that taking into account only this class of solutions, one ends up in nearly the same energy bands as obtained from bulk systems. The second solution exhibits a complex $\mathbf{k}$-vector in both directions, and will be discussed below. Summarizing, regarding only the first solution, i.e. nearly Bloch states, the electronic energy band structure has almost bulk character up to the very surface [40].

3.3.1 Intrinsic Surface States; Tamm- and Shockley-States

Due to the interrupted periodicity at the crystal surface an additional range of $\mathbf{k}$-vectors appears for the crystal region that contributes solutions. These additional solutions assume complex $\mathbf{k}$-values everywhere, even inside the crystal[10]. These complex $\mathbf{k}$-vectors lead to an exponentially decaying envelope in both z-directions (where z is assumed to be along the surface normal), with maximum amplitude at the surface. Hence, these states are localized at the surface region and are therefore called *surface states*, see Fig. 3.2 c). Being more explicit, these states are *intrinsic surface states*, since they only appear due to the breaking of the symmetry at the crystal surface. Intrinsic surface states can therefore be called "crystal derived", following Lüth [40]. Based on the fact that the $\mathbf{k}$-values of these states differ from that of Bloch states, their real energy eigenvalues do the same. This

[10] These solutions would always be zero if the crystal periodicity is infinite.

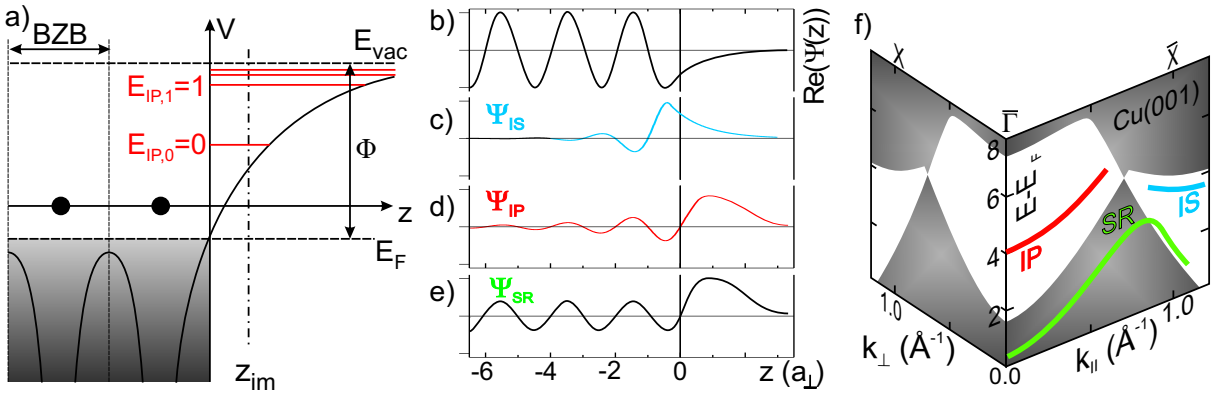

Figure 3.2: *Schematic of a crystal surface. a) shows the crystal potential V in the surface region, modified taken from [41]. Φ is the work function of the crystal. z_{im} is the image plane position and is an auxiliary boundary representing the effective location of the surface plane [42]. BZB stands for Brillouin zone boundary. b) Bulk Bloch waves which approach the surface of the crystal have to match an exponential decaying tail in the vacuum region. In addition, surface states emerge at the crystal-vacuum region, like* intrinsic surface states Ψ_{IS}, *shown in c),* image potential states Ψ_{IP} *d), and* surface resonances Ψ_{SR} *e). f) shows the surface-projected band structure of Cu(001). The shaded areas show the surface-projected Bloch spectral function in parallel and perpendicular direction to the surface and represent the areas where bulk bands occur. Additionally an image potential state (IP), an intrinsic surface state (IS) and also a surface resonance (SR) band are shown, modified taken from [43].*

means that intrinsic surface states usually lie in band gaps of the corresponding band structure, confer Fig. 3.2 f), where the intrinsic surface states are labeled with "IS". See also [44–48].

The separation into *Tamm* and *Shockley* states is more fictitious, since both are "crystal derived", i.e. originate from the breaking of the symmetry of the crystal. However, Tamm and Shockley [49, 50] used two individual models in order to set up the basis functions for their derivation of surface states. Tamm used the LCAO[11] and Shockley the nearly-free-electron model. These two models constitute the two limiting cases in describing electronic states, as pointed out in section 3.2.2. Hence, the choice of the model by Tamm and Shockley led to non-dispersing and dispersing intrinsic surface states, respectively.

[11] Linear combination of atomic orbitals.

3.3.2 Image Potential States and Work Function

A second kind of surface states is referred to as *image potential states*, and has been derived from the extension of the surface potential into the vacuum region [39]. Therefore these states originate neither from crystal states nor from the symmetry-breaking effect of a surface as the intrinsic surface states do, but only from the progression of the surface potential into the vacuum referenced to the vacuum level E_{vac}.

The energy difference between the Fermi energy E_F and the vacuum energy E_{vac} is called *work function* $\Phi = E_{vac} - E_F$ [51–53]. Roughly speaking, in case of an electron approaching a metal surface, the electronic cloud within the metal forms a positive image of the electron outside the crystal, which then leads to an attractive potential of these two charges of Coulomb character, i.e. [40]

$$V(z) \sim -\frac{1}{z}, \quad z > 0 \ . \tag{3.18}$$

Electrons can be trapped in this potential outside of the crystal, Fig. 3.2 d). Due to the positive image in the crystal these states are called *image potential states*. Also for these states the surface potential is referenced to the vacuum level. In Fig. 3.2 a) image potential energy levels are shown, where only the first two are labeled with $E_{IP,0}$ and $E_{IP,1}$. It should be pointed out, however, that image potential states form a quasi-2D electron gas above the surface, confer Fig. 3.2 d). Therefore, changing the surface potential by for example adding some adatoms leads to dramatic changes or even quenching of image potential states.

3.3.3 Surface Resonances

The energy bands of intrinsic as well as image potential surface states can in some cases intersect with energy bands obtained from bulk states, see Fig. 3.2 f) labeled with "SR". In this case the surface states hybridize with the corresponding bulk states, leading to the effect that the surface state character is carried deep into the crystal. Hybridized image potential states can therefore survive even if large fractions of other materials are deposited onto the surface. The same phenomenon also occurs for intrinsic surface states.

3.3.4 Surface Potential for Photoemission-Calculations

A general result of electronic structure calculations within LDA, section 3.2.2, is an exponential rather than the natural $\frac{1}{|z|}$-decay of the potential into the vacuum region, confer Eq. (3.18). As a consequence of this incorrect asymptotic behavior [39] surface states and surface state energies are predicted incorrectly. Furthermore, image potential states cannot exist in this case as they require the long range image tail of the surface potential, i.e. the $\frac{1}{|z|}$-progression [46]. Therefore and additionally due to the fact that the crystal surface is an integral part of almost all experiments, it is indispensable for theory to have a surface potential as realistic as possible, leading to the correct surface states and energies [15, 35, 46–48, 54]. There are at least two ways to treat this problem. The first one is to use full potential calculations, which are computationally intensive. The second way, usually done, is to simulate the surface potential by a suitable function containing some parameters to be adjusted by experimentally obtained values.

In a natural manner, the simulation of the surface potential can be realized in various ways [27, 35, 39, 54]. In general, the artificial function has to combine the crystal potential from the very last atom and the $\frac{1}{z}$-decay in the far vacuum region within a certain z-range. Furthermore, it has to satisfy some additional constraints, like continuity and differentiability of the whole function. This leads to four constraints, two on each side. The most simple function fulfilling these constraints is a cubic spline, i.e. a polynomial of degree 3. In the SPR-KKR code of H. Ebert [35], used in this thesis, this first and most simple choice is implemented. Other groups [39] introduce some self-defined surface functions fulfilling all constraints. However, they have to use more than four parameters defining the overall progress of the function, whereas only four are well-determined by constraints. An important parameter is the image plane distance z_{im}, as shown in Fig. 3.2 a), since the binding energy of surface states is a function of this image plane position [42, 55].

Unfortunately, this easy and elegant way of simulating the surface potential instead of fully calculating it *ab-initio* comes along with the requirement of justification and verification of the used function and the inserted parameters. This can be done by comparing spectral features obtained from theory and experiment and subsequently re-adjusting the parameters. The results of this procedure are given in section 4.2.2 and [12]. The exact form of the surface potential used for all one-step photoemission calculations can be found in [54]. Further information about the origin and development of this function is given in [27, 44–46, 56, 57]. An introduction to solid surfaces is given very thoroughly in [40].

3.4 Models of Photoemission

The photoemission process is, in general, a sequence of complex, mutually intertwined steps[12]. Nowadays, this sequence of processes can be fully treated numerically. The corresponding model is referred to as the *one-step* photoemission model. Within this model the photoelectric current is derived from Fermi's golden rule, Eq. (3.1),

$$I(\hbar\omega) \sim W_{i_N \to f_N} = \frac{2\pi}{\hbar} \left| \langle f_N | \Delta | i_N \rangle \right|^2 \delta(\varepsilon_{f,N} - \varepsilon_{i,N} - \hbar\omega) \ , \tag{3.19}$$

where $\varepsilon_{f,N}$ and $\varepsilon_{i,N}$ represent the final and initial energies of the N-electron states $|f_N\rangle$ and $|i_N\rangle$, respectively. According to [58–62] the operator Δ mediating the coupling to the electromagnetic field is generally defined as

$$\Delta = \frac{e}{2mc}(\mathbf{A} \cdot \mathbf{p} + \mathbf{p} \cdot \mathbf{A}) - e\Phi + \frac{e^2}{2mc^2}\mathbf{A} \cdot \mathbf{A} \ , \tag{3.20}$$

where $\mathbf{A}$ and Φ denote the vector and scalar potentials and $\mathbf{p}$ the momentum operator. Neglecting two-photon photoemission (2PPE) processes, i.e. last term of Eq. (3.20), using the Coulomb gauge $\nabla \cdot \mathbf{A} = 0$, $\Phi = 0$, and applying the dipole approximation, i.e. approximate $\mathbf{A} = \mathbf{A}_0 exp(i\mathbf{q} \cdot \mathbf{r}) \simeq \mathbf{A}_0$, Eq. (3.20) can be written as

$$\Delta \approx \frac{e}{mc}\mathbf{A}_0 \cdot \mathbf{p} \ . \tag{3.21}$$

In order to combine band structure calculations based on a multiple-scattering approach and photoemission theory, one may follow [58] and expand the square in Eq. (3.19), which provides the total photocurrent in the sudden approximation[13] for the *one*-electron initial and final states $|i\rangle$ and $|f\rangle$ [58, 59]

$$I(\hbar\omega) = -\frac{1}{\hbar\pi} Im \sum_{f,i,i'} \langle f|\Delta|i\rangle A_{i,i'}(\varepsilon_f - \hbar\omega) \langle i'|\Delta^*|f\rangle \ , \tag{3.22}$$

where $A_{i,i'}(\varepsilon_f - \hbar\omega)$ is the spectral function of the whole state, i.e. for the N-electron state instead of the one-electron state. The requirement of inelastic scattering for the initial as well as the final states is inherently fulfilled by the multiple scattering approach,

[12] Consider for example the first step in the 3-step model. The excitation of an electron into a state above the Fermi energy leaves a system in the state $|N-1\rangle$, where N is the number of electrons. This system, however, is different to the initial system $|N\rangle$. Hence, the second step, i.e. the transport to the surface, has to be considered for a system in the state $|N-1\rangle$.

[13] In the sudden approximation "the removal of the photoelectron from the rest of the system is expected to be so fast that the interaction between the two systems is negligible" [59].

which itself is closely related to low energy electron diffraction (LEED) theory. "The great advantage from LEED theory clearly consists in the possibility of treating all scattering events successively by starting with the single ion core scattering and ending up with the multiple scattering within a layer and between the layers of the semi-infinite bulk crystal" [59]. The spectral function $A_{i,i'}$ is connected to the Green function $G_k(\varepsilon)$ in Bloch representation by

$$A_k(\varepsilon) = -\frac{1}{\pi} G_k(\varepsilon) \ . \tag{3.23}$$

Note that all many-body effects and correlations have been implemented within this last equation (3.23), by means of the Dyson equation Eq. (3.17), which links the non-interacting Green function $G^0(\varepsilon)$ with all many-body effects represented by the self-energy $\Sigma(\varepsilon)$. The spectral density can now be rewritten as

$$A_k(\varepsilon) = -\frac{1}{\hbar\pi} \frac{Im[\Sigma_k(\varepsilon)]}{\left(\varepsilon - \varepsilon(\mathbf{k}) - Re[\Sigma_k(\varepsilon)]\right)^2 + Im[\Sigma_k(\varepsilon)]^2} \ , \tag{3.24}$$

where $\varepsilon(\mathbf{k})$ is the one-particle energy obtained from the band structure calculation. The imaginary part of the self-energy in Eq. (3.24) leads to a broadening of the peaks in the resulting photoemission spectra, corresponding to the finite lifetime of the initial state. Further, the real part of the self-energy shifts the peaks in energy [56]. This dependence of the peak positions and widths on the self-energy becomes very important if the kinetic

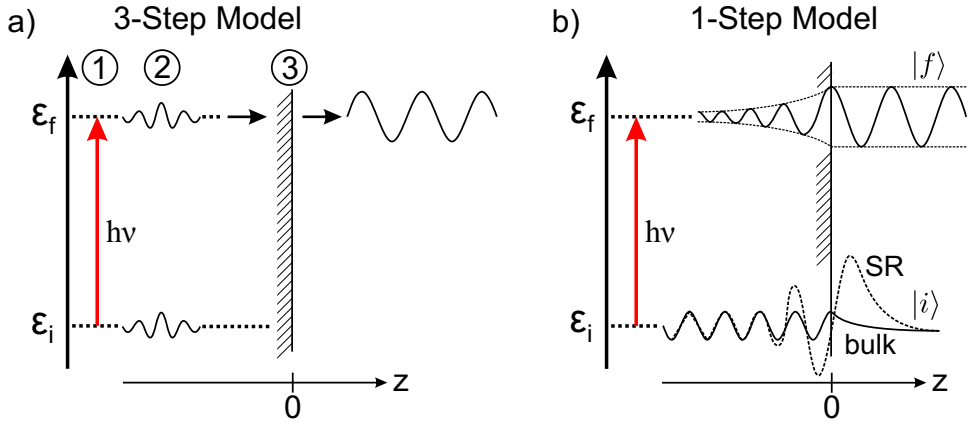

Figure 3.3: *a) Cartoon of the 3-step model consisting of 1) optical excitation of an initial electronic state with energy ε_i into the final Bloch state with energy ε_f by absorption of a photon with energy $h\nu$; 2) transport to the surface and 3) transmission through the surface. b) sketches the 1-step model, in which an initial state is promoted by a photon into a damped final state taking into account the limited mean free path of the photoelectron, which in addition has to match a freely moving state outside the sample, modified taken from [63].*

energy of the photoelectrons is in the range of the self-energy of the corresponding state. Small variations of the parameters lead to dramatic changes in the spectra. This fact will be further discussed in section 4.2.2.

As demonstrated, the one-step photoemission model treats the whole photoemission process at once [63, 64]. However, exactly this unification demands simplifications and approximations. In fact, for the interpretation of photoemission data, approximations are usually made in order to identify the relevant and irrelevant contributions. Disregarding the mutual interactions and treating in this way each step of the photoemission process as independent is a common approximation. In general, three steps have emerged as important, and therefore the corresponding description of such a stepwise photoemission process is referred to as the *three-step* photoemission model as shown in Fig. 3.3 a). The first step is the photon absorption process promoting an electron into an excited state. The second step is the electron transport to the surface and the third step is the escape of the photoelectron into the vacuum. This photoemission model will also be applied in the discussion of the experimental data and will lead to further insight into the TP-MCD effect.

Chapter 4

Experimental Results: TP-MCD

Parts of this chapter have been published in [12].

4.1 Experimental Results: Ni/Cu(001)

4.1.1 TP-MCD Data

In this chapter experimental as well as theoretical results describing threshold photoemission magnetic circular dichroism (TP-MCD) measurements on ultra thin Ni-films on Cu(001) will be presented. As shown in 2006 by Nakagawa et al. [11] the TP-MCD effect of Ni/Cu(001) can reach up to 12 %, confer Fig. 4.1 a). Nakagawa et al. concluded that the maximum of the TP-MCD asymmetry occurs at the threshold energy for photoemission, where the work function equals the photon energy. In addition, they support the experimentally obtained TP-MCD-dependence on the maximum kinetic energy of the photoelectrons by computing the optical conductivity within the dipolar approximation[1], see Fig. 4.1 b), where $E_{max.kin.} = E_{ph} - \Phi$, E_{ph} is the photon energy and Φ is the work function of the system. The correspondence between work function value and Cs-deposition time in their experiment was calibrated by a two-grid electron energy analyzer. The energy dependence prior to the peak, where the asymmetry increases from zero to the maximum value right at the threshold, was ascribed to the blurring effect of the Fermi function at finite temperatures.

Kronseder et al. [12] verified the general behavior of the MCD effect of Ni/Cu(001) around the Fermi level, compare Fig. 4.1 d) with a), which is in essence a smooth function increasing from zero to a single peak and slowly decaying to zero again. This measurement

[1] The band structure calculation of bulk *fcc* Ni was calculated with the WIEN2K package.

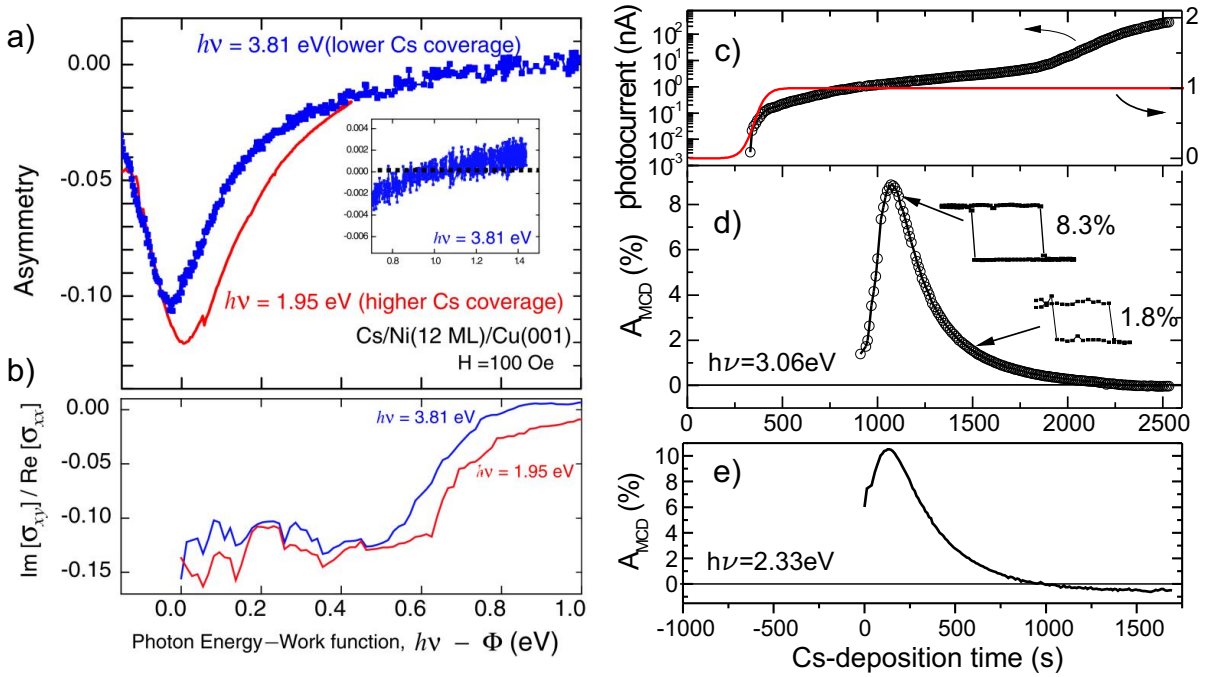

Figure 4.1: *a) dependence of the TP-MCD-asymmetry on the maximum kinetic energy of the photoelectrons, measured by Nakagawa et al., published in [11]. b) WIEN2K calculations of the MCD asymmetry of bulk* fcc *Ni of the same group [11]. c) measurement of the total electron yield during Cs-deposition as a function of time. d) same as in a) but with a photon energy of 3.06 eV. c) and d) were measured simultaneously in our PEEM setup. The Fermi function for* $k_BT = 26\,meV \hat{=} 32.5\,s$ *(room temperature) and a Fermi energy in seconds of* $E_F \hat{=} 350\,s$ *is also plotted in c) (red curve) in order to see the blurring effect of the Fermi function at finite temperatures. Note, the Fermi function plot has a linear ordinate. e) shows the dependency of the TP-MCD asymmetry of 16 ML Ni/Cu(001) for 2.33 eV photon energy measured by S. Günther from our group. Note that the setup and the current through the Cs-dispenser differ from the measurements in d), resulting in different time scales.*

was performed by tracing the dependence of the TP-MCD-asymmetry on the maximum kinetic photoelectron energy by varying the work function with the aid of Cs-adatoms using a constant photon energy of 3.06 eV (405 nm). The TP-MCD signal was obtained by reversing the magnetization instead of changing the helicity of the incident photons, which was set to *right* circular polarization, and inserting the obtained photocurrents for magnetization out-of-plane and into-the-plane (up and down) in Eq. (3.2). The overall behavior did not change as different photon energies were used, which has already been shown by Nakagawa [11] and has also been verified by another measurement in our group using a photon energy of 2.33 eV (532 nm), as can be seen in Fig. 4.1 a) and e), respectively.

The overall TP-MCD dependence seems to be *in*dependent of the work function Φ and the photon energy $h\nu$ in the particular case of Ni/Cu(001), but is only implicitly dependent on these parameters, and depends only on the difference $E = h\nu - \Phi$. Hence, the underlying physical photoemission processes, i.e. the transition from initial to final states, may play only a minor role in the description of the TP-MCD effect for Ni/Cu(001) unlike for other materials and other photon energies. This finding indicates that a much simpler photoemission model may lead to an adequate description of this effect. This will be further discussed in the three-step photoemission description in section 4.2.3.

In addition, Nakagawa et al. found a negative peak in the MCD-asymmetry versus energy [11], Fig. 4.1 a). However, the sign convention in [11] is somewhat ambiguous, since they defined the MCD-asymmetry dependent either on the helicity *or* on the magnetization state. An unambiguous convention is given in [16], and has been used in this thesis, as can be seen by Eq. (3.2). This asymmetry definition leads, however, to a positive peak for Ni/Cu(001), independent of either changing the magnetization state while keeping the helicity constant or vice versa. In fact, the first case was used for the measurement shown in Fig. 4.1 d).

4.1.2 Total Electron Yield

The simultaneous measurement of the *total electron yield* (TEY) during the TP-MCD-measurement is crucial in order to obtain a reference for the energy, which is shown in Fig. 4.1 c). Nakagawa et al., who did not show the TEY versus energy plot, concluded that the peak position occurs at the threshold energy of photoemission. However, as can be seen in our TEY-measurement Fig. 4.1 c), which has the same time (and energy) scale as our TP-MCD plot, the threshold of photoemission is around $\sim 350\,\mathrm{s}$, whereas the asymmetry peak occurs around $\sim 1070\,\mathrm{s}$ [2]. Further, a sign reversal of the MCD-asymmetry occurs around $\sim 2300\,\mathrm{s}$. Unfortunately, the setup used in this thesis does not allow to perform kinetic energy spectroscopy of the photoelectrons. For this reason the plots in Fig. 4.1 c) and d) only have a Cs-deposition time scale rather than an energy scale. Nonetheless, a time-energy conversion factor can be deduced by comparing significant features in this plot with experimental and theoretical data. However, such a comparison has to be done very carefully, and will be discussed in the following.

The first possibility to deduce a time-energy scaling factor is to extract the abscissa differences between the peak of the TP-MCD-asymmetry as well as the zero crossing point in our measurement and in the measurement performed by Nakagawa. For $E_{ph} = 3.81\,\mathrm{eV}$ Nak-

[2] The current through the Cs-dispenser (SAES) was $\sim 4.1\,\mathrm{A}$, which is actually only a relative value since it changes over years.

agawa measured an energy difference of $\sim 1.0\,\mathrm{eV}$ between peak and zero crossing point of the MCD-asymmetry, compared to $\sim 1230\,\mathrm{s}$ from our measurement. This results in a time-energy scaling factor of $\sim 0.81\,\mathrm{eV}/(1000\mathrm{s})$, leading to a MCD-peak position at $\sim 0.5\,\mathrm{eV}$, if $350\,\mathrm{s}$ is taken to be the threshold. The main result of this derivation is that the peak of the asymmetry is around $\sim 0.5\,\mathrm{eV}$ and not right at the threshold, i.e. at zero energy, as stated in [11]. A second possibility to obtain a scaling factor is to perform band structure calculations and to extract the relevant photoemission spectra, as shown in the next section. In addition to the scaling factor, the underlying physical mechanism of the large magnetic contrast will be revealed as well.

4.2 Band Structure Calculations and Photoemission Models: Ni/Cu(001)

As pointed out in section 3.2, band structure calculations for transition metals are still a demanding task, since it is not clear how to theoretically treat the mutually interacting forces on electrons in the valence orbitals which lead to neither free nor fully localized electronic states. In addition, in order to compare experimentally accessible information with theoretical results it is necessary to simulate the experimental measurement process by theory. An example is photoemission spectra deduced from band structure calculations. The comparison of theory and experiment as well as the fine-tuning of parameters in the calculation process may lead to a consistent explanation of the underlying physics and additional information obtained from theory may then, in turn, lead to an improvement of the experiments as well.

For the theoretical investigation of the TP-MCD effect, two individual photoemission models are applied. The first, which is the subject of the next subsection, is the *one-step* model, which properly accounts for all effects of the photoemission process as for example dipole selection rules or surface emission [12, 64]. The second model is the three-step model, which will be illuminated in section 4.2.3. Actually, this is the first time that photoemission calculations are applied for such low photoelectron energies ($< 1\,\mathrm{eV}$) in 1PPE (One-Photon-Photo-Emission). Note, however, that almost all available photoemission experiments have been done so far in the UV spectral range (UPS) or at very high photon energies (soft and hard X-rays). Hence, theoretical calculations as well as experimental data for low energy photoemission spectra are rather sparse. Therefore, no clear consensus exists on the interpretation of this MCD effect at the threshold of photoemission [11, 15]. In this thesis, however, the TP-MCD mechanism is investigated theoretically, with an astonishing agreement between the various models.

4.2.1 Remarks on the Band Structure Calculation: Ni/Cu(001)

The electronic structure of the Ni/Cu(001) system, is the result of a spin-polarized relativistic Korringa-Kohn-Rostoker Green's function (SPR-KKR) method [13] and was calculated self-consistently within the local spin-density approximation in combination with the dynamical mean field theory (LSDA+DMFT) [12, 65–67]. A short introduction of these theories is given in chapter 3.2 (in particular 3.2.3 and 3.2.4). The SPR-KKR method comprises not only the ability to perform realistic electronic structure calculations especially for transition metals but also to investigate photoemission processes or other electronic transitions and transport processes in a natural manner due to the fact that it is a *multiple scattering* method. In addition, slab or semi-infinite calculations for a system consisting of a thin, free-standing film or on a substrate are possible. These advantages are in contrast to other band structure calculation methods like for instance VASP and make this method the first (and only) choice for our photoemission spectra. All calculations belonging to the one-step model were done in collaboration with the group of Prof. H. Ebert in Munich, especially with Dr. Jan Minár and Dr. Jürgen Braun.

As pointed out in the surface potential section of this thesis 3.3, the film-vacuum interface influences both the crystal structure due to atomic rearrangements and also the electronic structure for several reasons. This is also true for the film-substrate interface. Hence, *bulk* band structure calculations, disregarding surface and interface effects by considering an infinite and periodic crystal, can only provide an approximation to real systems. However, as will become clear in subsection 4.2.3, bulk calculations can be used to deduce a simple explanation of the complex sequence of processes in photoemission.

For the one-step photoemission calculation the surface and interface effects on the electronic structure are incorporated within a so-called *relaxation* calculation of the electronic structure, which is a standard procedure in the SPR-KKR code. Within this relaxation calculation structural modifications are accounted for as shifts and changes to the electronic structure. Although the lattice constant is a variable in SPR-KKR, it has to be kept constant during the calculation. As pointed out in 3.2.4, the self-energy of the relevant electronic states takes these energetic shifts into account. However, since the experimentally given kinetic energy range (a few $\sim 100\,\mathrm{meV}$ to about $2\,\mathrm{eV}$) overlaps with the energetic region of the self-energy (a few $100\,\mathrm{meV}$ [68]), the relevant convergence criteria in the SCF cycle, section 3.2.1, of the band structure calculation has to be chosen much stricter than for photoemission processes with higher photon energies. This means that the limits of convergence have to be smaller than usually set for UPS or X-ray spectroscopic issues. This limitation was not known prior to these calculations.

4.2.2 One-Step Photoemission Model

To begin with, the theoretical key results of the one-step photoemission calculations for the system Ni/Cu(001) are presented in Fig. 4.2 c) and d). In c) the theoretically calculated photocurrent is shown, and d) presents the calculated MCD-asymmetry. In order to aid comparison, the experimental measurements, already shown in Fig. 4.1 c) and d), are plotted again in Fig. 4.2 a) and b). The photon energy used in the calculation is set to the corresponding experimental value of 3.06 eV (405 nm).

Each point in Fig. 4.2 c) represents an integral over the allowed range of binding energies spherically averaged in order to simulate the experimental total electron yield (TEY). In order to illustrate this procedure and to highlight the main features in a more effective way, all spherically averaged spectra for both circularities meaning the photocurrent intensities $I(E, \Phi, \mathbf{h})$ are plotted comprehensively in Fig. 4.3 b). $E = E_F - E_{KIN}$ and $\mathbf{h}$ is the helicity.

In Fig. 4.3 b), the difference between the TEY for *lcp* and *rcp* light, which is proportional to the asymmetry, is highlighted in red and shows a pronounced peak around ~ 0.4 eV. The peaks in each spectrum close to the highest binding energy, marked by ii), are due to surface-resonances (SR), confer section 3.3, also mentioned in [69]. Similar states have been found for Ni(110) [65], Fe(110) [67] and Co(0001) [70]. In fact, for Ni(001) surfaces there are two SR in the relevant energy range. Each of them with a large bulk contribution due to the hybridization with bulk states, which explains the "survival" of these SR, even when large fractions of the surface are covered by adatoms [54]. This is in agreement

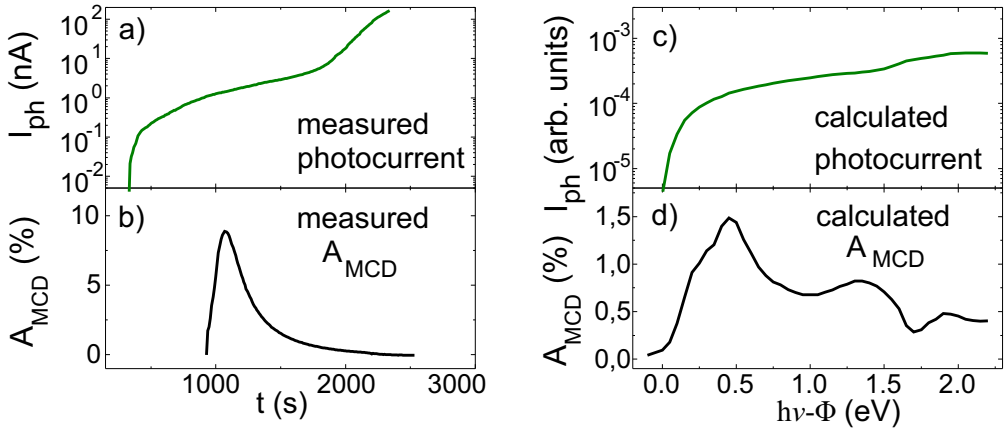

Figure 4.2: *a) and b) The photocurrent and TP-MCD-asymmetry obtained as a function of Cs-deposition time. Before ∼900 s the signal-to-noise ratio with an applied magnetic field was to low. The one-step model calculations of the dichroic signal and yield are shown in panel c) and d), respectively. This figure and caption is modified published in [12].*

with the survival of these states in our experiment where Cs has to be deposited onto the magnetic films in order to lower the work function. The Cs coverage however, is less than ~ 0.5 ML, since above this thickness the sticking coefficient becomes zero [71, 72]. What is more, the energetically lower SR is located at ~ 0.5 eV binding energy and stays constant in energy while lowering the work function, whereas the other SR, around ~ 1.5 eV, shifts as a function of Φ and strongly increases in intensity for lower work function values. However, these SR's exhibit almost no dichroic behavior in the photoemission intensity, but only enlarges the TEY. The main MCD-signal originates therefore from an energetic region around ~ 0.4 eV, as magnified and plotted in inset i). This large MCD-asymmetry derives from spin-split *d*-bulk states, where the corresponding transitions from initial to final states can roughly be identified from the bulk band structure. This is shown in Fig. 4.5 and is calculated within the LSDA+U framework along the perpendicular direction Γ to X.

Besides, Fig. 4.3 a) summarizes the TP-MCD-asymmetry derived from the individual *lcp* and *rcp* intensities from plot b) by using the asymmetry definition Eq. (3.2). As can clearly be seen, a large positive MCD-signal is located in the region below ~ 0.4 eV binding energy, increasing with decreasing work function. But exactly this large increase in Fig. 4.3 a) appearing at low kinetic energies and low work function values is a rather unexpected feature, as in the total MCD-signal, Fig. 4.2 d), the MCD-signal decreases with decreasing work function. Note, this region exhibits up to $\sim 25\,\%$ asymmetry. Obviously, to access this region experimentally energy filtering of the photoelectrons is required.

Coming back to Fig. 4.2, the asymmetry peak and other features can now be explained. The total photocurrent (Fig. 4.2 a)) exhibits two features, the first is the starting point falling off according to the Fermi function, and the other is this kink-like feature around ~ 1800 s in the experimental photocurrent. The latter can be attributed to the strong increase in photoemission intensity, when the second SR takes part in the photoemission process which can be seen in Fig. 4.3 b) marked by ii). With this, the reduction of the MCD signal beyond ~ 0.5 eV can be explained. The large asymmetry for low energies is more and more diluted by the large non-dichroic signal caused by the two SR-transitions and other bulk state transitions leading to an increasing total photocurrent.

However, by way of comparison of Fig. 4.2 a) and c), the kink-like increase of the total yield in the experimental data appears more pronounced than in the calculation. This is most probably since theory underestimates the intensity variation of the surface resonance with Φ. With the same argument the deviation in the maximum value of the dichroic signal can be understood. Concerning the energy the agreement is quantitative, reflecting therewith the rather accurate description of electronic correlations in Ni by the LSDA+DMFT

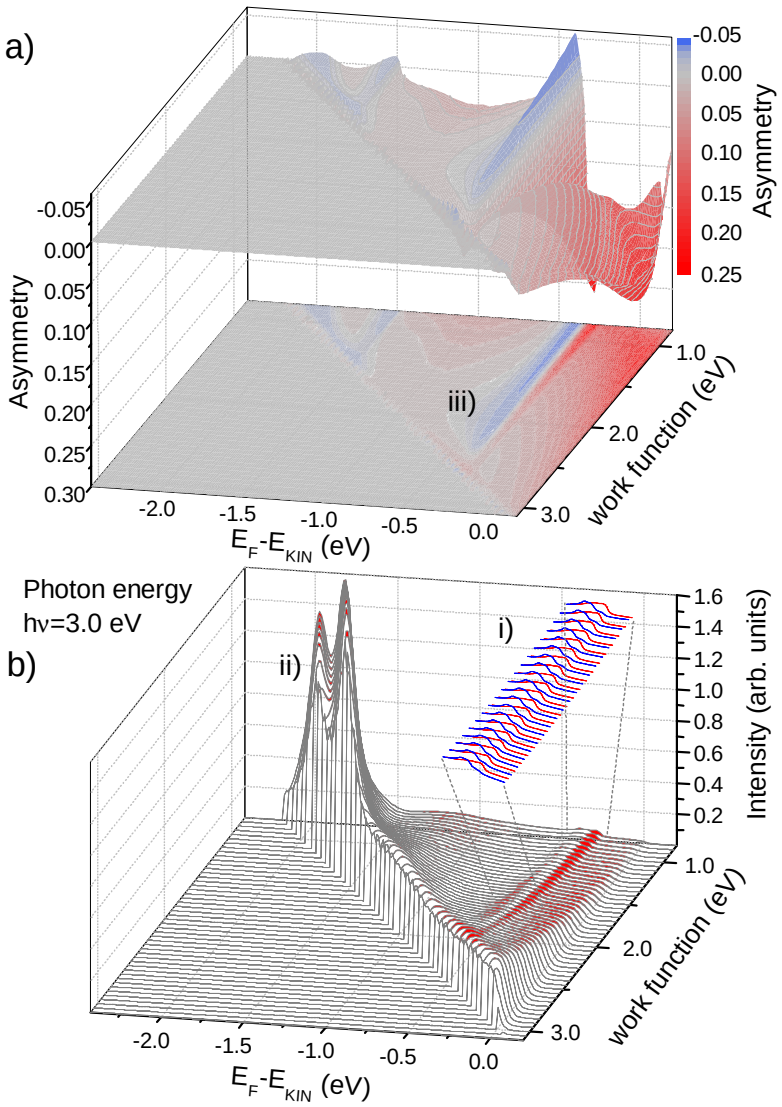

Figure 4.3: *a) According to Eq. (3.2) the TP-MCD asymmetry is calculated for various binding energies and work function values from spectra shown in b). Each line in b) consists of two photoemission spectra, rcp and lcp light illumination, calculated in the framework of LSDA+DMFT within the one-step photoemission model. The difference in the rcp and lcp spectra is highlighted by red color, and is magnified plotted in inset i), where the spectrum for right (left) circularly polarized light is in red (blue) color. The peaks marked by ii) occurring at lowest binding energies in each spectra up to work function values of 3 eV are caused by d-surface resonance states which shift in energy by changing the work function, due to changing the effective surface potential. Features in the asymmetry plot a) marked by iii) are due to spin-split d-bulk states exhibiting large asymmetries which can also be seen in the inset i) of b).*

method [12, 65]. Additionally, as pointed out in the photoemission model section, the energetic position of the surface resonances strongly depends on marginal variations of the simulated surface potential since the photoelectron kinetic energy and self-energy of these states are energetically comparable.

At this point, we are able to deduce another way to obtain a Cs-deposition-time to energy conversion factor. From Fig. 4.2, by using the position of the two peaks in the asymmetry plots, we obtain a time-energy scaling factor of $\sim 0.63\,\mathrm{eV}/(1000\mathrm{s})$, which is close to $\sim 0.81\,\mathrm{eV}/(1000\mathrm{s})$ as given above, section 4.1.2. However, by using the kinks in the photocurrent plots, located at $\sim (1800 - 350)\,\mathrm{s}$ (Fig. 4.2 a)) and $\sim 1.5\,\mathrm{eV}$ (Fig. 4.2 c)), we end up in a time-energy scaling factor of $\sim 1.03\,\mathrm{eV}/(1000\mathrm{s})$. This discrepancy indicates that the binding energy of the second SR may be underestimated, i.e. located at too low binding energy, whereas the influence of these states on the asymmetry, i.e. the photoemission intensity, may be overestimated. Several attempts to map these two values by varying the surface potential has led to an even smaller total MCD-asymmetry. Note, that this fine tuning process simultaneously adapts the features in the theoretical plots to the experimentally measured ones. The mean value of both time-energy scaling factors are $\sim 0.83\,\mathrm{eV}/(1000\mathrm{s})$, which is close to the time-energy scaling factor found in section 4.1.2.

4.2.3 Three-Step Photoemission Model

In addition to the one-step photoemission calculation a less accurate but simpler and hence more instructive approach is used to further investigate the TP-MCD effect of Ni/Cu(001), i.e. the so-called *three-step model* [40], see section 3.4. This model separates the photoemission process into absorption of light, transport to the surface and emission of the excited electrons. Since the major contribution to the MCD-signal originates in the absorbtion process, only this single process is examined in the following. Furthermore, only the initial states participating in the absorption process will be investigated. This simplification is based on the experimentally verified dependence of the MCD-asymmetry on solely the difference between the work function and the photon energy, i.e $E = h\nu - \Phi$, confer Fig. 4.1. This explicit independence on solely one of them leads to the result that the final states may only play a minor role in the TP-MCD process and will therefore be neglected in further investigations. These facts can be summarized in a very coarse picture: The spin-polarization of the initial states is a measure of the TP-MCD-asymmetry since the photon helicity couples to the spin of the electrons via spin-orbit-coupling and the spin-polarization of the initial states results from the magnetization. Therefore the larger the spin-polarization, the larger the TP-MCD-asymmetry, provided that suitable transitions of the participating states exist.

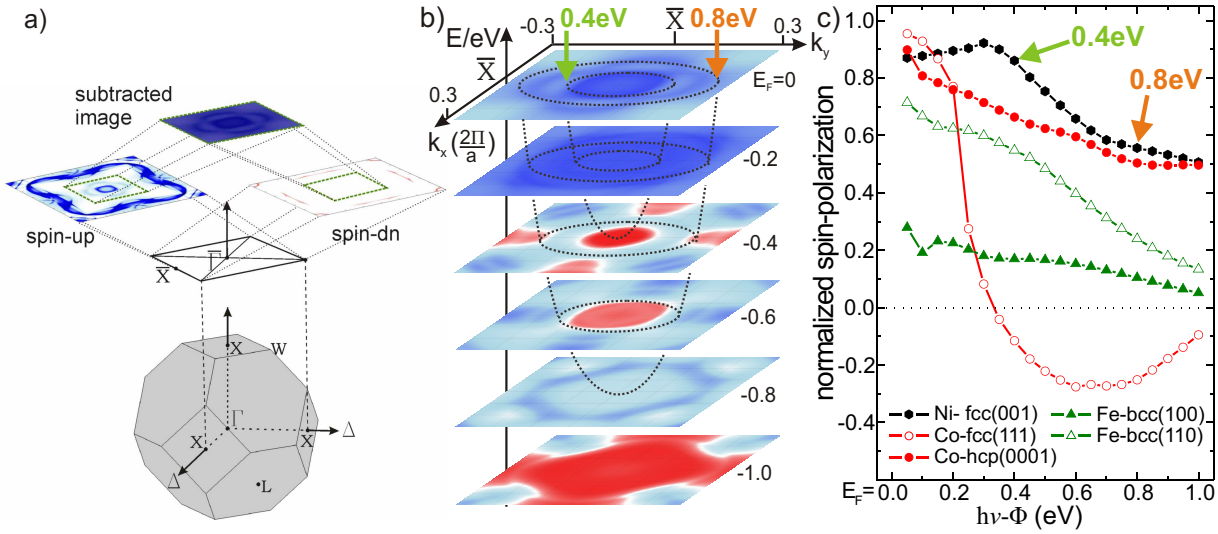

Figure 4.4: *a) outlines the method to calculate the spin-polarization for a given energy via the k-dependent surface-projected Bloch spectral function in this case for Ni/Cu(001). The subtracted image shows minority minus majority spins. b) same as a) but for various energies, where blue color means more minority electrons, and red color means more majority electrons. Due to the energy-wave-vector relation in the free electron approximation, the photoemission process takes only place in a certain* **k***-range, a paraboloid. Two of those paraboloids (0.4 eV and 0.8 eV) are also shown in b). The evolution of the normalized spin-polarization within those paraboloids is plotted in c) for fcc(001)-Ni, fcc(111)- and hcp(0001)-Co as well as for bcc(100)- and bcc(110)-Fe, where hν is the photon energy and Φ is the work function. All calculations are done with LSDA+DMFT and for out-of-plane magnetization. The arrows in b) indicate the calculated spin-polarization values for the paraboloids shown in b).*

By anticipating the result, the spin-polarization around $\sim 0.4\,\mathrm{eV}$ below E_F is the fundamental basis for the TP-MCD signal of Ni/Cu(001), which is in line with the one-step model in the case of Ni/Cu(001). Based on this agreement, the three-step model will also be applied to other systems in order to predict the possibility of such systems to show a TP-MCD signal. The one-step model is not used for these predictions, since firstly, it is computational quite expensive and even more importantly, the determination of the needed parameters, e.g. the image plane distance, surface potential evolution etc. is very time-consuming and so far not very well validated by experiments for the interesting energy range. However, in addition to this calculation, the code written as part of this thesis to evaluate the spin-polarization of thin magnetic films within the three-step model is also

used to investigate the spin-polarization of the individual layers of such systems, as will be shown below.

The spin-polarization can be calculated by subtracting surface-projected[3] Bloch-spectral functions for spin-up and spin-down states, see Fig. 4.4 a). The Bloch-spectral function can be viewed as the **k**-dependent density of states (DOS) function. In Fig. 4.4 b) subtracted ($n^{\text{min.}}(\mathbf{k}) - n^{\text{maj.}}(\mathbf{k})$) LSDA+DMFT Bloch spectral functions, i.e. the spin-polarization, for fcc-Ni are plotted for various energies below the Fermi energy E_F. The main result from Fig. 4.4 b) is the reversal of the spin-polarization between 0.2-0.4 eV in some **k**-regions. By lowering the work function with the aid of Cs, the energetic range of the photoelectrons is increased and therefore more states below E_F are accessible. Since in the photoemission process the initial state vector $\mathbf{k}_i$ is coupled to the final state vector $\mathbf{k}_f$ by an energy and wave vector conserving transition, the available initial $\mathbf{k}_i$-vectors are located within a paraboloid, described by the energy-wave-vector relation in the free electron approximation $E = \frac{\hbar^2 k_\perp^2}{2m}$, where $k_\perp = \sqrt{k_x^2 + k_y^2}$ is the magnitude of the electron wave vector perpendicular to the surface and m is the electron mass. For a specified penetration depth the spin-polarization of the initial states results from the summation of all spin-polarization values within the paraboloids normalized to all available states within the corresponding paraboloid. Fig. 4.4 c) summarizes these summations for different work function values at a fixed photon energy. This plot reveals that the maximum TP-MCD-asymmetry should be achieved at ∼0.3-0.4 eV. By way of comparison the agreement between both photoemission models, Fig. 4.2 d) and Fig. 4.4 c), is very good [12].

Based on this agreement, the spin-polarization for various other materials is also calculated in order to get an indication for the strength of the TP-MCD signal that can be expected from those systems, which is also shown in Fig. 4.4 c). The very low TP-MCD signal in 1PPE in the case of *fcc*-Co(111) [73] has already been verified in [15]. Even the opposite sign (above ~ 0.3 eV in the spin-polarization calculation Fig. 4.4 c)) of the asymmetry has been shown in [15], although it was actually positive in that paper. However, as pointed out in the beginning, section 4.1.1, these authors used an ambiguous definition of the asymmetry. The sign reversal of the spin-polarization, however, has not occurred in the experiment.

In order to directly see the relevant photoemission transitions, the LSDA+U *bulk* band structure of Ni(001) is plotted in Fig. 4.5 a) along the Δ-direction (Γ to X), which is the most relevant direction for a (001)-crystal surface in the photoemission process. In Fig. 4.5 a) the spin-dependent bulk band structure is shown, where blue (red) color means

[3]The projection onto the surface has to be done in order to get the thin film band structure including explicitly the effect of the surface and not only the bulk electronic structure.

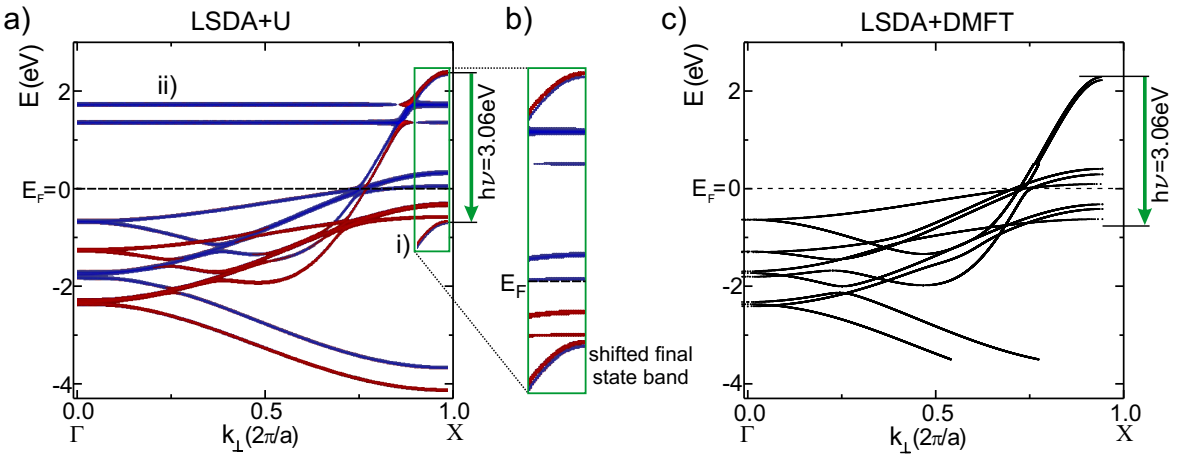

Figure 4.5: *The spin-resolved LSDA+U band structure of bulk* fcc-*Ni along the* Δ*-direction from* Γ *to* X *is shown in a) with blue (red) color means minority (majority) spin. In order to directly see the relevant transitions by crossing points of the initial and final bands, a part of the final state p-band is shifted downwards about* $3.06\,eV$*, which is the used photon energy, marked by i) and is also plotted magnified. Unfortunately, no crossing points are visible, which can be attributed to the fact that this is only a bulk band structure. The non-dispersing bands in a) marked by ii), are artificial states, which are only due to the spin-projection process neglecting some non–diagonal non-zero matrix elements. In b) the LSDA+DMFT band structure is shown. Again no crossing points would be visible, when shifting the final states downwards.*

minority (majority) spins and is plotted for an energy region from -4 eV to 3 eV, where $E_F = 0$. One can clearly see the spin-split bands around the Fermi-level, and the final state band reaching the X-point at ~ 2.4 eV. The horizontal lines marked by ii) are somewhat artificial and a consequence of neglecting some non-zero, non-diagonal matrix elements in the spin projection process of the respective Green's function. b) shows a magnified plot in which the final states, marked by i) in Fig. 4.5 a), are lowered by the photon energy (3.06 eV). What can clearly be seen is the fact that the final states do not intersect with the initial states, resulting in a zero transition probability regarding only energy conservation. However, this obvious discrepancy with experimental as well as theoretical data is due to the fact that only a *bulk* band structure is considered. For comparison, the spin-*un*resolved band structure calculated by LSDA+DMFT is plotted in c) which clearly shows the influence of the used DMFT framework on the band structure. However, a transition would again not occur by shifting the final state band, i.e. no crossing points between the initial and final bands would occur, which can again be attributed to the effect of the surface on the electronic structure. Nevertheless, even from these plots some conclusions can be drawn. At first, transitions occur only close to the X-point along the

perpendicular Γ to X direction. Second, there is only a single final state band, which is only slightly spin-polarized. Hence, the spin-polarization of the initial states is the main ingredient for the observed large MCD-asymmetry, which is in turn a consequence of the large exchange splitting of the $3d$-bands around the Fermi energy. Therefore, the approximations made in this less accurate but more instructive explanation of the large TP-MCD signal are justified.

4.3 TP-MCD of Fe/Ni/Cu(001)

The most thoroughly studied sample in this thesis with respect to the magnetic properties is a layer structure consisting of an ultra thin Fe film on thin ($\leq$12ML) Ni-films deposited on a Cu(001) substrate. The ferromagnetic films are investigated in both a continuous wedge as well as a stepped-wedge shape. The motivation to investigate this particular system is given in section 6.2.3.3. However, with respect to the TP-MCD effect, this system also exhibits a rather unique property, of a large TP-MCD asymmetry ($\sim 10\,\%$) over a large Cs-coverage region. This combination of a huge magnetic signal proportional to the photocurrent and simultaneous a large photocurrent has allowed the development of a unique experimental setup able to track the dynamics of magnetic domains with a temporal resolution below milliseconds and a spatial resolution of about $\sim 100\,\mathrm{nm}$.

Unfortunately, within this thesis it was not possible to directly measure the TP-MCD asymmetry versus the Cs-deposition time for the system Fe/Ni/Cu(001) as done for Ni/Cu(001) shown in Fig. 4.2 a) and b). One reason is that after installing a liquid-Nitrogen cooling cryostat in order to perform also measurements at lower temperatures, the manipulator is grounded (i.e. the TEY cannot be measured). Second, even when the total electron yield is recordable, the photocurrents after applying a positive or negative magnetic field pulse, would not represent the TEY of a fully magnetized state. This is due to the fact, that the system Fe/Ni/Cu(001) exhibits small domains in the vicinity of the spin-reorientation point, which are actually smaller than the laser spot size. This can also be seen in section 7.4.1, where a hysteresis loop measurement is extracted from a wide field movie of the magnetic domain structure while sweeping the magnetic field. The coercive fields were around $\sim$2-5 Oe depending on the thickness of the Fe layer. Due to the existence of domains, the remanent magnetization is usually less than the saturation magnetization or almost zero. However, the application of a magnetic field while measuring the TEY leads even for those small field values to a reduction of the photocurrent due to a slight misalignment of the sample surface with respect to the magnetic field normal.

The theoretical investigation of the TP-MCD effect for the system Fe/Ni/Cu(001) is also in many ways quite difficult. It is the very base, i.e. the crystal structure, of the thin Fe layers, either on top of Ni(001) or on Cu(001), which is not very well understood in the case of ultra thin films. This is mainly based on the lack of a theoretical model taking all experimentally found properties of this exceptional system into account, see section 6.2.3.2. In section 6.2.3.3 it will be shown that from a crystallographic point of view Fe on Ni/Cu(001) or Fe grown on Cu(001) directly is the same. The complex nature of the crystal as well as the spin structure of Fe/Cu(001) has been shown by Müller et al. [74,75] (crystal structure) and recently by Meyerheim et al. [76] (spin structure), who calculated the spin structure in perpendicular direction for 6 ML and 8 ML Fe on Cu(001). The spin structure in perpendicular direction comprises blocks of spins, where each block has its own inner spin structure, which is known as a non-collinear spin structure. However, as has been shown by Marsman [77] this non-collinearity should also hold true in the planar direction and not only along the normal direction. Besides the spin also the crystal structure is quite complicated in the ultra thin limit. Below 4 ML, which is actually the interesting thickness range, Fe on Cu(001) exhibits a (4x1) superstructure which continuously becomes a (5x1) superstructure at 4 ML. This was measured by quantitative LEED spot analysis, where the line profiles were traced while evaporation [75] and verified within this thesis by RHEED measurements in 6.2.3.3. This fact in combination with a strong dependence of the exchange interaction for iron on the interatomic distance, which even changes the sign by varying the lattice constant less than a percent, makes the computation of the band structure for this system quite challenging.

However, trying to determine the Fe contribution to the TP-MCD signal leads to the investigation of the penetration depth of the used wavelength (405 nm). Applying Beer-Lamberts law for the attenuation of light in this metallic films, results in a penetration depth or attenuation length of ~ 14 nm for Ni ($\hat{n}(405\,\text{nm}) = 1.61 - 2.39\text{i}$ [61, 78]) and ~ 18 nm for Fe (with $\hat{n}(640\,\text{nm}) = 3.03 - 1.78\text{i}$ as approximation [61], due to the lack of any measured $\hat{n}(405\,\text{nm})$). This follows from the exponential dependence of the intensity on the penetration depth δ_{pen}, i.e. $I = I_0 e^{-\alpha x}$, where $\alpha = \frac{2}{\delta_{pen}}$ is the attenuation or absorption coefficient. The attenuation coefficient, in turn, is connected to the imaginary part of the refractive index by [79]

$$\alpha = \frac{2}{\delta_{pen}} = \frac{2\omega}{c} Im(\hat{n}(\omega)) = \frac{2\pi}{\lambda} Im(\hat{n}(2\pi\frac{c}{\lambda})) \; . \tag{4.1}$$

Since the investigated magnetic films are always less than ~ 3 nm thick, the light intensity can be approximated to be constant for all magnetic layers. In addition, the mean free path of the excited photoelectrons has to be considered in order to assess the contribution of the ultra thin Fe top-layers (< 3 ML) to the total photocurrent yield. The mean free

path is according to the universal curve of the mean free path [80] for energies below $\sim 7\,\mathrm{eV}$ larger than $\sim 45\,\text{Å}$. Although there are indications [81] for a shorter mean free path in the case of $3d$ ferromagnetic systems for such low electron energies, the assumption neglecting the contribution of the ultra thin Fe top layer to the total electron yield compared to that relatively thick Ni film ($9\,\mathrm{ML} < d_{\mathrm{Ni}} < 12\,\mathrm{ML}$), is verified.

The TP-MCD signal of the system Fe/Ni/Cu(001) hence should be approximately equal to that of Ni/Cu(001). Ni/Cu(001) shows a single narrow peak of the TP-MCD asymmetry, confer Fig. 4.2 b). The reduction of the signal is due to the participation of SR's in the photoemission process, exhibiting no circular dichroism. However, these SR's come only into being due to the interface between the Ni-crystal and vacuum and do not exist in the case of Fe/Ni/Cu(001). Hence, reducing the work function enlarges the region of accessible states without the contribution of these non-dichroic surface resonances. This may lead to a broader maximum and may even increase the asymmetry. However, all asymmetry values extracted from images are in the range from zero to $\sim 10\,\%$. The broadening of the peak has not directly been measured so far, but the asymmetry extracted from images obtained after several cycles of Cs-deposition, seems to support this assumption.

Despite all these rather unknown facts, the spin-polarization for *fcc* (2ML)Fe/(10ML)Ni on Cu(001) is calculated. This is done, since the spin-polarization calculation has led to a qualitative agreement between theory and experiment in the case of Ni/Cu(001). Hence, the above described spin-polarization calculation within the 3-step photoemission model is exploited for this purpose as well. The photon energy used for this calculation is again $3.06\,\mathrm{eV}$. The result, both layer and energy resolved, is shown in Fig. 4.6 c). The crystal structure is approximated to be a *fcc* structure (confer section 6.2.3.3) and the electronic structure has been subsequently relaxed by a relaxation process within the band structure calculation. Nevertheless, in spite of all these approximations, Fig. 4.6 b) exhibits a more stable TP-MCD signal for a broader energy region, i.e. for a larger range of Cs-coverage, here for e.g. the fifth Ni layer. This is again in agreement with the experiment. In addition, this calculation reveals a spin-polarization of up to $\sim 33\,\%$ in the first Cu layer (Fig. 4.6 c) i)) as well as a lower spin-polarization for the second Fe layer compared to the first Fe layer and even a negative spin-polarization (Fig. 4.6 c) ii)).

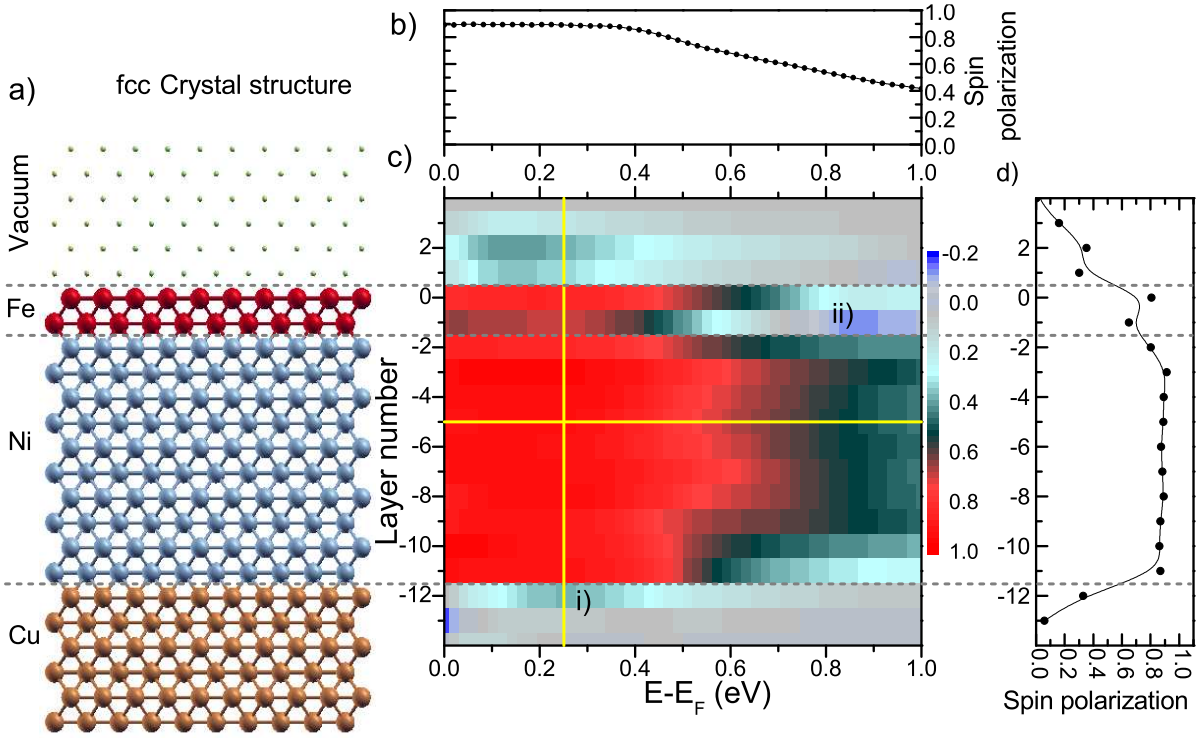

Figure 4.6: *a) fcc-Crystal structure for the half-infinite system of (2ML)Fe/(10ML)Ni/Cu(001). c) shows the layer-resolved spin polarization for energies E below E_F. b) and d) are linescans to the corresponding (yellow) lines in c). Two features are highlighted in plot c): i) the first Cu-layer has a spin-polarization of up to 33%; ii) the second Fe-layer exhibits a smaller spin-polarization and even shows a negative spin-polarization around 0.9 eV.*

Chapter 5

Experimental Setup and Sample Preparation

5.1 Measurement Setup

The measurement setup comprises three UHV chambers: surface analysis chamber, MBE (molecular beam epitaxy) and examination chamber. The first chamber contains X-ray photoemission spectroscopy (XPS) for sample surface analysis with respect to the chemical composition. It also offers Ar-ion sputtering for cleaning and depth profiling of the samples. The manipulator allows for rotating the sample during the sputtering process resulting in less severe damage to the sample surface. The base pressure of this chamber is $\sim 4 \cdot 10^{-10}$ mbar. During the sputtering process the pressure rises to $\sim 2 \cdot 10^{-8}$ mbar. This chamber was used to remove contamination and oxide layers or previously deposited ferromagnetic thin films and also to verify the quality of evaporated materials under investigation.

The MBE chamber was assembled at the beginning of this thesis and contains besides five low capacity electron beam evaporation sources for Fe, Ni, Cu, MgO and Gd evaporation, a five-pocket high capacity evaporation source (Thermionics) with Au, Permalloy (Py), Fe, Cu and Pt as evaporation materials. A quadrupole mass spectrometer (Balzers, QMG421) for rest gas analysis is installed, as well. In order to investigate the substrate and sample quality with respect to crystallinity and roughness and also to investigate and pursue the growth process during evaporation a RHEED (reflection high energy electron diffraction) gun and fluorescence screen is mounted. Further, for thickness calibration, four quartz micro balances are mounted in such a way that each evaporation source can be monitored. In order to prepare wedge-shaped or stepped-wedge samples, a piece of a Silicon crystal is

mounted onto a stepper motor-driven linear translator. The manipulator of the chamber also offers the possibility of cooling the sample with liquid nitrogen and of resistive heating up to $\sim 900\,\mathrm{K}$. The base pressure is better than $\sim 2{\cdot}10^{-10}\,\mathrm{mbar}$.

The PEEM chamber contains a photoemission electron microscope (Focus PEEM). The manipulator is not directly mounted onto the PEEM extractor lens, as usually done in PEEM setups, but is attached to the UHV-chamber. The manipulators heating and cooling capability covers a sample temperature range from $\sim 170\,\mathrm{K}$ to $\sim 330\,\mathrm{K}$. The application of a magnetic field perpendicular to the film surface of up to $\sim 300\,\mathrm{Oe}$ is realized by an air coil mounted onto a wobble stick in order to make the sample transfer possible and also to align the coil with respect to the sample position. In the first run the sample was insulated and connected to an electrical feedthrough, which was used to measure the photocurrent from the sample. However, after installing a liquid nitrogen cooling cryostat attached to the sample by copper braids in order to retain the ability of sample manipulation and obtain the above given temperature range, the sample has been grounded.

5.2 Substrate and Sample Preparation

In this thesis all measurements are conducted on a Cu(001) single crystal disk (manufactured by Mateck), 3 mm thick and 10 mm in diameter. It is mounted into a titanium sample holder by a tungsten wire. In order to guarantee a good thermal contact required by the annealing process, the tungsten wire gently presses the Cu-crystal onto the titanium sample holder. The design and fabrication of the sample holder and also the crystal itself avoids sharp edges and thereby reduces the tendency for arcing at high voltages.

The substrate was ordered with highest accuracy in crystallographic alignment ($< 0.1°$) and also with the smallest possible roughness of the surface ($< 0.03\,\mu\mathrm{m}$). However, an additional substrate preparation process is required in order to further increase the substrate quality. The preparation process comprises cycles of Ar-ion sputtering with kinetic energies of the ions of up to $\sim 1200\,\mathrm{eV}$. This energy is subsequently decreased with increasing cycle number down to $\sim 800\,\mathrm{eV}$. In each cycle the sample is annealed at up to 800 K for ∼20-30 minutes. Rotating the sample while sputtering leads to less severe damage to the sample surface, which is reflected by a less blurred RHEED pattern. The sputtering process is performed until solely the Cu peaks are visible in the XPS-spectrum, which can be seen in Fig. 5.1 a). Right after sputtering the RHEED pattern of the Cu(001) substrate contains broad, smeared peaks according to the intersection of the Ewald sphere in reciprocal space Fig. 5.1 c) left. After the annealing process, the RHEED spots become sharper

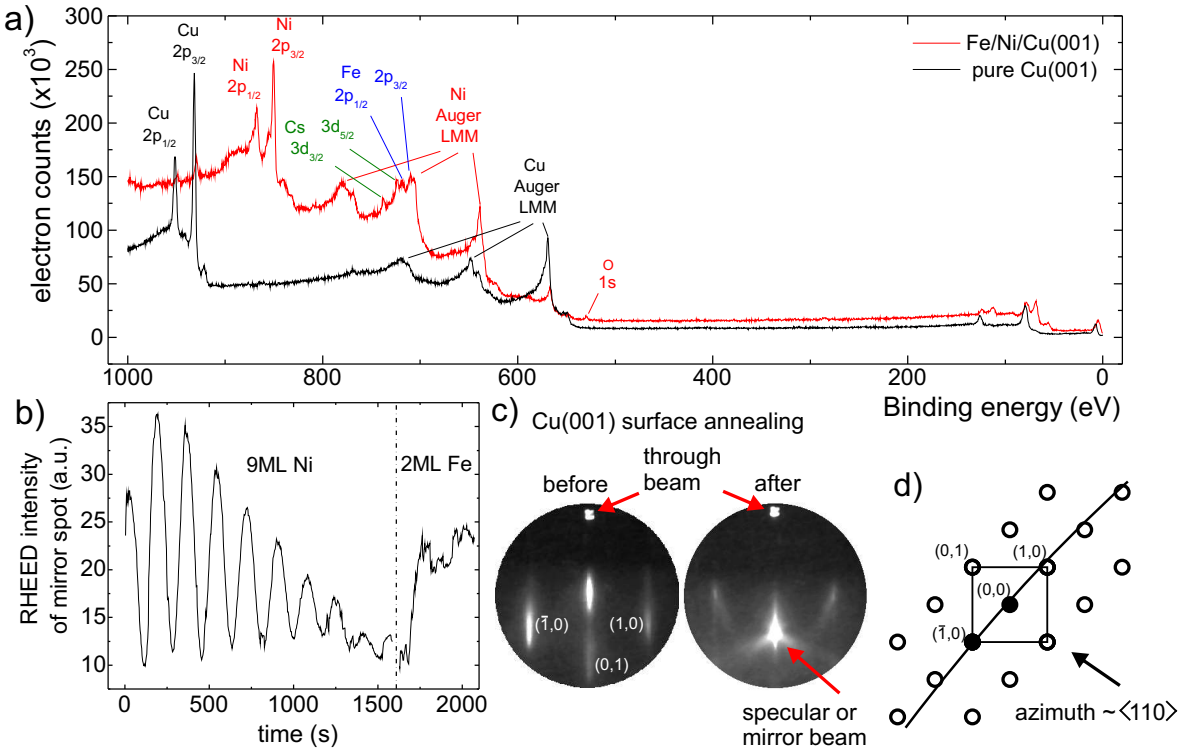

Figure 5.1: *a) shows two typical XPS spectra for a clean Cu(001) (black) surface and a Fe/Ni/Cu(001) (red) surface. b) presents RHEED oscillations of the specular* $(0,0)$ *beam during the growth of (9ML)Ni and (∼2ML)Fe. c) shows the RHEED pattern before and after annealing of the Cu(001) crystal. A schematic drawing of the reciprocal lattice, projected along the lattice rods in reciprocal-space onto the surface is shown in d). The curved line represents represents the intersection of the Ewald sphere. The azimuthal angle of the incident electron beam was roughly along the* $\langle 110 \rangle$ *direction, which can be seen in the different intensities of the* $(\bar{1},0)$ *and* $(1,0)$ *spots [82].*

and brighter. In addition, by approaching the maximum annealing temperature, Kikuchi lines become visible, Fig. 5.1 c) right, indicating an improved crystalline surface quality. In addition, the specular spot of the RHEED pattern becomes visible and subsequently moves towards the (0,1) spot. The pressure in the chamber remains below $7 \cdot 10^{-10}$ mbar while heating up the sample. The higher the number of sputtering-annealing-cycles, the better the quality of the substrate surface. In the case of ultra thin Fe/Ni films the quality of the substrate and also of the magnetic films is directly reflected by the disorder of the domain pattern, as will be seen in the chapter 7.

The fabrication of ultra thin magnetic films is performed by using the low-capacity evaporation sources in the MBE-chamber, as described above. The evaporation rate for Nickel

was typically $0.34\,\frac{\mathrm{ML}}{\mathrm{min}}$ and for Iron $0.43\,\frac{\mathrm{ML}}{\mathrm{min}}$, while the pressure during evaporation does not exceed $4 \cdot 10^{-10}$ mbar. During the growth process the intensity oscillations of the specular RHEED spot is monitored, as shown in Fig. 5.1 b). This is a very accurate method to measure the evaporated thicknesses and also provides a calibration method for other evaporation control units such as atomic flux monitoring or quartz micro balances. Unfortunately, the roughness of the surface increases with increasing number of grown layers in the case of Ni/Cu(001). This leads to the reduction of the amplitude of the RHEED oscillations. The subsequent growth of ∼2 ML Fe therefore results only in weak RHEED oscillations, as can be seen in Fig. 5.1 b). In Fig. 6.3 of section 6.2.3.3, the RHEED oscillations of 6 ML Fe on only ∼ 5.4 ML Ni are presented. In this case the amplitude of the RHEED oscillations is still large and remains almost constant during the Fe growth up to ∼ 4 ML. After transferring the sample into the PEEM chamber, the PEEM is adjusted with a mercury arc lamp, possessing UV-wavelength components in its light spectrum which energetically exceed the work function of pure Ni and Fe. Subsequently, Cs-adatoms are deposited onto the sample surface in order to obtain photoelectrons and, hence, magnetic contrast with the 405 nm laser source. Only in some cases, separately indicated in chapter 7, the Ni film has been annealed to $620 - 670$K and subsequently cooled to room temperature before evaporating the Fe top layer in order to obtain a smoother substrate for the Fe film.

Chapter 6

Magnetic Energies and Phase transitions

The following chapter is dedicated to magnetic properties and energies of ultra thin ferromagnetic films determining both the general spin orientation as well as the formation of intricate patterns especially in the out-of-plane phase. Particular emphasis is placed on phase transitions which occur in the model system Fe/Ni/Cu(001). The most obvious transition is the spin-reorientation transition, where the magnetization changes its direction from in-plane to out-of-plane or vice versa. The transformation of domain patterns within the out-of-plane phase characterized by a suitable order parameter are thought to exhibit critical behavior.

6.1 Itinerant Ferromagnetism and Exchange Interaction

In $3d$ transition metals ferromagnetic ordering of the magnetic moments, i.e. the parallel alignment of spins, may be the ground state in a certain temperature range. The reason for this is that the gain of Coulomb energy due to a reduced probability to find two electrons at the same position having the same spin direction (Pauli principle), can in some cases overcompensate the corresponding increase in kinetic energy. The increase in kinetic energy is caused by the parallel spin alignment of half as many states per unit volume which accompanies an occupation of a larger area in reciprocal space. A criterion for magnetic ordering is given by the expression

$$I\, n(E_F) > 1 \ , \tag{6.1}$$

formulated by Stoner, where I[1] is the Stoner parameter and $n(E_F)$ is the density of states at the Fermi edge. According to [84,85], I contains exchange as well as correlation effects and is related to the Hubbard term (Eq. (3.15)). The exchange interaction strength is given by the exchange integral J, which can be written for a two electron system with Coulomb interaction as

$$J_{ij} = \frac{e^2}{4\pi\varepsilon_0} \int \mathrm{d}^3 r_1 \int \mathrm{d}^3 r_2 \frac{\phi_i^*(r_1)\phi_j^*(r_2)\phi_j(r_1)\phi_i(r_2)}{|\mathbf{r}_1 - \mathbf{r}_2|} \ , \tag{6.2}$$

where $\phi(\mathbf{r})$ is the orbital part of the wave function, confer [84–86]. For $J > 0$ this leads to the appearance of ferromagnetic order, for $J < 0$ to anti-ferromagnetic order. The exchange interaction is typically isotropic and temperature dependent. Further, for a discrete lattice with spins on each lattice site represented by a unit vector $\mathbf{s}_i$ the exchange energy can be written as

$$E_{ex} = -\frac{1}{2} \sum_{\langle i,j \rangle} J_{ij} \mathbf{s}_i \cdot \mathbf{s}_j \ , \tag{6.3}$$

where the sum takes only neighboring sites into account. For a cubic system with q nearest neighbors, Eq. (6.3) takes a simpler form and the exchange energy is then usually called Γ,

$$\Gamma = \frac{1}{2} q s^2 J \ . \tag{6.4}$$

What is more, J is a microscopic parameter and its direct quantitative determination is still difficult. However, a measurable, macroscopic parameter, which is closely related to the exchange integral, is the exchange constant which is defined as

$$A = \frac{1}{2g\mu_b} M_{S,0} (2JSa^2) = \frac{1}{2g\mu_b} M_{S,0}\, D \ , \tag{6.5}$$

where g is the Landé-factor, $M_{S,0}$ is the saturation magnetization at $T = 0\,\mathrm{K}$, a is the lattice constant and S is the spin at each site [87,88]. D is the spin wave stiffness.

[1] An explicit form of I is given in [83] but is beyond the scope of this thesis.

6.2 Anisotropic Magnetic Interactions

The origin of magnetic *an*isotropies, responsible for the alignment of the magnetization along preferred axes, can be categorized into two groups. On the one hand, the dipolar energy leads to shape anisotropies, also called the magnetostatic anisotropy. On the other hand, spin-orbit coupling (SOC) is responsible for magnetocrystalline as well as magnetoelastic anisotropies [89].

6.2.1 Dipolar Energy and Magnetostatic Anisotropy

The dipolar energy density is given by

$$\varepsilon_{ms} = \frac{1}{2}\mu_0 \mathbf{H}_d \cdot \mathbf{M} \ , \tag{6.6}$$

where $\mathbf{H}_d$ represents the magnetic dipolar field or demagnetizing field [87] and is a result of the magnetization $\mathbf{M}$ itself. The magnetic surface and volume charges, given by $\rho_s = \mathbf{n}\cdot\mathbf{M}$ and $\rho_v = -\nabla \cdot \mathbf{M}$, respectively, lead to a scalar potential, which in turn can be used to calculate the demagnetizing field. $\mathbf{n}$ is the surface normal of the magnetic sample. For an ultra thin ferromagnetic film with uniform magnetization the magnetostatic energy becomes

$$E = \frac{1}{2}\mu_0 M_S^2 \cos^2\theta \ , \tag{6.7}$$

where M_S is the magnetization at saturation and θ is the angle between the magnetization and the surface normal $\mathbf{n}$. Hence, the magnetostatic anisotropy favors in-plane magnetization. Eq. (6.7) is based on the short range part of the dipolar interaction introduced in Eq. (6.17).

6.2.2 Magnetocrystalline Anisotropies: Bulk and Surface

In bulk 3*d*-transition metals the orbital momentum is said to be "quenched"[2]. However, the coupling of the remaining orbital momentum to the spin via SOC, leads to a magneto*crystalline* anisotropy K_V for bulk materials in the range of a few μeV/atom [89]. This causes preferred directions of the spontaneous magnetization, like for example in bulk Ni along the $\langle 111 \rangle$ and in bulk Fe along the $\langle 100 \rangle$ directions. At surfaces or interfaces the crystal symmetry is reduced, accompanied by a change in the occupancy of the orbitals and an increased orbital momentum. This introduces a surface magnetocrystalline

[2] In a classical picture, the electrons are confined to certain directions, i.e. the bonds, by the crystal environment and, hence, the orbital motion is suppressed [90].

anisotropy K_S and is known as the Néel type anisotropy [91, 92]. What is more, at the interface between substrate and film material an equivalent effect occurs. This interfacial anisotropy K_I also originates from hybridization of substrate and film atomic orbitals. In summary, the effective magnetocrystalline anisotropy is given by

$$K_{\text{eff}} = K_V + \frac{K_S + K_I}{d} \ , \tag{6.8}$$

where the first term has a unit of volume energy density and the surface and interface anisotropies are area energy densities. The representation of these anisotropy terms in units of energy per atom facilitates the comparison to other energy terms [93]. The thickness d is given in units of monolayers. Note, that (although commonly used) Eq. (6.8) is rather counterintuitive, since the surface and interface terms are more or less constant energy terms with respect to the film thickness, while the volume anisotropy depends strongly on the film thickness. Some anisotropy values for the System Fe/Cu(001), Ni/Cu(001) and Fe/Ni/Cu(001) are given in Table 6.1. Furthermore, when considering a uniaxial anisotropy, it is convenient to combine the magnetostatic ($-2\pi M_S^2$) and the uniaxial volume magnetocrystalline anisotropy K_V^u to an *effective* volume anisotropy term $K_{V,\text{eff}}^u$, since both exhibit the same angle and film thickness dependence except for the sign. Hence, the effective anisotropy becomes

$$K_{\text{eff}}^u = K_{\text{V,eff}}^u + \frac{K_{\text{S}} + K_{\text{I}}}{d} \ , \tag{6.9}$$

with [94]

$$K_{\text{V,eff}}^u = K_{\text{V}}^u - 2\pi M_S^2 \ . \tag{6.10}$$

If K_{eff}^u is larger than zero the out-of-plane configuration for the magnetization is the ground state, whereas for $K_{\text{eff}}^u < 0$ the magnetization lies in-plane.

From a more general point of view, the energy densities related to magnetocrystalline anisotropy can be written as

$$\varepsilon_{mc}^{uni} = K_1^u(1-\alpha_3^2) + K_2^u(1-\alpha_3^2)^2 \cdots \ , \tag{6.11}$$

$$\varepsilon_{mc}^{cub} = K_1^c \sum_{i>j} \alpha_i^2\alpha_j^2 + K_2^c\alpha_1^2\alpha_2^2\alpha_3^2 + \cdots \ , \tag{6.12}$$

where K^u and K^c are the uniaxial and the cubic magnetocrystalline constants and $\alpha_i = \cos\theta_i$ are the direction cosines of the magnetization [87]. θ_i is the angle between the magnetization $\mathbf{M}$ and an crystallographic axis with for instance $i = x, y, z$. For a cubic system with out-of-plane magnetization, like for example thin Fe or Fe/Ni films on Cu(001), both anisotropy terms have to be taken into account. On the one hand, the uniaxial anisotropy is responsible for the orientation of the magnetization along any out-of-plane

direction, which does not have to be exactly perpendicular. As was shown by Millev and Kirschner [94], the second term of the uniaxial anisotropy, proportional to K_2^u, leads for values in the range $-\frac{1}{2}K_{1,\text{eff}}^u \leq K_2^u$, for $K_{1,\text{eff}}^u < 0$ to a canted orientation of the magnetization at the SRT. This will be discussed further in chapter 7.1.2. Furthermore, both uniaxial anisotropy terms, K_1^u and K_2^u, have in lowest order a bulk and a surface and interface dependence, see Eq. (6.8) [94, 95]. On the other hand, the cubic anisotropy reflects the favorable in-plane easy axes and determines the stripe orientation for striped magnetic phases with perpendicular magnetization, confer section 6.3.5. In the case of Fe/Ni/Cu(001) this in-plane anisotropy is complicated. Since the easy axes for bulk-Fe are along the $\langle 100 \rangle$-directions and for bulk-Ni they are along $\langle 111 \rangle$, in the exchange-coupled stack of Fe and Ni films, both easy axes come into play. For thick Fe layers a small fourfold behavior along the $\langle 100 \rangle$-directions is favorable, whereas for thinner Fe layers a preference of the domain orientation along the $\langle 110 \rangle$-directions may be visible. The (110)-direction is the 2D projection of the (111)-direction of bulk Ni. This is one of the main differences between the extensively studied systems Fe/Cu(001) and Fe/Ni/Cu(001). At a certain Fe thickness, the superposition of both easy axes ($\langle 100 \rangle$- and $\langle 110 \rangle$-directions) may lead to an isotropic behavior without any preferred axes. For Fe thicknesses in the vicinity of this thickness, a small anisotropy remains and causes, in general, a more undulated/corrugated (i.e. wavy) stripe pattern compared to the highly ordered stripe formation in Fe/Cu(001), as shown e.g. in [3]. Hence, the patterns are less orientationally ordered, which will be seen in almost all images. In the following, the index u for the uniaxial anisotropy terms will be omitted.

6.2.3 Magnetoelastic Anisotropy and Crystallography

In ultra thin ferromagnetic films an unavoidable or intentional strain is induced due to the differences between the lattice constants of the substrate and the film crystal structure. For a given set of lattice constants a_F and a_S of the film material and the substrate, a lattice mismatch [96] according to $\eta = (a_\text{S} - a_\text{F})/a_\text{F}$ is the result. The corresponding lattice strain is then a function of this lattice mismatch and the film thickness d. The latter dependence is due to a relaxation process in the film material, for example, by inserting crystal defects like misfit dislocations leading to a gradual or stepwise reduction of the strain. This strain, in turn, induces a so-called magneto*elastic* anisotropy, which significantly determines the orientation of the magnetization in ultra thin ferromagnetic films. For a cubic (001) system with perpendicular magnetization, the magnetoelastic energy density is given by the relation

$$\varepsilon_{me}^{cub} = B_1(\epsilon_\parallel - \epsilon_\perp) \ , \tag{6.13}$$

where $\epsilon_{\parallel}$ and $\epsilon_{\perp}$ are the in-plane and perpendicular strains, respectively [89] [3]. In the case of pseudomorphic growth, $\epsilon = \eta$ holds [98] and the strain has to be calculated for the in-plane as well as the out-of-plane direction individually. However, as pointed out in [89], the induced strain can significantly change the magnetoelastic constants. In order to take this fact into account the authors in [89,99] added an additional term to the magnetoelastic constant

$$B_1 = B_1^{bulk} + D_{\mathrm{S}}\, \epsilon_{\parallel} \ , \tag{6.14}$$

where D_{S} is the strain correction term and has quite large values, as can bee seen in Table 6.1. For simplicity, in the following the abbreviations *mc* and *me* will be used for magnetocrystalline and magnetoelastic, respectively. Summarizing, the total anisotropy energy density is given by

$$\varepsilon_{tot} = K_V - \frac{1}{2}\mu_0 M_S^2 + \frac{K_S + K_I}{d} + B_1 \cdot \big(\epsilon_{\parallel}(d) - \epsilon_{\perp}(d)\big) \ . \tag{6.15}$$

Unfortunately an analytical formula as a function of d for the *me* term is not known.

[3] The microscopic origin of the magnetocrystalline anisotropy as well as the magnetoelastic anisotropy is the combination of SOC and a change of the orbital occupancy of the $3d$-electrons while the system experiences either a change of the crystal field or a tetragonal strain. In the case of the magnetocrystalline anisotropy consider, for example, atoms in the surface layer. They experience a different crystal field than those atoms within the bulk region. Hence, the degeneracy of the d-orbitals is lifted and a splitting into the so-called e_g (d_{z^2} and $d_{x^2-y^2}$) and t_{2g} (d_{xy}, d_{xy} and d_{xy}) orbitals occurs. Assuming the z-direction parallel to the film normal, the in-plane d_{xy} and $d_{x^2-y^2}$ orbitals experience a stronger crystal field than the out-of-plane d_{zx}, d_{zy} and d_{z^2} levels [90]. This induces an easy magnetization direction either within the film plane or pointing out-of-plane, which depends on the band filling as well as the considered $\mathbf{k}$ point in the band structure, see [97]. Since this effect originates from the surface of the system, this is called the *surface anisotropy* term. Regarding the magnetoelastic effect, in [89,97] the electron density of the $3d$-states for bulk Fe is calculated for the two cases of an unstrained and a compressed system, where the compression is applied along the z-axis. The calculation is performed orbital-resolved with respect to the $d_{x^2-y^2}$ and d_{z^2} orbitals. The main result is a redistribution from the $d_{x^2-y^2}$ to the d_{z^2}-orbitals, which induces an in-plane easy magnetization axis in the case of bulk Fe. This has also been confirmed by Sander [89], and can be seen by the negative B_1^{bulk} in table 6.1.

6.2.3.1 Ni/Cu(001)

For Ni/Cu(001), Bruno [100, 101] suggested a thickness dependence of the film strain as

$$\epsilon(d) = (\mp)\eta\frac{d_c}{d} \ , \tag{6.16}$$

where d_c is the critical thickness at which the insertion of misfit dislocations sets in, and the sign depends on the definition of the constants (in this thesis the definition of Sander will be used, i.e. with a positive sign). However, as has been shown by Sander [89], who used a cantilever technique for a quantitative stress measurement during film growth, the proposed strain function Eq. (6.16) represents only a rough approximation to the actual strain evolution, as can be seen in Fig. 6.1 a). Below a critical thickness of $d_c \sim 3\,\text{nm}$ the system shows pseudomorphic growth with an in-plane lattice constant of $a_p = 2.53\text{Å}$ for the first (3-5) ML [102] and grows subsequently with the in-plane lattice constant of bulk Cu, i.e. $a_p = 2.55\text{Å}$. Compared with the lattice constant of bulk Ni $a_p = 2.49\text{Å}$, confer Table 6.1, this results in a tensile in-plane lattice mismatch of $\eta_{\|} = 2.5\%$ and a compressive out-of-plane lattice mismatch of $\eta_{perp} = -3.2\%$ [102, 103], resulting in a positive, i.e. favoring the out-of-plane direction, magnetoelastic anisotropy energy (Eq. (6.13)) of $\varepsilon_{me}^{Ni/Cu(001)} = (64-40)(0.025-(-0.032))\frac{\text{meV}}{\text{atom}} = 1.37\frac{\text{meV}}{\text{atom}}$ for $d < d_c$. The shape anisotropy for thin Ni/Cu(001) is a function of the film thickness and shows a strong temperature dependence for thin films around room temperature [102]. It ranges from $0.0075\frac{\text{meV}}{\text{atom}}$ [102, 104] to $0.015\frac{\text{meV}}{\text{atom}}$ [99] in the pseudomorphic growth range. Hence, for very thin Ni films on Cu(001) the negative interface and surface *mc*-terms lead to an in-plane easy axis. Around (6-8) ML the positive volume *mc* as well as the positive *me* anisotropy causes a transition from in-plane to out-of-plane easy axis. The relaxation of the strain eventually leads to the second SRT from out-of-plane to in-plane magnetization in the thickness range of $\sim 40\,\text{ML}$ [87, 105].

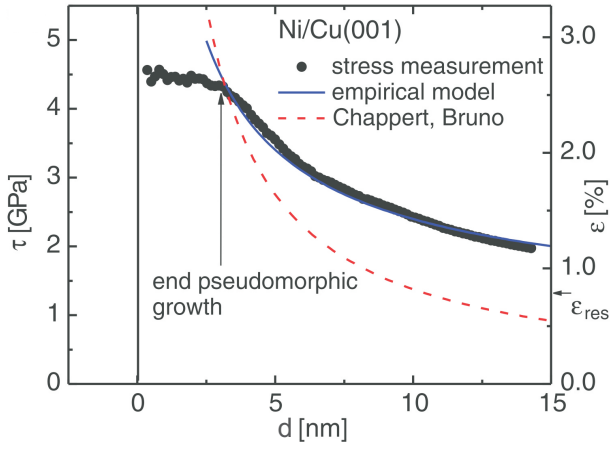

Figure 6.1: *The Measurement of the film stress while depositing Ni on Cu(001), measured with the cantilever technique, exhibits a nearly constant film stress τ below $d_c = \sim 3\,nm$, taken from [89]. Above this critical film thickness relaxation processes lowers the strain.*

	fcc-Cu(001)	*fcc*-Ni(001)	*bcc*-Fe(001)	*fcc*-Fe(001)
a (Å)	3.61	3.52	2.87	3.56
a_p (Å)	2.55_c	2.49_c	2.87_c	2.52_a
v ($\frac{Å^3}{atom}$)		10.93_a	11.78_a	11.4_a
M_S (G)		510_c	1752_c	
K_V ($\frac{meV}{atom}$)		0.033_f		0.077_g
K_S ($\frac{meV}{atom}$)		(-Vac):-0.177_f		(-Vac):+0.064_f
K_I ($\frac{meV}{atom}$)		(-Cu):-0.059_g		(Ni-Fe):-0.236_f
B_1^{bulk} ($\frac{meV}{atom}$)		$+64_b$		-25_b
$D_S{}^{bulk}$ ($\frac{meV}{atom}$)		-$1600\epsilon_{\parallel\, b}$		+$7340\epsilon_{\parallel\, b}$
MJ m^{-3}		6.83_d $\frac{meV}{atom}$	7.34_d $\frac{meV}{atom}$	$6.60\frac{meV}{atom}$

Table 6.1: *This table summarizes a few system relevant properties, taken from different publications: a) [75], b) [89], c) [87] d) [102] e) [106], f) [93] g) [107]. For a* fcc *crystal structure* $a_p = a/\sqrt{2}$ *and for a* bcc*-structure* $a_p = a$*, and denotes the in-plane lattice constant, where a is the lattice constant of the unit cell, v is the equilibrium atomic volume [106],* B_1 *is from [89].* fcc*-Fe(001), also called "γ-Fe", normally exist only at elevated temperatures (1185 K < T < 1667 K) but also in the ultra thin limit.*

6.2.3.2 Fe/Cu(001)

The statement found in [108], "a few atomic layers of Fe on Cu(001) make up the single most complex and complicated ultrathin magnetic system of all", puts the complexity of the crystallographic as well as the magnetic and electronic structure in a nutshell. In particular, below ∼11 ML, Fe on Cu(001) grows in the so-called γ-Fe phase, i.e. in a *fcc* crystal structure, which normally exists only at high temperatures (1185 K < T < 1667 K). The analysis of the LEED pattern of those ultra thin films by Heinz et al. [75, 109–111], revealed a (n x 1) superstructure, where $n = 4$ below 2 ML, $n = 5$ below 4 ML and $n = 1, 2$ ([75, 112], confirmed in [113]) in the range up to 10 ML. Below 4 ML the crystal structure is, in addition, tetragonally distorted and is therefore called face-centered-tetragonal (*fct*). Above 11 ML a (3x1) *bcc* structure is formed. Summarizing, three crystal phases can be distinguished, the ultra thin *fct*, medium *fcc* and the thick *bcc* crystal structure.

From a magnetic point of view, these three phases are also distinguishable. The most important phase for this thesis, is the *fct* phase, which shows ferromagnetic order. Fe films in the *fcc* phase are anti-ferromagnetic and in the *bcc* phase ferromagnetic, but usually in-plane magnetized [112]. The exact magnetic structure in the ultra thin and medium

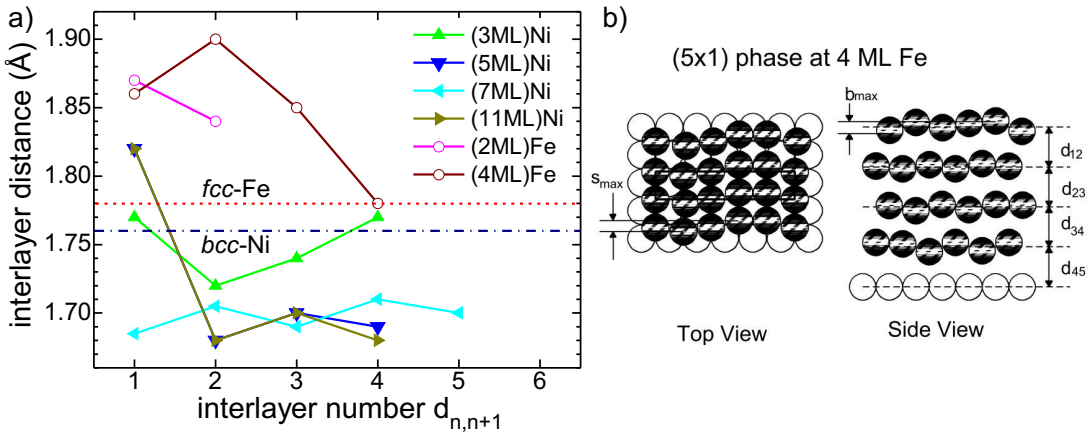

Figure 6.2: *a) shows the interlayer distances for different film thicknesses of Ni (3, 5, 7 and 11 ML) as well as Fe films (2 and 4 ML) grown on Cu(001). These values have been obtained by analysis of I(E)-LEED-spectra, published in [75, 103]. b) shows a schematic drawing of the best fit model for the (5x1) superstructure for Fe/Cu(001), taken from [114]. Open circles represent Cu atoms and hatched circles represent Fe atoms. The average sinusoidal in-plane corrugation is* $s_{max} = 0.35\,\text{Å}$*, whereas the out-of-plane corrugation has a value of* $b_{max} = 0.18\,\text{Å}$ *[75].*

phase is, however, still a demanding task for theory as well as for experiments. As pointed out by Meyerheim et al., who published in 2009 a "New model for magnetism in ultra thin fcc Fe on Cu(001)" [76], a non-collinear spin structure along the normal direction is the ground state in the intermediate thickness range above 4 ML. Combining soft-x-ray resonant magnetic scattering measurements and first-principle DFT calculations, Meyerheim et al. determined the spin structure in perpendicular direction to the film plane of 6 ML and 8 ML Fe films on Cu(001) and found a surprising spin structure mainly formed into blocks. As pointed out in section 4.3, Marsman [77] showed (not for this system) that such a non-collinearity should also occur along the in-plane directions. Calculations done by M. Vogel, from our group, in collaboration with C. Mewes, from the University of Alabama, who used the VASP package to perform DFT calculations in order to determine the spin structure, find a first hint of the complicated non-collinear, in-plane spin alignment, also in the ultra thin thickness range (not published so far).

In order to be able to give at least an approximation for the magnetoelastic anisotropy of ultra thin Fe films on Cu(001), the crystal structure has to be investigated further. Due to the (5x1) superstructure, each atom exhibits a certain sinusoidal displacement with respect to the underlying Cu(001) lattice, as can be seen in Fig. 6.2 b). These displacements lead to a considerably enlarged interlayer spacing ($\eta_{perp} = \sim 5\,\%$) in the Fe film compared to the interlayer spacing of the high-temperature *fcc* phase of Fe, which is $d_0 = 1.78\,\text{Å}$, see Fig. 6.2 a). Accordingly, the atomic volume is enlarged to $12.1\,\text{Å}^3$.

Surprising is the fact, that the analysis of I(E)-LEED-spectra, shown in [110], revealed an in-plane lattice constant that corresponds to a rather unstrained *fcc* Fe-lattice, i.e. it has the value of the ideal *fcc*-Fe ($a_p = 2.52\,\text{Å}$). This results in $\eta_{\parallel} = 0$ in this phase. In [115], however, an in-plane strain of $\sim 1.5\,\%$ is reported for Fe films on Cu(001) grown at low temperatures. Since in this thesis the samples are grown at room temperature, even a small in-plane strain will be neglected. Hence, the magnetoelastic energy results in $\varepsilon_{me}^{Fe/Cu(001)} = +1.25\frac{\text{meV}}{\text{atom}}$, favoring an out-of-plane magnetization in the ultra thin limit. As the film thickness increases to about 4 ML, a transition from *fct* to *fcc* occurs and the in-plane strain grows. This, in turn, leads to an increasing strain correction term, which favors in-plane magnetization and results in the spin-reorientation transition.

6.2.3.3 Fe/Ni/Cu(001): Crystallography

With respect to the TP-MCD effect as well as the spin-reorientation transition the system Fe/Ni/Cu(001) exhibits unique properties which are due solely to the interplay of both ferromagnetic layers. The system combines a large TP-MCD signal (up to 10 % due to the Ni film, confer chapter 4) and a stable out-of-plane phase (again due to the Ni layers) in a narrow thickness range (due to the Fe layers). The spin-reorientation transition is accompanied by a wealth of different domain patterns, ranging from stripe through labyrinthine and bubble to completely disordered patterns, which is again due to the Fe layer. However, the determination of the magnetic anisotropy constants of this system is rather complicated, due to the highly complicated interplay of the individual magnetic parameters. This has led to a wide range of published values for the individual magnetic anisotropies, such as surface, interface and volume constants of the magnetocrystalline and magnetoelastic terms, respectively. Nevertheless, some properties can be given or derived from the above given parameters. Since the growth of Ni on Cu(001) is pseudomorphic up to the critical thickness of ~ 17 ML (~ 3 nm) exhibiting a rather constant lattice structure and lattice constant, the growth of Fe on top of Ni/Cu(001) is indeed comparable to the case of Fe/Cu(001) without the Ni buffer, except for hybridization effects occurring at the interface and influencing the magnetic anisotropy terms. Fig. 6.3 shows the RHEED intensity oscillations of the specular beam, recorded while growing the stack of (6 ML)Fe/(5.4 ML)Ni/Cu(001). The pronounced change in the RHEED oscillations from the third to the fourth peak while growing the Fe film is in perfect agreement with oscillations observed for the system Fe/Cu(001) published in [116] which was attributed to the *fct* to *fcc* transition. It is exactly due to this transition, that the growth of Fe on either Ni(001) or Cu(001) can be regarded as similar for Ni thicknesses below ~ 17 ML.

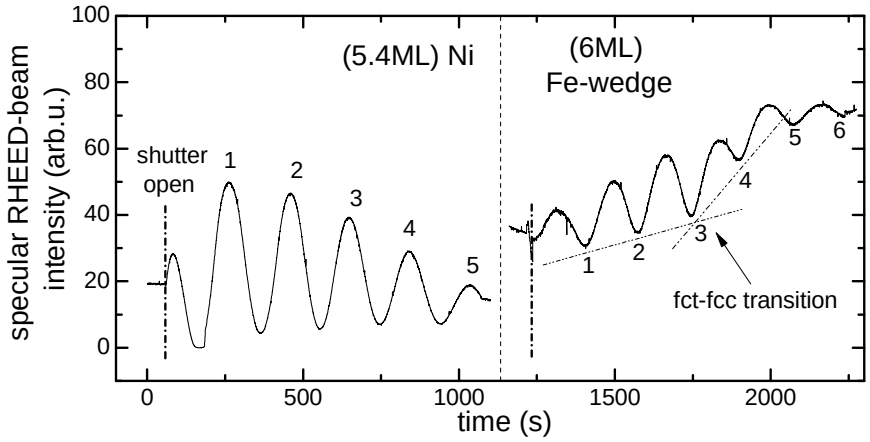

Figure 6.3: *Intensity oscillation of the specular beam in the RHEED-pattern while depositing 5.4 ML Ni, a wedge-shaped Fe-film with a thickness range from (0-6) ML. The change in the RHEED oscillations from the third to the fourth peak is due to a fct-fcc crystal structure transformation, which has also been observed in the case of Fe/Cu(001) in [116]. This transition justifies the analogous crystallographic treatment of Fe grown on Ni(001) and on Cu(001).*

6.2.4 Summary: Spin-Reorientation-Transition: Fe/Ni/Cu(001)

With respect to the presented magnetic and crystallographic properties of Ni/Cu(001) and Fe/Cu(001), the deduction of the magnetic properties of the system Fe/Ni/Cu(001) is attempted in the following. For thicknesses ranging from 5-10 ML the underlying Ni film has a negative (Cu-Ni) interface anisotropy of $K_I^{Ni} = -0.059 \frac{\text{meV}}{\text{atom}}$, a positive volume anisotropy of $K_V^{Ni} = 0.033 \frac{\text{meV}}{\text{atom}}$ and also a positive magnetoelastic anisotropy of $\varepsilon_{me}^{Ni/Cu(001)} = 1.37 \frac{\text{meV}}{\text{atom}}$. Without any capping layer, the *mc* surface term would be $K_S^{Ni} = -(0.177 \pm 0.030) \frac{\text{meV}}{\text{atom}}$ [93]. As has been shown by various studies [87, 118] (and references therein), the SRT from in-plane to out-of-plane takes place at the critical thickness of ~ 7 ML. Growing minute amounts of Fe (below 1 ML) on top of Ni with thicknesses in the vicinity of this critical thickness, even lowers the surface *mc* term to an effective (Ni-Fe) surface/interface *mc* term $K_I^{Ni-Fe} = -0.236 \frac{\text{meV}}{\text{atom}}$, as given in Table 6.1. Hence, the Ni-film becomes in-plane magnetized. For larger Ni thicknesses this effect does not occur, i.e. the film stays magnetized out-of-plane which will be shown in Fig. 6.4 e). With a coverage of nearly a single closed monolayer, the positive surface *mc* as well as the positive *me* anisotropy of Fe favor out-of-plane magnetization and due to the large exchange coupling between the bilayer stack of Fe and Ni, both layers have the same magnetization direction [107]. Hence, the whole stack becomes out-of-plane magnetized. However, the rapid change in the interlayer distance from 1 to 2 ML in the Fe film, shown in Fig. 6.2 a), leads to a relaxation

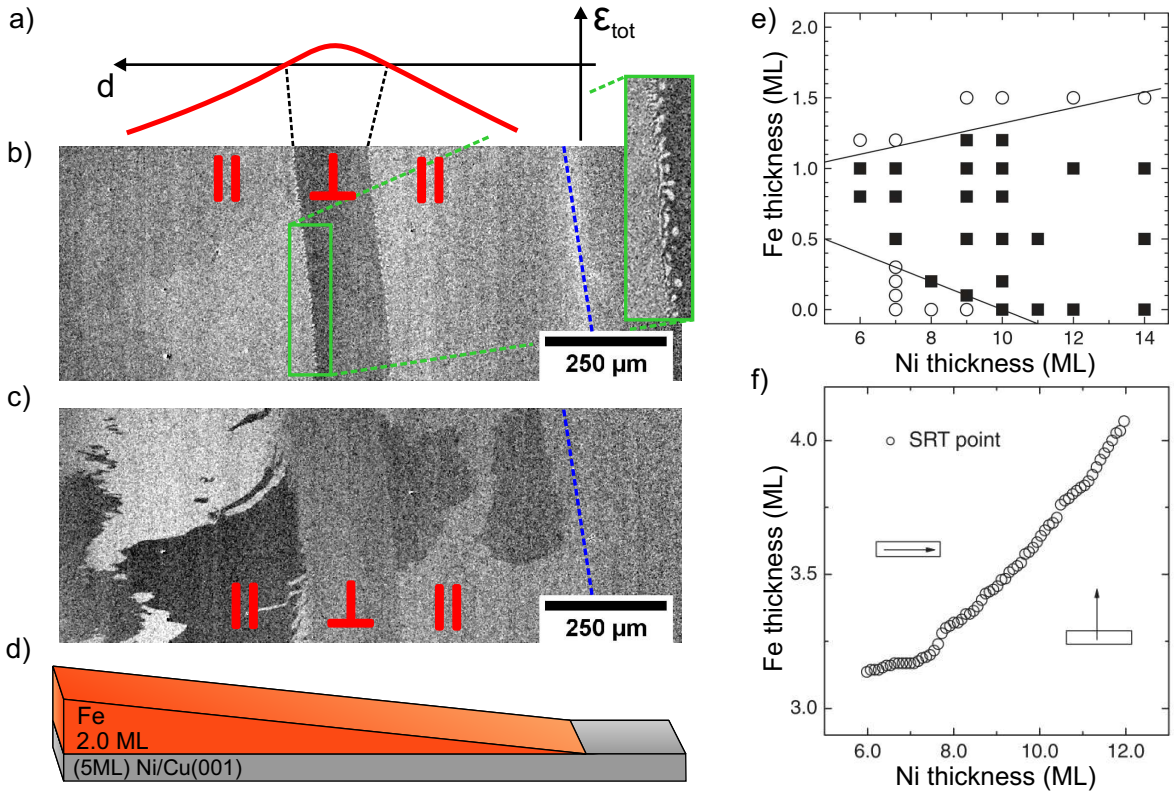

Figure 6.4: *A qualitative plot of the total anisotropy energy ϵ_{tot} (Eq. (6.15)) versus Fe film thickness of the system Fe/Ni/Cu(001) is shown in a). For $\epsilon_{tot} > 0$ the system is out-of-plane magnetized and for $\epsilon_{tot} < 0$ the magnetization lies in the plane. SEMPA measurements with magnetic sensitivity to the out-of-plane component b) as well as the in-plane component c) confirm the magnetization evolution of a) and reveal the two SRT's. The blue dashed line shows the onset of the Fe wedge. The inset in image b) shows out-of-plane domains featuring generally quite different shapes of the domains. d) shows a schematic drawing of the sample. e) presents the magnetic anisotropy phase diagram, where open circles denote in-plane and solid squares out-of-plane magnetization, taken from [93]. f) shows the same as e), but with a 20 Å Cu-capping layer shifting the SRT to thicker Fe layers, taken from [117].*

of the strain from $\sim 5\,\%$ to about $\sim 3\,\%$, which eventually accompanies the second SRT to in-plane magnetization. The presented scenario has exactly been verified by SEMPA (scanning electron microscopy with polarization analysis) measurements on wedge-shaped Fe films on Ni/Cu(001), Fig. 6.4 b) and c) by F. Freund, from our group, and also with the TP-MCD-PEEM setup used in this thesis. The magnetic phase diagram with respect to the orientation of the magnetization vector is shown in Fig. 6.4 e) without (taken from [93]) and in f) with a Cu-capping layer (taken from [117]). However, a qualitative description of the magnetic anisotropy energies remains still to be done. Although some energy terms

are known to within a few percent, the variation of others is huge and even the sign seems to be a matter of discussion. Comprehensive and also controversial discussions can be found in [87, 89, 102, 119].

6.3 Relevant Magnetic Energies for Domain Patterns

Parts of this section are prepared for publication [120, 121].

In out-of-plane magnetized ferromagnetic systems competing interactions may lead to intricate pattern formation. In such systems, usually a strong but short range interaction, the exchange interaction, favors a uniform phase, but is in competition with a much weaker but long range interaction, the dipolar interaction, that favors a non-uniform distribution of the magnetization. The competition of these interactions leads to energetic frustration and the evolution of complex domain patterns manifested in phase separation on mesoscopic or even macroscopic length scales. For the case of out-of-plane magnetized systems these phases are the two opposed directions: out-of-plane and into-the-plane magnetization. As a result the order parameter, which may in this case be the lateral size of the individual phase, e.g. the domain width, is modulated on length scales determined by the strength of the competing interactions.

Before proceeding with the presentation of the relevant magnetic interactions responsible for the formation of such domain pattern, a few comments should be made. Since all experiments are carried out at finite temperatures, and for this thesis, in particular, within the temperature range of (200-350) K, thermal fluctuations have to be taken into account. The incorporation of finite temperature and the resulting effects on the individual spins as well as the magnetic state is still a demanding task. Even the global dependence of the magnetization on temperature $M(T)$ has to be divided into regions far below the critical temperature T_C and a region in the vicinity of T_C. Certainly, the description of the behavior of the magnetization around T_C, for example within the Landau theory, leads to a qualitative reproduction of experimental results, but fails in the correct prediction of the critical exponents. The reason for this is that fluctuations are neglected by this simple theory. The formation and transformation of domain pattern, ranging from stripe domains to some other morphological domain patterns like bubble or labyrinthine, can, however, only be described when thermal fluctuations are included in the model. For instance, the application of an external field leads to the occurrence of the famous Barkhausen jumps. This phenomenon is in fact a direct observation of thermal fluctuations. Theories which treat fluctuations and their consequences such as the renormalization group theory will be considered in the following sections.

6.3.1 Mean-Field Hamiltonian of a 2D out-of-plane magnetized Ferromagnet

The magnetization can be considered as a classical vector field with three components. Following Kashuba and Pokrovsky [122], for a two-dimensional ferromagnet and a normalized magnetization vector $\mathbf{m}(\mathbf{r}) = \frac{\mathbf{M}}{|\mathbf{M}|}$ at site $\mathbf{r}$ the Hamiltonian reads

$$\begin{aligned} H &= \frac{1}{2}\Gamma(T)\int \mathrm{d}r^2\,[\nabla\cdot\mathbf{m}(\mathbf{r})]^2 - \lambda(T)\int \mathrm{d}r^2\, m_z^2(\mathbf{r}) - \mu_0\int \mathrm{d}r^3\,\mathbf{M}\cdot\mathbf{H}_{ext} + \\ &\quad \frac{1}{4\pi}\Omega(T)\iint \mathrm{d}r_1^2\,\mathrm{d}r_2^2 \frac{\mathbf{m}(\mathbf{r}_1)\cdot\mathbf{m}(\mathbf{r}_2) - 3[\hat{\mathbf{r}}_{12}\cdot\mathbf{m}(\mathbf{r}_1)][\hat{\mathbf{r}}_{12}\cdot\mathbf{m}(\mathbf{r}_2)]}{|\mathbf{r}_1-\mathbf{r}_2|^3}\ , \end{aligned} \tag{6.17}$$

where Ω is the dipole interaction strength, $\Gamma = \frac{1}{2}qs^2J$ is the exchange energy, given in Eq. (6.4), λ is the effective single-ion anisotropy constant, and $\hat{\mathbf{r}}_{12} = \frac{\mathbf{r}_1-\mathbf{r}_2}{|\mathbf{r}_1-\mathbf{r}_2|}$. In our case it holds $\lambda = \varepsilon_{\mathrm{tot}}$, where $\varepsilon_{\mathrm{tot}}$ is given in Eq. (6.15). The assumption of a 2D system is justified for all systems treated within this thesis, since the film thicknesses are below $\sim 3\,\mathrm{nm}$ whereas the lateral dimensions are in the mm range. Note, within this thesis the iron thickness is below the critical thickness at which the *fct* to *fcc* transition occurs accompanied by a transition of the spin structure. In addition, any non-collinear spin alignment, which should be quite small, will be neglected, confer section 6.2.3.2.

Due to the finite temperature at which all experiments are done, the parameters in Eq. (6.17) have to be renormalized, since thermal fluctuations disturb the uniform magnetization and even lead to the destruction of the ferromagnetic order above the critical temperature T_{C}. However, a large fraction of these fluctuations occur far below any observable scale. Without the loss of system relevant information, these fluctuations can be merged into a single constant. It is due to renormalization group theory (RGT), which will be discussed in section 6.4, that a mean field approach like Eq. (6.17) can be used for the description of this temperature dependent system. Within this mean field approach and, in particular, due to the assumption of a restricted spin direction along the out-of-plane direction, the renormalization of the coupling constants can be performed and leads to their explicit temperature dependence [1, 123]

$$\Gamma(T) = \Gamma Z\ , \quad \lambda(T) = Z^3\left(\lambda + \frac{3\Omega}{2}\int_0^{\xi}\frac{e^{-\xi}}{Z^2}\frac{\mathrm{d}Z}{\mathrm{d}\xi}\mathrm{d}\xi\right)\ , \quad \Omega(T) = \Omega Z \tag{6.18}$$

with

$$Z = 1 - \frac{T\xi}{2\pi\Gamma}\ , \quad \xi = \frac{1}{2}\ln\frac{\Gamma}{\lambda a^2}\ . \tag{6.19}$$

In general, the renormalization of the dipolar energy can not be performed due to its long ranging character [123, 124]. However, within the assumption of a strong perpendicular

anisotropy, leading to a restriction of the spin direction, the dipolar energy can be simplified and becomes renormalizable [123], as given in Eq. (6.18). In the following some frequently used parameters will be listed

$$t_{\mathrm{DW}} = \begin{cases} \frac{\pi^2}{8}\frac{J}{\Omega}, & \text{if } \lambda \ll \Omega \text{ at the SRT} \\ \pi\sqrt{\frac{J}{\lambda}}, & \text{if } \Omega \ll \lambda \text{ otherwise} \end{cases} \qquad \text{domain wall thickness} \tag{6.20}$$

$$\varepsilon_{\mathrm{DW}} = \begin{cases} 2\sqrt{2J\lambda} & \text{for } \lambda/J \leq 2/3 \\ 2J & \text{for } \lambda/J > 2/3 \end{cases} \qquad \begin{matrix} \text{domain wall energy} \\ \text{per domain wall length} \end{matrix} \tag{6.21}$$

Eq. (6.20) is taken from [125] and Eq. (6.21) is taken from [126]. As shown by Kwon, the stripe domain wall thickness is generally given by [125]

$$t_{\mathrm{DW}} = 4\left(\frac{\sqrt{\Omega^2 + \frac{\pi^2}{2^4}J\lambda}}{\lambda} - \frac{\Omega}{\lambda}\right) , \tag{6.22}$$

where Eqs. 6.20 represent the limiting cases.

6.3.2 Equilibrium Stripe Domain Width w_{D}

As a general result from theory [1, 122, 127], in a domain pattern forming system with perpendicular anisotropy the stripe phase, i.e. a domain pattern where all the domain walls are aligned in parallel, is energetically the most favorable state. Hence, in the following a stripe domain pattern with stripe period $2w_D$ will be considered as ground state. The energy density of such a system is given by [122]

$$\varepsilon(w_{\mathrm{D}}, \delta) = \frac{\varepsilon_{\mathrm{DW}}}{w_{\mathrm{D}}} - \frac{\Omega}{\pi w_{\mathrm{D}}} \ln\left(\frac{2w_{\mathrm{D}}}{\pi t_{\mathrm{DW}}} \cos\left(\frac{\pi\delta}{2w_{\mathrm{D}}}\right)\right) - 2h\frac{\delta}{w_{\mathrm{D}}} , \tag{6.23}$$

where the first term is due to the domain wall energy and the second term represents the dipole energy density. The last term is due to the Zeeman energy in an applied magnetic field H leading to a domain wall displacement of δ in favor of the domain with magnetization parallel to H, and $h = g\mu_{\mathrm{B}}H$. For zero applied field $h = 0$, the domain wall displacement is $\delta = 0$, and minimization of the energy density Eq. (6.23) results in the equilibrium domain width [1, 122]

$$w_{\mathrm{D}}(T) = \frac{\pi\, t_{\mathrm{DW}}(T)}{2} \exp\left(1 + \frac{\pi\, \varepsilon_{\mathrm{DW}}(T)}{\Omega(T)}\right) . \tag{6.24}$$

At low temperatures $\Omega(T)$ is much smaller than $\varepsilon_{\mathrm{DW}}$ [122] leading to a domain width w_{D} exceeding the size of the system, i.e. the magnetic state becomes uniform. However, since

the spin-reorientation transition is induced by a zero crossing of the effective anisotropy, the domain wall energy $\varepsilon_{\mathrm{DW}}$ becomes small in the vicinity of the SRT (see Fig. 1 in [126]). In the case of 9 ML Ni and a Fe thickness of (1.2-1.4) ML, Eq. (6.24) leads to a minimum of the domain width at the SRT of $w_{\mathrm{D,min}} = (0.31 \pm 0.02)\,\mu$m, confer [128–130]. The Fe thickness range of (1.2-1.4) ML for this calculation is extracted from the experiment, shown in Fig. 7.12.

6.3.3 Applied Magnetic Field: Stripe-Bubble Transition

Following Kashuba [122], in the case of an applied magnetic field, the expression for the domain width becomes

$$w_{\mathrm{D}}(T,h) = \frac{w_{\mathrm{D}}(T)}{\sqrt{1-\left(\frac{h}{h_{c,u}}\right)^2}}\ , \tag{6.25}$$

where $h_{c,u} = \frac{\Omega(T)}{4w_{\mathrm{D}}(T)}$ is the critical field value at which the system assumes the uniform magnetic state and $w_{\mathrm{D}}(T)$ is from Eq. (6.24). The domain wall displacement is then given by

$$\delta(T,h) = \frac{2w_{\mathrm{D}}(T,h)}{\pi}\arcsin\left(\frac{h}{h_{c,u}(T)}\right)\ . \tag{6.26}$$

This is schematically shown in Fig. 6.5 a). As a consequence of this domain wall displacement (Eq. (6.26)), the net magnetization changes, which can be expressed by the geometric magnetization, defined by

$$\overline{m} = \frac{A_\uparrow - A_\downarrow}{A_\uparrow + A_\downarrow}\ , \tag{6.27}$$

where $A_{\uparrow,\downarrow}$ are the area fractions of the sample with magnetization up ($\uparrow$) or down ($\downarrow$). For the given stipe phase, this equation becomes

$$\overline{m} = \frac{(w_{\mathrm{D}}+\delta)-(w_{\mathrm{D}}-\delta)}{(w_{\mathrm{D}}+\delta)+(w_{\mathrm{D}}-\delta)} = \frac{\delta(T,h)}{w_{\mathrm{D}}(T,h)} \tag{6.28}$$

$$= \frac{2}{\pi}\arcsin\left(\frac{h}{h_{c,u}(T)}\right)\ , \tag{6.29}$$

where the dependence of both parameters, $w_{\mathrm{D}}(T,h)$ and $\delta(T,h)$ on the temperature T and the applied magnetic field h for the first expression was not written explicitly. As shown, the application of a magnetic field leads in general to a domain wall displacement in favor of the domain with magnetization pointing along the applied magnetic field. Above the critical field value $h_{c,u}$ a crossover into the uniformly magnetized state occurs. However, the application of a magnetic field may also result in a transformation of the domain pattern.

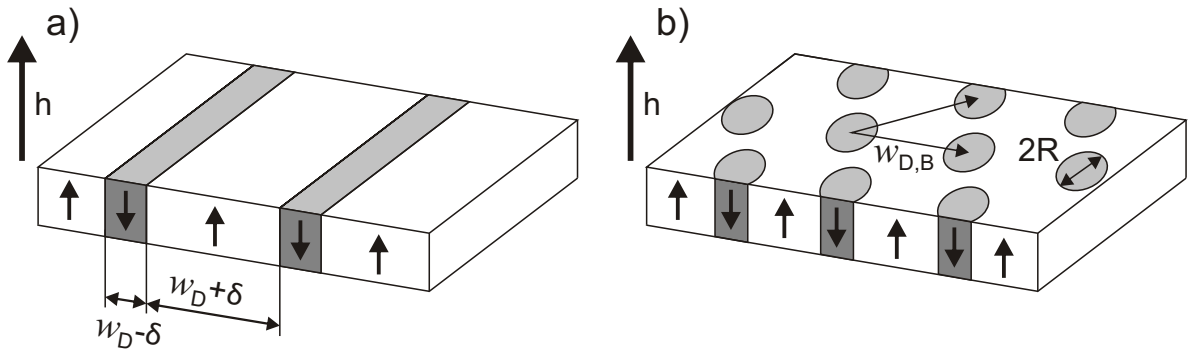

Figure 6.5: *a) schematic drawing of a stripe domain phase with an applied magnetic field along the z-direction, leading to a shift of the domain walls in favor of the magnetization direction parallel to the applied magnetic field. b) same as a) but for a hexagonal bubble domain state with bubble diameter $2R$ and lattice spacing $w_{\mathrm{D,B}}$.*

Saratz [131] investigated stripe domain patterns as well as hexagonal bubble structures, as shown in Fig. 6.5 b). A simple geometrical consideration of the domain wall length per unit area for the stripe and the bubble domain state provides an adequate approximation of the equilibrium pattern with an applied magnetic field, i.e. stripe or bubble. The basis for the approximation is, that the long range dipolar energy is not as sensitive to the exact domain configuration as the exchange energy. In addition, the latter is to be paid by the system in units of the domain wall length. Hence, consider the domain wall lengths l_{wall} for the stripe as well as the hexagonal bubble domain state, which are given by

$$\begin{aligned} &\text{Stripes} \quad l_{\mathrm{wall,S}} = \frac{1}{w_{\mathrm{D}}} && A_{\mathrm{S}} = \frac{w_{\mathrm{D}} - \delta}{2\, w_{\mathrm{D}}} \\ &\text{Bubbles} \quad l_{\mathrm{wall,B}} = \frac{2\pi R}{\sin(60^\circ) w_{\mathrm{D,B}}^2} = \frac{4\pi R}{\sqrt{3} w_{\mathrm{D,B}}^2} && A_{\mathrm{B}} = \frac{2\pi R^2}{\sqrt{3} w_{\mathrm{D,B}}^2} \quad , \end{aligned}$$

where $A_{\mathrm{S,B}}$ are the local area fractions of the minority domains [131], w_{D} denotes the stripe domain width and $w_{\mathrm{D,B}}$ is the lattice spacing of the bubble lattice as shown in Fig. 6.5. Since the domain wall length in the stripe domain state is independent of the area fraction A_S, but in the bubble state it is not ($l_{\mathrm{wall,B}} = \frac{2}{w_{\mathrm{D,B}}} \sqrt{\frac{2\pi}{\sqrt{3}}} \sqrt{A_{\mathrm{B}}}$) the ratio of the individual domain wall lengths depends on the occupied area fraction. If we assume $w_{\mathrm{D}} = w_{\mathrm{D,B}}$ in the vicinity of the transition region, this ratio results in the plot shown in Fig. 6.6. Hence, the transition from stripes to bubbles occurs at a geometrical magnetization of $\overline{m} = 0.45$. According to Eq. (6.29), the corresponding magnetic field value for the transition from stripes to bubbles is $h_{\mathrm{SB}} = 0.65 \cdot h_{c,u}$. According to Saratz, a direct comparison of the energy densities for the stripe and the bubble domain states (in this thesis only the stripe energy density is given in Eq. (6.23)) leads to a numerical value of $h_{\mathrm{SB}} = 0.545 \cdot h_{c,u}$.

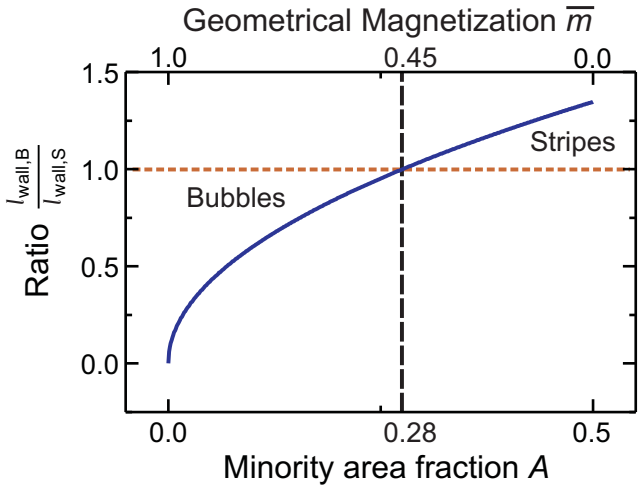

Figure 6.6: *The ratio of the domain wall density of the stripe phase to the bubble phase provides a first approximation for the equilibrium domain pattern of a system with an applied magnetic field. The crossover from stripes to bubbles occurs at a geometrical magnetization* $\overline{m} = 0.45$*, following [131].*

Hence, the geometrical approximation is reasonable. Experimental results for the stripes to bubbles transition will be presented in section 7.4.1.

6.3.4 Elastic Energy of Stripe Domains

Thermal energy induces fluctuations which range in the case of a ferromagnet from individual spins through blocks of spins to even whole domains. The impact of thermal fluctuations on the individual coupling constants and therefore on the magnetization itself, will be presented in section 6.4. In this and the next subsection, the impact of thermal energy on the domain pattern will be discussed and along with this, the transformation of the domain pattern and the loss of long range order (positional as well as orientational) as a consequence of thermal fluctuations.

Consider a stripe domain pattern, where each domain wall randomly deviates from its ideal position, as schematically shown in Fig. 6.7 a). Without limiting generality, consider the domain walls to be parallel to the y axis. Hence, the deviations in the x-direction are locally described by a function $u(x, y)$. From elastic theory the corresponding energy density for meandering domain walls is given by

$$\varepsilon_{\mathrm{el}} = \frac{K}{2}\left[\partial_x u + \frac{1}{2}(\partial_y u)^2\right]^2 + \frac{\mu}{2}(\partial_y^2 u)^2 + \frac{\nu}{2}(\partial_y u)^2 \ . \tag{6.30}$$

The first term is the *compression* energy density, due to a compressive deformation $\partial_x u + \frac{1}{2}(\partial_y u)^2$ [122], either by local deviations of a single domain wall or by a variation of the domain width concerning two neighboring domain walls. As was pointed out in [122], the justification for the term proportional to $(\partial_y u)^2$ is questionable. The second term of Eq. (6.30) describes any bending ($(\partial_y^2 u)^2$) of the domain walls, and is therefore called *bending* energy density. The last energy term in Eq. (6.30) takes into account anisotropies

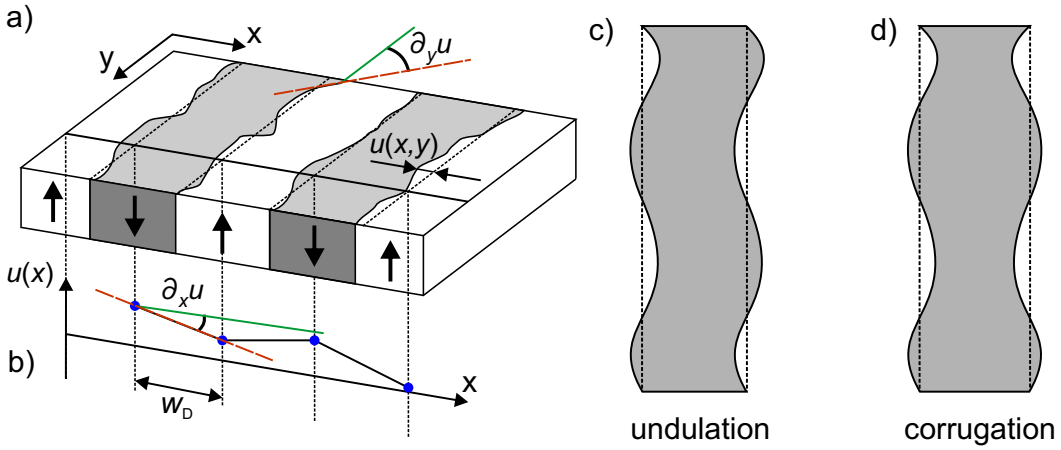

Figure 6.7: *a) Thermal fluctuations lead to local deviations $u(x, y)$ of the domain walls from the ideal position, i.e. the ground state (dashed line) in the stripe phase, modified taken from [1, 127, 128]. Since the local deviation $u(x)$ is a discrete function, the partial derivative of $u(x, y)$ with respect to x has to be calculated as shown in b). The two main deviations from the ground stripe state are undulations c) and corrugations d).*

regarding the domain wall orientation, and is based on some symmetry breaking magneto-crystalline or -elastic terms. Hence, it is referred to as the *orientation* energy density.

The individual constants within this elastic model can be connected to the coupling constants of the mean-field Hamiltonian given in Eq. (6.17) by [1, 122]

$$K \propto \frac{\Omega}{w_\mathrm{D}} \qquad \text{compression constant} \tag{6.31}$$

$$\mu \propto \Omega w_\mathrm{D} \qquad \text{bending constant} \tag{6.32}$$

$$\nu \propto \frac{\Gamma}{w_\mathrm{D} t_\mathrm{DW}^3} \qquad \text{orientation constant.} \tag{6.33}$$

Hence, a stripe domain state with a large domain width is more likely to exhibit corrugations due to a small K, as shown in Fig. 6.7 d). In contrast, a small domain width may exhibit more undulating excitations, Fig. 6.7 c), rather than local changes of the domain width, i.e. corrugations, due to a large compression constant K. This is also mediated by a smaller bending constant μ for a small domain width w_D. Hence, in the vicinity of the SRT a more wavy domain pattern may occur with a narrower but more rigid domain width, which is known as *transverse instability* [132]. Eq. (6.33), however, implies that for a small domain configuration near the SRT the tendency towards orientation is enhanced. This is the reason, why there are two scenarios for the domain pattern evolution beginning from a stripe domain phase through various other domain patterns until the magnetization direction becomes eventually in-plane, which will be further discussed in section 7.2.

6.3.5 Pattern Evolution: Phase Diagram

In Fig. 6.8 the phase diagram of a perpendicularly magnetized system is shown as a function of applied magnetic field and temperature, modified taken from [1,128,131]. Starting from high temperatures $T > T_{\mathrm{C}}$, the system shows paramagnetic behavior. Below T_C the system is ferromagnetic and the magnetization lies in-plane for temperatures $T_R < T < T_C$. At $T = T_{\mathrm{R}}$, the spin-reorientation transition takes place, i.e. the magnetization turns out-of-plane. For $T < T_{\mathrm{R}}$, the application of an external magnetic field along the perpendicular direction leads to the emergence of three regions. For high magnetic field values the uniform magnetic state is lowest in energy. Within the magnetic field range of $h_{\mathrm{SB}} = 0.545 \cdot h_{c,u}(T) < h < h_{c,u}(T)$, the domain structure takes the form of bubbles, which is the region between the blue and red line in Fig. 6.8. Roughly speaking, this is due to a smaller total domain wall length which minimizes the exchange energy, as shown in section 6.3.3. Below the field value h_{SB} the stripe phase is the equilibrium domain pattern. Note, that the pattern formation and transformation of this phase is strongly reminiscent to patterns displayed by liquid crystals, which has led to the nomenclature of the individual patterns, like the smectic and nematic phases.

According to Kashuba, Abanov, Kalatsky, Pokrovsky and Saslow [1,122,127], (the theory is called the *K2APS*-theory) four phases of the stripe domain pattern should be distinguishable: the mono-domain (MD), the smectic (SM), the Ising nematic (IN) and the tetragonal liquid phase (TL). The mono-domain phase is developed only at sufficiently low temperatures. At increased temperatures, the magnetization exhibits the highly ordered, modulated smectic phase. This phase is characterized by a long range orientational order of the parallel stripes, where the directional orientation of the stripes is induced by the substrate and the magnetic film properties and is four-fold for cubic materials. In the smectic phase only one of these directions is preferred, although both are equal. The positional order parameter decays algebraically[4], which is due to long-wavelength fluctuations of the domain walls as well as topological excitations such as bound dislocations in the domain structure [134]. The consequences of thermal fluctuations on the magnetization and the domain pattern will be discussed in section 6.4. By increasing the temperature and decreasing the domain width accordingly, bound dislocations become unbound and the individual defects proliferate. Since the substrate induces two favored directions for domain walls which are perpendicular to each other, see section 6.2.3.3, the domain walls gradually align along both. The initial direction, i.e. the preferred direction

[4]This means that a polynomial function accurately describes the decaying envelope of, for instance, the auto-correlation function of the domain pattern.

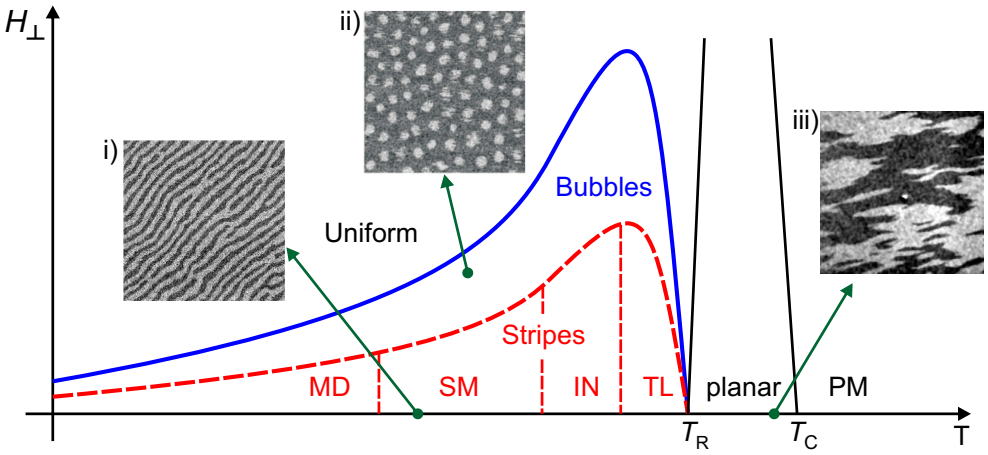

Figure 6.8: *Pattern phase diagram of a perpendicularly magnetized ferromagnetic film, after [1,128,131]. For $T > T_C$ there is no ferromagnetic long range order, i.e. the system is paramagnetic (PM). For $T_R < T < T_C$ the magnetization direction is in the film plane (planar region) and T_R marks the temperature of the spin-reorientation transition to a perpendicularly magnetized configuration. The insets show SEMPA images of i) the smectic (SM) stripe (FOV 42μm, $T = 293$ K) (taken from [133]), the bubble domain state ii) (FOV 41μm, $H = 0.95$ Oe, $T = 327$ K) (taken from [131]) and iii) the in-plane magnetization (FOV 155μm, $T = 294$ K) (obtained by F. Freund from our group). The pattern evolution predicted by Abanov [1] in zero applied magnetic field with increasing temperature is as follows: mono-domain (MD), smectic (SM), Ising nematic (IN) and tetragonal liquid (TL).*

within the smectic phase, remains more pronounced, and the resulting phase is referred to as the Ising nematic phase. The transformation process is mediated by proliferation of dislocations within the domain pattern. The Ising nematic phase is characterized by an exponentially decaying positional order parameter. For even higher temperatures, but still below the SRT temperature T_R, the two perpendicular directions become equally occupied by domain walls. This phase is called tetragonal liquid, where an "exponentially rapid spatial decorrelation from one stripe orientation to the other" occurs [1]. Due to experimental evidence [130,135], the disordered (DO) phase has to be added to the list of possible phases. This phase is not mentioned in any theoretical description and exhibits neither positional nor orientational long range order.

Even from theory the existence of the Ising nematic phase was not so clear in the first run [1], which has led to the introduction of two scenarios. The first scenario exhibits a transition[5] from the SM to the IN phase which is followed by a first-order transition to the TL phase. The second scenario comprises a single, first order transition from the

[5]This transition is expected to be a Kosterlitz-Thouless transition.

SM to the TL phase, without any IN phase. Abanov showed that the IN phase is only stable for a certain range of the elastic constants. Pighín and Cannas [136] theoretically investigated the 2D-Ising model within Mean-field theory and contrasted the results to Monte Carlo simulations. These authors showed that the IN phase only occurs in very small regions between the SM and TL phase, if the temperature or the ratio between exchange and dipolar energy is varied. In most cases the IN phase does not occur. So far, no experimental measurement evidences the existence of this phase. This may lead to the conclusion, that the elastic constants in the experiments are not within the required range. In fact, none of the temperatures below T_C at which transitions between individual pattern phases occur are very well known from theory. Hence, the Ising nematic and the tetragonal liquid phases may occur only in very small temperature windows. In addition, the local variation of all magnetic properties such as the anisotropy, for instance, may destroy the formation of these delicate phases on large scales. Hence, they may be experimentally only observable in very small regions on the sample.

In addition to the previously mentioned scenarios about the existence of the IN phase, beyond the TL phase towards the in-plane configuration there are also two different paths for domain pattern formation. These two pattern evolutions emerge from mutually exclusive consequences on the orientational tendency of the domain walls while approaching the SRT. The first scenario is based on a dominating orientational affinity due to a large orientational constant ν for small domain width w_{D} just before the SRT. This leads to the emergence of a second smectic phase and has already been demonstrated by Portmann et al. [137]. Since the evolution of the domain pattern with increasing temperature, can be regarded as a melting process, in which the order is successively decreased and the symmetry is increased, this process has been called "inverse melting" [137] due to a lower symmetry in the reentrant smectic phase while increasing the temperature.

The second scenario constitutes the normal heating process i.e. the reduction of order or an increase in symmetry while increasing the temperature. To be more precise, increasing the temperature in the tetragonal liquid phase, means a decrease of the domain width w_{D}, accompanying a lower bending constant μ and a larger compression constant K. If the corresponding energy terms dominate over the orientational affinity, the domain walls become more and more curved and constant in thickness. Hence, the underlying crystal structure with its favoring directions becomes invisible. The result is a fully disordered domain pattern.

6.4 Critical Exponents and Renormalization: Temporal and Spatial Fluctuations on different scales

The *order parameter* is a quantity which characterizes the phase of a system. Any phase transition of the system is indicated by a discontinuous (*first order*) or continuous (higher order) change of the order parameter. The magnetization $\mathbf{M}(T)$ (first derivative of the Gibbs free energy $G(T,H) = U - TS - MH$, i.e. $M = -\left(\frac{\partial G}{\partial H}\right)_T$), for instance, is an order parameter which is non-zero below and zero above T_C. The transition from the ferromagnetic to the paramagnetic phase is continuous and since the magnetic susceptibility (second derivative of the Gibbs free energy, i.e. $\chi_T = -\left(\frac{\partial^2 G}{\partial H^2}\right)_T$) is discontinuous, this transition is referred to as *second order* phase transition [138].

One of the first theories describing second order phase transitions is the *Landau theory*. Landau assumed that the free energy is expandable in a Taylor series in the order parameter in the vicinity of the critical point. The points where the minima of the free energy occur represent the magnetization $M(T)$ in the case of a ferromagnetic system. As a consequence the order parameter follows a power law as a function of temperature. This critical point behavior holds true for various other quantities as well [138, 139], such as

$$c_H(T) \propto \tau^{-\alpha} \qquad \text{specific heat at constant magnetic field} \tag{6.34}$$

$$M(T) \propto \tau^{\beta} \qquad \text{magnetization} \tag{6.35}$$

$$\chi(T) \propto \tau^{-\gamma} \qquad \text{susceptibility} \tag{6.36}$$

$$\xi(T) \propto \tau^{-\nu} \qquad \text{correlation length} \tag{6.37}$$

$$\zeta(T) \propto \tau^{-z\nu} \qquad \text{relaxation time [140]} \tag{6.38}$$

where α, β, γ, ν and z are critical exponents and τ is the reduced temperature introduced for convenience

$$\tau = \begin{cases} \frac{T_\mathrm{C} - T}{T_\mathrm{C}}, & \text{for } T < T_\mathrm{C} \\ \frac{T - T_\mathrm{C}}{T_\mathrm{C}}, & \text{for } T > T_\mathrm{C} \end{cases} . \tag{6.39}$$

In order to have an impression of the critical behavior of these quantities and since the magnetic properties of the samples investigated within this thesis are close to the 2D-Ising case, i.e. a spin lattice with only two spin values, the critical exponents are presented only for this case: $\alpha = 0$, $\beta = 1/8$, $\gamma = 7/4$, and $\nu = 1$ (these values are exact [138]). Other critical exponents for different systems are listed elsewhere [138, 141, 142]. For $\tau \to 0$ some quantities such as χ, ξ or ζ exhibit critical behavior in the 2D-Ising model, which means that they diverge. These power law behaviors are experimentally verified for three-dimensional systems and one finds, for instance, $\beta \approx \frac{1}{3}$. From Landau's theory,

however, follows $\beta = \frac{1}{2}$, which does not adequately describe the experimentally measured critical behavior. The reason for this discrepancy is the basic assumption of the Landau theory that the free energy is expandable in a Taylor series around the critical temperature [138, 141] and the neglect of fluctuations. Considering the second derivative of the Gibbs free energy which is the susceptibility χ_T, a quantity which diverges at the critical point, results in a non-convergent expansion of the thermodynamic potential. However, the Landau theory successfully provides a first impression of the properties of phase transitions and is therefore often used as a first step to describe the critical behavior of a system. Although the microscopic basis for temperature driven phase transitions, i.e. thermal energy expressed by fluctuations of the order parameter on various time and length scales, are completely neglected by the Landau theory [138].

The critical behavior of the above presented parameters occurs in diverse systems ranging from fluids (e.g. water) $\{\rho - \rho_0$: density$\}$ to superconductors $\{\Delta$: complex gap parameter$\}$ or superfluids $\{\langle\Psi\rangle$: condensate wave function$\}$, where the quantities in the parenthesis correspond to the order parameters of the respective systems [138]. For all these systems, thermodynamic quantities exhibit critical behavior and follow a power law behavior with a certain critical exponent while approaching the critical point. It is remarkable, that the critical exponents are nearly the same and independent on the system and the type of interaction. This phenomenon is called the *universality* of critical behavior.

In order to adequately describe a system by incorporating the critical behavior expressed by fluctuations occurring on mainly all length and time scales, a nearly infinite number of degrees of freedom would have to be taken into account. Since this is impossible, the degrees of freedom have to be reduced to the point that a theoretically tractable system remains, while the relevant system properties are retained. This procedure was successfully demonstrated by Kadanoff [141] and Polyakov [143] and many others, within the *Renormalization group theory* (RGT). This approach replaces the original microscopic degrees of freedoms by a smaller set of effective degrees of freedom [139]. Hence, a set of spins on a lattice with lattice constant a, is replaced by a lattice comprising blocks of spins separated by La, where each block of spins contains only a single effective spin. Simultaneously, the interaction between these block of spins is replaced by an effective interaction derived from the initial one. The transformation from the initial interaction to the scaled interaction can only be done by the assumption that the interaction is a *local* interaction meaning that it affects only neighboring spins. With respect to the exchange interaction this requirement is fulfilled. The scaling procedure can then be repeated until some characteristic length scale, the *cut-off length*, is reached naturally given by the correlation length ξ Eq. (6.37). In Fig. 6.9 the magnetization profile within a domain is shown for the ferromagnetic and also the paramagnetic phase. The correlation length is

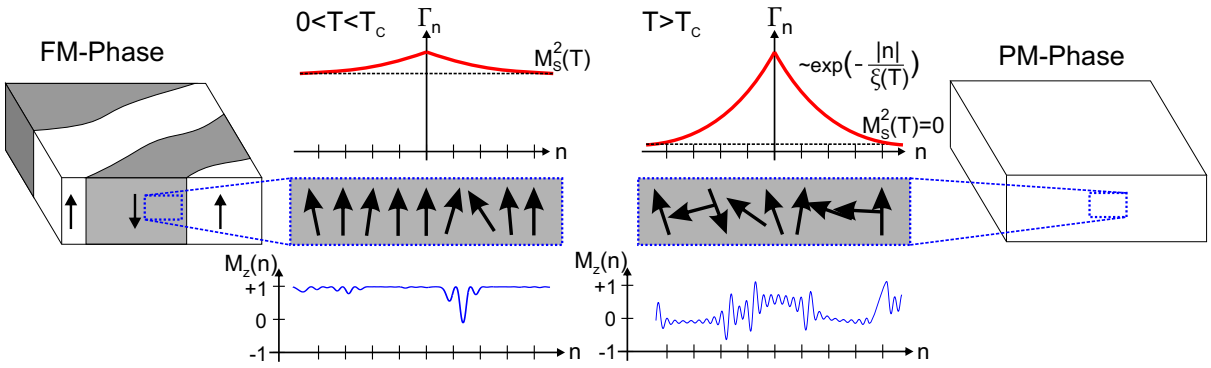

Figure 6.9: *The correlation of localized spins in a system leads to ferromagnetic ordering. Thermal fluctuations, however, induce disorder at any temperature $T > 0$ [141]. This leads to the reduction of the correlation function and the temperature dependence of the saturation magnetization $M_S(T)$. At temperatures $T > T_C$ disorder in the system eliminates long range order and the correlation function decreases exponentially to zero.*

the decay length of the correlation function[6] Γ depending on the distance to neighboring spins. As can be seen in Fig. 6.9, at any temperature $0 < T$ thermal fluctuations reduce ferromagnetic order and eventually eliminate any long range order at $T_C < T$. However, for our perpendicularly magnetized system with domains well separated by domain walls, the domain wall thickness t_{DW} replaces the cut-off length. Beyond this scale only long-wavelength fluctuations remain, see the subsequent section 6.5.

RGT enables much simpler theories, which neglect thermal fluctuations in a natural manner, to adequately describe the properties of a thermodynamic system. As shown in the previous section 6.3.5, Abanov used a mean-field Hamiltonian with renormalized coupling constants, including thereby the effect of fluctuations, in order to describe the effect of thermal energy on the domain structure. Another result from RGT is an expression of the critical exponents in form of an expansion in dimensionality and isotropy[7] as shown e.g. in [144]. The predictions for the critical exponents are remarkably precise, and reproduce also the exact values from the 2D-Ising model.

[6]The correlation function representing the correlation or influence of the order parameter from one place to another is defined as [138]

$$\Gamma(\mathbf{r}) = \langle \mathbf{m}(\mathbf{r})\mathbf{m}(0)\rangle - \langle \mathbf{m}(\mathbf{r})\rangle\langle \mathbf{m}(0)\rangle \ . \tag{6.40}$$

[7]The isotropy n is connected to the dimensionality of the spin vector, for example $n = 1$ for the Ising model, $n = 2$ for the XY-model, and $n = 3$ for the Heisenberg model.

Now we return to the system Fe/Ni/Cu(001) relevant for this thesis. The ferromagnetic state of this system undergoes a second order phase transition to the paramagnetic state at T_C. Moreover, the domain patterns within the ferromagnetic out-of-plane state also undergo phase transitions which depend on the individual scenarios (with or without the Ising nematic phase), see section 6.3.5. These transitions in form of pattern transformations exhibit again critical behavior. According to Abanov et al. [1], the phase transitions in the first scenario (i.e. SM→IN→TL) are thought to be of Kosterlitz-Thouless type[8] for the SM→IN pattern transformation and of second order for the IN→TL transition. In the other scenario without the IN phase, the system exhibits a first order transition from the SM phase to the TL phase. Experimental results will be presented in the section 7.6.4.

6.5 PEEM-Measurement relevant Fluctuations

In general the magnetization $\mathbf{M}$ can be written as the statistical average of some magnetic density $\mathbf{m}(\mathbf{r})$ integrated over the entire volume

$$\overline{\mathbf{M}} = \left\langle \int \mathrm{d}^3 r \, \mathbf{m}(\mathbf{r}) \right\rangle \ . \tag{6.41}$$

The statistical average within, for instance, the Ising model is given by $\overline{M} = \langle M \rangle = \sum_{\{s_i\}} M \exp(-\beta E)$, where $\beta = 1/k_\mathrm{B}T$ and $M = \sum_i s_i$. $\{s_i\}$ means a domain configuration. For ultra thin ferromagnetic films the volume integral becomes an area integral. In fact, the experimental measurement of a physical quantity like the magnetization represents in any case an averaging process. In order to describe this, Eq. (6.41) can be divided into two parts. These two parts are determined by the spatial and temporal resolution of the experimental setup. Hence,

$$\mathbf{M} \approx \left\langle \sum_i \left\langle \int_{A_i^\mathrm{res}} \mathrm{d}^2 r \, \mathbf{m}(\mathbf{r}) \right\rangle_{t_e} \right\rangle_{t > t_e} \ , \tag{6.42}$$

where A_i^res represents at least the area of the sample imaged onto a single pixel of the measurement unit of the microscope and t_e is the exposure time required for a single image. In general, the area A_i^res is larger than the area imaged onto a single pixel, since the resolution limiting factor is the electron microscope instead of the camera. Nevertheless, the analysis of fluctuations of the order parameter $\mathbf{M}$, which generally means the investigation of $\mathbf{m}(\mathbf{r}, t)$, has therefore to be adapted to the experimental constraints and results

[8] This is a phase transition of infinit order and breaks no system symmetry [145].

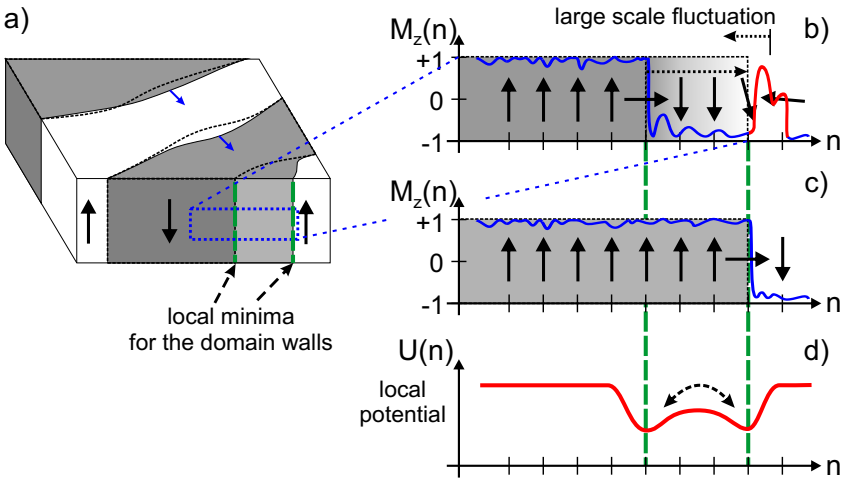

Figure 6.10: *Domain wall fluctuations are shown in a) where due to a large scale spin fluctuation the domain wall is enabled to move from one pinning site to a neighboring one. b) and c) schematically show the spin configuration across a domain wall, where the blue line represents a snapshot of the magnetization profile and the red line in b) represents a large scale fluctuation. In d) a schematic drawing of the local potential with two minima is shown.*

in

$$\overline{\mathbf{m}}_{A^{\mathrm{res}}}(\mathbf{r}, t_e) = \left\langle \int_{A_i^{\mathrm{res}}} \mathrm{d}^2 r \, \mathbf{m}(\mathbf{r}) \right\rangle_{t_e} . \tag{6.43}$$

This equation implies, that any fluctuations of the magnetization within the area A_i^{res} faster than the exposure time t_e leads only to a reduction of the signal. Since our experimental setup has a resolution of about $\sim 100\,\mathrm{nm}$, depending on the PEEM settings, thermal fluctuations of individual spins or blocks of spins leads only to a reduction of the contrast, in our case the TP-MCD signal, which can be seen in the schematic drawing of the reduction of spin-spin correlation function in Fig. 6.9. However, thermally activated domain wall motions with a spatial displacement larger than $\sim 100\,\mathrm{nm}$ and frequencies up to $\sim 2000\,\mathrm{Hz}$ are detectable in this experimental setup, such as schematically shown in Fig. 6.10.

6.6 State Characterizing & Phase Transition Parameters

In order to identify different phases of the domain pattern and also to quantify the state of the system, various parameters will be used in this thesis. The *geometrical magnetization* $\overline{m}$, already introduced in Eq. (6.27), is a measure of the asymmetry between the areas occupied by spin-up and spin-down domains and corresponds to the magnetization state with respect to an applied magnetic field. Especially for stripe forming systems exhibiting a distinct evolution of the stripe width, the equilibrium *domain width* w_{D} is a second parameter required to characterize the state of the system. This parameter will lead to the introduction and successful application of a simple model which can explain many experimental results. A quantification of the symmetry of the domain pattern is given by the *orientational order parameter*

$$g_n = \left| \frac{1}{N} \sum_{\mathbf{r}\in \mathrm{DW}} e^{i\,n\,\Theta(\mathbf{r})} \right| = \left| \langle e^{i\,n\,\Theta(\mathbf{r})} \rangle_{\mathbf{r}\in \mathrm{DW}} \right| \ , \tag{6.44}$$

where $\Theta(\mathbf{r})$ is the director field of the domain configuration, which refers to the angle of the domain wall (DW) at site $\mathbf{r} \in DW$ with respect to the x-axis [128,146–148]. Note, that g_n does not depend on the reference axis and is only a measure of the average deviation from a predominant orientation of the domain walls with respect to a n-fold symmetry. For instance, in the case of an ideal stripe pattern oriented along an arbitrary direction, one has $g_n = 1$ for all n. Adding the same amount of stripes with perpendicularly oriented domain walls to the original pattern, results in $g_2 = 0$ but $g_4 = 1$. A description for the explicit computation and examples for realistic as well as fictive domain patterns are given in the Master's thesis of M. Buchner [128], from our group.

6.7 Glassiness in Uniformly Frustrated Systems

The balance between the strong, positive but short range exchange interaction and the weak, long range, but negative dipolar interaction leads to phase separation of spin up and spin down states on mesoscopic as well macroscopic length scales (domain pattern). In the absence of any defects the ground state of a system comprising these interactions is a well-ordered stripe domain pattern. However, in any real system the energy landscape in configuration space has a certain corrugation due to structural imperfections of the substrate or the magnetic film, or steps at surfaces and interfaces. This induces local minima, as can be seen in Fig. 6.11 by the black dashed line. When the system is forced to change the domain configuration, domain nucleation or collapse may occur but certainly involves domain wall motion [131]. The relaxation time for such transformations is given by the Arrhenius law

$$\tau = \tau_\infty \exp\left(\frac{E_\mathrm{A}}{k_\mathrm{B}T}\right) \ , \tag{6.45}$$

where E_A is the activation energy representing an energy barrier for a single domain wall motion. For real systems the activation energy is replaced by a distribution function $f(E_A)$ taking into account the random distribution of various barriers. At high thermal energies the system samples all individual configurations q with the corresponding Boltzmann probability $\exp(\frac{E_q}{k_\mathrm{B}T})$ [131]. The system is then called *ergodic*, since the time average equals the phase-space average of an observable and, hence, the expectation value is independent of the initial value.

In a natural manner, the competing interactions responsible for pattern formation induce a *uniform frustration* as well, since both interactions cannot be satisfied simultaneously.

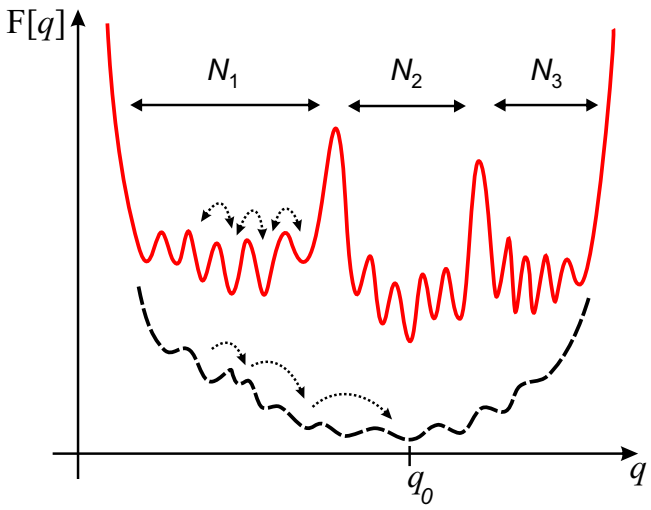

Figure 6.11: *In any real system comprising disorder and imperfections (black dashed line) the free energy $F[q]$ may have only a single global minimum at the ground state configuration q_0. A system with entropy crisis (red line) exhibits a large number of metastable states separated by high energy barriers. Below the glass transition temperature T_G the system samples only a subset of metastable states N_ms.*

The general result from frustration is the emergence of a large amount of metastable states N_{ms} energetically comparable, where the barriers between these metastable states grow as the temperature decreases [2]. Below a transition temperature T_{A}, the dynamics of the system become "viscous", i.e. energy-landscape dominated and exhibits extremely long relaxation times due to the emergence of these numerous metastable states [149]. An important feature of the number of metastable states is, that they exponentially increase with the system size and, in addition, depend on, for instance, the cooling rate. At some temperature $T_{\mathrm{G}} < T_{\mathrm{A}}$ the system freezes into a *glass state*, and stays there virtually forever. However, since $T_{\mathrm{G}} > 0$ the system still exhibits, albeit very slow, a dynamical character, which is due to the configurational environment, i.e. reachable metastable states in the vicinity of a single configuration. This is illustrated in Fig. 6.11, where sets of reachable configurations are separated by high energy barriers. The configurational entropy S_c is then given by

$$S_c \simeq k_{\mathrm{B}} \log N_{\mathrm{ms}} \ . \tag{6.46}$$

In case that the system is further cooled at infinitely slow cooling rates and does not undergo a phase transition into the solid regime, all degrees of freedom freeze out at some temperature $0 < T_{\mathrm{K}} < T_{\mathrm{G}}$ and the system becomes stationary. The configurational entropy vanishes in this case like $S_c(T) \sim T - T_{\mathrm{K}}$ and would be negative for $T < T_{\mathrm{K}}$. This effect is referred to as the "entropy crisis" [149][9]. Nevertheless, the relaxation time for a system in the glass state is found to increase faster than the Arrhenius law Eq. (6.45), and is given by the Vogel-Fulcher law [2]

$$\tau = \tau_\infty \exp\left(\frac{DT_{\mathrm{K}}}{T - T_{\mathrm{K}}}\right) \ , \tag{6.47}$$

where T_{K} is the Kauzmann temperature and D is the fragility and usually a small number.

As described before, the glassy behavior can also be a result of strong structural defects. However, as pointed out in [2], even the smallest amount of disorder due to external defects in combination with competing interactions on different length scales can lead to so called *self-generated glassiness* [150] and leads to the above mentioned *uniform frustration*.

[9] In any real system under real conditions the entropy crisis is avoided, since the system would undergo a phase transition into the solid regime before this happens.

Chapter 7

Experimental Results: Phase Transitions & Fluctuations

Parts of this chapter are prepared for publication [120, 121].

7.1 Static Properties of the Magnetic Model System

7.1.1 Out-of-plane and In-plane Magnetic Contrast

According to Eq. (3.3) the MCD-asymmetry depends on the scalar product of the magnetization and the helicity vector. Since the magnetization is inside the sample also the helicity vector of the photons inside the sample has to be used. For the given experimental conditions, with an incidence angle of 65° with respect to the sample surface normal, the transmission angle of the incident light with respect to the surface normal is 17° for a Fe-surface and 21° for a Ni-surface [151]. Hence, both in-plane as well as out-of-plane directions of the magnetization should lead to magnetic contrast, while the perpendicular orientation results in a larger contrast due to the *cosine*-dependence of the scalar product. Fig. 7.1 a) and b) show the magnetic domain patterns in the vicinity of the SRT obtained by TP-MCD PEEM. The image in Fig. 7.1 a) may lead to the conclusion that a paramagnetic phase with zero magnetic contrast exists between the out-of-plane and in-plane regions. However, the magnified image, shown in Fig. 7.1 b), reveals the presence of small out-of-plane magnetized domains all the way up to the in-plane region where both regions are distinguishable by different domain patterns. This is in agreement with measurements by Won et al. [130] performed at room temperature. These authors also showed images of the SRT region for increased temperatures with a region exhibiting zero magnetic contrast

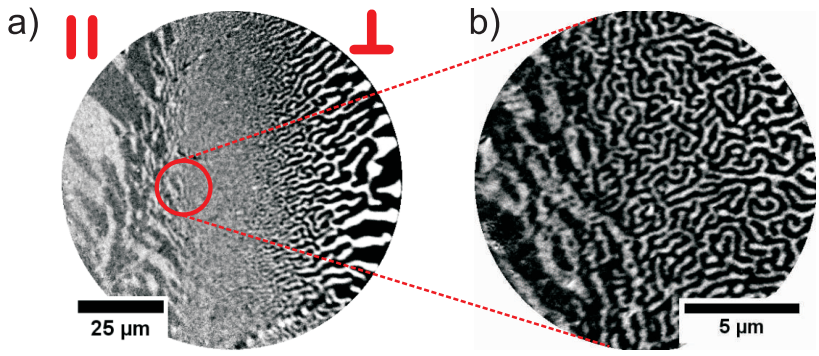

Figure 7.1: *a) shows an image of the SRT region with out-of-plane as well as in-plane contrast* (FOV 100 μm). *In the in-plane region with magnetization direction parallel to the film plane (∥) an irregular domain pattern formation is observable, while in the out-of-plane region (⊥) a disordered stripe domain pattern is formed. A zoomed-in image* (FOV 15 μm) *reveals the same domain pattern evolution but no region with zero magnetic contrast between out-of-plane and in-plane magnetization, as shown in a).*

between the in-plane and out-of-plane region. This region with non-magnetic contrast increases in size with increasing temperature, while the position of the onset of the in-plane magnetization region stays constant with increasing temperature. The authors concluded that the region with zero magnetic contrast is either due to the existence of a paramagnetic phase between the ferromagnetic out-of-plane and the ferromagnetic in-plane region, or caused by fast moving domains. This fact will be further discussed in section 7.1.3, where the temperature has been increased while examining the SRT region.

7.1.2 Continuous Spin-Reorientation Transition

In the following description, the magnetoelastic contribution B_1 to the anisotropy will be treated as a contribution to the uniaxial magnetocrystalline constant $K^u_{1,\text{eff}}$, since this energy has the same symmetry, although B_1 is far from being a negligible term, as shown in section 6.2.3. As pointed out in section 6.2.2, the SRT takes place when the effective total anisotropy $K^u_{1,\text{eff}}$ becomes zero. In the case of a non-zero second order magnetocrystalline anisotropy constant K^u_2 within the range of $-\frac{1}{2}K^u_{1,\text{eff}} \leq K^u_2$, for $K^u_{1,\text{eff}} < 0$ [94], the reorientation transition is continuous, i.e. the magnetization vector gradually rotates from out-of-plane to in-plane or vice versa. The magnetization configuration is then referred to as a *canted* state. This can be understood by considering the following. For an

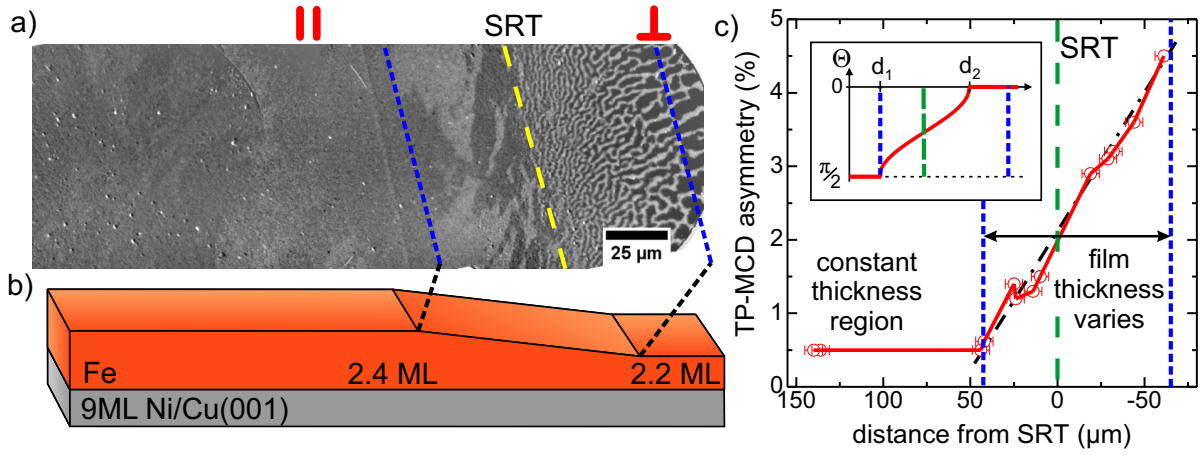

Figure 7.2: *In a) the magnetic domain pattern across a thickness evolution of the Fe top layer as schematically depicted in b), is shown* (FOV $283 \times 95\,\mu\text{m}^2$). *c) The dependence of the TP-MCD asymmetry on the distance to the SRT reveals a nearly linear behavior. The dash-dotted line is a guide to the eye and the dashed green [yellow] line in c) [a)] marks the SRT. The blue short-dashed lines mark the region where the Fe thickness is thought to increase linearly, found by analysis of the change in the domain width (out-of-plane limit) and change in the magnetic contrast (in-plane limit). The inset shows the evolution of the rotation angle* Θ *of the magnetization with increasing thickness, in accordance with [94].* d_1 *and* d_2 *are defined in Eqs. (7.1) and (7.2).*

out-of-plane configuration right at the SRT, the first order anisotropy constant becomes negative $K^u_{1,\text{eff}} \leq 0$. If $K^u_2 \leq 0$ the reorientation takes place abruptly. However, for $K^u_2 \geq 0$ and $-\frac{1}{2}K^u_{1,\text{eff}} \leq K^u_2$, the second order anisotropy constant K^u_2 is large enough to keep the magnetization along the out-of-plane direction even when $K^u_{1,\text{eff}} < 0$. Decreasing $K^u_{1,\text{eff}}$ even further also leads to the reduction of K^u_2 due to a similar thickness dependence. This results in a continuous transition and a canted magnetization state due to the balance between $K^u_{1,\text{eff}}$ favoring the in-plane direction and K^u_2 favoring the out-of-plane direction. However, the determination of K^u_2 is delicate, since it cannot be measured separately due to the interplay with various other anisotropy terms.

The analysis of the TP-MCD signal across the SRT, shown in Fig. 7.2, exhibits a clear continuous evolution[1]. Assuming a linear evolution of the TP-MCD signal, Fig. 7.2 c), and taking into account the *cosine*-dependence of the scalar product on the angle between magnetization and helicity vector, the rotation of the magnetization vector across the SRT

[1]The linear increase in thickness between two terraces of the Fe top layer is due to the smearing effect of a shutter which is located approximately ~ 5 mm in front of the sample during the evaporation process. The distance of the sample to the evaporation source is about ~ 15 cm. This shutter has been used to fabricate samples with non-constant thicknesses.

results in an *arccos*-dependence [152], as shown in the inset of Fig. 7.2 c). This is in accordance with the predicted evolution of the magnetization vector in the continuous regime by Millev and Kirschner [94]. These authors also deduced equations for the thicknesses corresponding to the onset and completion of the reorientation process, which are given by

$$d_1(T) = \frac{2K^u_{1,\mathrm{S}}}{\frac{1}{2}\mu_0 M_S^2 - K^u_{1,\mathrm{V}}} \tag{7.1}$$

$$d_2(T) = \frac{2(2K^u_{2,\mathrm{S}} + K^u_{1,\mathrm{S}})}{\frac{1}{2}\mu_0 M_S^2 - (K^u_{2,\mathrm{V}} + K^u_{1,\mathrm{V}})}\ , \tag{7.2}$$

where the magnetocrystalline anisotropies K^u_1 and K^u_2 are divided into a bulk and surface contribution

$$K^u_1 = K^u_{1,\mathrm{V}} + \frac{K^u_{1,\mathrm{S}}}{d} \tag{7.3}$$

$$K^u_2 = K^u_{2,\mathrm{V}} + \frac{K^u_{2,\mathrm{S}}}{d}\ , \tag{7.4}$$

and d is the film thickness. Following Millev and Kirschner and assuming $|K^u_{1,\mathrm{V}}| \ll \frac{1}{2}\mu_0 M_S^2$ and $|2K^u_{2,\mathrm{V}} + K^u_{1,\mathrm{V}}| \ll \frac{1}{2}\mu_0 M_S^2$ simplifies Eqs. (7.1) and (7.2) and leads to the width of the SRT, correspondingly to $\Delta d \approx 8K^u_{2,\mathrm{S}}/\mu_0 M_S^2$. We further assume that at a rotation angle of 45° of the magnetization vector, the configuration which dominates the domain pattern changes, i.e. to out-of-plane (stripe pattern) or to in-plane (irregularly shaped). This results in $\sim 44\,\mu$m for the half width of the SRT region, extracted from Fig. 7.2 b) and leads to a thickness variation $\Delta d \approx 0.16$ ML (approximated thickness slope $\sim 0.2\,\mathrm{ML}/110\,\mu\mathrm{m}$). Hence, the second order magnetocrystalline surface anisotropy term can be approximated to $K^u_{2,\mathrm{S}} \approx 0.04\,\frac{1}{2}\mu_0 M_S^2$, which is a reasonable value compared to the other anisotropy constants presented in Table 6.1. Unfortunately, the shape anisotropy $\frac{1}{2}\mu_0 M_S^2$ depends strongly on thickness and temperature. Since there are no published values for Fe/Ni/Cu(001), $K^u_{2,\mathrm{S}}$ can only be given relative to the shape anisotropy. However, we are currently constructing a new UHV setup for in-situ MOKE measurements, providing the possibility to apply strong in-plane magnetic fields allowing the measurement of hard-axis loops. From these loops the thickness dependence of $K^u_1(d)$ and also $K^u_2(d)$ can be determined. In addition, the dependence of the MOKE signal on the thickness can then be extrapolated to bulk values. In this way the thickness and temperature dependence of the shape anisotropy $\frac{1}{2}\mu_0 M_S^2$ can be estimated.

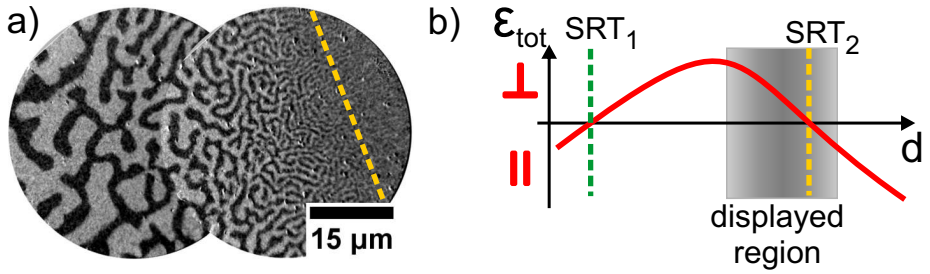

Figure 7.3: *A typical out-of-plane domain pattern evolution near the SRT is shown in a). The Fe thickness increases linearly from left to right by about* $\sim 0.08\,ML$. *The dependence of the total uniaxial anisotropy energy density, which determines the magnetization orientation, versus the thickness d is shown in b). The shaded area represents the region shown in a).*

7.1.3 Domain Width Dependence on d, T and K^u_{eff}

As discussed in the theory part, the basis for pattern formation is the interplay between various magnetic interactions, where the ratio between uniaxial anisotropy K^u_{eff}, Eq. (6.9), dipolar energy Ω and exchange energy Γ, Eq. (6.17), plays the decisive role. Since all of these parameters are thickness as well as temperature dependent, the domain width depends on these parameters as well. In fact, according to Eq. (6.24) the dependence of the equilibrium domain width on these parameters leads to an exponential evolution of the domain width. Fig. 7.3 a) shows a typical domain pattern evolution for the system Fe/Ni/Cu(001) with a constant thickness slope of the Fe top layer of 1.1 $\frac{\text{ML}}{\text{mm}}$ in the vicinity of the SRT. In Fig. 7.3 b) the corresponding total uniaxial anisotropy energy (Eq. (6.15)) is qualitatively plotted as a function of thickness d. Since the domain width evolution should not depend on the slope of the thickness, a similar domain width dependence has been measured for different samples with different slopes and also for a single sample but at different effective anisotropies. Fig. 7.4 a) comprehensively presents these measurements. The main result that can be extracted from Fig. 7.4 a) is that the overall dependence of the domain width with respect to the distance to the SRT remains similar, in agreement with [117, 130]. Since the samples were grown with a thickness wedge of the Fe layer, the analysis of the domain width with respect to the distance to the SRT is equal to the analysis of the domain width dependence on film thickness. In agreement with other measurements [129, 130] we extract a minimum domain width of $w_{\text{D}}^{\text{min}} \approx 300\,\text{nm}$ from several measurements, which agrees with the value deduced in section 6.3.2.

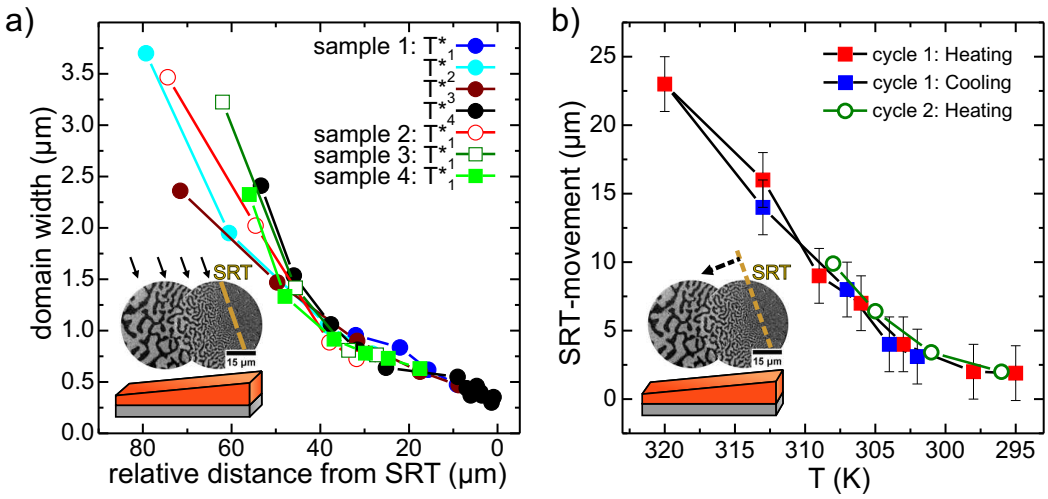

Figure 7.4: *a) The dependence of the equilibrium domain width w_D on the thickness of the Fe layer is shown for one sample with different effective anisotropies (sample 1) as well as for individual samples with different thickness slopes (samples 2-4). In the latter case the distances to the SRT are re-scaled to sample 1. The inset representatively shows the measurement positions for the domain width. The domain pattern shown in the inset is the same as in Fig. 7.3 a). In b) the shift of the SRT while varying the temperature is plotted, also illustrated in the inset.*

In addition to the thickness dependence, all microscopic coupling constants also depend on temperature, confer Eq. (6.17). Fig. 7.5 a) shows a typical domain pattern in the vicinity of the SRT, where the Fe thickness increases from top to bottom. In Fig. 7.5 b) the change in the domain pattern as well as the shift of the SRT, due to an increase of temperature, is shown. The temperature dependence of the SRT is summarized in Fig. 7.4 b). Two results can be obtained from Figures 7.5 b) and 7.4 b). First, in addition to the lateral shift of the SRT the formation of in-plane oriented domains can be observed in regions that exhibit an out-of-plane domain pattern at lower temperatures (Fig. 7.5 b)). This excludes at first glance the existence of any paramagnetic phase between the out-plane and in-plane magnetization region as discussed by Won et al. [130]. However, Cannas et al. [153] performed Monte Carlo simulations for a 2D Heisenberg model for ultra thin films with perpendicular anisotropy. These authors showed that only in a narrow temperature and effective anisotropy interval, a paramagnetic phase exists between the ferromagnetic out-of-plane and ferromagnetic in-plane phase. This region is only observable when the effective anisotropy, which may be different from sample to sample, is within a certain narrow interval. Hence, both results remain possible. What is more, Won et al. also discussed the possibility of the appearance of fast moving domains in the vicinity of the SRT which may blur the images and lead to a loss of magnetic contrast. Such fast moving

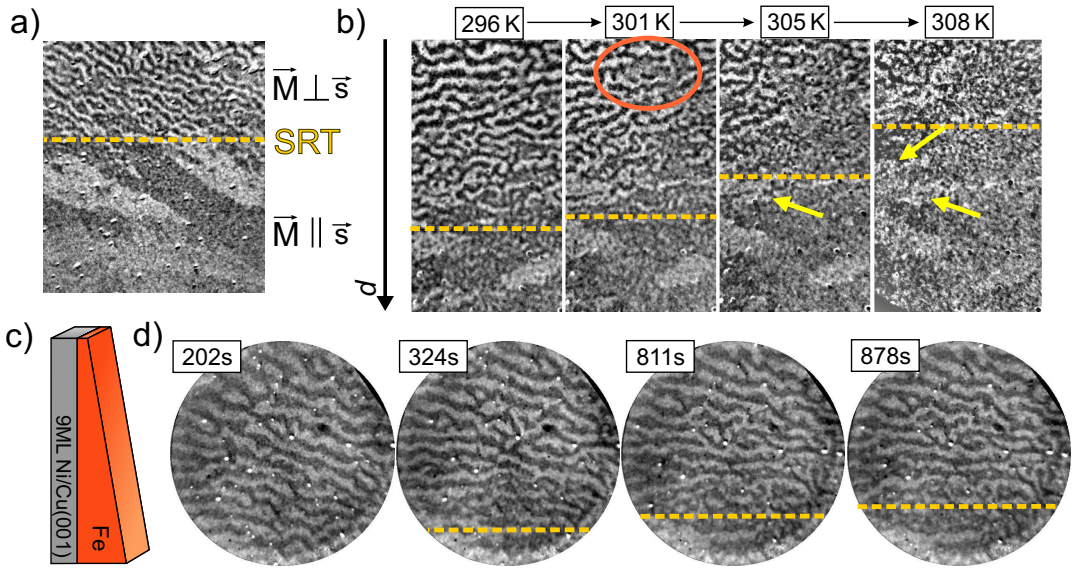

Figure 7.5: *a) shows a typical domain pattern in the vicinity of the SRT, where* **s** *is a vector parallel to the surface of the sample. The influence of temperature on the domain pattern is shown in b) which shows the images corresponding to the measured values of cycle 2 in Fig. 7.4 b)* (FOV $18 \times 32.5\,\mu\mathrm{m}^2$)*. Encircled in orange color is a region with zero magnetic contrast, indicating a fast pattern change. The in-plane regions show a clear formation of domains in regions which are out-of-plane magnetized at lower temperatures, marked by the yellow arrows. The dashed lines mark the SRT and the thickness configuration is schematically plotted in c). Depositing Cs adatoms leads to a shift of the SRT, as shown in d), and has therefore the same effect as heating the sample.*

domains can be confirmed by the images presented in Fig. 7.5 b). In each image some small areas occur which exhibit almost zero magnetic contrast surrounded by stripes exhibiting large magnetic contrast (e.g. the domain structure encircled in orange color). The exposure times for all images were only 12 ms. The study of these fast moving domains will be the subject of section 7.5.

The second result obtained from the temperature evolution of the SRT is that Fig. 7.4 b) surprisingly shows almost the same evolution as the thickness dependence in Fig. 7.4 a). Note, that a change of the SRT induced by a variation of temperature accompanies also a transformation of the whole domain pattern, due to the exponential dependence of the domain width on the thickness of the magnetic layer. The evolution of the domain pattern as a function of temperature was measured by Portmann [154] and shows the exponential dependence as shown in Fig. 7.4 a) and b). F. Freund from our group measured the evolution of the SRT for a temperature range from 170 K to 390 K [155] by scanning electron

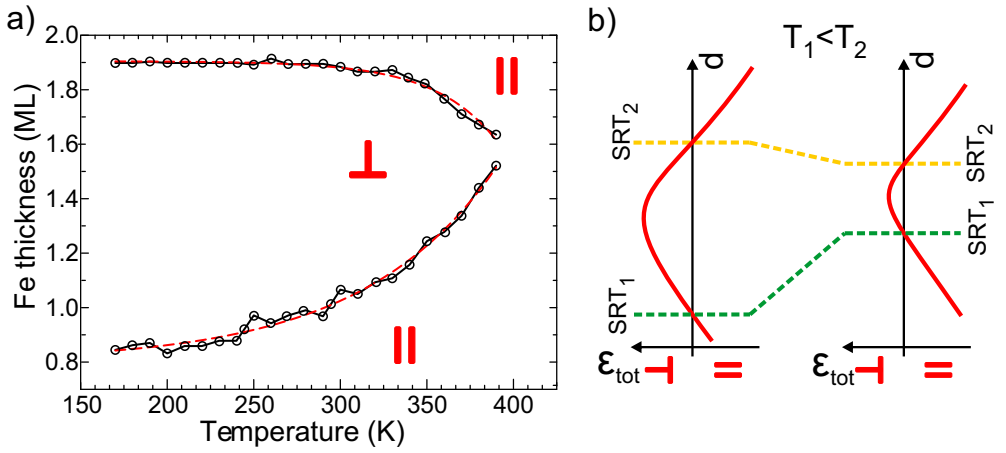

Figure 7.6: *In a) the phase diagram of the magnetization orientation for the system Fe/(5 ML)Ni/Cu(001) as a function of temperature and Fe thickness is shown, which was extracted from SEMPA images by F. Freund [155], from our group. The out-of-plane region becomes smaller since the first SRT moves to larger thicknesses and the second SRT to lower thicknesses with increasing temperature. b) shows schematic drawings of the total anisotropy energy for low temperatures (left) and high temperatures (right).*

microscopy with polarization analysis (SEMPA). The sample structure is a continuous wedge Fe/(5 ML)Ni/Cu(001) which exhibits both SRT's, i.e. from in-plane to out-of-plane at thin Fe layers, and vice versa at thicker Fe. The main result is shown in Fig. 7.6 a). Again the evolutions of the SRT's show a clear exponential behavior. Summarizing, these findings signify that the interplay of $K_{\text{eff}}(d,T)$, $J(d,T)$ and $\Omega(d,T)$ leads to a thickness and temperature dependence that can be interpreted as a dependence on one single parameter in the vicinity of the SRT. This parameter will be referred to as the effective temperature $T^*(d,T)$ in the following.

Since the TP-MCD contrast mechanism requires the reduction of the work function, achieved by depositing Cs adatoms, also the influence of Cs adatoms on the out-of-plane phase has to be investigated. Cs adatoms change the surface anisotropy term K_s, which is susceptible to the chemical composition of the surface. The deposition of Cs adatoms leads to a reduction of the positive surface anisotropy K_s, hence *de*stabilizes the out-of-plane phase. This is shown in Fig. 7.5 d) for a small shift of the second SRT. In Fig. 7.7 is shown that a small amount of Cs (Fig. 7.7 a)) leads to a large out-of-plane region, whereas a large Cs coverage (Fig. 7.7 c)) reduces this region. The first SRT (SRT_1), occurring at low film thickness d, shifts to higher d, while the second SRT (SRT_2) shifts to lower d, but less than the shift of SRT_1. This effect is schematically depicted in Fig. 7.7 b) and d).

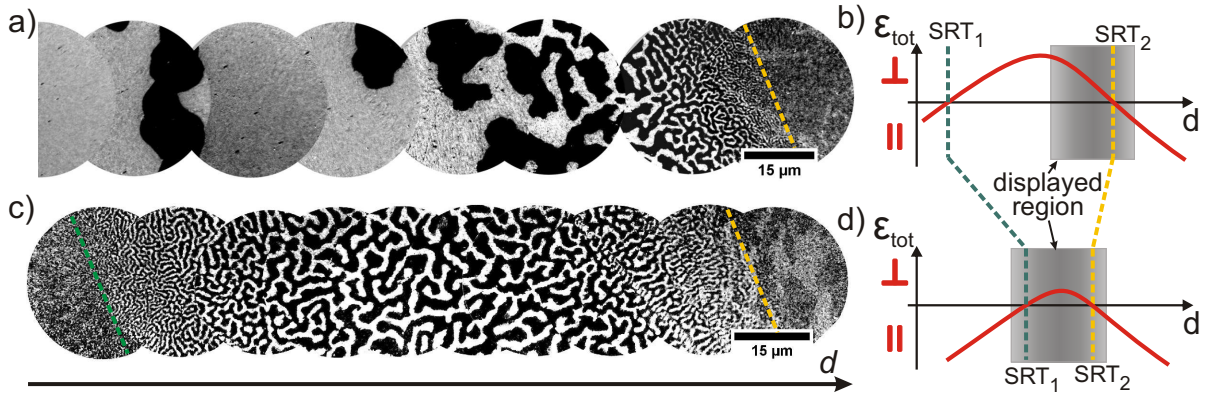

Figure 7.7: *Changing the effective anisotropy by depositing Cs adatoms leads to a shift of the second SRT to lower thicknesses and of the first SRT to higher thicknesses, accompanying a reduction of the out-of-plane magnetized region, as shown in a) and c). The temperature was kept constant. In b) a qualitative plot of the total anisotropy energy is shown for a large surface anisotropy favoring out-of-plane magnetization. d) shows the same as b) but for a smaller surface anisotropy due to a larger Cs coverage. Note, that b) and d) show the same quantitative evolution as shown in Fig. 7.6 b).*

Note, that depositing Cs has the same effect as changing the temperature, compare the schematic drawing presented in Fig. 7.7 b) and d) with Fig. 7.6 b). The total Cs coverage is less than $\sim 0.3\,\mathrm{ML}$ [71, 72], since above this thickness the sticking coefficient becomes zero, confer section 4.2.2.

Summarizing, the measurements of the thickness and temperature dependence of w_D, Fig. 7.4 a) and b), show that temperature and thickness affect the domain width and therefore the domain pattern in a similar manner. In addition, the deposition of Cs decreases the effective SRT temperature which is therefore analogous to increasing the temperature. Hence, the introduction of an effective temperature $T^*(d,T)$, depending on film thickness d and temperature T is reasonable. The equilibrium domain width therefore depends on $T^*(d,T)$. Based on this effective temperature, a comprehensive model of the domain width transformation near the SRT can be derived. It will be shown that this model allows a complete and simple description of the experimentally measured transition front.

7.1.4 Model for Domain Width Evolution

The model is based on the experimentally measured and theoretically found [130, 156] domain width dependence on the effective temperature. As shown in section 6.3.2 by Eq. (6.23), the local energy density of a stripe domain configuration for zero applied magnetic field is given by [127]

$$\varepsilon(w_\mathrm{D}) = \frac{\varepsilon_\mathrm{DW}}{w_\mathrm{D}} - \frac{\Omega}{\pi w_\mathrm{D}} \ln\left(\frac{2w_\mathrm{D}}{\pi l}\right) , \tag{7.5}$$

where $\varepsilon_\mathrm{DW} = 2\sqrt{2J\lambda}$ is the domain wall energy per wall length and $l = \sqrt{J/2\lambda}$ is the domain wall width. For $w_\mathrm{D} > 0$, Eq. (7.5) is continuously differentiable, hence, a Taylor expansion around the equilibrium domain width provides an approximation of the energy landscape and results in a parabola with a minimum at the equilibrium domain width w_D0 (only in this section the equilibrium domain width is called w_D0; in the following sections the 0 will be omitted). Neglecting corrugations in the energy landscape, a qualitative plot of the energy density on the 2D map of domain width and effective temperature can be given, as shown in Fig. 7.8 a). The dependence of w_D0 on the effective temperature

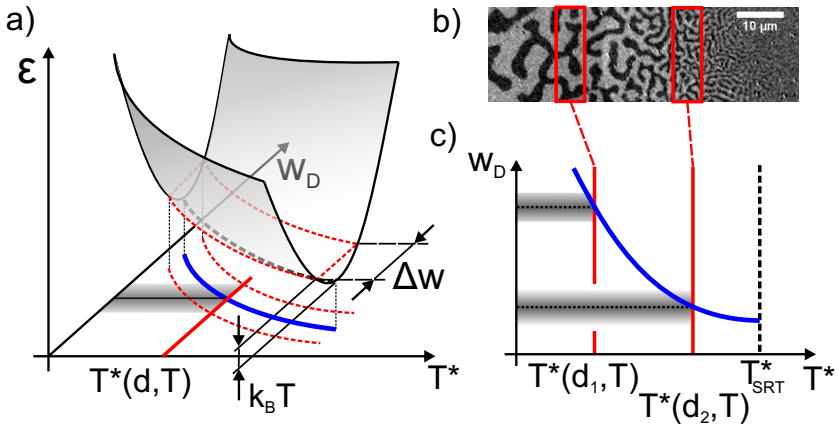

Figure 7.8: *a) Schematic drawing of the approximated energy landscape determining the equilibrium domain width w_D0 for a given effective temperature $T^*(d,T)$. The available thermal energy $k_\mathrm{B}T$ leads to a variation Δw in the domain width for a given $T^*(d,T)$. b) Domain width evolution when continuously increasing the Fe film thickness. The overall domain width decreases with increasing thickness, while for a constant film thickness a certain domain width variation related to the thermal energy is observable (shown e.g. by the red slices). c) 2D projection of a) with the SRT assumed to occur at an effective SRT temperature T^*_SRT. The shaded areas represent the variation Δw of the domain width, also shown in a).*

is obtained experimentally, as shown in the previous sections. As in any real system, thermal energy results in a finite probability for obtaining a variation of the domain width Δw around the equilibrium domain width w_{D0}. The expected variation Δw of the domain width can be estimated by considering the energy landscape and the thermal activation. As shown in Fig. 7.8 a) the domain width variation is related to the average available thermal energy $\mathrm{k_B}T$. This variation of the domain width for a given thickness and temperature can be observed in almost all images, see for instance in Fig. 7.8 b). Variations in the thickness d as well as in the effective anisotropy K_{eff} also lead to variations of the domain width. For simplicity, variations in thickness and temperature will be expressed using only one parameter, the effective temperature. In each slice a certain variation around a mean domain width can be recognized. A quantitative investigation may reveal the local curvature of the energy landscape, but has not been performed so far. For the sake of simplicity, the 2D scheme plotted in Fig. 7.8 c) will be used in the following. The shaded area represents the thermal effect on the equilibrium domain width, i.e. represents the variation Δw in the domain width. Note, that for each slice in Fig. 7.8 b) a graph similar to Fig. 7.8 c) can be extracted, since keeping the thickness constant and increasing the temperature leads to exactly the same evolution of the domain width, as shown in c). Summarizing the influences of the individual parameters on the domain width evolution: i) increasing the temperature T or the film thickness d, increases the effective temperature $T^*(d,T)$; ii) since the deposition of Cs (which decreases the effective anisotropy, section 7.1.3) has the same influence on the magnetization as increasing the temperature, the effect of depositing Cs adatoms can be taken into account by a reduction of the effective SRT temperature T^*_{SRT}. This leads to a shift of the whole domain width evolution, and hence the domain width in the out-of-plane region changes accordingly, confer Fig. 7.8 c).

7.2 Topological Defects and Stripe Pattern Phases

The path of a highly ordered smectic phase towards a disordered state or vice versa is still subject to numerous studies [1,3,127,134,137,153,154,157–159]. The analogy to a melting process of a crystal structure, to be more precise, of a liquid crystal structure, is obvious (and has led to the nomenclature [122]). The main ingredient of this melting process is the proliferation of dislocations, i.e. topological defects, which reduce the translational and/or rotational order of the pattern [132,160]. It has been shown by Abanov et al. [1,135], that the smectic crystal phase supports, besides long-wavelength excitations, also four types of topological excitations usually appearing in bound pairs. Fig. 7.9 a) shows a smectic domain pattern with a large number of topological defects, where some are highlighted

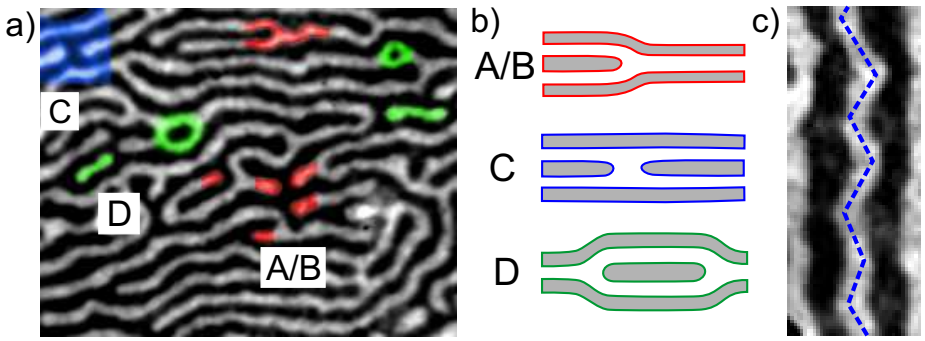

Figure 7.9: *a) shows a domain pattern exhibiting a large number of individual defects: A/B defects (domain ending from left/right, red), C defect (bridge, blue) and D-defects (island, green). In b) a schematic drawing of these individual defects is shown (labeling is according to Abanov [1]). The transverse instability causes undulations of stripe domains, as shown in c).* (FOV: *a)* $22.3 \times 28.3 \mu m^2$, *c)* $10 \times 4 \mu m^2$)

by colors. Fig. 7.9 b) schematically shows the individual defects, where the labeling of the individual defects was introduced by Abanov et al. [1]. With rising temperature, straight domains become more and more instable (transverse instability [132], see Fig. 7.9 c)) and topological defects appear in the domain structure. Subsequently, bound pairs of dislocations become abundant and finally unbind. The proliferation of dislocations eventually causes melting of the smectic crystal.

The evolution of the domain patterns within the stripe phase can take several paths when increasing the effective temperature towards the SRT-temperature. According to the *K2APS*-theory, confer section 6.3.5, four phases may be distinguishable: mono-domain (MD), smectic (SM), Ising nematic (IN), and tetragonal liquid (TL). The MD phase will not be considered in the following. At low effective temperatures the domains form parallel stripes (SM phase). Due to long-wavelength excitations as well as topological defects the strict parallel alignment of the stripes is disturbed at higher temperatures. An example for this phase is shown in Fig. 7.10 a) i) and in Fig. 7.9 a). The FFT of this image exhibits two spots, which is characteristic for a stripe pattern. The second image in Fig. 7.10 a) may show the Ising nematic (IN) phase, but the assignment is not unambiguous. In addition, this image was obtained from a pure smectic phase after applying a field pulse. The FFT also shows two broad peaks, instead of two bright and two less bright peaks along the perpendicular direction. In Fig. 7.11 d) another domain pattern which may be assigned to the IN phase is shown, as well as the FFT of this image, presented in Fig. 7.11 e). In the real-space image the dominant direction as well as some perpendicularly oriented domains are clearly visible.

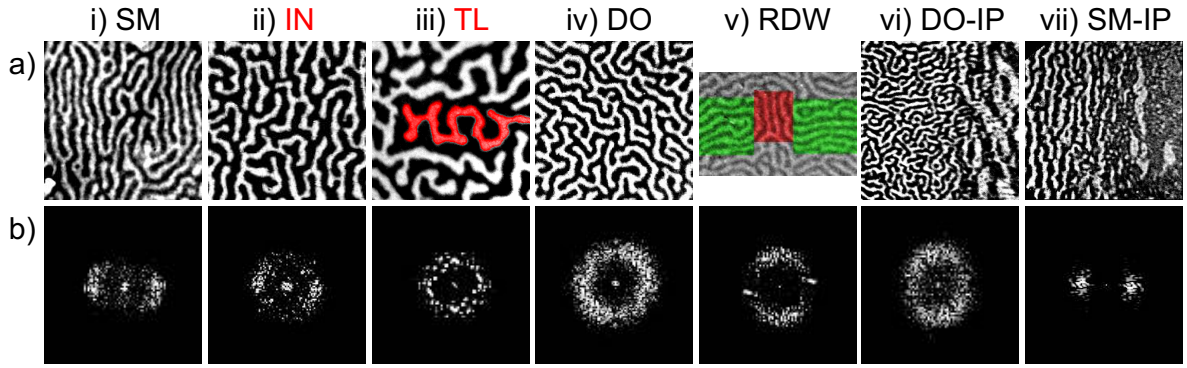

Figure 7.10: *According to the K2APS theory four phases (MD: mono-domain, SM: smectic, IN: Ising nematic, TL: tetragonal liquid) should be distinguishable. a) shows real domain images, and b) shows the FFT's of a). The MD phase is not shown. An unambiguous assignment of images ii) and iii) in a) to the IN and TL phases is not possible. Image a) iii) shows a domain structure (highlighted in red) where two perpendicular directions are equally occupied, i.e. may be a small section of a TL phase. iv) shows a disordered domain pattern, where the FFT features a circle. A rotational domain wall (RDW) is shown in v). Image vi) shows a disordered phase prior to the in-plane (IP) region. In contrast, image vii) shows a re-entrant transition into the smectic phase prior to the SRT.* (FOV *i)* 24μm, *ii)* 12μm, *iii)* 22μm, *iv)* 27μm, *v)* $23 \times 15\mu\text{m}^2$, *vi)* 10$\mu$m, *vii)* 31$\mu$m)

According to Abanov et al. [1], "a new type of topological excitation occurs in the Ising nematic phase", which the authors have called a *rotational domain wall* (RDW). These RDW's are stripe domains, oriented along a preferred direction. At some point all stripes bend at once about 90°. So far, no experimental measurement evidences the existence of such RDW's. However, in Fig. 7.10 a) v) such a 90°-rotation of several stripe domains is shown. The FFT of this image shows two broad spots and two narrow spots in the perpendicular direction (where the latter refers to the middle part, highlighted in red in Fig. 7.10 a) v)). In Fig. 7.11 a) and b) two other examples for such RDW's are shown. These RDW's occur only in small regions of the sample embedded by a stripe pattern either close to the smectic phase with a large amount of topological defects or the disordered phase.

Following again Abanov, subsequent to the IN phase, the tetragonal liquid phase emerges with increasing effective temperature. This phase exhibits an equal occupation of the two perpendicular domain orientations. Up to now this phase has not been observed unambiguously. However, the investigation of the pattern evolution while heating the

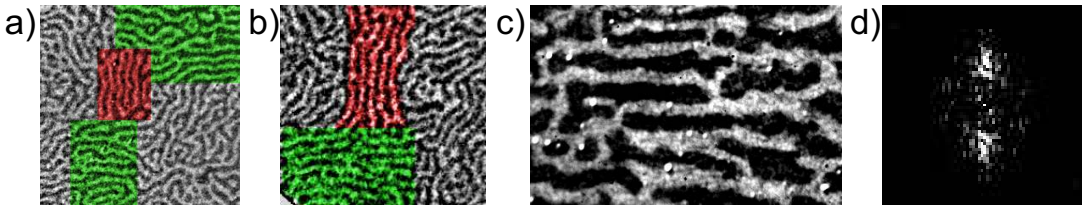

Figure 7.11: *Within the IN phase, a new kind of topological excitation occurs, i.e. rotational domain walls, which were observed in a very small region on the sample, a) and b). c) shows another example of a supposedly IN phase, and d) shows the corresponding FFT.* (FOV *a)* 50μm, *b)* 32μm, *c)* $33 \times 21\mu\text{m}^2$)

sample, done by M. K. and M. Buchner from our group, revealed at the beginning a growth regime of some elongated domains, which have been attributed to the smectic phase, see [128]. Further increasing the temperature, and thereby decreasing the domain width, led to an undulation of the individual domains due to transverse instabilities, which will be further discussed in section 7.6.4. The result of this undulation is shown in Fig. 7.10 a) iii). The domain highlighted in red clearly exhibits the two preferred, perpendicular axes. However, on large scales such an equal occupation of two, perpendicular domain wall orientations has never been observed. Fig. 7.10 a) iv) shows a disordered state, with almost no preferred direction as can be seen in the FFT Fig. 7.10 b) iv). In general, in most cases the sample quality (density of pinning centers) was not sufficient for the formation of a pure phase on a large scale, which means that the large defect density induces various topological defects and destroys thereby the positional and orientational order. In addition, a distinct transformation from one phase to the other, as predicted by theory, has been observed only in very few cases and even then only in a very restricted region of the sample, as will be shown below.

As discussed in the theory part in section 6.3.5, there are two scenarios for the pattern evolution beyond the IN and TL phases, just prior to the SRT. In the first case the orientational tendency, which increases while approaching the SRT, dominates over the higher affinity for bending, which is due to a lower bending constant when reaching the SRT. This leads to the emergence of the so-called "inverse melting" process and was first demonstrated by Portmann et al. [137]. This process is also called a re-entrant transition, since the formation of a more ordered smectic phase emerges at even higher temperatures from a more symmetric, i.e. less ordered IN, TL, or disordered phase. In the second scenario the lower bending constant leads to the formation of a more wavy pattern and hence to a disordered state prior to the SRT. In this thesis both scenarios are observed, as shown in Fig. 7.10 a) vi) and vii), where vi) shows a disordered state and vii) clearly shows

a smectic phase. In both images the different domain patterns of the in-plane configuration compared to the out-of-plane pattern can be recognized in the right parts. The FFT's shown in b) for these two images are performed only for the out-of-plane magnetized region.

Since the evolution of patterns depends on the combination of the exchange and dipolar energy as well as the magnetic anisotropy in a very subtle way (which may vary locally in any real sample), the clear pattern evolution as predicted by the K2APS theory was not measured. Furthermore, the theory predicts the evolution as a function of temperature T, which is similar to an evolution of thickness d (according to section 7.1.3), but maybe not exactly the same?

7.3 Slow Dynamics: Domain Pattern Transformation

7.3.1 Transition Front driven by Thermal Fluctuations

Motivation In the vicinity of the SRT the domain width becomes narrower before the magnetization vector rotates into the plane of the film. Any variation of the equilibrium domain width has to be accompanied by a transformation of the domain pattern. In any real system, however, the energy landscape shows local corrugations caused by imperfections of the substrate or the ferromagnetic film or arising from self-generated topological defects in the domain pattern (section 6.7). It is due to these ripples in the energy landscape that pattern transformations, initiated by the change of e.g. the equilibrium domain width, are, in general, step-by-step reactions driven by thermal fluctuations. Transitions can also be driven by modulating external parameters. In this case ripples in the energy landscape remain observable as long as the strength of the external driving parameter is of the same order of magnitude as the thermal fluctuations. In the case of tuning the externally applied magnetic field the corrugated energy landscape is evidenced by the famous Barkhausen jumps. As in any statistical process thermally driven transitions have a certain finite rate of change determined by the thermal energy and the local corrugation of the energy landscape. As a consequence, after a parameter change faster than the system's inherent reaction time, which is determined by thermal fluctuations, a metastable state emerges in which the system may remain for a long time. For the transition into the equilibrium state a local activation across a certain energy barrier is sufficient which eventually initiates a global transition.

Realization In the vicinity of the SRT, the system Fe/Ni/Cu(001) exhibits a monotonically decreasing evolution of the domain width with increasing effective temperature converging to a finite value. Here, vicinity refers to the vicinity to the zero crossing of the effective anisotropy, hence, is not meant to be any length scale in real space as can be seen in Fig. 7.12 a)-c). These images show the domain pattern evolution across several individual steps of the Fe thickness of 0.2 ML which are macroscopically separated by $\sim$(0.9-1.1) mm. However, the exact domain width is solely determined by the temperature dependent ratio of the anisotropy, dipolar, and exchange coupling constants (Eq. (6.24)). Consequently, when this ratio is changed the domain pattern has to adapt by inserting or eliminating domains, where each single domain wall displacement must be thermally driven. Thus, when rapidly changing the ratio of the coupling constants while simultaneously suppressing thermal fluctuations by cooling the system to low temperature, the system is unable to adapt to the new equilibrium domain configuration adiabatically. In

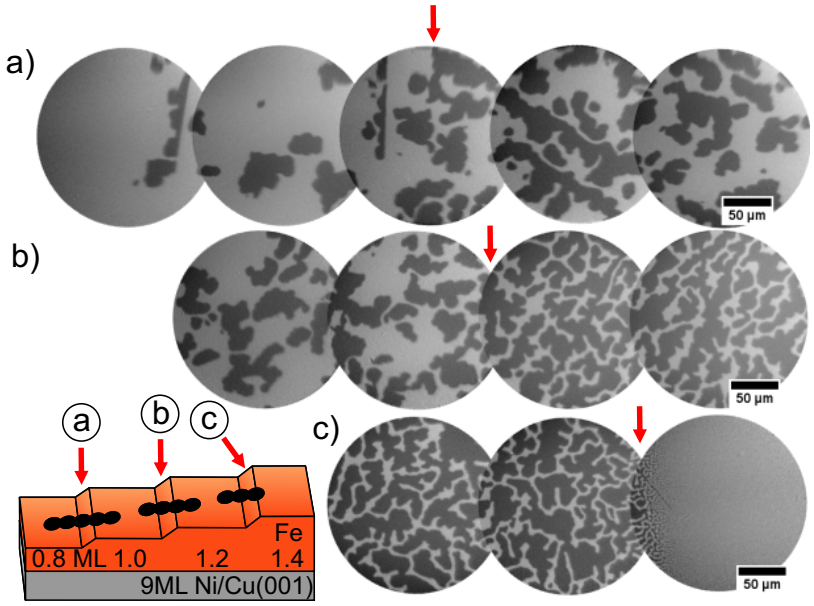

Figure 7.12: *Outline of the domain pattern evolution at individual thickness steps of 0.2 ML, separated by ∼(0.9-1.1) mm, as shown in the schematic drawing. These measurements were done by M. Buchner from our group and M.K., modified taken from [128]. The FOV of each single image is* 187 *µm in diameter.*

other words, in the absence of large thermal fluctuations the system cannot leave the initial state and cannot gradually condensate into its new equilibrium state. However, a local transition may take place in regions where the final state is still energetically reachable even with reduced thermal fluctuations or by the occurrence of rare events. This initialization, in turn, leads to the emergence of a transition front gradually moving across the system. This behavior is known e.g. from supercooled water as the condensation front [161]. In our case the system forms well separated regions with large and small domain widths. As in the case of supercooled liquids, where the crystallization front affects the surrounding liquid molecules by absorbing their kinetic energy, the magnetic transition front lowers the local energy in front of the transition region by reducing the long range dipolar energy due to a higher domain wall density behind the front[2]. This process will be further discussed below in the framework of the model presented in section 7.1.4.

The generation and observation of such a transition front in magnetic ultra thin films is realized as follows. As seen before, the investigated stepped wedge Fe/Ni/Cu(001) film exhibits large modifications of the domain width at the individual 0.2 ML thickness steps of the Fe layer which are equally spaced by ∼(0.9-1.1) mm (Fig. 7.12). The magnetization

[2]The dependence of the dipolar energy on temperature is much weaker than its dependence on the actual domain state, which is based on the long-range behavior of the dipolar interaction.

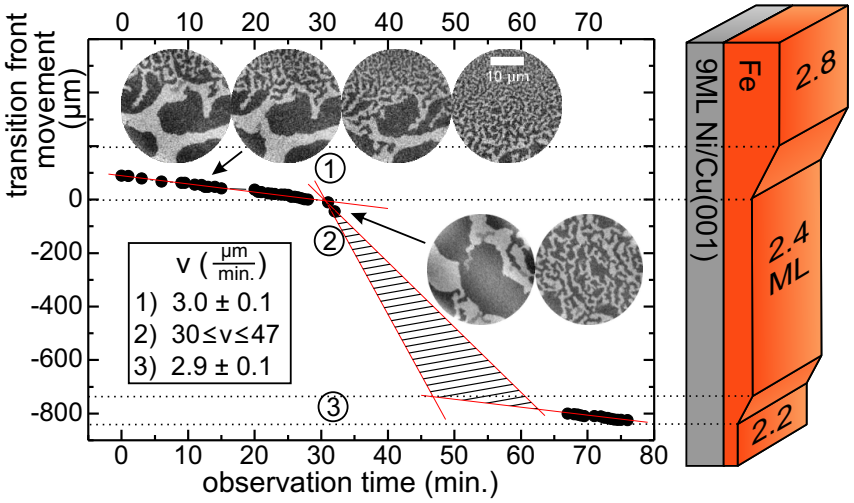

Figure 7.13: *The movement of the main transition front is plotted versus observation time. The error bars are smaller than the symbols. Three regions with individual transition front velocities can be recognized corresponding to a region with constant Fe thickness (region 2) and regions with varying Fe thickness (regions 1 and 3).*

eventually rotates into the plane at a Fe-thickness of ∼(1.2-1.4) ML. Prior to cooling the sample to about 180 K, a small amount of Cs has been deposited, in order to be able to image the domain evolution at the individual steps of the sample. The cooling process shifts the SRT point towards the in-plane region, i.e. stabilizes the out-of-plane phase which is equivalent to reducing the effective temperature $T^*(d,T)$ in our model, section 7.1.4. However, the effect of changing the real temperature is, in general, smaller than the effect of a change of the effective anisotropy or thickness. In accordance with [135], cooling a large domain state does not alter the state but merely affects a narrow region near the SRT.

Subsequently, the effective uniaxial anisotropy is further reduced due to a reduction of the surface anisotropy term K_S by additionally depositing Cs for ∼5 min. At room temperature, reducing K_S with the same amount of Cs, leads to a shift of the critical film thickness at which the SRT occurs of more than 0.2 ML. However, at low temperatures this is not observed. The system remains in the initial state at all terraces of the stepped wedge sample for an undefined period of time (15-40 min), until, starting at a step of the film thickness, smaller domains rapidly spread out of larger domains, as shown in the insets of Fig. 7.13.

Analysis Three features can be extracted from this sequence of images. First, there is a clear front with finite width of smaller domains slowly moving across the sample. Second, all spreading domains have an almost equal domain width. And third, only very few domains with the 'final' domain width emerge at larger distances from the transition front (tens of micrometers) but still in its vicinity. When the position of the transition front is plotted as a function of time, a straight line results leading to a velocity of $\sim 3.0\,\frac{\mu\mathrm{m}}{\mathrm{min}}$. Surprisingly, this velocity is about one order of magnitude larger in regions with constant film thickness e.g. at constant K^u_{eff}. At each step in film thickness, corresponding to a rather large variation of the effective anisotropy, the velocity returns to the lower value. Due to the small field of view of the PEEM only two images could be obtained in the region of a terrace leading to a large unknown region, represented by the hatched area in Fig. 7.13. Consequently a large error in the determination of the velocity of the transition front arises. However, due to the exponential dependence of the domain width on the film thickness, the position of the transition front could be mapped onto the layer thickness by simple analysis of the change of the domain width induced by thickness variations. Hence, the transition front movement can be restricted to the hatched area in Fig. 7.13.

Discussion As seen before, a reduction of the real temperature has a much smaller impact on the SRT than changes of the effective anisotropy or the film thickness; it simply reduces the variation of the domain width at constant $T^*(d,T)$. Hence, only the shaded area in Fig. 7.8 c) becomes smaller, which represents the domain width variation Δw. A change of the effective anisotropy, due to additional Cs deposition, however, is equal to a shift of the effective SRT temperature T^*_{SRT}, as shown in section 7.1.3. This change of T^*_{SRT} consequently shifts the whole domain width evolution in the vicinity of the SRT, see Fig. 7.14 a). An explanation for the observed transition front can be given in terms of the above mentioned model by dividing the process into two parts. The first is the activation process, which is the initialization of the transition front. The second one is the transport of the activation energy, eventually leading to the movement of the transition front. The activation process can be induced either by a rare event in the sense of an extremely large thermal fluctuation changing the domain state in a sufficiently large area or simply by a large enough film thickness variation. Consider that close to the SRT, where the domain width evolution converges, an overlapping area of the initial (grey line) and final (black line) domain width evolution occurs, as can be seen in Fig. 7.14 b). This overlap makes the transition into the new domain phase via thermally fluctuating domain walls possible. The transport of the activation energy, i.e. the translation of the transition front, is based on the reduction of the long range dipolar energy after the first step of the transition has occurred. The dipolar energy is given by the actual state of the system and is reduced when it transforms into a state with smaller domains. Hence, the energy is locally reduced

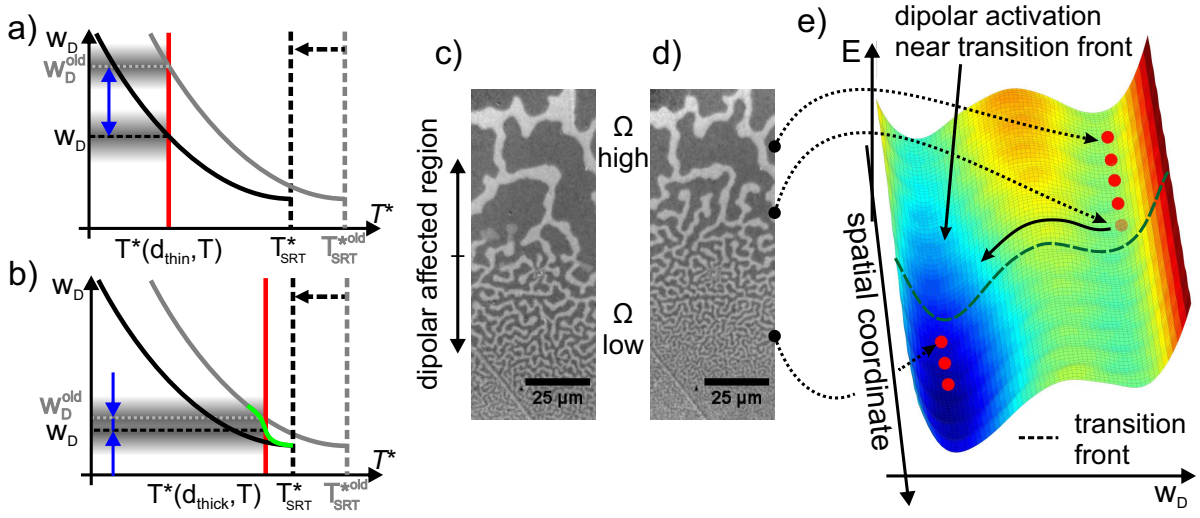

Figure 7.14: *Cs adatoms decrease the effective SRT-temperature $T^{*old}_{SRT} \rightarrow T^{*}_{SRT}$, also shifting the whole domain width evolution. A gap between the thermally reachable initial and final states opens up at small effective temperatures as shown in a). Only in overlapping regions, as depicted in b), the transition from the former (gray line) to the new (black line) domain width occurs, which represents the activation process. The curve connecting both lines (green curve) represents the actual evolution. Images in c) and d) show such a transition front, where the time duration between these images was ∼16 min. These images also show the continuous decrease of the domain width behind the transition front, as predicted by the model. In e) a scheme of the energy landscape versus domain width and a spatial coordinate is shown. After the transition to the smaller domain width, the dipolar energy Ω decreases, which further decreases the equilibrium state energy and also the energy in the vicinity of the transition.*

further, schematically shown Fig. 7.14 e). This plot represents a fictive energy landscape of a domain pattern forming system which exhibits a small domain width in the lower part and a large domain width in the upper part of this landscape. The state of this fictive system along the spatial coordinate is represented by the red dot. Although the states with smaller domain width are energetically favorable, a certain energy barrier inhibits the transition. Subsequent to the transition, the dipolar energy is reduced and thereby the local energy in the landscape is also reduced, as shown in Fig. 7.14 e) by the dark blue color.

A micromagnetic simulation using the OOMMF package [162], performed by H.G. Bauer, from our group, further supports this argument. The dipolar energy density, extracted from this simulation with realistic domain configurations, is about 13 times smaller for the smaller domain width configuration than for the large domain state. The initial

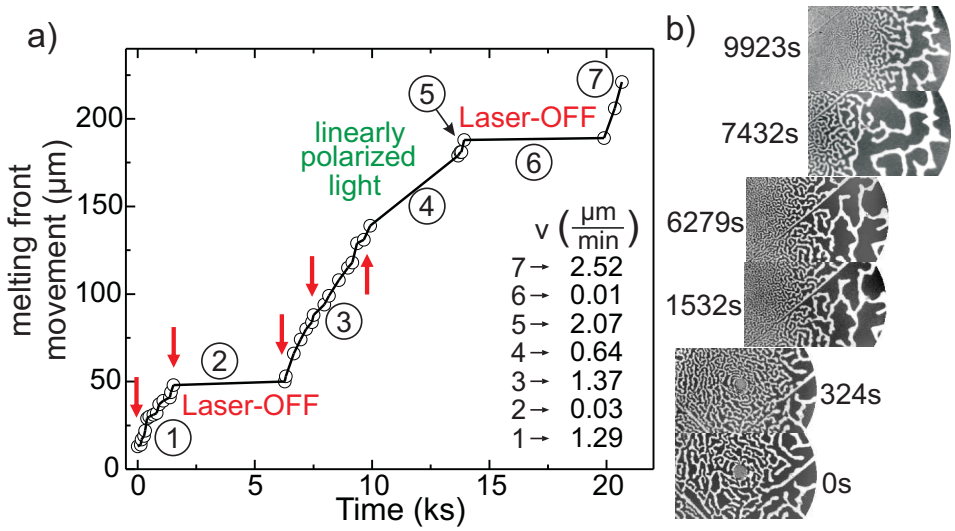

Figure 7.15: *In a) the laser heating effect is investigated, where the red arrows indicate the temporal position of the images shown in b). The images in b) are aligned to the first image at 0 s. The velocities of the individual sections (1-7) are shown in the inset in a). The sample temperature only slightly increases during the whole measurement from 252 K to 254 K. The whole measurement was conducted on a terrace of a stepped-wedge Fe/(9 ML)Ni/Cu(001) sample.*

configurations for the two simulations were extracted from different regions of a measured image, Fig. 7.14 c), i.e. one initial configuration before the transition front (upper part of Fig. 7.14 c)), with a domain width $w_D = 6.8\,\mu$m, and the other after the transition front has passed with $w_D = 2.1\,\mu$m. Hence, the domain state in the upper region of Fig. 7.14 c) has a significantly higher dipolar energy Ω than the lower part exhibiting small domains. Due to the long, but finite interaction range of the dipole interaction, this additional reduction affects the domain states only in the vicinity of the SRT, as shown in Fig. 7.14 e) and c). In addition, since the transition process is driven by thermal fluctuations, each single domain wall displacement occurs from pinning site to pinning site, resulting in a distinct transition front velocity. The velocity is determined by the strength of thermal fluctuations, the local energy corrugation as well as the range of the dipolar interaction. Note, that it is only due to the corrugations of the energy landscape that this transition is continuous and that this metastable state occurred. In regions with varying thickness the energy gap between the initial and final state becomes even larger with proceeding transition front. In regions with constant thickness this energy gap stays constant. Hence, the velocity of the transition front must be smaller in regions with increasing thickness, as observed in Fig. 7.13.

Since the corrugation of the energy landscape can neither be measured nor changed, the influence of changing the available thermal energy externally supplied to the transition front velocity is further investigated. To do so we vary the parameters of the illumination unit. The used laser diode is set to an output power of ∼(100-150) mW and focused down to about ∼(0.5-1) mm in diameter. Hence, the local heat input, which cannot be measured with the current setup, enhances the possibility for any domain pattern transitions. In order to determine the influence of the heat input from the focused laser beam on the transition front velocity, the transition front velocity is plotted in Fig. 7.15 a) for different illumination conditions. Without laser light or illumination with linearly polarized light, no images with magnetic contrast can be obtained, hence, there are no data points. The main result from this plot is, that the heat input by the illumination unit is the main energy source for the thermally driven transition front. When turning off the laser, the transition front velocity is quite slow ($\sim$(0.01-0.03)$\frac{\mu m}{min}$) but still non-zero. This shows again the strong dependence of the transition front velocity on thermal energy and the corrugation of the energy landscape.

7.3.2 Inverse heating

Motivation In the previous section the system was kept in a domain state with a larger domain width while the equilibrium domain width has been changed by external stimuli. The reduction of the domain width was achieved by insertion of a large amount of additional domains with a smaller domain width spreading out of larger domains. The domain structure, in turn, became more disordered by this process due to the large amount of additional domain endings, i.e. topological defects, see section 7.2. The inverse process which means cooling the sample or increasing the effective anisotropy certainly increases the domain width and may also increase the order of the domain structure by reducing the amount of topological defects. An increase of the domain width requires either the shift of the whole domain pattern due to a homogeneous enlargement of the individual domains or the generation of "free space" due to the reduction of topological defects, which then can be occupied by an expansion of the remaining domains. A shift of the whole domain pattern is, however, in many cases energetically unfavorable due to the existence of strong pinning sites which have to be overcome simultaneously. In addition, the bending constant μ (Eq. (6.32)) of the domains increases with increasing domain width, hence, favoring a straight domain wall instead of a domain ending [1, 163]. As a result, the system becomes more ordered. Note, however, that the pattern transformation process is, in general, a step-by-step reaction, which is based either on a certain density of structural defects or the existence of a large amount of metastable states due to a uniform frustration, i.e. the

glassiness of the system, see section 6.7. However, neither the structural defects can be neglected nor estimated which kind of pinning sites (structural defects or due to the glassy nature) has a larger impact. In any case, according to the Arrhenius-law (Eq. (7.7)), lowering the temperature exponentially increases the relaxation time. Hence, in order to measure the reduction of topological defects by an ordering process, the cooling rate has, in general, to be very low. However, depositing Cs adatoms which influences the magnetic properties as well, provides an opportunity for an "inverse heating" process, which will be presented in the following.

Result Fig. 7.16 a) shows a domain pattern evolution starting at 23 °C from a smectic phase with a large number of topological defects and ending at 47 °C again with a smectic phase but a larger domain width and fewer topological defects. The sample was a continuous wedge sample with a small thickness slope of only $0.3\,\frac{\mathrm{ML}}{\mathrm{mm}}$. In Fig. 7.16 a) three individual topological defects are highlighted: A (finger, shown in blue), D (islands, shown in green) and C (bridge, shown in red). With increasing temperature fingers and islands are reduced in size and finally vanish, whereas the bridge defect enlarges in size and remains up to the end of this measurement. The analysis of the domain width and the number of defects with increasing temperature or recording time, is shown in Fig. 7.17 a). The domain width clearly increases, while the number of defects shrinks.

Discussion In general, an increase in temperature results in a reduction of the equilibrium domain width. Depositing Cs on top of the sample shifts the effective SRT temperature to lower effective temperatures, as shown in section 7.1.3. This also leads to a reduction of the equilibrium domain width for a given effective temperature $T^*(d,T)$. However, in this measurement the increase in temperature is accompanied by an increase in the domain width. Before applying the model above presented and in order to explain this at first unexpected result, a few comments need to be made on the behavior of Cs as adatoms. The coverage density of Cs adatoms is stabilized by the adsorption of Carbon atoms or by oxidation [71,72], which is, however, a very slow process at a base pressure of $\sim 5 \cdot 10^{-11}$ mbar in the PEEM chamber. The desorption of unbound Cs adatoms depends strongly on temperature [164] and is illustrated in Fig. 7.16 c)[3]. Increasing the temperature by ΔT immediately after Cs deposition may lead to a higher desorption rate of Cs. The effective anisotropy thereby increases, which increases the effective SRT temperature by $\Delta T^*_{\mathrm{SRT}}$. This effect in turn shifts the evolution of the domain width, as shown in Fig. 7.16 b). In case that the increase in real temperature ΔT is lower than $\Delta T^*_{\mathrm{SRT}}$, the new equilibrium domain width is broader than the initial ones, although the sample is heated. As a result, the presented "cooling process" by actually heating the sample (called

[3] An enhanced affinity to oxidation of cesiated surfaces [72] is given as well, also shown in Fig. 7.16 c).

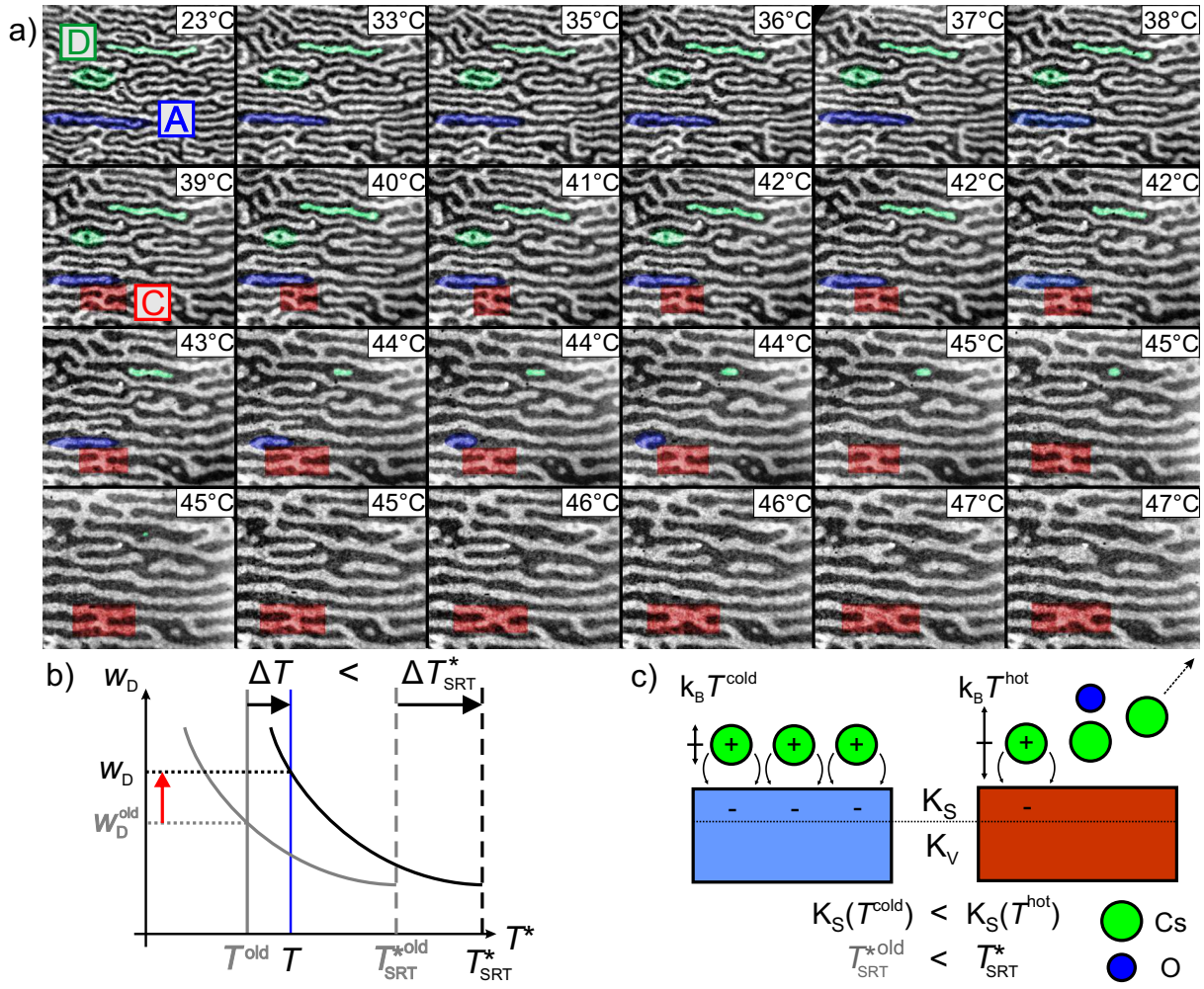

Figure 7.16: *a) shows selected images of the pattern evolution for the inverse heating process* (FOV $32.5 \times 24.5 \mu m^2$). *Green colored are two islands (D), blue colored is a single finger-defect (A), and red colored is a single bridge-type defect (C). b) an increase in the temperature by ΔT may cause a larger desorption of Cs adatoms, leading to a shift of the SRT temperature ΔT^*_{SRT}. Eventually, a larger equilibrium domain width by actually heating the sample may be the result. c) oxidation and desorption of Cs adatoms reduces the surface anisotropy and increases the effective SRT temperature.*

inverse heating) favors the process of ordering while condensing towards a larger domain width. This behavior is based on the fact, that an increased temperature decreases the relaxation time while simultaneously forcing the system into a larger domain state. As a result of the increased temperature, pinned domain endings, i.e. topological defects, are more likely to withdraw allowing the expansion of the large stripe domains.

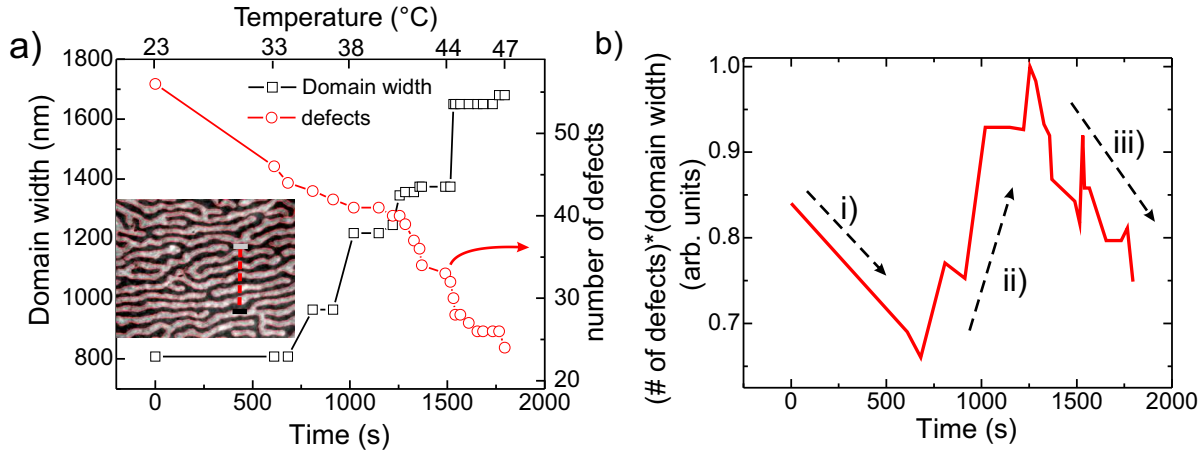

Figure 7.17: *The evaluation of the inverse heating process with respect to the local domain width (black squares) and number of defects (red circles) leads to graph a). The inset shows the region of interest by the red dashed line for the domain width determination and was kept constant for the whole measurement. While the domain width increases with increasing temperature, the number of defects shrinks. b) shows the number of defects times the domain width, which is equal to the number of defects per stripe domain. A reduction of this number, section i) and iii), means that the reduction of defects is faster than the growth in the domain width. In section ii) the growth in domain width is larger than the reduction of defects. The number of defects was taken from the whole FOV of 52µm, where the images in Fig. 7.16 a) show approximately 40% of the FOV.*

The analysis of the number of defects per stripe domain, which is proportional to the number of defects times the domain width, gives further insight into the annealing process while condensing towards a larger domain state. Note that the analysis can be done at least in two ways. The first is to extract the domain width locally, as done in Fig. 7.17 a). The second one is to use the Fourier transform of the whole image, which is presented in Fig. 7.18. The local domain width evolution, plotted in Fig. 7.17 a), exhibits a stepwise increase, which is due to two reasons: i) only a few images have been investigated and ii) the local domain width abruptly increases when defects in the vicinity of the investigated stripes are removed. Hence, the local domain width can slightly deviate from the mean value. The number of defects was manually extracted from the whole images. The local number of defects per stripe domain (Fig. 7.17 b)) is reduced at the beginning of the cooling process. This refers to a faster reduction of the number of defects compared with the increase in domain width, Fig. 7.17 b) region i). Subsequently, a growth regime of the stripe domains appears (from $\sim 700\,\mathrm{s}$ to $\sim 1250\,\mathrm{s}$), which implies that the stripe domains enlarge faster than the number of defects is reduced region ii) in Fig. 7.17 b); this process is reversed again at the end region iii) in Fig. 7.17 b).

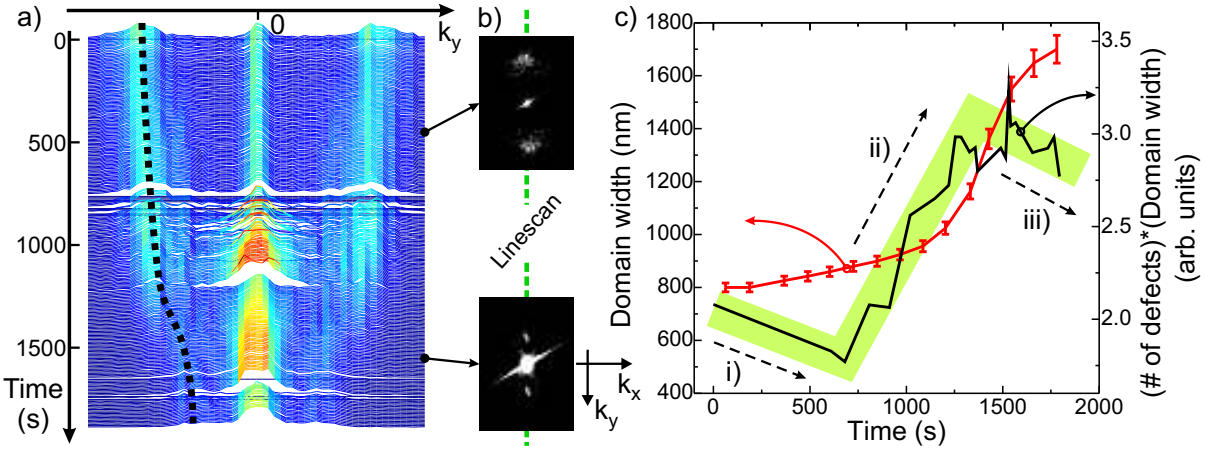

Figure 7.18: *a) shows the time evolution of the main features in the FFT during the inverse heating process, where in b) two representative FFT's of images taken at 457 s and at 1525 s are shown. The black dotted line in a) represents a guide to the eye of the maximum, and the green dashed line in b) shows the region of interest used to obtain graph a). The domain width is then given by the inverse distance from the maximum to $k_y = 0$ in Fourier space, and is plotted in c). Additionally plotted is the number of defects times domain width, which again reveals two decreasing i) and iii) as well as an increasing ii) regime, confer Fig. 7.17 b).*

The analysis of the global domain width is performed with the aid of the Fourier transformed images. In Fig. 7.18 b) the Fourier transforms of the domain pattern for the images measured at times 457 *s* and at 1525 *s* are shown clearly exhibiting two spots. The temporal evolution of these spots is shown in Fig. 7.18 a). The analysis of these Fourier patterns reveals the temporal evolution of the average domain width and is shown in Fig. 7.18 c). Due to a periodic ripple in all Fourier transforms (caused by side bands in the FFT), the guide to the eye, shown in Fig. 7.18 a), was used as reference to extract the distance from the spot to the point $k_y = 0$ which represents the average domain width. The red curve in Fig. 7.18 c) reveals a different behavior of the global domain width compared to that of the local domain width, shown in Fig. 7.17 a). Calculating the number of defects times the average domain width, also shown in Fig. 7.18 c), exhibits again two decreasing regimes, one in the beginning i) and the other at the end iii) as well as an increasing regime ii), where the latter starts again at ~ 700 s. The third regime is not as pronounced as in Fig. 7.17 b) (the guide to the eye in green color in Fig. 7.18 c) highlights the straight behavior in regime ii). Summarizing, the increase of the domain width by a simultaneous reduction of topological defects obeys a complicated dynamics due to the mutual interaction between gaining occupiable area by the reduction of topological defects and the coverage by expanding stripes.

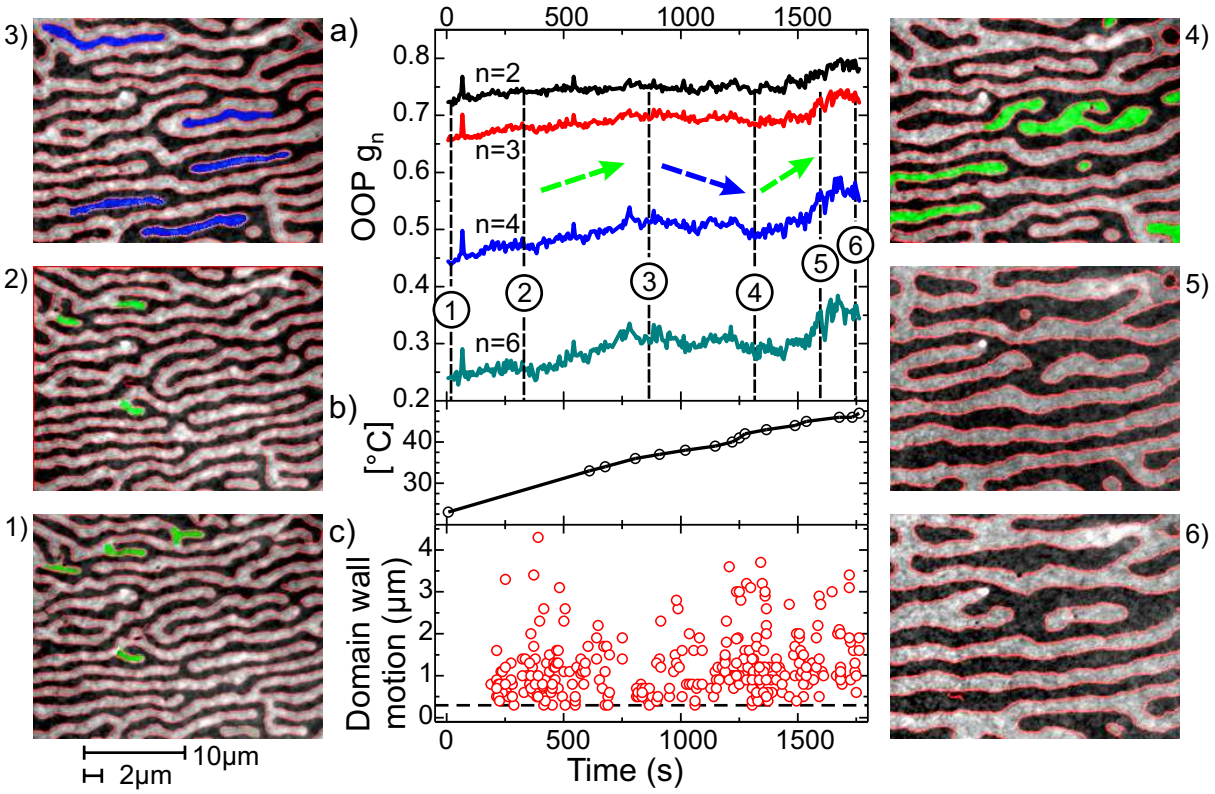

Figure 7.19: *In a) the orientational order parameters for $n = 2, 3, 4, 6$ are shown as a function of time, respectively temperature. A clear increase of all OOP's can be recognized until $\sim 800\,s$, which can be attributed to the reduction of short A-defects, colored green in images 1) and 2)* (FOV $28 \times 22\mu m^2$ *for all images*). *Subsequently a reduction of the OOP's follows which is due to the contraction of the blue colored long topological defects, resulting in a higher density of domain endings in relation to straight domain walls, image 3). The annihilation of the remaining bubble domains and residual short fingers eventually increases the order again. In b) the evolution of the temperature during the measurement is presented. c) shows the individual step sizes of the domain wall motions. Only the motion of domain walls that led to a reduction of topological defects are taken into account. In addition, only each 100th image has been investigated. In order to aid comparison scalebars with 10µm and 2µm are plotted below image 1).*

Since this inverse heating process leads to a larger domain state it is equivalent to cooling the system and the order in the system should increase as well. This property is investigated with the aid of the orientational order parameter (OOP) g_n, given in Eq. (6.44). The result is shown in Fig. 7.19 a). The sensitivity of the OOP to deviations from a predominant orientation of the stripe domains increases with order number n leading to a reduction of the average value with increasing n, as can be seen in Fig. 7.19 a). g_2 slightly

increases until $t \sim 800\,\mathrm{s}$, and strongly increases beyond $\sim 1500\,\mathrm{s}$. This evolution is even more pronounced in the other OOP's with higher order number n. Three regions may be recognized. The first one ranges up to $\sim 800\,\mathrm{s}$, where a general rise in amplitude is observable for all OOP's. In the range from $\sim$(800-1300) s, g_2 stays more or less constant, while g_4 and g_6 decrease. In the last region all OOP's strongly increase. The analysis of the corresponding domain structures reveals that the first increase is governed by eliminating small finger domains in the domain pattern, green colored in images 1) and 2). Such topological A-defects, which have a short length, result in a small ratio between straight and round domain wall sections. Hence, their elimination increases the OOP. In Fig. 7.19 3) all of the small fingers have disappeared and the OOP is large. However, there are still defects in the domain pattern such as the blue colored A and D defects, in Fig. 7.19 3), with a large ratio between straight and round domain walls. With increasing domain width, these defects shrink, accompanied by a reduction of their straight-to-round ratio, reducing thereby the OOP's as well. This process stops when island defects (D) become bubble domains or when long A defects are reduced in size, Fig. 7.19 4), and eventually disappear, Fig. 7.19 5). Hence, removing these bubbles and short domain endings leaves a more ordered domain pattern, as can be seen in Fig. 7.19 5) and 6), even when the number of stripe domains oriented along the same direction is much smaller than before. In general, this plot of the individual OOP's exhibits the inverse behavior compared to the graph shown in Fig. 7.17 b) where the number of defects times the domain width is plotted against time. This again shows the system's propensity to reach the most ordered state and, in addition, that this process is a dynamical process not only at small length scales such as domain wall jumps but also with respect to global order parameters like the OOP's.

What is more, due to structural defects or self-generated glassiness (section 6.7) the energy landscape may exhibit a certain corrugation leading to a large number of states with nearly equal energy. Hence, pattern transformations may be carried out in individual steps, as will be investigated in the following. Due to the frame rate of 16.4 images per second, a snapshot of the domain pattern is available every $\sim 61\,\mathrm{ms}$. All measurements shown in this section were done by using only a single circularity for the generation of photoelectrons, i.e. the definition of the TP-MCD asymmetry, Eq. (3.2), has not been used. Due to the large number of images (29400, in this measurement) and the rather long relaxation times of the motion of individual domain walls (in the range of several hundreds of ms) only every one hundreds image has been used to analyze the domain pattern transformation. This also holds true for the measurements shown in Fig. 7.19. Since the fluctuations of straight domain walls, i.e. corrugation and undulations, may trigger the reduction of topological defects, but play only a minor role for pattern transformations, these fluctuations are

neglected in the following analysis. Hence, only domain wall motions, that reduce the length of defects, are investigated. The result is shown in Fig. 7.19 c) and reveals that the domain wall motions take place in small steps of less than $\sim 4.5\,\mu$m. In order to give an impression about the average step size, two scalebars with $10\,\mu$m and $2\,\mu$m are shown below image 1) in Fig. 7.19. Note, that only domain wall displacements larger than $0.3\,\mu$m are taken into account. Furthermore, since the actual motion of domain walls are, in general, much faster than the temporal resolution in this measurement, each delayed movement of the domain wall represents a pinning site, either due to structural defects or due to the self-generated glassiness. Hence, the corrugation of the energy landscape of this pattern forming system seems to be very large compared to thermal energy.

Summarizing, the decay of a metastable domain pattern by a transition front as shown in section 7.3.1 and the inverse heating process, shown in section 7.3.2, represent two opposing experiments. In the former case the anisotropy is abruptly reduced while the relaxation times are increased due to reduced temperatures. The result is a metastable state. Subsequently, the decay into a domain pattern with smaller domain width abruptly reduces the order of the system. In the case of the inverse heating process the temperature is increased thereby decreasing the relaxation times, and the anisotropy is slowly increased. In this case the domain pattern becomes broader and a self-induced ordering of the domain pattern could be achieved, which is a rare process in nature.

7.4 Application of Magnetic Fields

A striped domain structure has, in general, no net magnetization on large length scales. The application of a perpendicular magnetic field leads via the Zeeman term to the expansion of one domain at the expense of the other, representing a paramagnetic-like response [165]. This paramagnetic behavior is, however, only expected in the vicinity of the SRT, where the effective anisotropy is close to a zero crossing point and the equilibrium domain width is small. According to Eq. (6.31), the compressibility of the domains becomes large close to the SRT and results in this paramagnetic response. However, for a large, positive effective anisotropy the compressibility is small due to a large domain width. Hence, pinning at defects caused by structural imperfections and/or self-generated inhomogeneities may lead to a temporary ferromagnetic response, i.e. showing a net magnetization after application of a magnetic field. This is known as the *magnetic aftereffect* [166]. However, this remanent magnetization is not the equilibrium state of a pattern forming system, and exists only due to the pinning effect of defects. The relaxation of the magnetization towards its equilibrium state by domain wall motion can in principle

be described by the relaxation approximation [166, 167]. Within this approximation it is assumed, that the rate of change of the magnetization is directly proportional to the deviation of the magnetization from its equilibrium value M_∞ [165]

$$\frac{\partial M(t)}{\partial t} = -\frac{1}{\tau}(M(t) - M_\infty) \ , \tag{7.6}$$

where $\frac{1}{\tau}$ is the relaxation rate. The relaxation time follows an Arrhenius law

$$\tau = \tau_0 \exp\left(\frac{E_\mathrm{A} + \kappa E_\mathrm{B}}{k_\mathrm{B} T}\right) \ , \tag{7.7}$$

where E_A is the *activation energy* representing an energy barrier to the domain wall motion, introduced in section 6.7, and $\kappa = \pm 1$ takes into account the sense of relaxation of the magnetization. In fact, due to the corrugation of the energy landscape, there should be a random distribution of various barriers. Hence, the single activation energy E_A in Eq. (7.7) should be replaced by a distribution function $f_\mathrm{A}(q)$, where q represents a domain configuration. The second term in the exponent, represents the Barkhausen energy $E_\mathrm{B} = \mu_0 H M_S V_\mathrm{B}$, where H is the applied magnetic field and V_B is the Barkhausen volume (rather a distribution of Barkhausen volumina $g_\mathrm{B}(q)$). This volume represents the amount of magnetic volume that is reversed in a single activation event [167]. In the fast dynamics section 7.5, this activation volume, where actually the area is measured, represents one of the main quantities to characterize the fluctuation properties of individual defects.

7.4.1 Strong Pinning Sites: Barkhausen Jumps & Magnetic Aftereffect

This section discusses the influence of strong pinning sites on the response of the magnetic sample due to the application of magnetic fields. In addition, the transition of the response function in a striped ferromagnetic film ranging from a paramagnetic behavior in the vicinity of the SRT to a ferromagnetic response slightly away from the SRT, is studied. The magnetic hysteresis loops are extracted from image sequences of the domain structure measured in the vicinity of the SRT while sweeping the magnetic field. In order to measure hysteresis loops at different distances to the SRT within a single measurement, the thickness slope of the wedge-type sample was chosen to be rather large, i.e. 2.05 $\frac{\mathrm{ML}}{\mathrm{mm}}$. Since the Ni layer of the sample was not annealed prior to the deposition of the Fe layer in this measurement, the samples have numerous and strong pinning sites and show a large disorder in the domain structure. This increased roughness of the samples investigated in this section also led to the loss of RHEED oscillations for the Ni film beyond ~ 7 ML's.

Annealing the Ni layer prior to depositing the Fe top layers removes a significant amount of these defects and changes not only the magnetic response of the samples but also the shape of the domain patterns. The application of a magnetic field was achieved by an air coil, which can be positioned in such a way that the sample is in the center. Unfortunately, the perpendicular orientation of the coil with respect to the sample surface can only be adjusted within $\sim 10\,^{\circ}$. Therefore, any applied magnetic field leads besides a rotation and a slight distortion of the image, also to an additional translation of the whole image, due to the Lorentz force exerted on the photoelectrons. Fortunately, the coercive fields of our samples are only a few Oe. At low fields, large fractions of the imaged sample section remain within the FOV.

In Fig. 7.20 hysteresis loops are shown, where the signals in c) and d) are defined by the geometrical magnetization

$$\overline{m} = \frac{A_{\uparrow} - A_{\downarrow}}{A_{\uparrow} + A_{\downarrow}} \,, \tag{7.8}$$

introduced in Eq. (6.27). $A_{\uparrow,\downarrow}$ are the area fractions of the sample with magnetization up ($\uparrow$) or down ($\downarrow$). In fact, the geometrical magnetization was extracted from the sequence of images only within a small quadratic region of $19.7{\times}19.7\mu\mathrm{m}^2$ instead of taking the whole field of view (FOV) into account. The applied magnetic field was changed in steps of 0.5 Oe each 400 ms, and the frame rate was in this case 2000 fps (frames per second). Each trace in c) represents a measurement on a slightly different sample position. Starting with the initial lines of the hysteresis loops, the black one is measured at largest distance (77 μm) and the red colored at nearest distance (50 μm) to the SRT. Sweeping the magnetic field from positive to negative field values, a reduction of the signal already occurs at zero applied magnetic field. However, taking into account a positive residual field within the PEEM chamber of $\sim$(0.7-0.9) Oe, the shift of the hysteresis loop is reasonable. Closer to the SRT the magnetic response changes, as can be seen in c) from the black to the red colored measurement. The hysteresis loop in d) has no longer a square shape, although still exhibiting a coercivity. The region of interest for this hysteresis measurement is shown in image Fig. 7.20 a) by the green square, about 30 μm away from the SRT. Summarizing, the response of the domain structure due to the application of a magnetic field can be described by a ferromagnetic response away from the SRT and by a paramagnetic response close the SRT, as proposed by Venus [165].

What is more, by analyzing the evolution of the signal while changing the magnetic field in steps of 0.5 Oe, two different regimes are obvious. In the first regime at small applied magnetic fields sharp jumps of the signal arise, whereas in the second one at larger magnetic fields, a more continuous evolution of the signal appears. The large jumps correspond

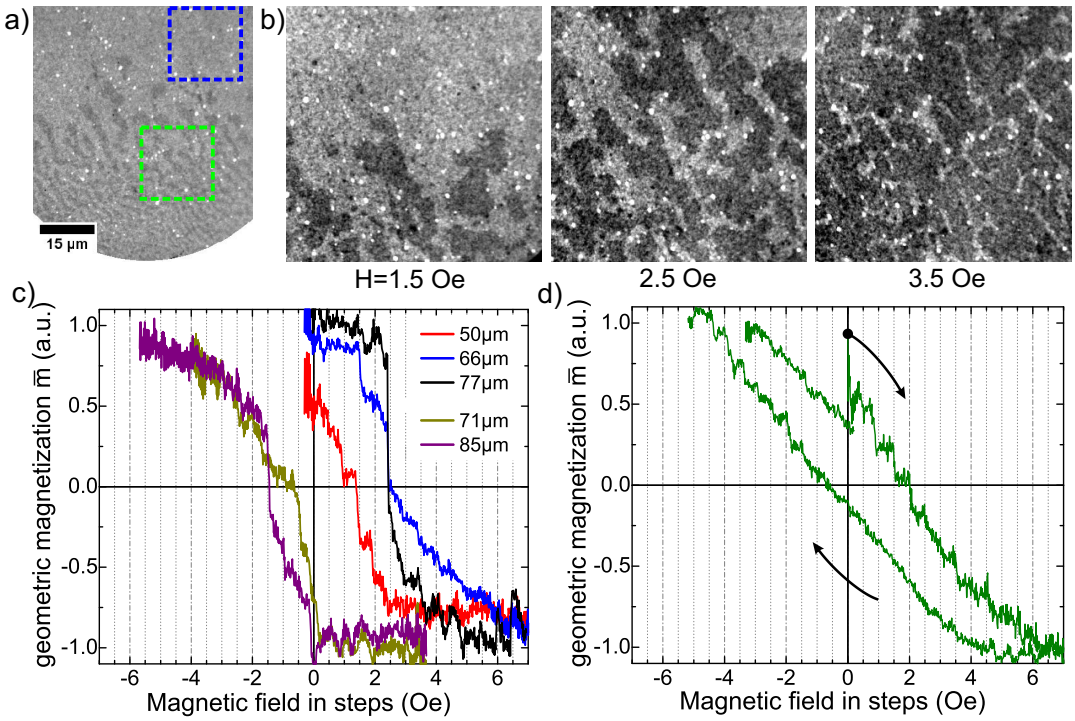

Figure 7.20: *a) shows an overview of the magnetic domain structure in the vicinity of the SRT* (FOV $50 \times 50\mu\mathrm{m}^2$, FR $= 2000$ fps)*. The SRT occurs just below this image. This image is taken after a field pulse, hence, the upper part of this image, where the Fe layer is thinner, is in a single domain state. b) shows the domain structure with different applied magnetic fields, where in the first two images the domain wall motion is erratic rather than a smooth evolution, which is the case in the last image* (FOV $50 \times 50\mu\mathrm{m}^2$)*. Extracting the geometrical magnetization $\overline{m}$ from regions of $19.7 \times 19.7\mu m^2$ at different positions to the SRT results in the hysteresis loops shown in c). In d) the hysteresis loop is shown with an average distance of $30\,\mu$m. The blue [green] square in image a) represents the area of interest for the blue [green] loop in c) [d)].*

to Barkhausen jumps. The corrugation of the energy landscape, as discussed before, provides barriers to the domain wall motion. Within a certain relaxation time $\tau(E_\mathrm{A}, H, T)$, Eq. (7.7), depending on the activation energy, the applied magnetic field and thermal energy of the system, the domain wall may overcome this barrier. In general, τ is smaller than 0.5 ms which is the frame rate in this measurement leading to an abrupt change in the geometrical magnetization when the applied magnetic field has changed. However, due to the existence of rather large defects in this sample, some of them even clearly visible

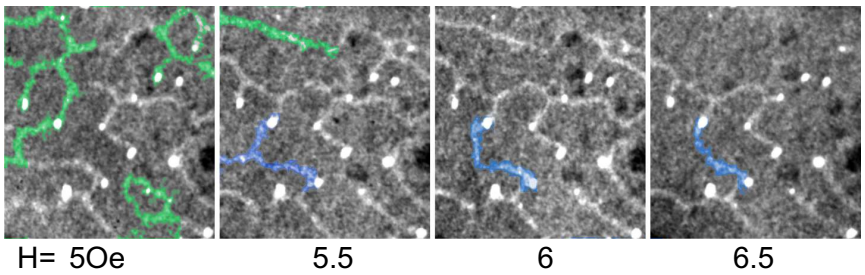

Figure 7.21: *In these images the Fe thickness increases from right top to left bottom by about* $\sim 0.03\,ML$ (FOV $19.3 \times 20.3\mu\mathrm{m}^2$, FR = 200fps). *The green and blue highlighted minority domains become more and more straight in order to decrease the area of the domain. The domains are pinned at defects, which can clearly be seen by the bright spots.*

by the bright spots in each image[4], the activation energies E_A can become quite large, causing long relaxation times.

Besides large jumps, a continuous evolution of the geometrical magnetization is observed at large magnetic fields. This continuous evolution is mainly caused by strong pinning sites, where the ends of already elongated, thin minority domains are pinned while the area occupied by the domain has to shrink. The last image in Fig. 7.20 b) supports this argument. The straightening and disappearing of such narrow, randomly pinned, minority domains, is also shown in Fig. 7.21. The minority domains highlighted in green and blue are suppressed by the external magnetic field until only two strongly repelling domain walls are left (360 ° domain walls). In order to further shrink the domain size while the external magnetic field is increased the meandering domains become as straight as possible until the Zeeman term eventually exceeds the activation energy of the pinning site or overcomes the energy barrier for eliminating the two neighboring domain walls[5]. In 2005 this behavior has been called the "deroughening of domain wall pairs by dipolar repulsion" [168].

Note that due to the high frame rate, any abrupt change of the applied magnetic field leads to a blurring in ∼1-3 images. This can be attributed to the luminescence of the fluorescence screen of the PEEM detector unit while the image is shifted. The decay time of the fluorescence screen has been measured and determined to be ∼0.47 ms, as shown in Fig. 7.22. The shift of the image is much faster than this time scale, and is directly given

[4]The reason why defects appear much brighter is that Cs has a liquid character and sticks with a higher probability to topographic inhomogeneities. Hence, the work function in the vicinity of defects is lower than in smooth regions.

[5]The latter has only been observed in a bubble domain state, where bubbles disappear while the applied magnetic field is increased. This, however, has only been measured in much smoother samples.

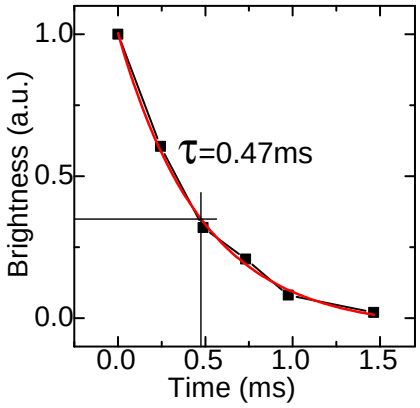

Figure 7.22: *Determination of the decay time of the fluorescence screen by tracing the brightness of a bright spot while applying a strong magnetic field pulse. The exponential fit results in a decay time of* ~ 0.47 *ms to 1/e of the brightness. In most cases the signal to noise ratio is sufficient when the brightness has changed to* $\sim 50\,\%$ *resulting in a decay time of* ~ 0.3 *ms.*

by the rate of change of the magnetic field (which is in the MHz range)[6]. Due to this, the vertical lines in Fig. 7.20 c) and d) indicate the time or field when the image is already stabilized.

The phenomenon of long relaxation times of magnetic textures is known as the *magnetic aftereffect* [166]. The relaxation time, given in Eq. (7.7), can assume values of even years [166]. In Fig. 7.23 the magnetic aftereffect is briefly investigated, again for a continuous wedge sample of Fe/(9 ML)Ni/Cu(001) with a thickness slope of $1.1\frac{\mathrm{ML}}{\mathrm{mm}}$. The image sequence was obtained with only one circularity of the incident light. The frame rate was 4100 fps. In Fig. 7.23 the SRT occurs outside the imaged part of the sample at a thicker Fe thickness. Decreasing the applied magnetic field from a value above the coercivity field,

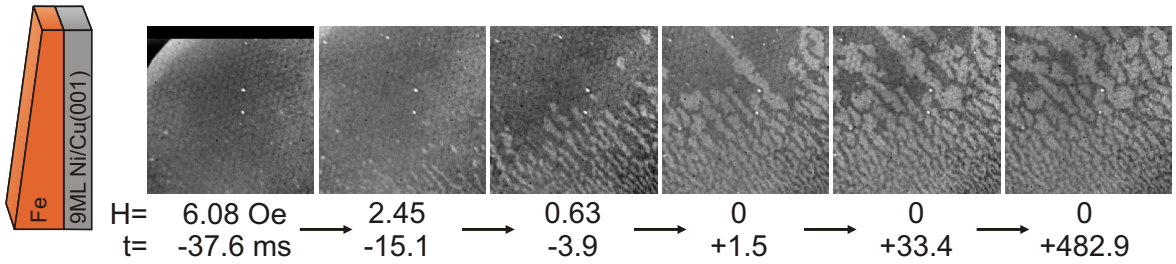

Figure 7.23: *In this sequence the applied field was linearly decreased from 20 Oe until zero* (FOV $31 \times 31\mu\mathrm{m}^2$, FR = 4100 fps). *The upper part of the sample remains in the mono domain state and gradually becomes a multi-domain state in time. Note, that the residual field in the PEEM-chamber is also positive, hence, the relaxation of the magnetization into the multi-domain state is suppressed.*

[6] A further blurring effect is also given by the charging effect within the PEEM. Since changing the applied magnetic field changes also the trajectories of the photoelectrons which may therefore be absorbed at different places in the PEEM column leading to a shift of the image.

leads to domain formation starting in the SRT region. This behavior is in accordance with the above measured paramagnetic response in the vicinity of the SRT. By further reducing the applied magnetic field, the domains grow towards smaller Fe layer thickness, i.e. towards the region with a broader equilibrium domain width. At zero magnetic field, the upper region in Fig. 7.23 is still uniformly magnetized, but gradually becomes a multi-domain state as a function of time. Investigating each single image of the image sequence, reveals that the formation of domains with zero applied magnetic field is always achieved by domain wall motion rather than domain nucleation.

7.4.2 Stripe-Bubble Domain Phase Diagram

As pointed out in the theory part, the application of a magnetic field may lead to a pattern transformation due to the propensity of the system for energy minimization. In the case of a large asymmetry between the two domain states, it may be favorable to form domains with the largest ratio of enclosed domain area to circumference. This behavior can be understood by considering the domain wall energy density which can be minimized in this way. The result is the formation of bubble domains, confer section 6.3.3. The field at which the bubble domain state becomes energetically more favorable is theoretically determined to be $h_{\mathrm{S,B}} = 0.545 \cdot h_{c,u}$. Beyond $h_{c,u}$ the system prefers the mono domain state. Fig. 7.24 shows the formation of bubble domains while applying a perpendicular magnetic field. In Fig. 7.24 c) the evolution of the out-of-plane as well as the in-plane magnetization in the vicinity of the SRT is shown. The sample was a stepped wedge sample where all images are taken in a region with strongly increasing thickness at a thickness step. Fig. 7.24 b) summarizes the observed pattern. The image with the highest applied magnetic field value, which was -4.88 Oe (shown in Fig. 7.24 a) right), also exhibits some bubble domains in a very narrow region. Hence, the field value $h_{c,u}$, at which the transition to the mono domain state occurs, has not been reached. Note, that the residual field (∼0.7-0.9 Oe) in the PEEM chamber has not been taken into account. Unfortunately, due to the strong intermixing of both patterns, i.e. stripes and bubbles, the determination of the critical field values $h_{\mathrm{S,B}}$ (stripe to bubble transition) is not very accurate. Fig. 7.25 a) shows the same phase diagram as Fig. 7.24 b), however with interchanged axes, in order to aid comparison to plots in literature [131, 157]. The hatched area represents the bubble domain state. The maximum applied magnetic field of $|-4.88(+0.8)|$ Oe, at which bubble domains are measured (see Fig. 7.24), is also taken into account (the value in parenthesis is the residual field of the PEEM chamber). The main result from this phase diagram is, that the bubble domain pattern is limited to a narrow region with respect to the distance

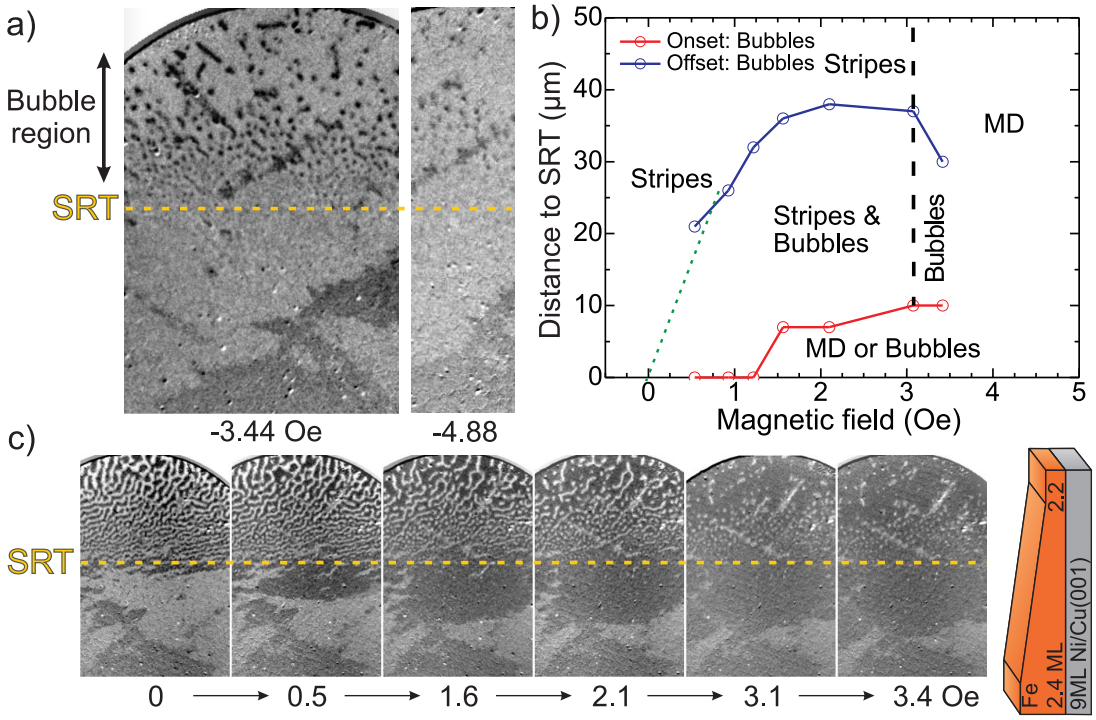

Figure 7.24: *a) shows the domain pattern with a clear formation of bubbles in a narrow region at an applied magnetic field of -3.44 Oe and -4.88 Oe* (FOV *a) left and c)* $63 \times 93 \mu m^2$). *b) summarizes the observed domain pattern with respect to the applied magnetic field and distance to the SRT. A bubble domain state without any stripe is only reached above 3.1 Oe. Below the red line either the resolution with an applied magnetic field is to low or the system is in a mono domain state. c) shows the evolution of the domain pattern in the vicinity of the SRT. Note, that even the domains in the in-plane region (lower part) change. The thickness is assumed to increase linearly from top to bottom by about 0.2 ML within a distance of* $\sim 110\,\mu$m, *as described in section 7.1.2.*

to the SRT. This behavior is in contrast to the phase diagram presented in the theory part (Fig. 6.8), which is a combination of the theoretically found stripe domain evolution (e.g. Abanov [1]) and the experimentally measured stripe and bubble domain region by Saratz [131]. In addition, due to the limitation of the bubble phase to a small region in the phase diagram, the stripe-to-bubble magnetic field $h_{\mathrm{S,B}}$ must have an additional thickness dependent parameter. Recently, Cannas et al. [157] could show by simulations that the region of bubble domains occupies only a narrow region in the phase diagram near $T_{\mathrm{c,u}}$, where $T_{\mathrm{c,u}}$ is the critical temperature at which the uniform solution becomes unstable. The main result of this simulation is shown in Fig. 7.25 b). These authors

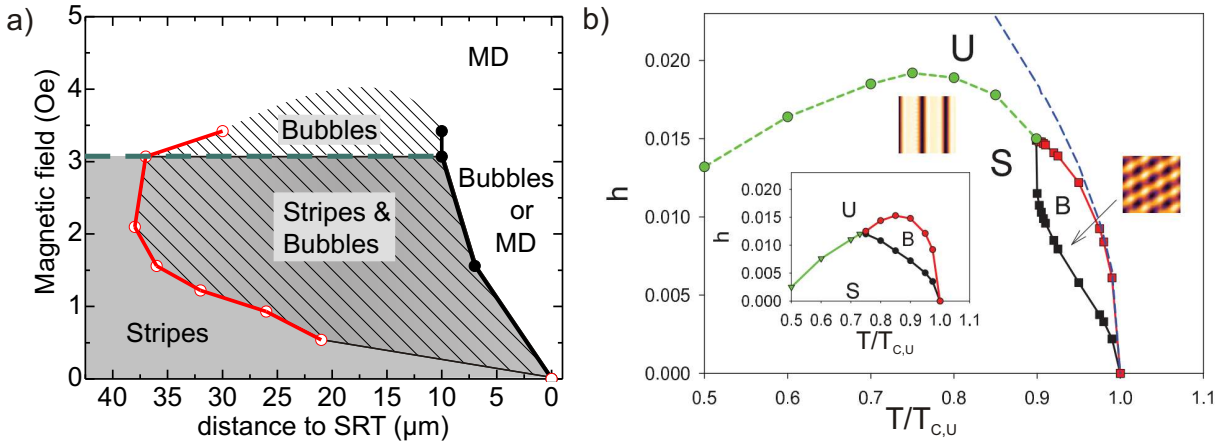

Figure 7.25: *a) The stripe-bubble phase diagram with respect to applied magnetic field and distance to the SRT is shown, extracted from Fig. 7.24 b). Cannas et al. [157] showed a comparable phase diagram, as depicted in b), taken from [157]. The large plot shows the calculation results for the three-mode approximation of the magnetization profile and the inset for the single-mode approximation, where $T_{\mathrm{c,u}}$ is the critical temperature at which the uniform solution becomes unstable. In this plot U=MD, S=Stripes, B=Bubbles and h is the applied magnetic field.*

considered a mean-field model described by the Landau-Ginzburg[7] free energy for an out-of-plane magnetized system. For the simulation the Fourier expansion of the scalar field representing the out-of-plane magnetization density was truncated after the first harmonic (single-mode approximation) or after the third harmonic (third-mode approximation). The difference between these two modes can be seen in Fig. 7.25 b). These calculations already show the existence of different phases while applying a magnetic field and range from uniform to stripes as well as bubble domains. In the three-mode approximation the bubble domain phase (B) exists only in a very small region close to the SRT. The temperature range of the bubble phase covers only 10 % of the temperature range given in reduced temperatures $T/T_{\mathrm{c,u}}$. The broad peak in the phase diagram is mainly covered by the stripe domain phase (S). In the single-mode approximation (inset in Fig. 7.25 b)) the bubble domain phase covers a much larger area in this phase diagram. The bubble domain phase is still only observable in the vicinity of the SRT, but covers about $\sim$30 % of the temperature range and is more stable at higher magnetic fields in the region of the

[7]The Landau-Ginzburg free energy reads

$$F[\phi] = \frac{1}{2}\int \mathrm{d}^2\mathbf{x}\left[[\nabla\phi(\mathbf{x})]^2 + r_0\phi^2(\mathbf{x}) + \frac{u}{2}\phi^4(\mathbf{x})\right] + \frac{1}{2\delta}\int \mathrm{d}^2\mathbf{x}\int \mathrm{d}^2\mathbf{x}'\phi(\mathbf{x})\phi(\mathbf{x}')J'(|\mathbf{x}-\mathbf{x}'|) - \int \mathrm{d}^2\mathbf{x}h(\mathbf{x})\phi(\mathbf{x})\,, \tag{7.9}$$

where $\phi(\mathbf{x})$ is a scalar field and represents the out-of-plane magnetization density, and J' may represent the dipolar interaction [157], and $r_0 \sim T - T_C$.

SRT than the stripe domain phase. The rough phase diagram measured within this thesis, Fig. 7.25 a), is better described by the single-mode result. However, due to the unknown evolution of the stripe domain phase with applied magnetic field and decreasing effective temperature or increasing distance to the SRT an unambiguous assignment to one of these approximations cannot be done.

7.5 Thermal Fluctuations of Domain Walls

Thermal energy is the driving force for phase transitions. The direct consequence of thermal energy are fluctuations expressed by the constituents of the system. These thermal fluctuations are random, statistical processes and range in the case of a ferromagnetic system from ultra fast femtosecond single spin fluctuations to large scale fluctuations of domain walls which can reach time scales even of years [166]. The observation of domain fluctuations has previously only been achieved indirectly by monitoring average quantities such as the ac-susceptibility [169,170]. So far in microscopic imaging techniques fluctuations in 2D systems have only appeared as blurry regions, or have been evidenced by changes of the domain pattern between individual linescans in scanning microscopy [3,130,137,171,172]. Due to the statistical character of thermal fluctuations a stroboscopic measurement technique is not useful for the investigation of thermal fluctuations. The experimental method used in this thesis allows a fast image acquisition as well as the recording of non-stroboscopic real time movies of fluctuating domains. In the following results on thermal fluctuations of domain walls for the system Fe/Ni/Cu(001) will be presented.

Before explaining the methods for the evaluation of fluctuations, a few technical comments will be made. As mentioned in the introductory section 1.2, two camera systems are used in this thesis. Both cameras are able to record image sequences with predefined exposure times as well as frame rates. In the case of the low noise, high sensitivity camera the exposure time is usually set to 11-12 ms, while the acquisition of a single image takes ~ 61 ms. This results in a maximum frame rate of 16.4 fps (frames per second). In the case of the high-speed camera, the exposure time is set to maximum which means that it is determined by the frame rate. The frame rate (FR) can be as high as 2200 fps at full resolution (1280×800 pixels). At reduced resolution it can reach up to 80000 fps (128×8 pixels). However, the present fluorescence screen limits the maximum frame rate to about 2000-5000 fps (depending on the magnetic contrast as well as the brightness of the image). This is due to the decay time or afterglow of the fluorescence screen, which was measured to be ~ 0.47 ms, where the intensity has reached 1/e of the maximum value, shown in Fig. 7.22.

7.5.1 Method: Determination of Domain Wall Motion

In order to extract fluctuations of individual domains, in the sense of tracing the motion of domain walls, the following procedure is used. Due to vibrations in the experimental setup, the individual images of the recorded movie have to be realigned. This is achieved by spatial autocorrelation using features which are constant in time such as defects or dust particles on the sample surface. The next step is the domain wall identification by an edge detection algorithm (Matlab)[8]. An example image of the result of this edge

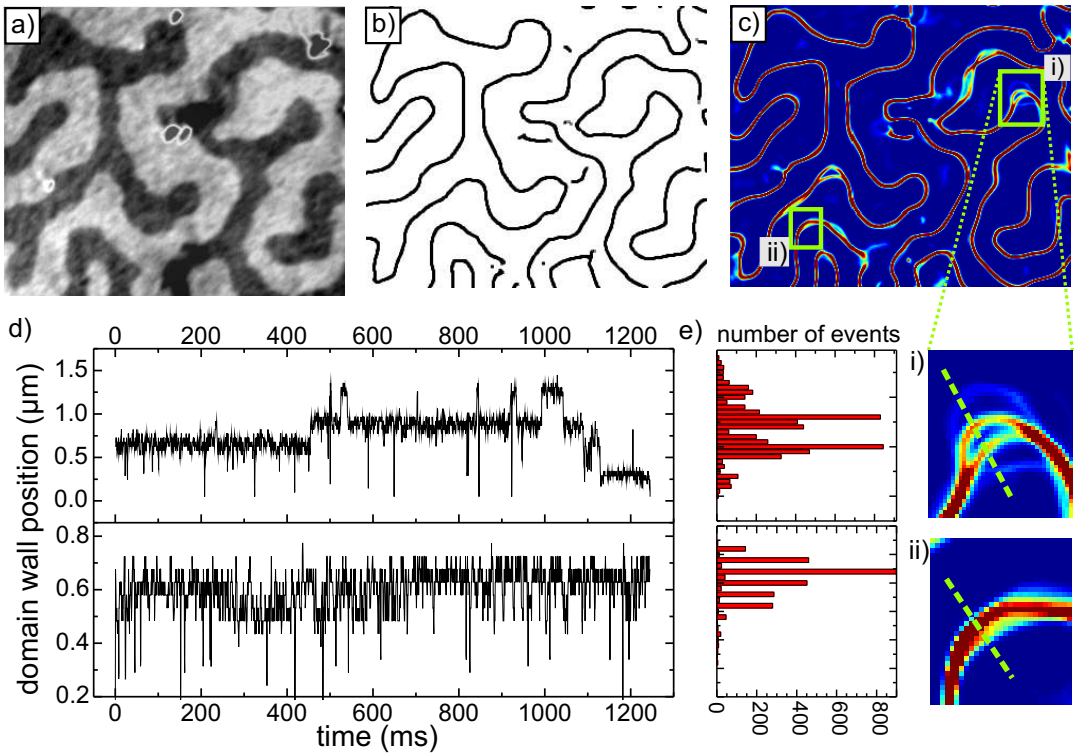

Figure 7.26: *The method to extract the domain wall motion from a sequence of images, such as shown in a), comprises the realignment of the images as well as the domain wall identification, shown in b). The summation of all domain wall images (2738) reveals regions in the domain pattern exhibiting large fluctuations, as shown in c). The time evolution of the individual domain walls can then be extracted by linescans across domain walls for all chronologically ordered images, as shown in d). In case that the algorithm for the domain wall identification has failed, a spike in the graph appears. e) shows histograms of the occupation of the different positions of the domain walls.* (FOV : $15.4 \times 12.8\mu$m, FR = 2200fps, T = 21°C.)

[8]This algorithm determines any edges in a gray scale image with a predefined increase in intensity. In addition, the range of the radius at each point of this edge can be defined, which significantly reduces the

detection algorithm is shown in Fig. 7.26 b), which comprises solely the domain walls from Fig. 7.26 a) and will therefore be called the domain wall image in the following. The summation of all these domain wall images, as shown in Fig. 7.26 c), reveals domain regions exhibiting fluctuations and regions of domain walls which are constant in time (as far as the resolution and measurement duration are concerned). The temporal evolution of an individual domain wall can then be extracted by linescans across the interesting domain wall of interest performed for all images in chronological order, as shown in Fig. 7.26 d). As can be seen in the upper plot of Fig. 7.26 d) which shows the temporal evolution of the domain wall depicted in the inset of Fig. 7.26 i), the domain wall is trapped in only four positions. This means, that the local energy landscape comprises four minima. In this measurement the pixel separation of the camera corresponds to a distance of $\sim 48\,\mathrm{nm}$ on the sample. The resolution in these images was about 70-100 nm measured at different domain walls. Note, that in the lower panel of Fig. 7.26 d) the fluctuations of the domain wall are mainly between two states, very close in distance.

7.5.2 Method: Evaluation of Domain Pattern Fluctuations

Another way to evaluate the observed fluctuations is to calculate the local change of the domain area and register the time the fluctuating area remains in the new state before it jumps back into its original configuration or into a new state. The change in the area has to be larger than a predefined value, given by a certain amount of pixels (usually less than 15 pixels). This parameter depends, for instance, on the resolution of the images or the magnetic contrast. In addition, if the fluctuation occurs in such a fashion that the area stays constant in size but shifts in position by more than a few pixels (usually $\sim\pm 5$ pixels), then this state is also assumed to be a new state. The reference image was usually the first image of the sequence.

noise and increases the accuracy of this algorithm.

7.6 Fluctuations of Individual Topological Defects

In the previous sections, it was shown that the transformation of domain patterns is driven by thermal fluctuations. In the following, fluctuations of individual defects (A, C and D) will be investigated in detail. Further, the influence of geometrical constraints on the individual defects given by the surrounding domains will be investigated. In general, the constraints reduce the mobility of domains and may also reduce the degrees of freedoms for fluctuations of defects. In many cases the geometrical constraints induce a high density of domain states with nearly equal energy and thereby initiate fluctuations. An example for a domain state with a large amount of topological defects exhibiting large fluctuations is presented in Fig. 7.27. Fig. 7.27 a) shows a domain pattern close to the SRT with an average domain width of $\sim 800\,\mathrm{nm}$. In the summarized image (shown in Fig. 7.27 c)) of all domain wall images (Fig. 7.27 b)) the stationary domain walls appear in yellow color.

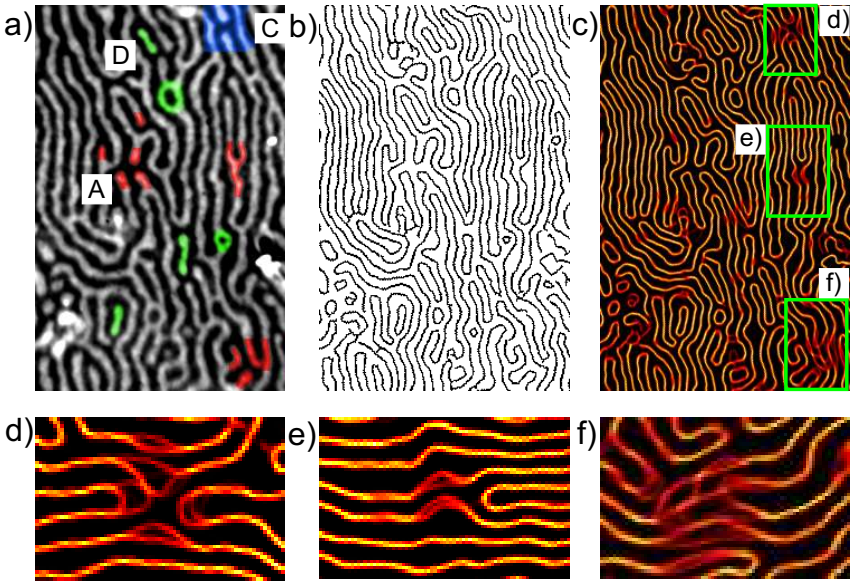

Figure 7.27: *In a) the domain pattern close to the SRT is shown with an equilibrium domain width of* $w_D \approx 800\,\mathrm{nm}$. *The Fe/(9ML)Ni/Cu(001) sample has a Fe thickness slope of 0.33* $\frac{\mathrm{ML}}{\mathrm{mm}}$. *Some A-defects are highlighted in red, D-defects in green, and a C-defect is colored in blue. A domain wall image is shown in b). The summarized image (of 2738 domain wall images), shown in c), reveals areas with fluctuating domain walls. d) shows a region with fluctuating domain walls for a C-defect, for an A-defect this is shown in e) and for a state with multiple A-defects in f). Images d)-f) are rotated by 90°.* (FOV : *a)-c)* $39.8 \times 25.8\mu\mathrm{m}$, *d)* $7.9 \times 5.2\mu\mathrm{m}$, *e)-f)* $9.1 \times 5.9\mu\mathrm{m}$, FR = 200fps, T =21°C.)

This means that the positions of these domain walls are constant in time. Red colored domain walls indicate a reduced occupation of this position in time, and hence, indicate a fluctuating domain wall. In d) the fluctuation profile of a C-defect is shown, in e) of an A-defect and in f) of a complicated case of many A-defects. In the following some fluctuating domain walls will be examined in detail.

7.6.1 Proliferation of A-Defects

The proliferation of defects is the key element of pattern transformations. The direct observation by resolving each individual step in time has not been achieved so far. The reversed process, i.e. the reduction of finger domains (A-defects), was shown in section 7.3.2 in the context of the inverse heating process using a time resolution of only 6.1 s (since only each one hundredths image has been investigated). A first example of a proliferation of an A-defect is shown in Fig. 7.28. This A-defect fluctuation is extracted from the domain structure presented in Fig. 7.27, where the sample had a thickness slope of 0.33 $\frac{\text{ML}}{\text{mm}}$. Since the effective temperature in this measurement was close to the effective SRT-temperature, the average domain width is around $\sim 800\,\text{nm}$. The images in Fig. 7.28 a) show both the enlargement of the A-defect colored in blue and the reduction of another A-defect colored

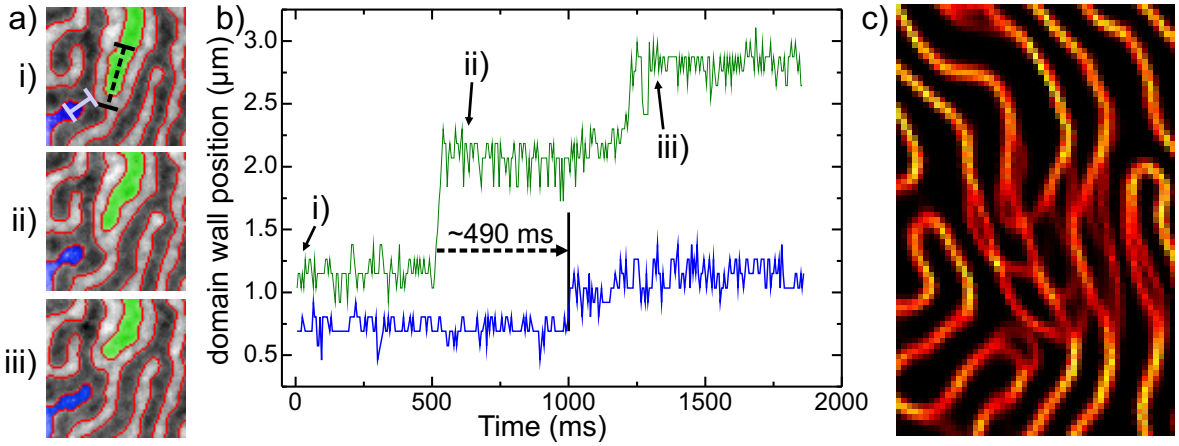

Figure 7.28: *The sample and the measurement position is the same as shown in Fig. 7.27 (a) and f)). This measurement shows the proliferation (blue-colored) and reduction (green-colored) of two A-type defects, as shown in a). The lines, as depicted in the first image in a), represent the linescan regions (black dashed line for the green curve in b) and white line for the blue line in b)). c) shows the summarized image of all (2738) domain wall images.* (FOV : *a)* $7.9 \times 7.9\mu\text{m}$, *c)* $9.1 \times 5.9\mu\text{m}$, FR = 200fps, T = 21°C)

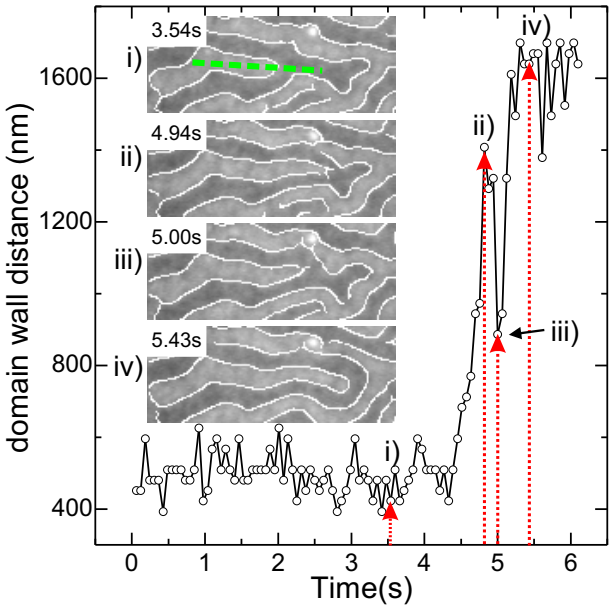

Figure 7.29: *The proliferation of this A-defect is not unidirectional. The white dot in the center part of all images is a large defect. The Fe-thickness slope in this measurement was 2.1* $\frac{\text{ML}}{\text{mm}}$ *and the Ni-layer was not annealed. The red dotted arrows mark the temporal position of the images i)-iv).* (FOV : $4.2 \times 1.6\mu$m, FR = 16.4fps, T = 21°C)

in green. In fact, the reduction of the green domain triggered the proliferation of the blue domain (although the growth is very small). The relaxation time, i.e. the time delay for the response of the blue domain, however, is about ~ 490 ms. Within this time period the black and white domains between the blue and green colored domains remain fixed with an enlarged domain width. This unfavorable larger domain width acts as the driving force for the proliferation of the blue domain.

The measurement in Fig. 7.29 shows another proliferation of an A-defect and was observed on a different sample. In this case the Ni layer was not annealed and the Fe-thickness slope was 2.1 $\frac{\text{ML}}{\text{mm}}$. For images i)-iv) the Fe-thickness increases from left to right by about 0.008 ML leading already to a recognizable change in the domain width from left ($\sim 0.34\,\mu$m) to right ($\sim 0.25\,\mu$m). The linescan used for tracing the domain wall is marked in image i) by the green dashed line. Even with the rather slow frame rate of 16.4 fps, individual steps of the proliferation can be recognized, as can be seen by the measured domain wall positions at the rising edge from 4.4 s to 4.94 s. This rather slow dynamics may be caused by the strong corrugation of the energy landscape. The unannealed Ni layer probably leads to a strong enhancement of the individual relaxation times. In addition, the growth of this finger domain is not unidirectional, which can be seen by the reversed direction of proliferation within the time duration from 4.94 s to 5.00 s. The temperature was constant during this measurement, whereas a certain heat input is always given by the illumination unit, but has led to no measurable increase in temperature, i.e. was less than 1 K.

7.6.2 Local Non-Equilibrium State

A single A-defect within a region comprising only stripe domains aligned in parallel (smectic phase) inevitably leads to a localized increase of the domain width of domains in the vicinity of this A-defect. Such a domain configuration can induce fluctuations, either of the A-defect or of the neighboring domains. In the following example of a smectic phase with a single A-defect, see Fig. 7.30 a) or b), the white domain in the center of the image is affected. The overall domain structure can be seen in Fig. 7.27, where this defect was

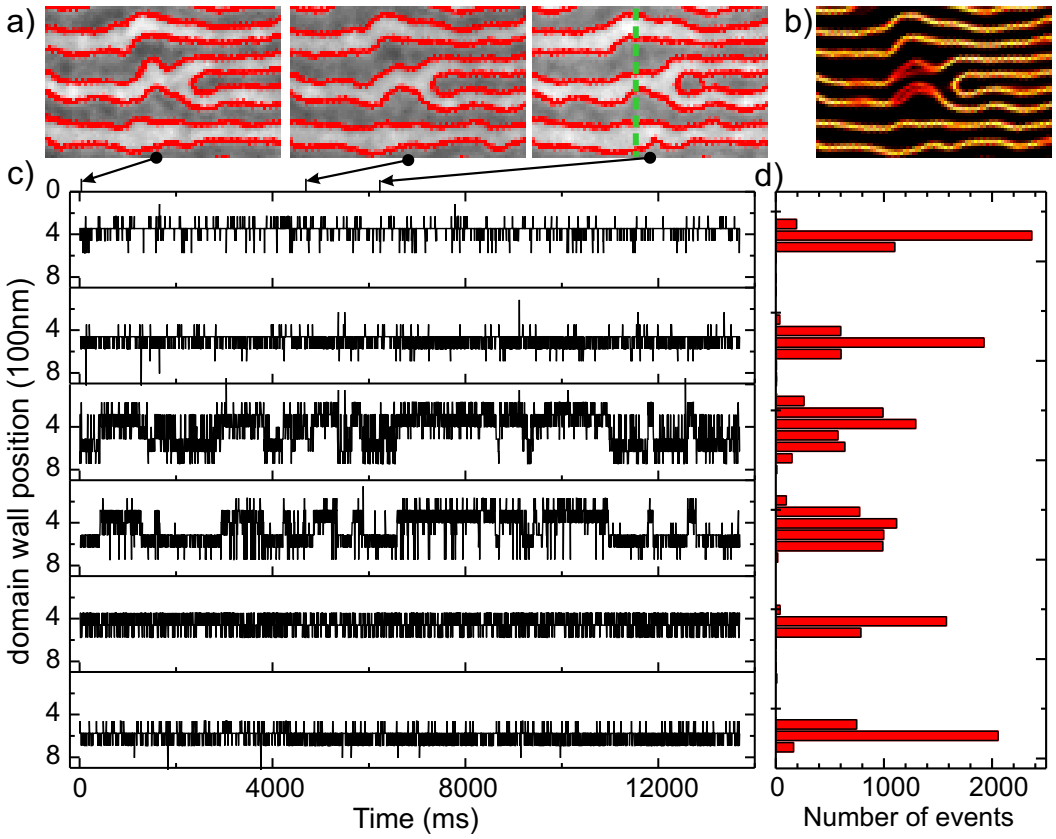

Figure 7.30: *A single A-defect within a smectic phase (average domain width* $w_D \approx 800\,nm$*), may induce a frustrated situation due to the local increase of the domain width of the neighboring domains. In a) snapshots of the different domain wall positions are shown. b) shows the summarized image. c) shows the temporal evolution of the six domain walls along the green dashed line, shown in a). d) shows the histograms of the individual positions for each linescan. The sample is the same as shown in Fig. 7.28, i.e. the Ni layer was annealed and the Fe-thickness slope is* $0.33\,\frac{ML}{mm}$. (FOV: *a) and b)* $9.1 \times 5.9\mu m$, FR = 200fps, T = 21°C)

already shown as inset labeled e). As can be seen in Fig. 7.30 c) only the domain walls which terminates the white domain in the center exhibit fluctuations. The reason why only this white domain exhibits fluctuations is complicated.

To a large extent the pinning of the surrounding domains (either by structural defects or by geometrical constraints due to the neighboring domains) is responsible for the induced fluctuations. Furthermore, the small residual field of $\sim 0.7\,\mathrm{Oe}$ within the PEEM chamber, which can be recognized by the larger domain width of the black domains, plays the decisive role in this case. Due to the presence of this weak residual magnetic field, the symmetry of the compression constants is broken, leading to a higher compression constant for the white domains than for the black domains, see Eq. (6.31). Hence, the white domains show a larger rigidity with respect to the domain width than the black domains. This, however, makes the white domains susceptible for undulations (transverse instability). In addition, a local increase of the domain width of the black domains is induced by the A-defect, keeping the black domains in a non-equilibrium state. The combination of this artificially induced local broadening of the black domains in the vicinity of the A-defect, and the unequal compression constants cause the undulation of the white domain in the center, since in this case either of the black domains becomes narrower. However, this requires an increase in the domain width of the other black domain. The driving force for fluctuations is therefore the induced non-equilibrium state of the neighboring black domains due to an alternating increase and reduction of their domain width, respectively, while the domain width of the white domain in between remains nearly constant (due to the higher compression constant).

7.6.3 C-type Defect

A C-defect has two main possibilities for fluctuations. The first one is a synchronous translation of the bridge, which means that the two endings move simultaneously in the same direction. The other possibility is the opening of the gap between the endings, i.e. one or both endings move away from each other. However, the latter requires that the surrounding domains take part in this pattern transformation process, since otherwise the domain width of the domain between the two endings increases in size. Hence, the propensity of the system to keep the domain width as constant as possible is thereby satisfied. This is also the reason for the synchronous movement of the two endings in the former case and is also responsible for the fluctuations in the measurement shown in Fig. 7.30.

In this thesis both fluctuation types of C-defects have been observed. The synchronous,

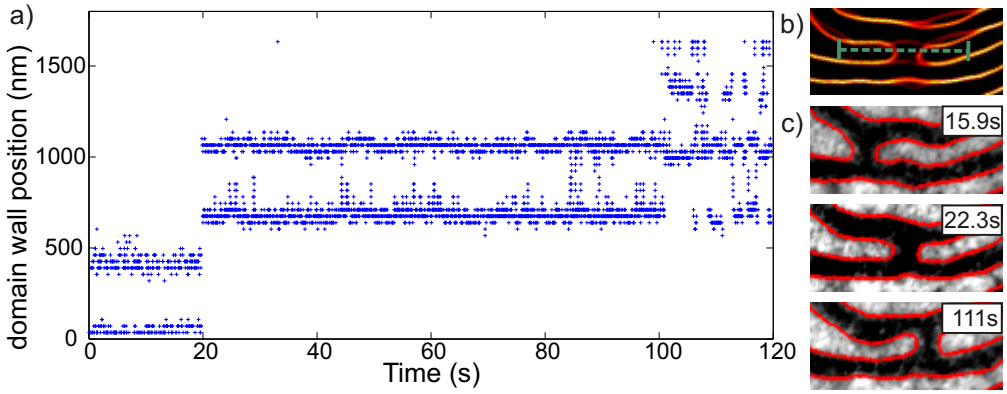

Figure 7.31: *The synchronous, in-phase fluctuation of the two endings of a C-defect is presented for a smectic domain pattern with an equilibrium domain width of* $w_D \approx 400\,nm$. *a) shows the result of the temporal evolution of the linescan across both domain endings, as shown by the green dashed line in b). The domain width of the black domain is kept constant. Beyond* $\sim 100\,s$ *the fluctuations are to rapid to be resolved. b) shows again the summarized image of all domain wall images. Snapshots of the individual positions are shown in c).* (FOV : *b)-c)* $3.5 \times 1.6\mu m$, FR = 16.4fps, T = 21°C)

translational fluctuation of the bridge is shown in Fig. 7.31. The sample was the same as in Fig. 7.27 but the investigated region was even closer to the SRT, which leads to a domain width of $w_D \approx 400\,nm$. Tracing the domain walls, as plotted in Fig. 7.31 a), shows that the domain width (in this case of the black domain) remains almost constant. Beyond $\sim 100\,s$ the fluctuations are too fast to be resolved. The other possibility for fluctuations of a C-defect is presented in Fig. 7.32. In this case the motion of the two domain endings of the C-defect occurs in opposite directions. Hence, the black domain between these two endings becomes larger. As a result the surrounding, initially straight domains have to bend. As can be seen from Fig. 7.32 b), all four domain walls move (jump). The red dotted lines mark the two jumps of the left domain ending, which seems to be the trigger event for the domain transformation. Due to the rather high frame rate of 200 fps, a delayed response of the individual participants is revealed as shown in Fig. 7.32 c). This magnified view shows the region around the second jump of the left domain ending. The rather large delay times may be caused by the unfavorable 'final' domain state of the stripe domains, since the undulated state is energetically not very favorable. It is surprising that the left domain can perform this thermal fluctuation without an immediate relaxation. Again the motion occurs in well defined steps. In combination with the delayed response, these individual steps are an indication for the high density of different, energetically nearly equal states. Summarizing, this example again indicates the complexity of the dynamic process of domain pattern transformations.

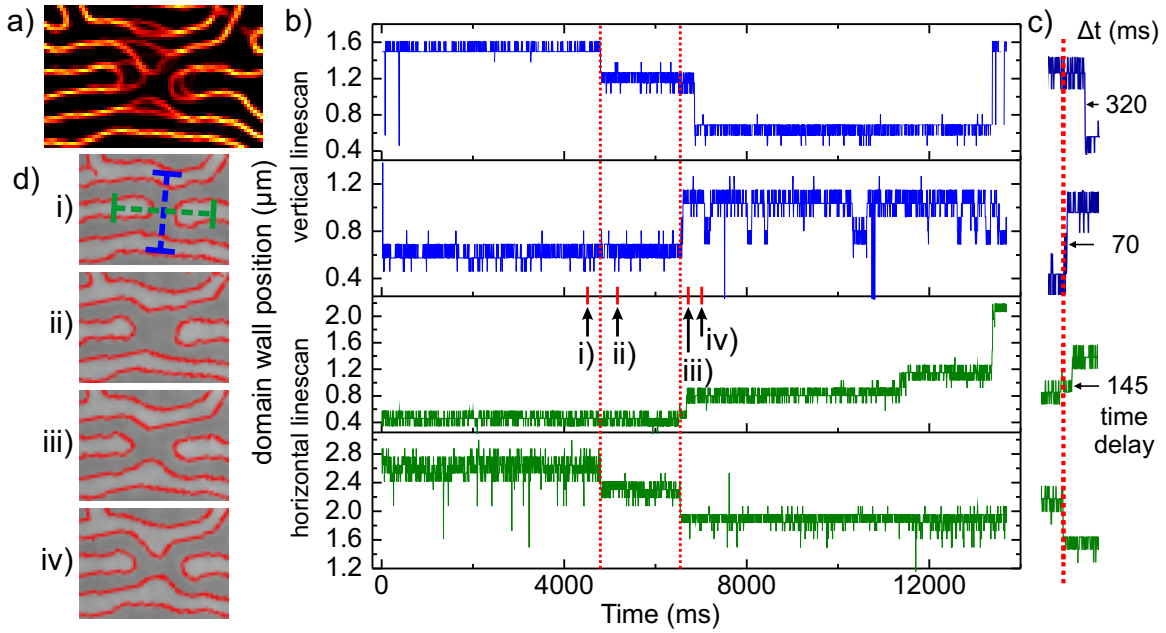

Figure 7.32: *The second possibility for fluctuations of a C-defect is presented. a) shows the summarized image. The temporal evolution of the domain walls along the blue, dashed line in a), is shown in the upper two panels in b). For the green, dashed line, this is shown in the lower panels, which represent the fluctuations of the domain endings, i.e. the C-defect. The red dashed lines mark the jumps of the left domain ending. c) shows the linescan region in the vicinity of the second jump of the left domain ending. Snapshots of the individual stages are presented in d).* (FOV *a)* $7.9 \times 5.2\mu$m, *d)* $6.7 \times 4.9\mu$m, FR = 200fps, T = 21°C)

7.6.4 Transverse Instability

The transverse instability [132] leads to longitudinal excitations in a stripe forming system[9]. The evolution of disorder and thereby the transformation of a smectic-like structure by increasing the effective temperature can be initiated by a sequence of transverse instabilities [132]. According to theory, section 6.3.5, the smectic phase exhibits either a Kosterlitz-Thouless transition into the nematic phase or a first order transition into the tetragonal liquid phase. The existence of the Ising nematic phase depends on the ratio between the exchange and dipolar energy parameters. In addition, in case that the Ising nematic phase occurs the transition from the Ising nematic into the tetragonal liquid phase is of second order. In Fig. 7.33 the transformation of a domain pattern with parallel aligned stripes due to an increase in temperature is shown. This domain pattern

[9]Even in dunes this kind of excitation has recently been found, see [173].

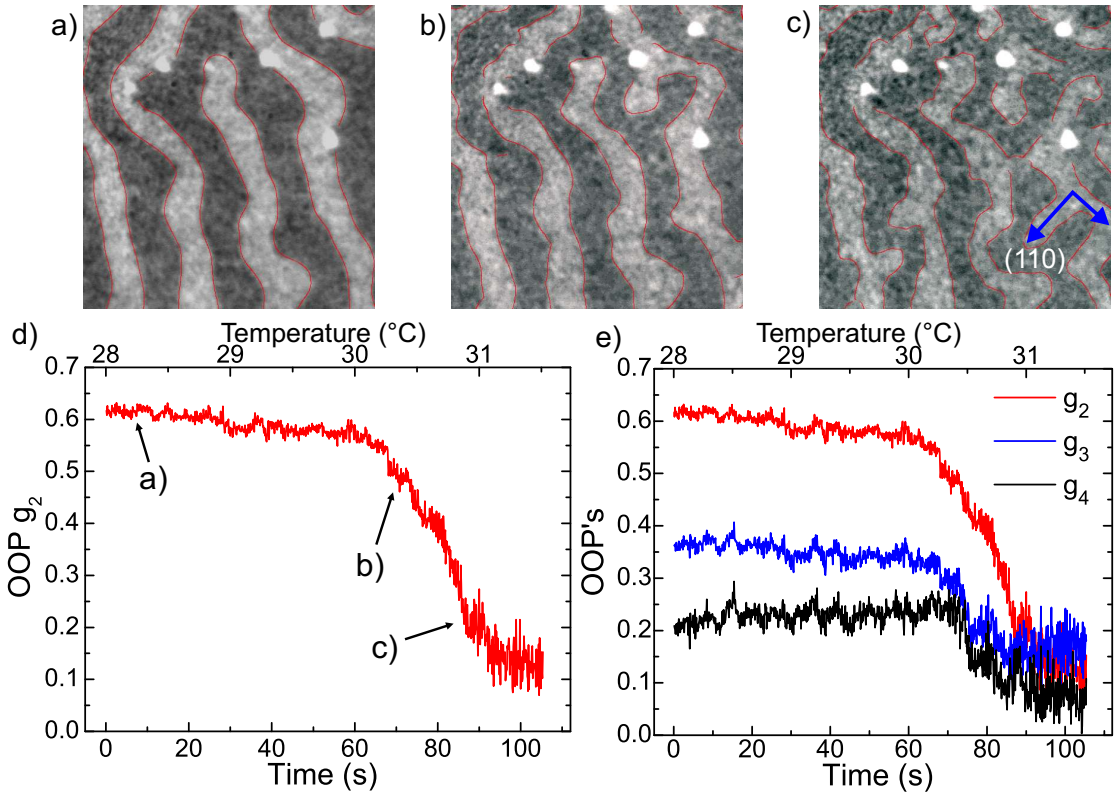

Figure 7.33: *a)-c) shows the transformation of stripe domains due to an increase in temperature. The crystallographic axis (110) is shown in image c). d) shows the evolution of the OOP g_2 for this transformation. e) shows the same as d) but for the OOP's g_n with $n = 2, 3, 4$.* (FOV: *a)-c)* $14.4 \times 15 \mu m$, FR = 9fps)

was surrounded by a mainly disordered stripe domain pattern on a stepped-wedge sample Fe/Ni/Cu(001), where again the Ni layer was not annealed and the Fe thickness was constant for this measurement. Increasing the temperature has led to a reduction of the domain width from w_D =(1.8-2.2) μm at 28°C to w_D =(1.4-1.6) μm at 31°C. The images in Fig. 7.33 a)-c) show, that the initially, more or less parallel aligned stripes undulate and small fingers, i.e. A-defects, emerge at some points. However, the transformation of the stripe domains is always initiated by transverse excitations, i.e. bending of a stripe domain in perpendicular direction to the stripe orientation (undulation). Note, that the initial stripes already show large corrugations and undulations, which can be attributed to the roughness of the unannealed Ni layer.

The A-defects and kink-like bendings in Fig. 7.33 c) form quite obvious, right-angled corners. Remarkable is the orientation of these excitations with respect to the crystallographic axes, as depicted in Fig. 7.33 c). Note that the (110) axis is the magnetic easy axis for Ni

thin films. The 90° orientation may be due to the formation of a tetragonal liquid or Ising nematic phase. A clear assignment is, however, not possible due to the small amount of stripes within this section of the sample. The direction of the A-defects enclose a rather broad range of angles from 30° to 60° with the initial stripes. Despite the small statistics, the evolution of the disorder is further investigated with the aid of the orientational order parameters g_n, here presented for $n = 2, 3, 4$, as shown in Fig. 7.33 d) and e). The assumption of a linear increase of temperature with time (in this range of temperatures) is justified due to the measured time dependence of the temperature rise by a constant heating power, as shown in Fig. 7.19 b), where the same heating power has been used. The second order OOP g_2 exhibits a rather flat decrease until an acquisition time of $\sim 60\,\mathrm{s}$, as plotted in Fig. 7.33 d). At this point a transverse bending occurred of the right domain in Fig. 7.33 a). At around $\sim 70\,\mathrm{s}$ an A-defect emerged from the undulated domain, which is shown in Fig. 7.33 b), top right.

In case that the initial phase can be regarded as a smectic phase, and the final phase belongs either to the tetragonal liquid or to the Ising nematic phase, the continuous evolution of the OOP means that this transition cannot be of first order. As predicted by theory, a second order phase transition occurs only from the Ising nematic to the tetragonal liquid phase. Hence, the assumption of an initial smectic phase may be incorrect. In the case of a second order transition, a power law fit may reveal the critical exponent and thereby indicates the kind of model required for this system. In doing so, we obtain a critical exponent of $\beta \approx 0.51 \pm 0.03$ if only the evolution beyond $\sim 60\,\mathrm{s}$ is taken into account. Taken into account the whole evolution the fit results in $\beta \approx 0.18 \pm 0.01$, where in both cases the critical temperature was fixed artificially to 30.9°C. The first value would correspond well to the classical Landau, i.e. mean-field, model and the second one corresponds to the 2D-Ising model, since it is close to $\frac{1}{8}$. These findings indicate a second order transition but due to the small statistics an unambiguous determination of the critical exponent is not possible.

In the analysis also higher order OOP's are considered. Remarkable is the slightly larger third order OOP g_3 compared to the value of g_2 at the end of Fig. 7.33 e). This is due to the orientation of the transverse perpendicular bending and the additional finger domains with respect to the initial domain orientation direction. As mentioned before, the excitations (transverse bending and A-defects) and the initial orientation form angles between 30° to 60°.

7.7 Area and Dwell Time Analysis of Fluctuations

7.7.1 Fluctuation Dependence on the Domain Width: SM phase

In this section the dependence of fluctuations on the domain width is investigated, in particular for a smectic phase exhibiting various topological defects. The following measurements were conducted on a single sample with a Fe thickness slope of 0.33 $\frac{\mathrm{ML}}{\mathrm{mm}}$. Three smectic phases with different domain widths ($\sim$400 nm, $\sim$800 nm, and $\sim$2060 nm) were observed on this sample, and are depicted in Fig. 7.34 a). The temperature was in all cases the same, i.e. room temperature. The procedure to evaluate the observed fluctuations is described in section 7.5.2. The parameters of interest are the changed domain area for each single fluctuation event as well as the dwell time of the system in each individual state. Note, that each change in the domain state is recorded as along as the change in the domain area or the movement of the changed area is larger than a predefined value which depends on the FOV, the resolution as well as the magnetic contrast, confer 7.5.2.

In Fig. 7.34 b) the result of the evaluation for a smectic domain phase with $w_{\mathrm{D}} \approx 400\,\mathrm{nm}$, $w_{\mathrm{D}} \approx 800\,\mathrm{nm}$ and $w_{\mathrm{D}} \approx 2060\,\mathrm{nm}$ is presented. Note, that each single point in the evaluation plots (Fig. 7.34 b)) represents a change in the domain state. Further note, that the amount of fluctuations is rather large, as can be seen by both the colors and the corresponding values as well as the high density of points. The maximum z-value changes from plot to plot. In addition, due to the individual FOV's the minimum value for the recorded change in the domain area increases with domain width. Further, again due to the different FOV's the exposure times for the different image sequences had to be changed. This is due to the fact, that the smaller the FOV, the smaller the sample section imaged onto a single pixel, the darker is the image (due to a smaller photoelectron density). Hence, the smaller the FOV, the larger the exposure time has to be, resulting in a larger minimum dwell time. Due to the limited spatial as well as temporal resolution, the occupation number as well as the fluctuation density increase for small domain areas as well as small dwell times in the plots shown in Fig. 7.34 b) and c).

The result of Fig. 7.34 b) is that the absolute fluctuating domain area increases with domain width. This shows that the effect of thermal energy, which is actually the same in all three cases, is different for different domain structures and depends on the domain width. A reason for this may be the different energy landscapes due to the effect of self-generated glassiness. Since the density of the external pinning sites such as structural defects should be the same (since these measurements are conducted on the same sample), the dependence of the energy landscape on the domain pattern, in particular on the domain

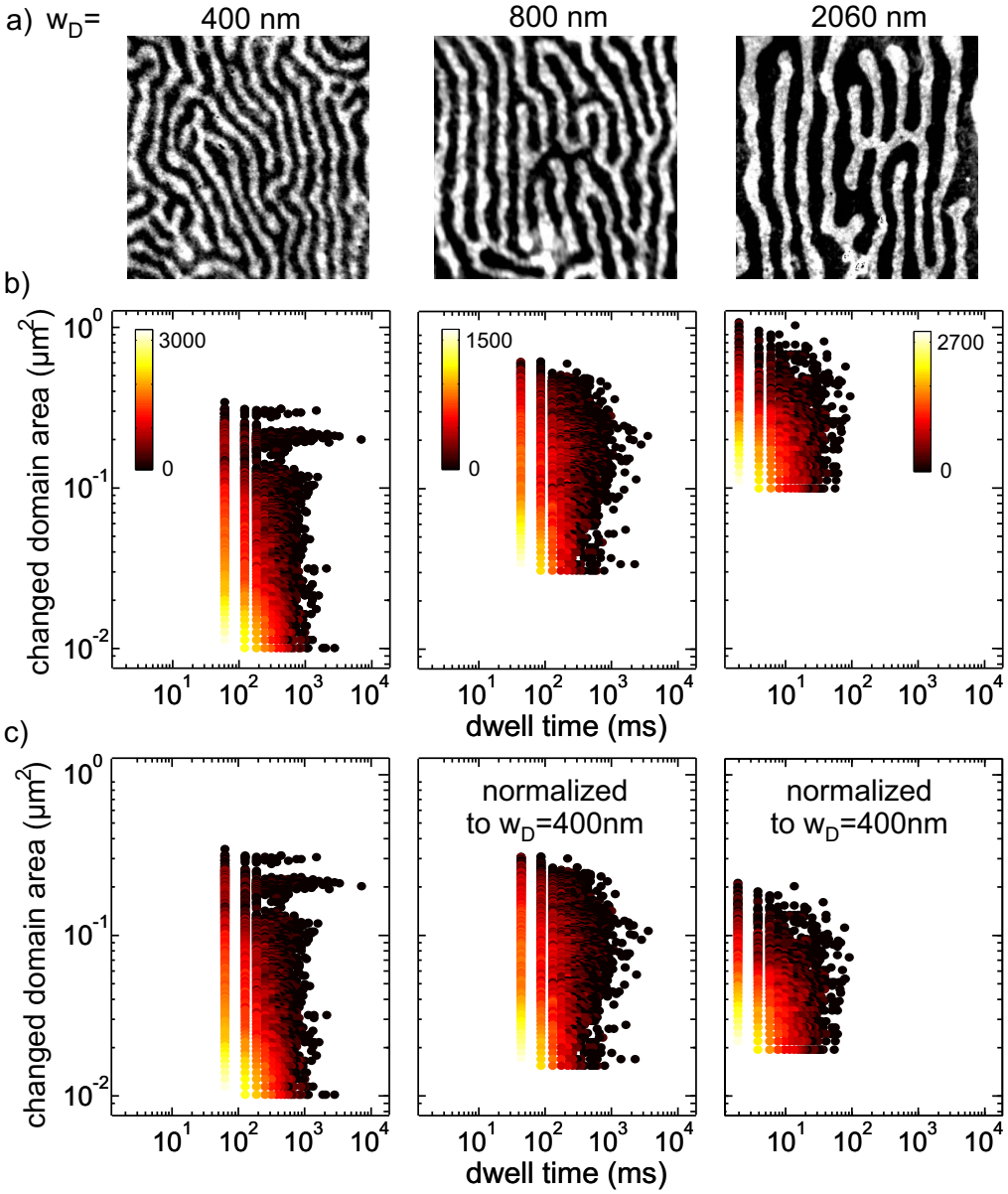

Figure 7.34: *a) shows the domain pattern with different domain widths of* $w_D \approx 400\,nm$, $w_D \approx 800\,nm$ *and* $w_D \approx 2060\,nm$. *The evaluation of the domain fluctuations with respect to changed domain area as well as dwell time is shown in b) for the individual domain patterns. The frame rates for the individual measurements were 16.4 fps, 24 fps, and 500 fps and the total recording times for the evaluations were 119 s, 114 s, and 5.48 s, respectively. c) shows the same as b) but the changed domain size is normalized to the smallest domain width, i.e.* $w_D \approx 400\,nm$. *All images are obtained by illuminating the sample with only one circularity.*

width, could lead to the formation of different metastable states with respect to energy as well as energy barriers between them. Accordingly, the fluctuation properties are different and become domain width dependent. Remarkable is the presence of the large amount of fluctuations which was unknown so far. In addition, the continuous spectrum of the fluctuations, in particular with respect to the changed domain area, indicates again a high density of different domain states. In virtue of the presented fluctuation properties of the individual defects in the previous sections, which revealed incremental fluctuations rather than continuous motions, this is surprising.

The smallest domain width even exhibits some large scale fluctuations, shown by the two peaks around $\sim 0.2\,\mu\mathrm{m}^2$ and $\sim 0.3\,\mu\mathrm{m}^2$. The changed domain area of these two peaks is in the range of the average changed domain size of the larger domains. In order to evaluate the relative strength of thermal fluctuations for the different domain patterns with respect to domain width, the data is re-scaled. Fig. 7.34 c) shows the same data as Fig. 7.34 b), but the changed domain areas for the domain widths $w_\mathrm{D} \approx 800\,\mathrm{nm}$ and $w_\mathrm{D} \approx 2060\,\mathrm{nm}$ are re-scaled to the case of $w_\mathrm{D} \approx 400\,\mathrm{nm}$. This plot reveals that the relative fluctuating domain area decreases with increasing domain width (Fig. 7.34 c)), whereas the absolute fluctuating domain area increases with increasing domain width (Fig. 7.34 b)). Thus, in average thermal energy induces larger domain wall jumps in a domain pattern with wide domains than in a narrow domain pattern. However, in relative terms, the impact of thermal energy is larger for thinner domains, which means that the strength of thermal fluctuations increases with decreasing domain width. This behavior can be addressed to the different compression constants of the domain patterns and will be further discussed below.

Since the real-space images and the locations of the individual fluctuations are available, the next step is to investigate the domain patterns for "hot spots" of fluctuations. Fig. 7.35 shows the full images of the different domain patterns. The individual fluctuations, with respect to changed domain area, position and dwell time, are cumulatively overlayed. Here the color represents the total time of a changed domain area. Note that the total acquisition time for the different image sequences are 119 s for the movie with $w_\mathrm{D} \approx 400\,\mathrm{nm}$, 114 s ($w_\mathrm{D} \approx 800\,\mathrm{nm}$), and 5.48 s ($w_\mathrm{D} \approx 2060\,\mathrm{nm}$). In accordance with the relative impact of thermal energy on the domain structure, these images also show that on average the changes of a single domain for a narrow domain structure are larger than for a broad domain structure. In contrast, the absolute change of domain areas is larger for broader domains, which is hardly recognizable in Fig. 7.34 b). What is more, the domain structure with the largest domain width shows more corrugations of the stripes rather than fluctuations of domain endings, since variations in the domain width for broad stripes are

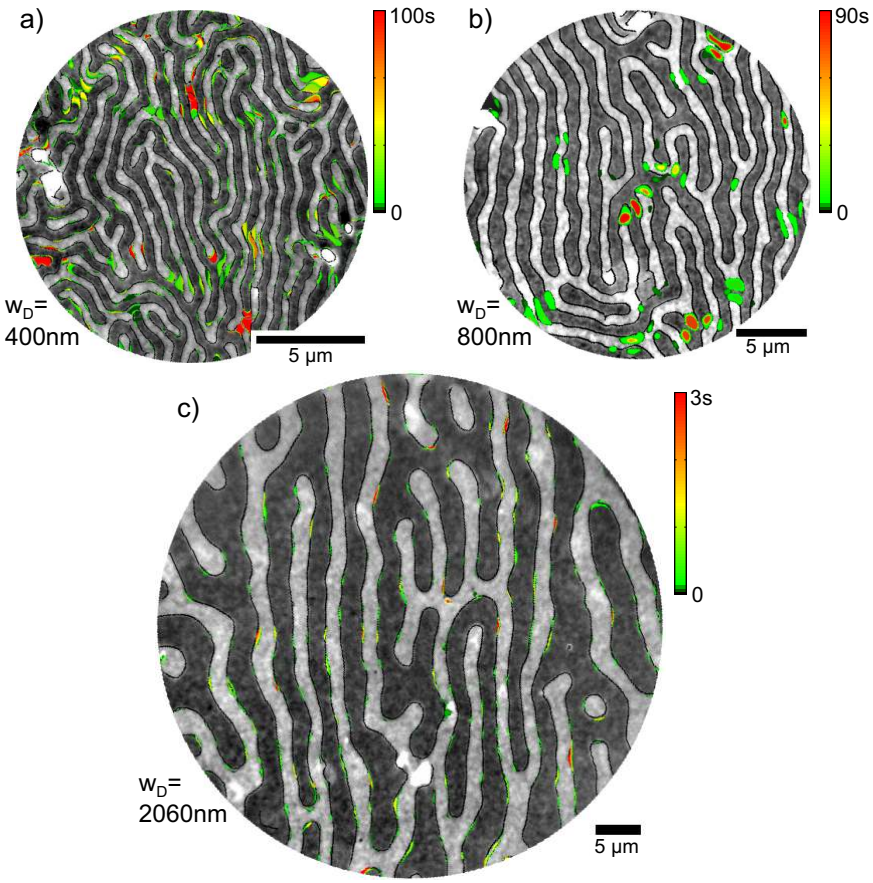

Figure 7.35: *These images show the domain patterns as well as the cumulated fluctuations in color code. The pattern with wide domains c) shows mainly corrugations, whereas the pattern with narrow domains a) exhibits mainly fluctuations of topological defects. (a)* FR = 16.4 fps*, b)* FR = 24 fps*, c)* FR = 500 fps*, recoding time: a)* 119 s*, b)* 114 s*, c)* 5.48 s)

energetically less costly than for narrow domains. In case of a narrow domain pattern, the combination of a large compression constant and a relatively stronger impact of thermal fluctuations, leads to fluctuations occurring mainly at domain endings rather than domain wall motions of straight domains walls. In addition, a few undulating domains also appear in this pattern. Here the large compression constant plays the decisive role.

According to theory [1], the proliferation of topological defects, which represents large scale fluctuations on long time scales, is the key element for any pattern transformation. Therefore the fluctuation properties of the individual topological defects (A, C, and D) will be investigated in the following.

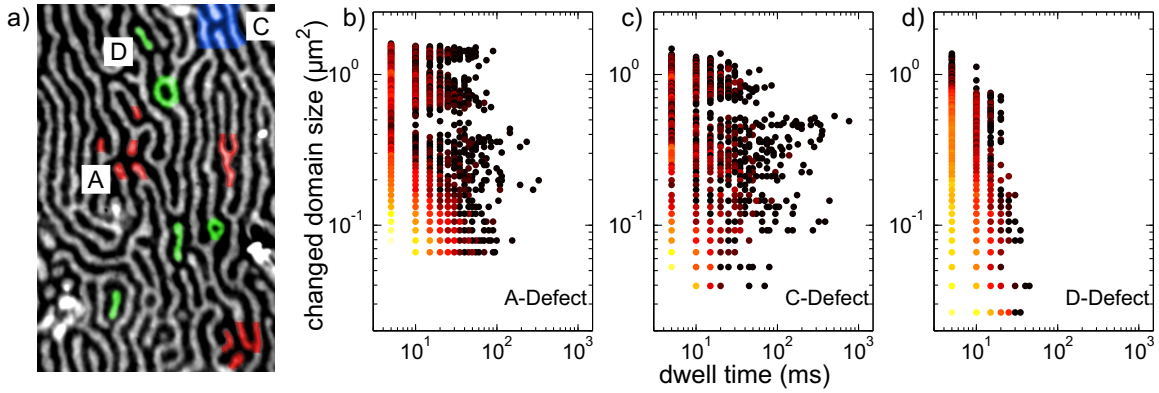

Figure 7.36: *a) shows the domain pattern used to evaluate the fluctuation properties of the individual types of defects. Some of these defects are highlighted in color in a). The fluctuation properties with respect to changed domain area as well as dwell time is shown for A-defects in b), C-defect in c) and D-defects in d).* (FOV: $9.8 \times 25.8 \mu m$, FR = 200fps, *recoding time:* 13.68 s)

7.7.2 Individual Defects

In this section the dynamical fingerprint of individual defects (A, C, and D) is illuminated, since it is the increase of their number that ultimately drives the transition into a more disordered state. For this evaluation the domain structure shown in Fig. 7.36 a) is used, since this domain structure, with a domain width of $w_D \approx 800$ nm, exhibits a region with a smectic domain structure as well as many topological defects. In particular, this domain structure comprises all topological defects, proposed by Abanov et al. [1]. The evaluation of the fluctuation properties of the individual types of defects is again performed with respect to changed domain area as well as dwell time for each individual state and is shown in Fig. 7.36. The D-defect shows reduced fluctuations when compared to A- and C-defects. This behavior is easy to interpret since the enclosing domain leads to both an isolation of the D-defect as well as a strong geometrical constraint. In this case, the geometrical constraints obviously suppress fluctuations, in contrast to the example presented in 7.6.2. On the other hand, the A as well as the C-defects show large area fluctuations and long dwell times. It is exactly this kind of fluctuation property that is required for pattern transformations. Nevertheless, before concluding that these two types of defects are responsible for pattern transformations, consider the following: taking into account the fluctuation properties of C-defects above measured (section 7.6.3), i.e. either the synchronous in-phase translation of both domain endings or the opening of the gap, leads to the conclusion that C-defects cannot be responsible for the pattern transformations. In the first case (synchronous movement) the pattern is not changed at all and in the second

case the two domain endings become unbound and proliferate as individual A-defects. In addition, A-defects can also emerge from transverse instabilities, as shown in section 7.6.4. This is exactly what has been proposed by Abanov et al. [1]: the long ranging positional order in the smectic phase decays algebraically due to long-wavelength excitation as well as pairs of dislocations, which become unbound and proliferate at increased temperatures. Hence, the conclusion can be drawn that mostly A-defects are responsible for the transformation of patterns.

Appendix A

TP-MCD versus incident polarization state

Parts of this chapter have been published in [12, 151].

The TP-MCD asymmetry is defined as the projection of the helicity vector of the illuminating photons onto the magnetization vector, confer Eq. (3.3). However, since the magnetization vector is defined inside the sample the projection should also be done with the light helicity vector *inside* the material, that is generally different from the incident polarization state, especially due to an incidence angle of 65° with respect to the surface normal given by the geometry of the PEEM instrument. This fact leads to an unapparent behavior of the TP-MCD asymmetry on the incident polarization state while gradually changing the incidence polarization from left to linear to right circular polarization, which will be shown below. There are two ways to calculate the transmitted helicity vector, either by using Fresnel's formulæ and Snell's law for absorptive media (complex refractive index) [60] or by exploiting a transfer matrix method [174], taking also non-diagonal elements of the transmission process into account. But, as will become clear, either method leads to an accurate, qualitative description within the 3-step photoemission model.

For the first, more instructive approach, the incident wave can be separated into two vectors, according to Fig. A.1 a), one perpendicular ($\mathbf{A}_\perp$) and the other parallel ($\mathbf{A}_\parallel$) to the plane of incidence

$$\begin{aligned} \mathbf{E}_i(\mathbf{r},t) &= \mathbf{A}_\parallel \; e^{i\phi_i} + \mathbf{A}_\perp \; e^{i\phi_i} \\ &= a_\parallel \begin{pmatrix} \cos\theta_i \\ 0 \\ \sin\theta_i \end{pmatrix} e^{i\delta_\parallel^i} \; e^{i\phi_i} + a_\perp \begin{pmatrix} 0 \\ 1 \\ 0 \end{pmatrix} e^{i\delta_\perp^i} \; e^{i\phi_i} \,, \end{aligned} \tag{A.0-1}$$

where $a_\parallel$ and $a_\perp$ are just amplitude constants, $\delta_\parallel^i$ and $\delta_\perp^i$ are phase constants, which can

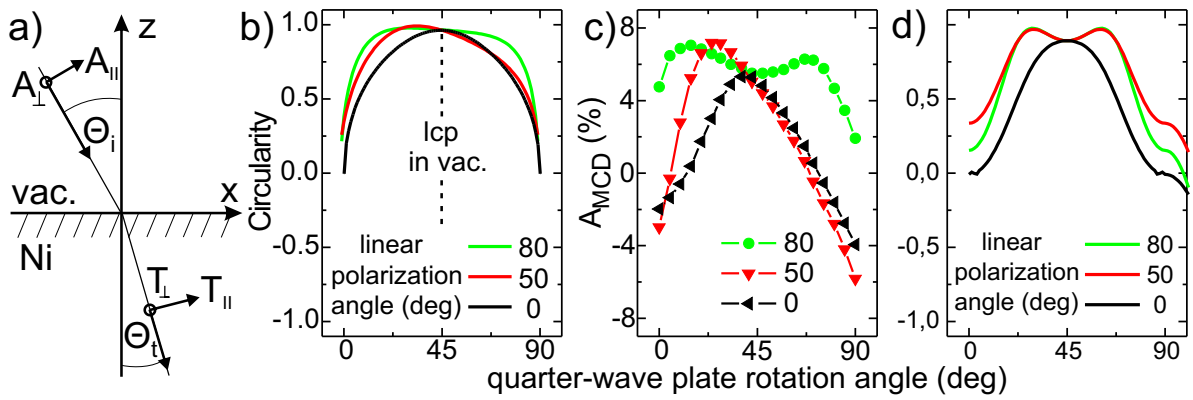

Figure A.1: *a) Coordinate system used for the calculation. The incident polarization state, fully described by $A_\perp$ and $A_\parallel$, can be set in the experiment by a rotatable linear polarizer and a rotatable quarter-wave plate. b) Theoretical dependence of the circularity on the incident polarization state, when the incidence angle $\theta_i = 65°$. b) Experimental dependence of the MCD-asymmetry A_{MCD} on the incoming photon polarization state. Both, b) and c), shown for different angles of the linear polarizer (80°, 50°, 0°) with respect to the incident plane, in a) the z-x-plane. d) shows the same as b) but followed Zak [174]*

be used to set the polarization as desired and $\phi_i(\mathbf{r},t) = \mathbf{k}_i \cdot \mathbf{r} - \omega t$ is the phase.

The transmitted wave can be written in the same form

$$\begin{aligned} \mathbf{E}_t(\mathbf{r},t) &= \mathbf{T}_\parallel \; e^{i\phi_t} + \mathbf{T}_\perp \; e^{i\phi_t} \\ &= t_\parallel \begin{pmatrix} \cos\hat{\theta}_t \\ 0 \\ \sin\hat{\theta}_t \end{pmatrix} e^{i\delta_\parallel^t} \; e^{i\phi_t} + t_\perp \begin{pmatrix} 0 \\ 1 \\ 0 \end{pmatrix} e^{i\delta_\perp^t} \; e^{i\phi_t} \, . \end{aligned} \tag{A.0-2}$$

With the aid of the Fresnel formulæ for the case of vacuum on the incidence side and an absorbing material on the other leading to a complex refractive index, the complex transmission angle as well as the transmission amplitudes can be deduced [60, 61] as:

$$\theta_t = \arcsin\left(\frac{\sin\theta_i}{n}\right) \tag{A.0-3}$$

$$\begin{aligned} t_\parallel &= \frac{2\,\cos\theta_i}{\hat{n}\,\cos\theta_i + \cos\theta_t}\, a_\parallel \\ t_\perp &= \frac{2\,\cos\theta_i}{\cos\theta_i + \hat{n}\,\cos\theta_t}\, a_\perp \, , \end{aligned} \tag{A.0-4}$$

where $\hat{n} = n + i\kappa$ is the complex refractive index. The refractive index for Ni and 3.06 eV is $\hat{n}(405\,\text{nm}) = 1.61 - 2.39\text{i}$ [61, 78] and for Fe $\hat{n}(640\,\text{nm}) = 3.03 - 1.78\text{i}$ [1] [61]. In order

[1] A value of the refractive index of Fe for a wavelength of 405 nm was not available.

to determine the dependence of the TP-MCD signal on the incident polarization state, the physical process of setting different polarization states has to be simulated. Hence, the rotation of a linear polarizer, used to enhance the linear polarization of the laser light, as well as the rotation of a quarter wave plate, which eventually produces circular polarization has to be taken into account. The laser polarization axis is set parallel to the incidence plane, i.e. parallel to $\mathbf{A}_{\parallel}$ of Eq. (A.0-1). Hence, the polarization state incident on the sample, $\mathbf{A}_{\perp}$ and $\mathbf{A}_{\parallel}$, follows than by taking into account two projections: the first projection maps the laser light onto the linear polarizer resulting in two parts. The second one projects these two parts onto the quarter wave plate axes, the ordinary (slow) and extra-ordinary (fast) axis, leading to four components, which than have to be suitably mixed to result in the required $\mathbf{A}_{\perp}$ and $\mathbf{A}_{\parallel}$. Subsequent Fresnel's formulæ and Snell's law can be applied to get the transmitted parts, $T_{\perp}$ and $T_{\parallel}$ Fig. A.1 a) or Eq. (A.0-2). The result of this calculation is given in Fig. A.1 b), where the degree of circularity, according to [175], of the transmitted wave is plotted for three individual linear polarization angles and a rotation angle range of the quarter-wave plate from 0 to $\frac{\pi}{2}$ with respect to the linear polarizer. The corresponding experimentally obtained plots are shown in Fig. A.1 c). Despite the fact that the photoemission process is not included the results of experiment and theory are in qualitative agreement with respect to the peaks appearing in the graphs, especially the unexpected double peak structure for an incident angle of 80° [12].

As already mentioned, the refraction-transmission problem can also be treated by a transfer matrix method, so done by Zak et al. [174]. The basis for this method is a medium boundary and medium propagation matrix, transferring the electric and magnetic field vector components parallel and perpendicular to the incidence plane. The first matrix describes the refraction of the individual field components at the interface of the two individual materials whereas the second one takes into account the lateral shifts of them during the propagation in the subsequent material due to a finite thickness. The latter can be disregarded in our case. The calculation of the individual field components has been done according to Zak et al. [174, 176, 177], but for only a single magnetic layer and a vacuum-ferromagnet interface. The result of this calculation, the dependence of the degree of circularity as described in the upper case, is plotted in Fig. A.1 d). Again the unique double peak structure of the MCD asymmetry is also reproduced by this approach. Even the narrower progression of the asymmetry for a linear polarization angle of 0° is reproduced. Only the asymmetric behavior with respect to a quarter-wave plate rotation angle of 45° cannot be observed. Again the results are in qualitative agreement with the measurements, reflecting the proportionality of the TP-MCD asymmetry on the helicity of the incident photons.

Bibliography

[1] Ar. Abanov, V. Kalatsky, V. L. Pokrovsky, and W. M. Saslow. Phase diagram of ultrathin ferromagnetic films with perpendicular anisotropy. *Phys. Rev. B* **51**, 1023–1038 (Jan 1995).

[2] M. Dzero, J. Schmalian, and P. G. Wolynes. Glassiness in Uniformly Frustrated Systems. *ArXiv e-prints* **1011.2261** (Nov 2010).

[3] O. Portmann. *Micromagnetism in the Ultrathin Limit*. PhD thesis ETH Zurich (2005).

[4] J. P. Gollup and J. S. Langer. Pattern formation in nonequilibrium physics. *Rev. Mod. Phys.* **71**, S396 (1999).

[5] H. Meinhardt and A. Gierer. Applications of a Theory of Biological Pattern Formation Based on Lateral Inhibition. *J. Cell Sci.* **15**, 321 (1974).

[6] A. M. Turing. The Chemical Basis of Morphogenesis. *The Royal Society* **237**(641), 37–72 (1952).

[7] Michael Seul and David Andelman. Domain Shapes and Patterns: The Phenomenology of Modulated Phases. *Science* **267**(5197), 476–483 (1995).

[8] A. Gierer and H. Meinhardt. A Theory of Biological Pattern Formation. *Kybernetik, Max-Planck-Institur für Virusforschung, Tübingen, Germany* **12**, 30–39 (1972).

[9] Motoomi Yamaguchi, Eiichi Yoshimoto, and Shigeru Kondo. Pattern regulation in the stripe of zebrafish suggests an underlying dynamic and autonomous mechanism. *Proceedings of the National Academy of Sciences* **104**(12), 4790–4793 (2007).

[10] Shigeru Kondo and Takashi Miura. Reaction-Diffusion Model as a Framework for Understanding Biological Pattern Formation. *Science* **329**(5999), 1616–1620 (2010).

[11] Takeshi Nakagawa and Toshihiko Yokoyama. Magnetic circular dichroism near the Fermi level. *Phys. Rev. Lett.* **96**, 237402 (2006).

[12] M. Kronseder, J. Minár, J. Braun, S. Günther, G. Woltersdorf, H. Ebert, and C. H. Back. Threshold photoemission magnetic circular dichroism of perpendicularly magnetized Ni films on Cu(001): Theory and experiment. *Phys. Rev. B* **83**(13), 132404 (Apr 2011).

[13] H. Ebert et al. *The Munich SPR-KKR package, version 5.4.* http://ebert.cup.uni-muenchen.de/ak/ebert/SPRKKR.

[14] Takeshi Nakagawa, Toshihiko Yokoyama, Masahito Hosaka, and Masahiro Katoh. Measurements of threshold photoemission magnetic dichroism using ultraviolet lasers and a photoelastic modulator. *Rev. Sci. Instr.* **78**(2), 023907 (2007).

[15] K. Hild, G. Schönhense, H. J. Elmers, T. Nakagawa, T. Yokoyama, K. Tarafder, and P. M. Oppeneer. Energy- and angle-dependent threshold photoemission magnetic circular dichroism from an ultrathin Co/Pt(111) film. *Phys. Rev. B* **82**(19), 195430 (Nov 2010).

[16] W. Kuch, A. Dittschar, K. Meinel, M. Zharnikov, C. M. Schneider, J. Kirschner, J. Henk, and R. Feder. Magnetic-circular-dichroism study of the valence states of perpendicularly magnetized Ni(001) films. *Phys. Rev. B* **53**(17), 11621–11630 (May 1996).

[17] J. Bansmann, L. Lu, K. H. Meiwes-Broer, T. Schlathölter, and J. Braun. Relationship between magnetic circular and linear dichroism in photoemission from Fe $3p$ core level: An experimental and theoretical investigation. *Phys. Rev. B* **60**(19), 13860–13868 (Nov 1999).

[18] J.B. Pendry. Theory of photoemission. *Surface Science* **57**(2), 679 – 705 (1976).

[19] J. Binder. *Giant Magnetoresistance- eine ab-initio Beschreibung.* PhD thesis Technische Universität Dresden (2000).

[20] A. Gonis and W. H. Butler. *Multiple Scattering in Solids.* Springer (2000).

[21] P. Strange, H. Ebert, J. B. Staunton, and B. L. Gyorffy. A relativistic spin-polarised multiple-scattering theory, with applications to the calculation of the electronic structure of condensed matter. *Journal of Physics: Condensed Matter* **1**(18), 2959 (1989).

[22] Antoine Georges, Gabriel Kotliar, Werner Krauth, and Marcelo J. Rozenberg. Dynamical mean-field theory of strongly correlated fermion systems and the limit of infinite dimensions. *Rev. Mod. Phys.* **68**(1), 13 (Jan 1996).

[23] D. Vollhardt. Korrelierte Elektronen im Festkörper. *Physik Journal* (8/9), 31 (2010).

[24] G. Kotliar and D. Vollhardt. Strongly Correlated Materials: Insights from Dynamical Mean-Field theory. *Physics Today* , 53 (March 2004).

[25] P. Hohenberg and W. Kohn. Inhomogeneous electron gas. *Phys. Rev.* **136**(3B), B864–B871 (Nov 1964).

[26] W. Kohn and L. J. Sham. Self-Consistent Equations Including Exchange and Correlation Effects. *Phys. Rev.* **140**(4A), A1133–A1138 (Nov 1965).

[27] M. Grass, J. Braun, G. Borstel, R. Schneider, H. Durr, T. Fauster, and V. Dose. Unoccupied electronic states and surface barriers at Cu surfaces. *Journal of Physics: Condensed Matter* **5**(5), 599 (1993).

[28] D. D. Koelling. Self-consistent energy band calculations. *Reports on Progress in Physics* **44**(2), 139 (1981).

[29] K. Held, I. A. Nekrasov, G. Keller, V. Eyert, N. Blümer, A. K. McMahan, R. T. Scalettar, Th. Pruschke, V. I. Anisimov, and D. Vollhardt. Realistic investigations of correlated electron systems with LDA + DMFT. *physica status solidi (b)* **243**(11), 2599–2631 (2006).

[30] Staemmler V. Introduction to Density Functional Theory and Exchange-Correlation Energy Functionals. *NIC Series* **31**, 45–70 (2006).

[31] A. G. Petukhov, I. I. Mazin, L. Chioncel, and A. I. Lichtenstein. Correlated metals and the LDA+U method. *Phys. Rev. B* **67**(15), 153106 (Apr 2003).

[32] A. I. Liechtenstein, V. I. Anisimov, and J. Zaanen. Density-functional theory and strong interactions: Orbital ordering in Mott-Hubbard insulators. *Phys. Rev. B* **52**(8), R5467–R5470 (Aug 1995).

[33] Staemmler V. Introduction to Hartree-Fock and CI Methods. *NIC Series* **31**, 1–18 (2006).

[34] W. Metzner and D. Vollhardt. Correlated Lattice Fermions in $d = \infty$ Dimensions. *Phys. Rev. Lett.* **62**(3), 324 (1989).

[35] J. Braun, G. Borstel, and W. Nolting. Theory of temperature-dependent photoemission in 3d-band ferromagnets: Application to Ni(110) and Ni(111). *Phys. Rev. B* **46**(6), 3510–3519 (Aug 1992).

[36] W. Kohn and N. Rostoker. Solution of the Schrödinger Equation in Periodic Lattices with an Application to Metallic Lithium. *Phys. Rev.* **94**(5), 1111–1120 (Jun 1954).

[37] U. von Barth and L. Hedin. A local exchange-correlation potential for the spin polarized case. *J. Phys. C: Solid State Phys.* **5**(1629) (1972).

[38] K. Capelle. A Bird's-Eye View of Density-Functional Theory. *Brazilian Journal of Physics* **36**(4A), 1318 (2006).

[39] E. V. Chulkov, V. M. Silkin, and P. M. Echenique. Image potential states on metal surfaces: binding energies and wave functions. *Surface Science* **437**(3), 330 – 352 (1999).

[40] H. Lüth. *Solid surfaces, interfaces and thin films*. Springer, Berlin (2001).

[41] Neil W. Ashcroft and N. David Mermin. *Festkörperphysik* volume 2. Oldenbourg Verlag, München, Wien (2005).

[42] S. Ossicini, C. M. Bertoni, and P. Gies. Image Plane for Surface Potential. *EPL* **1**(12), 661 (1986).

[43] M. Donath, M. Pickel, A. B. Schmidt, and M. Weinelt. Ferromagnetic Fe on Cu(001) throughout the fcc-like phase: arguing from the viewpoint of the electronic structure. *Journal of Physics: Condensed Matter* **21**(13), 134004 (2009).

[44] M. Nekovee and J.E. Inglesfield. Threshold behaviour of surface density of states at the vacuum level. *Europhysics Letters* **19**(6), 535 – 540 (1992).

[45] M. Nekovee, S. Crampin, and J. E. Inglesfield. Magnetic splitting of image states at Fe(110). *Phys. Rev. Lett.* **70**, 3099–3102 (May 1993).

[46] M. Nekovee and J.E. Inglesfield. Theory of image states at magnetic surfaces. *Progress in Surface Science* **50**(1-4), 149 – 158 (1995).

[47] C. S. Wang and A. J. Freeman. Surface states, surface magnetization, and electron spin polarization: Fe(001). *Phys. Rev. B* **24**, 4364–4371 (Oct 1981).

[48] C. S. Wang and A. J. Freeman. Surface states, surface magnetization, and electron-spin polarization: Ni(001). *Phys. Rev. B* **21**, 4585–4591 (May 1980).

[49] I. E. Tamm. *Phys. Z. Sowjetunion* **1**, 733 (1932).

[50] William Shockley. On the surface states associated with a periodic potential. *Phys. Rev.* **56**, 317–323 (Aug 1939).

[51] N. D. Lang. Theory of work function changes induced by Alkali adsorption. *Phys. Rev. B* **4**(12), 4235 (1971).

[52] N. D. Lang and W. Kohn. Theory of Metal surfaces: Work function. *Phys. Rev. B* **3**(4), 1215–1223 (1971).

[53] D. E. Eastman. Photoelectric work functions of transition, rare-earth and nobel-metals. *Phys. Rev. B* **2**(1), 1–2 (1970).

[54] J. Braun, C. Math, A. Postnikov, and M. Donath. Surface resonances versus surface states on Fe(110). *Phys. Rev. B* **65**, 184412 (Apr 2002).

[55] M. Weinert, S. L. Hulbert, and P. D. Johnson. Image Planes and Surface States. *Phys. Rev. Lett.* **55**, 2055–2058 (Nov 1985).

[56] M. Grass, J. Braun, and G. Borstel. Full-potential photoemission theory. *Phys. Rev. B* **47**(23), 15487–15499 (1993).

[57] J. E. Inglesfield. Surface electronic structure. *Reports on Progress in Physics* **45**(3), 223 (1982).

[58] G. Borstel. Theoretical aspects of photoemission. *Applied Physics A: Materials Science and Processing* **38**, 193–204 (1985).

[59] J Braun. The theory of angle-resolved ultraviolet photoemission and its applications to ordered materials. *Reports on Progress in Physics* **59**(10), 1267 (1996).

[60] Max Born and Emil Wolf. *Principles of Optics*. Pergamon Press Oxford 6 edition (1980).

[61] L. Bergmann and C. Schäfer. *Optik*. Walter de Gruyter, Berlin, New York 9 edition (1993).

[62] Richard P. Feynman, Robert B. Leighton, and Matthew Sands. *The Feynman Lectures on Physics*. Addison-Weslay Publishing Company London (1965).

[63] Stefan Hüfner. *Photoelectron Spectroscopy*. Springer 3. edition (2003).

[64] J. F. L. Hopkinson, J. B. Pendry, and D. J. Titterington. Calculation of photoemission spectra for surfaces of solids. *Computer Physics Communications* **19**(1), 69 – 92 (1980).

[65] J. Braun, J. Minár, H. Ebert, M. I. Katsnelson, and A. I. Lichtenstein. Spectral Function of Ferromagnetic 3*d* Metals: A Self-Consistent LSDA + DMFT Approach Combined with the One-Step Model of Photoemission. *Phys. Rev. Lett.* **97**, 227601 (Dec 2006).

[66] M. Pickel, A. B. Schmidt, F. Giesen, J. Braun, J. Minár, H. Ebert, M. Donath, and M. Weinelt. Spin-Orbit Hybridization Points in the Face-Centered-Cubic Cobalt Band Structure. *Phys. Rev. Lett.* **101**(6), 066402 (Aug 2008).

[67] J. Sánchez-Barriga, J. Fink, V. Boni, I. Di Marco, J. Braun, J. Minár, A. Varykhalov, O. Rader, V. Bellini, F. Manghi, H. Ebert, M. I. Katsnelson, A. I. Lichtenstein, O. Eriksson, W. Eberhardt, and H. A. Dürr. Strength of Correlation Effects in the Electronic Structure of Iron. *Phys. Rev. Lett.* **103**(26), 267203 (Dec 2009).

[68] Leonard Kleinman and Kenneth Mednick. Self-energy contributions to the electronic structure of Ni. *Phys. Rev. B* **24**, 6880–6888 (Dec 1981).

[69] H. Krakauer, A. J. Freeman, and E. Wimmer. Magnetism of the Ni(110) and Ni(100) surfaces: Local-spin-density-functional calculations using the thin-slab linearized augmented-plane-wave method. *Phys. Rev. B* **28**, 610–623 (Jul 1983).

[70] J. Sánchez-Barriga, J. Minár, J. Braun, A. Varykhalov, V. Boni, I. Di Marco, O. Rader, V. Bellini, F. Manghi, H. Ebert, M. I. Katsnelson, A. I. Lichtenstein, O. Eriksson, W. Eberhardt, H. A. Dürr, and J. Fink. Quantitative determination of spin-dependent quasiparticle lifetimes and electronic correlations in hcp cobalt. *Phys. Rev. B* **82**, 104414 (Sep 2010).

[71] C.A. Papageorgopoulos and J.M. Chen. Coadsorption of cesium and oxygen on Ni(100): I. Cesium probing of NiO bonding. *Surface Science* **52**(1), 40 – 52 (1975).

[72] C.A. Papageorgopoulos and J.M. Chen. Cesium enhanced oxidation of Ni(100). *Solid State Communications* **13**(9), 1455 – 1457 (1973).

[73] J. Thiele, R. Belkhou, H. Bulou, O. Heckmann, H. Magnan, P. Le Fvre, D. Chandesris, and C. Guillot. EXAFS study of the crystallographic structure of cobalt thin films on Pt(111). *Surface Science* **384**(13), 120 – 128 (1997).

[74] S. Müller, P. Bayer, C. Reischl, K. Heinz, B. Feldmann, H. Zillgen, and M. Wuttig. Structural Instability of Ferromagnetic fcc Fe Films on Cu(100). *Phys. Rev. Lett.* **74**, 765–768 (Jan 1995).

[75] K. Heinz, S. Müller, and P. Bayer. Multilayer reconstruction of ultrathin epitaxial fcc Fe films. *Surface Science* **337**(3), 215 – 223 (1995).

[76] H. L. Meyerheim, J.-M. Tonnerre, L. Sandratskii, H. C. N. Tolentino, M. Przybylski, Y. Gabi, F. Yildiz, X. L. Fu, E. Bontempi, S. Grenier, and J. Kirschner. New Model for Magnetism in Ultrathin fcc Fe on Cu(001). *Phys. Rev. Lett.* **103**, 267202 (Dec 2009).

[77] M. Marsman and J. Hafner. Broken symmetries in the crystalline and magnetic structures of γ-iron. *Phys. Rev. B* **66**, 224409 (Dec 2002).

[78] E. D. Palik. *Handbook of Optical Constants of Solids*. Elsevier, Amsterdam (1998).

[79] E. Hecht. *Optik*. Oldenbourg Wissenschaftsverlag GmbH (2001).

[80] Stefan Hüfner, Stefan Schmidt, and Friedrich Reinert. Photoelectron spectroscopy - An overview. *Nuclear Instruments and Methods in Physics Research Section A: Accelerators, Spectrometers, Detectors and Associated Equipment* **547**(1), 8 – 23 (2005).

[81] J. Hong and D. L. Mills. Spin dependence of the inelastic electron mean free path in Fe and Ni: Explicit calculations and implications. *Phys. Rev. B* **62**(9), 5589–5600 (2000).

[82] A. Schatz and W. Keune. Non-pseudomorphous epitaxial growth of fcc Fe on Cu(100) observed by reflection high-energy electron diffraction (RHEED). *Surface Science* **440**(12), L841 – L847 (1999).

[83] O. Gunnarsson. Band model for magnetism of transition metals in the spin-density-functional formalism. *Journal of Physics F: Metal Physics* **6**(4), 587 (1976).

[84] M.I. Brammall. *Stoner Criteria in Transition Metal Oxides and Heavy Fermions*. PhD thesis University of Birmingham (2011).

[85] L. Severin, M. S. S. Brooks, and B. Johansson. Relationship between the Coulomb integral U and the Stoner parameter I. *Phys. Rev. Lett.* **71**, 3214–3217 (Nov 1993).

[86] L. F. Mattheiss. Effective Exchange Integral. *Phys. Rev.* **123**, 1219–1225 (Aug 1961).

[87] C. A. F. Vaz, J. A. C. Bland, and G. Lauhoff. Magnetism in ultrathin film structures. *Reports on Progress in Physics* **71**(5), 056501 (2008).

[88] C. M. Srivastava and R. Aiyar. Spin wave stiffness constants in some ferrimagnetics. *Journal of Physics C: Solid State Physics* **20**(8), 1119 (1987).

[89] D. Sander. The magnetic anisotropy and spin reorientation of nanostructures and nanoscale films. *Journal of Physics: Condensed Matter* **16**(20), R603 (2004).

[90] G. Bihlmayer. *36th Spring School of the Institude of Solid State Research: Magnetism goes Nano*. Forschungszentrum Jülich GmbH (2005).

[91] D. S. Chuang, C. A. Ballentine, and R. C. O'Handley. Surface and step magnetic anisotropy. *Phys. Rev. B* **49**, 15084–15095 (Jun 1994).

[92] U. Gradmann and H.J. Elmers. Magnetic surface anisotropies in NiFe-alloy films: separation of intrinsic Neél-type from strain relaxation contributions. *Journal of Magnetism and Magnetic Materials* **206**(3), 107 – 112 (1999).

[93] H. Abe, K. Amemiya, D. Matsumura, S. Kitagawa, H. Watanabe, T. Yokoyama, and T. Ohta. Spin reorientation transitions of studied by using the depth-resolved X-ray magnetic circular dichroism technique. *Journal of Magnetism and Magnetic Materials* **302**(1), 86 – 95 (2006).

[94] Yonko Millev and Jürgen Kirschner. Reorientation transitions in ultrathin ferromagnetic films by thickness- and temperature-driven anisotropy flows. *Phys. Rev. B* **54**, 4137–4145 (Aug 1996).

[95] R. Skomski, D. Sander, C. Schmidthals, A. Enders, and J. Kirschner. Iron and nickel surface and interface anisotropies. *IEEE TRANSACTIONS ON MAGNETICS* **34** (1998).

[96] D. Sander. The correlation between mechanical stress and magnetic anisotropy in ultrathin films. *Reports on Progress in Physics* **62**(5), 809 (1999).

[97] R.Q. Wu, L.J. Chen, A. Shick, and A.J. Freeman. First-principles determinations of magneto-crystalline anisotropy and magnetostriction in bulk and thin-film transition metals. *Journal of Magnetism and Magnetic Materials* **177-181**, 1216 – 1219 (1998).

[98] H. Hug, B. Stiefel, H.-J. Guntherodt, G. Bochi, D. I. Paul, and R. C. O'Handley. Magnetization process in perpendicular epitaxial Cu/Ni/Cu/Si(001). *Journal of Applied Physics* **81**(8), 3896–3896 (1997).

[99] Th. Gutjahr-Loser, D. Sander, and J. Kirschner. Magnetoelastic coupling in Ni and Fe monolayers on Cu(001). *Journal of Applied Physics* **87**(9), 5920–5922 (2000).

[100] C. Chappert and P. Bruno. Magnetic anisotropy in metallic ultrathin films and related experiments on cobalt films. *J. Appl. Phys.* **64**, 5736 (1988).

[101] P. Bruno, Y. Suzuki, and C. Chappert. Magneto-optical Kerr effect in a paramagnetic overlayer on a ferromagnetic substrate: A spin-polarized quantum size effect. *Phys. Rev. B* **53**(14), 9214 (1996).

[102] M. Farle. Ferromagnetic resonance of ultrathin metallic layers. *Reports on Progress in Physics* **61**(7), 755 (1998).

[103] S. Müller, B. Schulz, G. Kostka, M. Farle, K. Heinz, and K. Baberschke. Pseudomorphic growth of Ni films on Cu(001): a quantitative LEED analysis. *Surface Science* **364**(3), 235 – 241 (1996).

[104] R. Vollmer, Th. Gutjahr-Löser, J. Kirschner, S. van Dijken, and B. Poelsema. Spin-reorientation transition in Ni films on Cu(001): The influence of H_2 adsorption. *Phys. Rev. B* **60**, 6277–6280 (Sep 1999).

[105] B. Schulz, R. Schwarzwald, and K. Baberschke. Magnetic properties of ultrathin Ni/Cu(100) films determined by a UHV-FMR study. *Surface Science* **307-309**, 1102 – 1108 (1994).

[106] Till Burkert, Olle Eriksson, Peter James, Sergei I. Simak, Börje Johansson, and Lars Nordström. Calculation of uniaxial magnetic anisotropy energy of tetragonal and trigonal Fe, Co, and Ni. *Phys. Rev. B* **69**, 104426 (Mar 2004).

[107] R. Ramchal, A. K. Schmid, M. Farle, and H. Poppa. Spiral-like continuous spin-reorientation transition of Fe/Ni bilayers on Cu(100). *Phys. Rev. B* **69**, 214401 (Jun 2004).

[108] T. Asada and S. Blügel. Total Energy Spectra of Complete Sets of Magnetic States for fcc-Fe Films on Cu(100). *Phys. Rev. Lett.* **79**, 507–510 (Jul 1997).

[109] M. Weinelt, S. Schwarz, H. Baier, S. Müller, L. Hammer, K. Heinz, and Th. Fauster. Structure of ultrathin Fe films on Cu(100) prepared by pulsed laser deposition. *Phys. Rev. B* **63**, 205413 (May 2001).

[110] S. Müller, P. Bayer, A. Kinne, P. Schmailzl, and K. Heinz. High precision LEED structure analysis of ultra-thin epitaxial fcc Fe films on Cu(100). *Surface Science* **322**(1-3), 21 – 33 (1995).

[111] P. Schmailzl, K. Schmidt, P. Bayer, R. Döll, and K. Heinz. The structure of thin epitaxial Fe films on Cu(100) in the transition range fcc to bcc. *Surface Science* **312**(1-2), 73 – 81 (1994).

[112] W. L. O'Brien and B. P. Tonner. Room-temperature magnetic phases of Fe on fcc Co(001) and Ni(001). *Phys. Rev. B* **52**, 15332–15340 (Dec 1995).

[113] A. Biedermann, R. Tscheliessnig, M. Schmid, and P. Varga. Local atomic structure of ultra-thin Fe films grown on Cu(100). *Applied Physics A* **78**, 807–816 (2004).

[114] K Heinz, S Müller, and L Hammer. Crystallography of ultrathin iron, cobalt and nickel films grown epitaxially on copper. *Journal of Physics: Condensed Matter* **11**(48), 9437 (1999).

[115] D. Peterka, A. Enders, G. Haas, and K. Kern. Adsorbate and thermally induced spin reorientation transition in low-temperature-grown Fe/Cu(001). *Phys. Rev. B* **66**, 104411 (Sep 2002).

[116] Dongqi Li, M. Freitag, J. Pearson, Z. Q. Qiu, and S. D. Bader. Magnetic phases of ultrathin Fe grown on Cu(100) as epitaxial wedges. *Phys. Rev. Lett.* **72**, 3112–3115 (May 1994).

[117] J. Choi, J. Wu, C. Won, Y. Z. Wu, A. Scholl, A. Doran, T. Owens, and Z. Q. Qiu. Magnetic Bubble Domain Phase at the Spin Reorientation Transition of Ultrathin Fe/Ni/Cu(001) Film. *Phys. Rev. Lett.* **98**, 207205 (May 2007).

[118] M. Farle, B. Mirwald-Schulz, A. N. Anisimov, W. Platow, and K. Baberschke. Higher-order magnetic anisotropies and the nature of the spin-reorientation transition in face-centered-tetragonal Ni(001)/Cu(001). *Phys. Rev. B* **55**, 3708–3715 (Feb 1997).

[119] M Farle, A.N. Anisimov, W Platow, P Poulopoulos, and K Baberschke. Magnetic anisotropy energy as a function of temperature in tetragonal Ni films and Fe superlattices. *Journal of Magnetism and Magnetic Materials* **198-199**, 325 – 330 (1999).

[120] M. Kronseder, M. Buchner, H. G. Bauer, and C. H. Back. Dipolar energy activated magnetic domain pattern transformation driven by thermal fluctuations. *to be published* (2013).

[121] M. Kronseder, M. Buchner, M. Vogel, and C. H. Back. Real time observation of fluctuations in a two dimensional magnetic model system. *to be published* (2013).

[122] A. B. Kashuba and V. L. Pokrovsky. Stripe domain structures in a thin ferromagnetic film. *Phys. Rev. B* **48**, 10335–10344 (Oct 1993).

[123] D. Pescia and V. L. Pokrovsky. Perpendicular versus in-plane magnetization in a 2D Heisenberg monolayer at finite temperatures. *Phys. Rev. Lett.* **65**, 2599–2601 (Nov 1990).

[124] T. Michaels Thomas, Alessandro Vindigni, and Danilo Pescia. *to be published.* (2013).

[125] H.Y. Kwon, S.S. Hong, J.H. Seok, K.M. Bu, Y.Z. Wu, Z.Q. Qiu, and C. Won. A study of the stripe domain phase at the spin reorientation transition of two-dimensional magnetic system. *Journal of Magnetism and Magnetic Materials* **322**(18), 2742 – 2748 (2010).

[126] Orlando V. Billoni, Vivien Pianet, Danilo Pescia, and Alessandro Vindigni. Static and dynamic properties of single-chain magnets with sharp and broad domain walls. *Phys. Rev. B* **84**, 064415 (Aug 2011).

[127] A. Kashuba and V. L. Pokrovsky. Stripe domain structures in a thin ferromagnetic film. *Phys. Rev. Lett.* **70**, 3155–3158 (May 1993).

[128] M. Buchner. Magnetische Untersuchungen ultradünner Eisenfilme auf unterschiedlichen Substraten. Master's thesis Universität Regensburg (2012).

[129] Y. Z. Wu, C. Won, A. Scholl, A. Doran, H. W. Zhao, X. F. Jin, and Z. Q. Qiu. Magnetic stripe domains in coupled magnetic sandwiches. *Phys. Rev. Lett.* **93**, 117205 (Sep 2004).

[130] C. Won, Y. Z. Wu, J. Choi, W. Kim, A. Scholl, A. Doran, T. Owens, J. Wu, X. F. Jin, H. W. Zhao, and Z. Q. Qiu. Magnetic stripe melting at the spin reorientation transition in Fe/Ni/Cu(001). *Phys. Rev. B* **71**, 224429 (Jun 2005).

[131] N. Saratz. *Inverse Symmetry Breaking in Low-Dimensional Systems.* PhD thesis ETH Zurich (2009).

[132] M. Seul and R. Wolfe. Evolution of disorder in two-dimensional stripe patterns: "smectic" instabilities and disclination unbinding. *Phys. Rev. Lett.* **68**, 2460–2463 (Apr 1992).

[133] O. Portmann, A. Gölzer, N. Saratz, O. V. Billoni, D. Pescia, and A. Vindigni. Scaling hypothesis for modulated systems. *Phys. Rev. B* **82**, 184409 (Nov 2010).

[134] Lucas Nicolao and Daniel A. Stariolo. Langevin simulations of a model for ultrathin magnetic films. *Phys. Rev. B* **76**, 054453 (Aug 2007).

[135] A. Vaterlaus, C. Stamm, U. Maier, M. G. Pini, P. Politi, and D. Pescia. Two-Step Disordering of Perpendicularly Magnetized Ultrathin Films. *Phys. Rev. Lett.* **84**, 2247–2250 (Mar 2000).

[136] Santiago A. Pighín and Sergio A. Cannas. Phase diagram of an ising model for ultrathin magnetic films: Comparing mean field and monte carlo predictions. *Phys. Rev. B* **75**, 224433 (Jun 2007).

[137] O. Portmann, A. Vaterlaus, and D. Pescia. An inverse transition of magnetic domain patterns in ultrathin films. *Nature* **422**, 701 (Apr 2003).

[138] H. Eugene Stanley. *Phase Transitions and critical phenomena* volume 1. Clarendon Press, Oxford (1971).

[139] Kenneth G. Wilson and J. Kogut. The renormalization group and the ε expansion. *Physics Reports* **12**(2), 75 – 199 (1974).

[140] M. J. Dunlavy and D. Venus. Critical susceptibility exponent measured from Fe/W(110) bilayers. *Phys. Rev. B* **69**, 094411 (Mar 2004).

[141] L. P. Kadanoff, W. Götze, D. Hamblen, R. Hecht, E. A. S. Lewis, V. V. Palciaukas, M. Rayl, J. Swift, D. Aapnes, and J. Kane. Static Phenomena Near Critical Points: Theory and Experiment. *Rev. Mod. Phys.* **39**, 395–431 (Apr 1967).

[142] E. Frey and F. Schwabl. Critical dynamics of magnets. *Advances in Physics* **43**(5), 577–683 (1994).

[143] A.M. Polyakov. Interaction of goldstone particles in two dimensions. Applications to ferromagnets and massive Yang-Mills fields. *Physics Letters B* **59**(1), 79 – 81 (1975).

[144] Michael E. Fisher. The renormalization group in the theory of critical behavior. *Rev. Mod. Phys.* **46**, 597–616 (Oct 1974).

[145] J. M. Kosterlitz and D. J. Thouless. Ordering, metastability and phase transitions in two-dimensional systems. *Journal of Physics C: Solid State Physics* **6**(7), 1181 (1973).

[146] Antitsa D. Stoycheva and Sherwin J. Singer. Stripe melting in a two-dimensional system with competing interactions. *Phys. Rev. Lett.* **84**, 4657–4660 (May 2000).

[147] M. M. Hurley and Sherwin J. Singer. Domain-array melting in the dipolar lattice gas. *Phys. Rev. B* **46**, 5783–5786 (Sep 1992).

[148] Tuomas Knowles. Non-Linear Aspects of Magnetism and Nanomagnetic Devices. Master's thesis ETH Zurich (2004).

[149] Jörg Schmalian and Peter G. Wolynes. Stripe Glasses: Self-Generated Randomness in a Uniformly Frustrated System. *Phys. Rev. Lett.* **85**, 836–839 (Jul 2000).

[150] H. Nishimori. *Statistical Physics of Spin Glasses and Information Processing- An Introduction*. Clarendon Press, Oxford (2001).

[151] M. Kronseder. Implementation of magnetic imaging in a photoemission electron microscope. Master's thesis Universität Regensburg (2009).

[152] R. Allenspach, M. Stampanoni, and A. Bischof. Magnetic domains in thin epitaxial Co/Au(111) films. *Phys. Rev. Lett.* **65**, 3344–3347 (Dec 1990).

[153] Sergio A. Cannas, Mateus F. Michelon, Daniel A. Stariolo, and Francisco A. Tamarit. Interplay between coarsening and nucleation in an ising model with dipolar interactions. *Phys. Rev. E* **78**, 051602 (Nov 2008).

[154] O. Portmann, A. Vaterlaus, and D. Pescia. Observation of stripe mobility in a dipolar frustrated ferromagnet. *Phys. Rev. Lett.* **96**, 047212 (Feb 2006).

[155] F. Freund. PhD thesis Universität Regensburg.

[156] N. Saratz, A. Lichtenberger, O. Portmann, U. Ramsperger, A. Vindigni, and D. Pescia. Experimental Phase Diagram of Perpendicularly Magnetized Ultrathin Ferromagnetic Films. *Phys. Rev. Lett.* **104**, 077203 (Feb 2010).

[157] Sergio A. Cannas, Marianela Carubelli, Orlando V. Billoni, and Daniel A. Stariolo. Inverse transition in a two-dimensional dipolar frustrated ferromagnet. *Phys. Rev. B* **84**, 014404 (Jul 2011).

[158] Marianela Carubelli, Orlando V. Billoni, Santiago A. Pighin, Sergio A. Cannas, Daniel A. Stariolo, and Francisco A. Tamarit. Spin reorientation transition and phase diagram of ultrathin ferromagnetic films. *Phys. Rev. B* **77**, 134417 (Apr 2008).

[159] Sergio A. Cannas, Mateus F. Michelon, Daniel A. Stariolo, and Francisco A. Tamarit. Ising nematic phase in ultrathin magnetic films: A Monte Carlo study. *Phys. Rev. B* **73**, 184425 (May 2006).

[160] W. Janke and H. Kleinert. First order in 2D disclination melting. *Physics Letters A* **105**(3), 134 – 138 (1984).

[161] O. Mishima and H. Eugene Stanley. The relationship between liquid, supercooled and glassy water. *Nature* **396**, 329 (1998).

[162] The code is available at http://math.nist.gov/oommf.

[163] Y. Yafet and E. M. Gyorgy. Ferromagnetic stripe domains in an atomic monolayer. *Phys. Rev. B* **38**(13), 9145–9151 (Nov 1988).

[164] Nicholas Sama. Field desorption of cesium ions. *Journal of Applied Physics* **39**(8), 3870–3878 (1968).

[165] D. Venus and M.J. Dunlavy. Dissipation in perpendicularly magnetized ultrathin films studied using the complex AC susceptibility. *Journal of Magnetism and Magnetic Materials* **260**, 195 – 205 (2003).

[166] G. Bayreuther, P. Bruno, G. Lugert, and C. Turtur. Magnetic aftereffect in ultrathin ferromagnetic films. *Phys. Rev. B* **40**, 7399–7402 (Oct 1989).

[167] P. Bruno, G. Bayreuther, P. Beauvillain, C. Chappert, G. Lugert, D. Renard, J. P. Renard, and J. Seiden. Hysteresis properties of ultrathin ferromagnetic films. *Journal of Applied Physics* **68**(11), 5759–5766 (1990).

[168] M. Bauer, A. Mougin, J. P. Jamet, V. Repain, J. Ferré, R. L. Stamps, H. Bernas, and C. Chappert. Deroughening of Domain Wall Pairs by Dipolar Repulsion. *Phys. Rev. Lett.* **94**, 207211 (May 2005).

[169] M. J. Dunlavy and D. Venus. Critical susceptibility exponent measured from Fe/W(110) bilayers. *Phys. Rev. B* **69**, 094411 (Mar 2004).

[170] N. Abu-Libdeh and D. Venus. Dynamical signature of a domain phase transition in a perpendicularly magnetized ultrathin film. *Phys. Rev. B* **80**, 184412 (Nov 2009).

[171] W. Kuch, K. Fukumoto, J. Wang, F. Nolting, C. Quitmann, and T. Ramsvik. Thermal melting of magnetic stripe domains. *Phys. Rev. B* **83**, 172406 (May 2011).

[172] N. Bergeard, J. P. Jamet, A. Mougin, J. Ferré, J. Gierak, E. Bourhis, and R. Stamps. Dynamic fluctuations and two-dimensional melting at the spin reorientation transition. *Phys. Rev. B* **86**, 094431 (Sep 2012).

[173] Eric J. R. Parteli, José S. Andrade, and Hans J. Herrmann. Transverse Instability of Dunes. *Phys. Rev. Lett.* **107**, 188001 (Oct 2011).

[174] J. Zak, E. R. Moog, C. Liu, and S. D. Bader. Magneto-optics of multilayers with arbitrary magnetization directions. *Phys. Rev. B* **43**, 6423–6429 (Mar 1991).

[175] D. T. Pierce, R. J. Celotta, G.-C. Wang, W. N. Unertl, A. Galejs, C. E. Kuyatt, and S. R. Mielczarek. The GaAs spin polarized electron source. *Review of Scientific Instruments* **51**(4), 478–499 (1980).

[176] J. Zak, E. R. Moog, C. Liu, and S. D. Bader. Fundamental magneto-optics. *Journal of Applied Physics* **68**(8), 4203–4207 (1990).

[177] J. Zak, E.R. Moog, C. Liu, and S.D. Bader. Universal approach to magneto-optics. *Journal of Magnetism and Magnetic Materials* **89**(12), 107 – 123 (1990).

Acknowledgement

Mein Dank gilt

Christian H. Back nicht nur für das Thema dieser Dissertation, welches von der Entwicklung mechanischer und elektrischer Komponenten, des Aufbaus und der Instandsetzung eines Elektronenmikroskops, über Laser und optische Bauteile zu Bandstrukturrechnungen, Beschreibung von Photoemissionsprozessen und Fluktuationen von magnetischen Strukturen bis hin zum stundenlangen Anstarren und Interpretieren von gemusterten Tierfellen ging, sondern auch für die Betreuung und die vielen Diskussionen.

Georg Woltersdorf für das Teilhabenlassen an seinem unglaublichen Wissen und Fachwissen. Darüber hinaus möchte ich Ihm für das Korrekturlesen dieser Arbeit ganz herzlich danken.

Florian Freund und Matthias Kießling für die angenehme, lustige Atmosphäre nicht nur im Büro und das Aushelfen "wenn's brennt".

"der Änderungsschneiderei": Tobias Stöckl, Dieter Schierl und Markus Hollnberger für all die strebsam erledigten Arbeiten rund um die Forschung und die aufheiternde Stimmung bei etwaigen Anliegen.

Matthias Sperl und Dieter Riedl für die Beantwortung vieler Fragen und der fruchtbaren und aufmunternden Zusammenarbeit.

Jan Minár und Jürgen Braun für die zeitaufwändige Einführung in Bandstrukturrechnungen und die vielen Diskussionen über Photoemissionsprozesse.

Martin Buchner und Michael Vogel für die gute Zusammenarbeit und die Einführung in die Kunst der Matlab-Programmierung.

Alessandro Vindigni, Danilo Pescia und Sergio Cannas für viele interessante Diskussionen und Hinweise.

Christoph Strunk, Jascha Repp, Günther Bayreuther und Dieter Weiss für die Beantwortung einiger fachlicher Fragen, insbesondere *Christoph Strunk* für das Korrekturlesen einer Publikation.

dem Lehrstuhl Back für die erfolgreiche und angenehme Zusammenarbeit.

Einen großen Dank schulde ich meinen Eltern und Schwiegereltern, die mich und meine Familie so gut es ging unterstützten und uns immer den Rücken frei hielten.

Mein herzlichster Dank gilt meiner Familie, Stefanie, Elisabeth und Luis. Vielen Dank für das Leben mit euch.